Constraints on the thermal conditions within the cratonic lithospheric mantle through time

PhD thesis

2022

Brendan C. Hoare

Trinity College Dublin
Coláiste na Tríonóide, Baile Átha Cliath
The University of Dublin

I declare that this thesis has not been submitted as an exercise for a degree at this or any other university and it is entirely my own work.

I agree to deposit this thesis in the University's open access institutional repository or allow the Library to do so on my behalf, subject to Irish Copyright Legislation and Trinity College Library conditions of use and acknowledgment.

I consent to the examiner retaining a copy of the thesis beyond the examining period, should they so wish (EU GDPR May 2018).

Brendan C. Hoare

TABLE OF CONTENTS

Commonly used acronyms

BSE – back-scattered electron (in reference to the imaging technique)

CL – cathodoluminescence

DI – diamond inclusion

EDS / SEM-EDS / SEM-EDX – energy dispersive x-ray spectroscopy via scanning electron microscopy

HPE – the key heat producing radioelements (K, Th and U) found within the Earth

KDE – kernel density estimation

LAB – lithosphere-asthenosphere boundary

LA-(Q)-ICP-MS – laser ablation (quadrupole) inductively coupled plasma spectrometry

MARID – mica-amphibole(K-richterite)-rutile-ilmenite-diopside, a modally metasomatised rock suite common to South Africa

MSWD – mean squared weighted deviation, where MSWD values ~ 1 indicate the data fit a univariate normal distribution expected of a single age population. MSWD > 1 indicate the observed data (age) scatter exceeds that predicted by the analytical uncertainties and are 'over-dispersed' indicating greater geological complexity than would be expected for a univariate normal distribution of a single age population. MSWD < 1 show an observed data scatter is less than that predicted by the analytical uncertainties and are 'under-dispersed' indicating analytical errors are overestimated.

PIC – phlogopite-ilmenite-clinopyroxene, a modally metasomatised rock suite common to South Africa

PKP – phlogopite-K-richterite-peridotite, a modally metasomatised rock suite common to South Africa

ppb – parts per billion

ppm – parts per million

PT – pressure-temperature

TIMS – thermal ionization mass spectrometry

$\boldsymbol{T_p}$ – Mantle potential temperature. The temperature the mantle would have at the surface, if it ascended along an adiabat without undergoing melting, the intercept of a geotherm and the isentrope defined by the T_P gives an estimate to the depth to the LAB.

Constraints on the thermal conditions within the cratonic lithospheric mantle through time

Brendan C. Hoare

SUMMARY

The stabilization of Earth's first continents is inescapably linked to the formation of the ancient cratonic lithospheric mantle. The cratonic lithospheric mantle is widely considered to have formed as a residue of extreme degrees of melting of the early mantle, which is not seen today. Such high degrees of melting inevitably lead to extreme depletion in Al_2O_3, CaO, FeO, Na_2O (i.e., basaltic components) and incompatible trace elements including the major heat-producing elements (HPE), K, Th and U. The depletion of HPE allows for the stabilization of a cool lithosphere whilst the extraction of dense basaltic components promotes a positive buoyancy that has been suggested to offset the negative buoyancy imparted from low temperatures observed in the thick cratonic root; the so-called 'isopycnic' hypothesis (Jordan, 1988). The longevity of Earth's cratons has led to several implicit assumptions about the thermal conditions in the lithosphere. These assumptions (summarized in Chapter 1) are:

1) Geothermal gradients or 'geotherms' within the cratonic lithosphere have remained similar throughout Earth's history,
2) The cratonic lithosphere has remained of similar thickness since formation,
3) That the internal radiogenic heat production in the cratonic mantle either real (i.e., generated by reintroduction of HPE by metasomatism) or 'apparent' (i.e., resulting from the thermal disequilibrium of the crust and lithospheric mantle) is essentially zero,

Yet, all three of these assumptions fail to consider the effect of the Earth's dynamic thermal evolution or the systemic refertilization of the cratonic lithosphere globally. Secular cooling of the Earth is an inescapable planetary phenomenon resulting from both the decrease in radioactive decay of radioelements through time and the gradual loss of primordial heat left over from accretion. Indeed, most current models of terrestrial mantle evolution propose that 2.7 Ga, the mantle potential temperature (T_p) of the convecting mantle was 150-200 °C warmer than today.

Chapter 2 of this thesis tackles the first two assumptions made of the cratonic lithosphere by modelling the effects of secular cooling on lithospheric geotherms within the Kaapvaal Craton of South Africa. It is found that geotherms in a secularly evolving lithosphere cannot be reconciled with either Proterozoic xenolith or diamond inclusion (DI) pressure-temperature (*PT)* conditions recorded in the Kaapvaal Craton, the latter finding irrespective of diamond age. Rather, to explain the *PT* conditions recorded by DIs from the Kaapvaal Craton it is required that the early lithosphere was substantially thicker than what is preserved today and that the geothermal gradients in the lithosphere have changed dramatically through time. Depending on the age of diamond formation and the prevailing mantle T_p at that time the total thickness of Kaapvaal Craton could have reached up to ~350 km.

Chapter 3 of this thesis investigates the timing of metasomatism (that may reintroduce HPE) in the Kaapvaal Craton. The mica-amphibole(K-richterite)-rutile-ilmenite-diopside (MARID) and the presumably

related phlogopite-K-richterite-peridotite (PKP) suites are examples of the most extreme modal metasomatism seen in the cratonic mantle with extreme HPE abundances. Due to a paucity of natural mineral chronometers in cratonic mantle xenoliths these rocks are attractive prospects to sense metasomatic events in the lithospheric mantle due to their hosting of zircon, which can be dated by the U-Pb method. Zircon ages recorded in these rocks fail to provide evidence of any metasomatic events that predate the Mesozoic as is demonstrated by previous workers, despite the significantly larger samples sizes of this study (n = > 40). Accordingly, HPE-rich metasomatism in the Kaapvaal Craton appears as a reflection of complex metasomatism at shallow levels of the lithosphere in response to the passage of orangeite and kimberlites magmas during the Cretaceous.

Chapter 4 of this thesis presents thermodynamic modelling of the Kaapvaal and Slave lithospheres using the heat equation to assess the potential for a non-zero internal radiogenic heat production of the cratonic lithospheric mantle. The resulting analysis suggests that both the Slave and Kaapvaal Cratons appear to have a relatively high internal radiogenic heat production (H_m) of between 0.04 and 0.05 μW/m^3 near to the present-day (i.e., post Mesozoic time). Similarly, mantle xenoliths from the 1.15 Ga Premier kimberlite suggest comparable high values of H_m (~ 0.04 μW/m^3) earlier in the Kaapvaal Craton's history. In the Archean, as such values would not allow for stabilization of an extensive diamond-hosting root earlier than 2.5 Ga. The first possibility is that the high H_m values modelled for the Slave and Kaapvaal Cratons, derives from an 'apparent' heat production resulting from the thermal disequilibrium of the crust and lithospheric mantle. A second scenario is that the H_m reflects real radiogenic heat production in the mantle lithosphere through the later metasomatic refertilization of the cratonic mantle with K, Th and U. The former scenario is favoured because: 1) an 'apparent' radiogenic heat production can be generated even if the lithospheric mantle has zero internal radiogenic heat production, which is required for craton stabilization and consistent with the low abundance of HPE in reconstituted peridotites ; 2) it would be required that both the Slave and Kaapvaal Cratons have similar metasomatic histories, which is unlikely; and 3) high HPE metasomatism of the Kaapvaal is seemingly restricted to the recent past (e.g., Chapter 3).

Finally, Chapter 5 of this thesis provides a new U-Pb methodology for dating pyrope garnet from mantle xenoliths to provide emplacement ages of their host kimberlite. Despite low U-concentrations (mostly < 0.1 ppm), sub-concordant mantle derived garnets can be dated using very large laser ablation spots (130 μm) measured by ICPMS. In both locations of the study, the U-Pb lower-intercept discordia ages of garnet, 84.1 ± 7.1 Ma at Bultfontein and 116.3 ± 15.8 Ma at Roberts Victor, reproduce previous emplacement ages. These ages imply that the garnet U-Pb system was open during mantle residence due to high ambient temperatures, and this inference is reinforced by Ni-thermometry data which indicate high equilibration temperatures (950 - 1075 °C). Yet, a discordia fit through garnets from the Roberts Victor separate also yields an upper-intercept age of 2560 ± 490 Ma, indicating that some ancient Pb was retained. This interpretation may be supported by Ni-thermometry data, which indicate much lower equilibration temperatures for some Roberts Victor garnet (~ 850°C). Our analytical protocol is not complex and uses widely available analytical methods. If applied to pyrope-rich garnet inclusions in diamond, it may be possible to provide ages of garnet-entrapment and thus diamond-growth if the U-Pb system remains undisturbed.

Chapter 1: Context of Thesis

The stabilization of the first continental landmasses is inexorably linked to the formation of Earth's ancient cratons, which form the ancient nuclei of the present-day continents (Fig. 1,1). Whilst the oldest preserved extant continental crust formed at 4 Ga (Bowring and Williams, 1999) and yet older continental materials dated to as early as 4.4 Ga (Wilde et al., 2001), the vast majority of the cratonic crust (see Kamber, 2015) and underlying lithospheric mantle formed in the mid to late Archean (see Pearson and Wittig, 2008). The coming of the continents and formation of the cratons has had a profound effect on Earth, impacting relative sea-level and climate change, continental dynamics, the endowment of significant mineral resources (e.g., diamond) in addition to hosting the first extant examples of terrestrial life (e.g., Allwood et al., 2006). The thermal structure of the continental lithosphere also plays a fundamental role in how the Earth dissipates heat through its history.

Yet, what precisely defines a craton? Surprisingly no conclusive definition exists. The name craton itself derives from the Greek term *krátos* literally 'power' or 'strength', somewhat prescient considering their now established long-term tectonic stability. Early geologists that set foot on Earth's cratons acknowledged that there is something altogether 'different' about these rocks which is distinct to that of orogenic continental crust formed in mountain-forming processes (Kamber, 2015; Kamber and Tomlinson, 2019). That cratonic crust was in some way special was confirmed by the pioneering dating studies in the early 70's confirming their great age and consequently their longevity (Black et al., 1971; Moorbath et al., 1972, 1973) with later complementary findings for the age of the underlying cratonic lithospheric mantle (e.g., Walker et al., 1989; Pearson et al., 1995b, 1995a). With the advent of global seismic tomography models, another defining characteristic of cratons, their anomalous thickness (~200 km) at least to post Archean lithosphere, has become apparent (Fig. 1.1). Recent suggestions expand the definition of cratons to encompass ~150 km thick Paleoproterozoic mobile belts (Pearson et al., 2021), whilst the formation of thick mantle roots underlying the Himalayas at the present day have been argued to be akin to a 'modern' cratonic lithosphere (McKenzie and Priestley, 2008, 2016). The inclusion of thick post Archean lithosphere under a cratonic 'umbrella' is complicated by the fact that Archean lithosphere hosts almost all of Earth's diamonds and

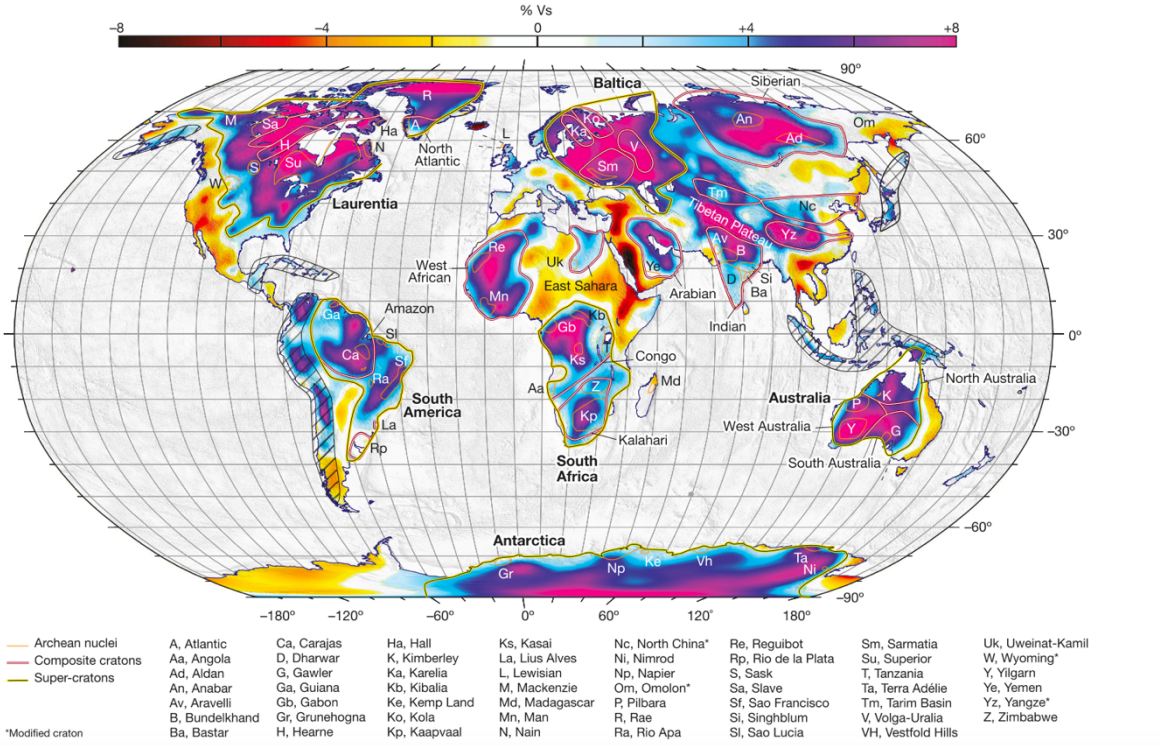

Figure 1.1: From Pearson et al. (2021). Global S-wave tomographic slice at 150 km depth within the Earth, displaying the fast wave-speed anomalies of deep cratonic mantle root (in shades of blue and purple). Asterisks identify modified cratons where ancient crust is underlain by recently thinned lithosphere (e.g., North China Craton). Composite cratons comprise multiple Archean nuclei/cratons (e.g., the Kalahari 'supercraton' and amalgamation of the Kaapvaal and Zimbabwe cratons.

the vast majority of its gold deposits (e.g., Clifford, 1966), which should support a notion that thick Archean lithosphere is indeed 'different' from their later (e.g., Paleoproterozoic or orogenic) equivalents. Nonetheless, in this thesis a craton is loosely defined as an old (i.e., Paleoproterozoic-Archean) thick (~150 km) coherent tectonically stable piece of continental lithosphere.

That cratons have remained stable to this day, and mostly unchanged for over half of Earth's history, requires anomalous characteristics that have promoted its longevity and survival, at least compared to post Paleoproterozoic-Archean lithosphere (which consensus suggests undergoes greater degrees of recycling; see Fig. 1 of Korenaga, 2018). The anomalous thickness of the cratonic lithosphere is widely considered to be a product of very high degrees of melting (~ 40 %) in the convecting mantle (e.g., Boyd and Mertzman, 1987; Boyd, 1989) that is simply not seen today. Such extreme melting led to a strong buoyant and extreme residue with strong depletion in Al_2O_3, CaO, FeO, Na_2O (i.e., basaltic components) and incompatible trace elements including the major heat-producing elements (HPE), K, Th and U. Importantly, this also led to led to dehydration of the

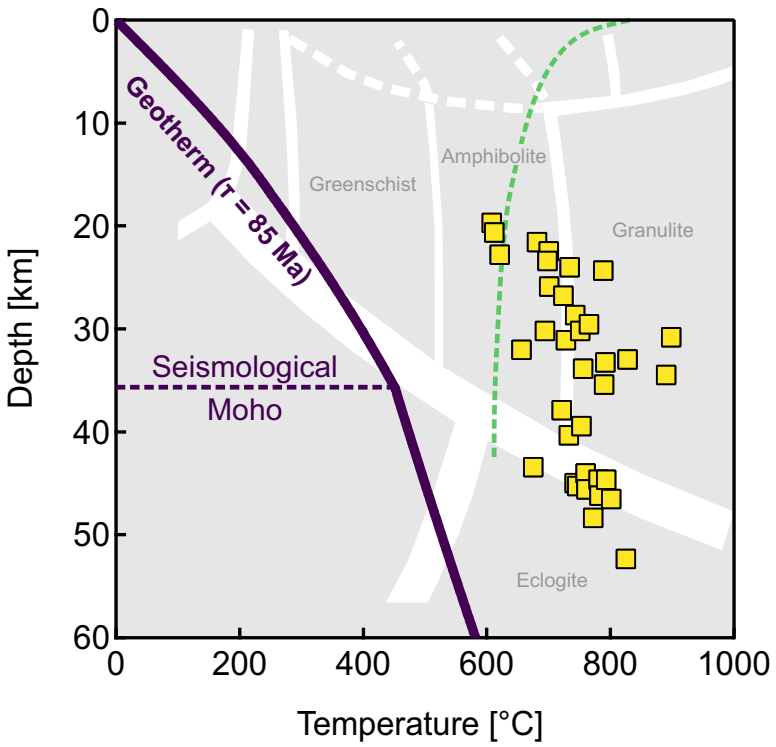

Figure 1.2: Peak *PT* conditions recorded in lower crust xenoliths with Archean age systematics from the Kaapvaal Craton, South Africa. Also shown is a crustal and uppermost lithospheric mantle geotherm for an expected lithospheric thickness of *196* km (for details concerning the parameters used in its calculation see Chapter 2 of this thesis). Seismological Moho from James et al., (2003). Crustal xenolith data from Huang et al., (1995) and Semprich and Simon, (2014).

chemically depleted mantle residue with respect to H_2O which also led to a high viscosity contrast between the cratonic lithosphere and underlying (e.g., Hirth et al., 2000; Peslier et al., 2010) producing a buoyant and viscous lithosphere (Doin et al., 1997; Sleep, 2003) compared to the underlying convecting mantle. It is argued that the positive buoyancy conferred from a high degree of melt depletion offsets the negative buoyancy imparted from low temperatures observed in the thick cratonic root; the so-called 'isopycnic' hypothesis (Jordan, 1975, 1988), whilst high depletion in HPE allowed for stabilization of a cool mantle lithosphere (Michaut et al., 2007). Collectively, the low internal heat production and depleted compositions of cratonic mantle led to their longevity in promoting cool temperatures and rheological properties in the lithospheric root that greater resists recycling. Yet, as with their definition, the formation of cratons remains controversial. The favoured hypothesis of craton formation proposes that shallow (< 3 GPa) melt depletion in either mid-ocean ridges or suprasubduction zones leads to the 'stacking' and imbrication of highly depleted oceanic mantle or arc residues (Helmstaedt and Schulze, 1989; Canil, 2004; Herzberg, 2004; Lee, 2005; Pearson and Wittig, 2008). An

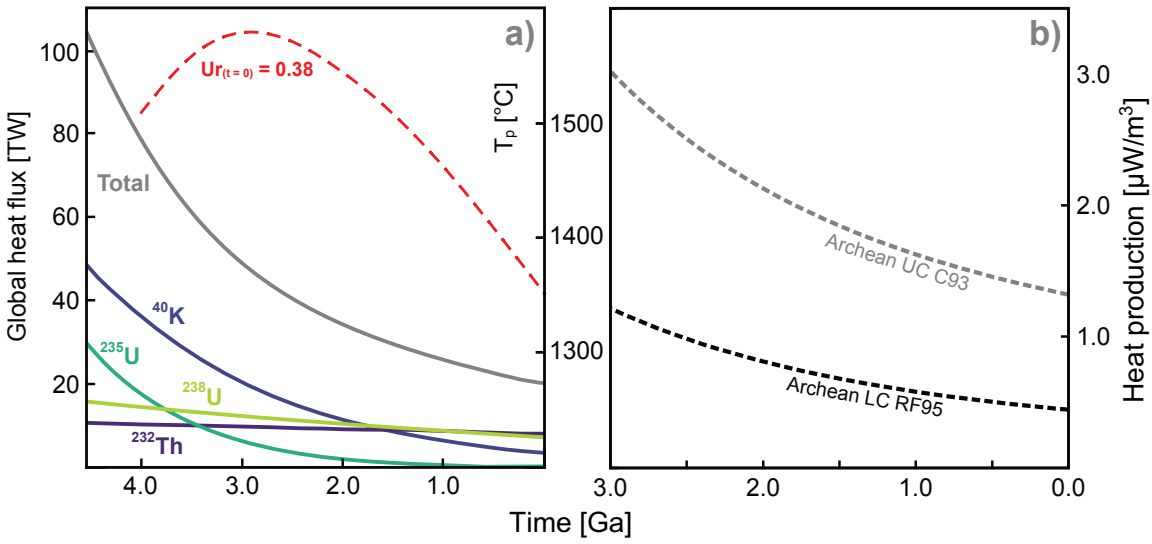

Figure 1.3: a) Global heat flux (in TW) at the Earth's surface as a function of the contribution of radioactive decay within the Earth through time from the principal heat-producing radioisotopes ^{40}K, ^{232}Th, ^{235}U and ^{238}U, adapted from Arevalo et al. (2009). Also shown is the evolution of the mantle potential temperature (T_p) as proposed by Korenaga, (2008) and Herzburg et al., (2010) for a present day convective Urey ratio ($Ur_{(t=0)}$) of 0.38. b) The internal heat production of the upper (UC) with a ρ = 2.75 g/cm^3 of and lower crust (LC) with a ρ = 2.86 g/cm^3 as a function of radioactive decay within the Earth through time. RF95: Archean intermediate granulitic LC of Rudnick and Fountain, (1995); C93: Archean UC (exposure) of Condie, (1993).

alternative scenario posits that cratons form as a residue of melting in at varying depths within mantle plumes that would indicate that it forms in-situ (Aulbach et al., 2007; Arndt et al., 2009; Griffin et al., 2009b; Kamber and Tomlinson, 2019; Tomlinson and Kamber, 2021).

The long-term survival of Earths cratons has led to several (often implicit) assumptions about the past and present state of the thermal conditions within the ancient lithosphere. Firstly, it is commonly assumed that the geothermal gradients or 'geotherms' within the cratonic lithosphere have remained constant through time. Secondly, it is assumed that the cratonic lithosphere has remained of constant thickness. And thirdly is assumed that the cratonic lithospheric mantle has a very low or zero internal radiogenic heat production. The first assumption largely derives from the ubiquitous formation and survival of diamond in the cratonic mantle globally since the Archean (e.g., Richardson et al., 1984, 2001, 2004; Pearson et al., 1998, 1999; Stachel et al., 2006; Westerlund et al., 2006; Aulbach et al., 2009b; Smart et al., 2016; Koornneef et al., 2017). However, a non-changing geotherm in the cratonic lithosphere through time hard to reconcile with peak *PT* conditions recorded on-craton Archean lower crustal xenoliths (e.g., Huang et al., 1995; Davis et al., 2003; Semprich and Simon, 2014), which testify to far higher

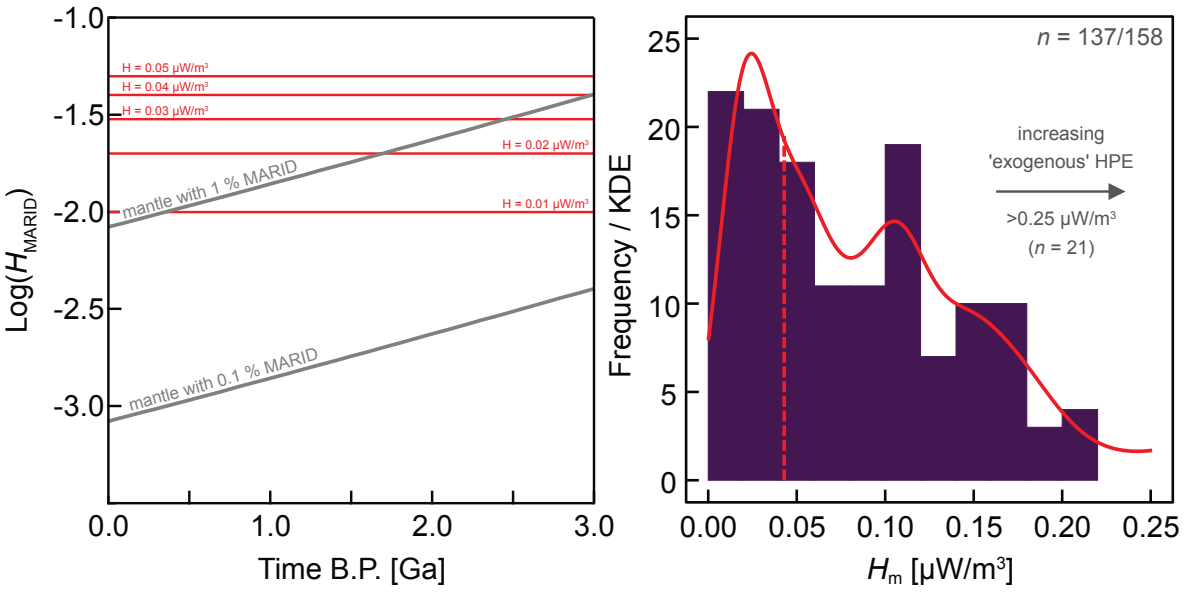

Figure 1.4: a) Log heat production of MARID xenoliths assuming 1% and 0.1% abundance in the cratonic lithosphere through time. b) internal radiogenic heat production of cratonic peridotites measured directly from K, Th and U contents for a ρ = 3.3 g/cm^3. Data in a) from Fitzpayne et al., (2018a) and b) from the GEOROC database (http://georoc.mpch-mainz.gwdg.de/georoc/).

temperatures in the Archean crust than is expected today (Fig. 1.2). Similarly, most current models of terrestrial mantle evolution (e.g., Korenaga, 2008; Herzberg et al., 2010) propose that 2.7 Ga, the mantle potential temperature (T_p) was 150-200°C hotter than today (Fig. 1.3a). That the Early Earth was hotter in the Archean is an inescapable planetary phenomenon resulting from secular cooling because of both the decrease in radioactive decay of radioelements and the gradual loss of residual primordial heat left over from planetary accretion (Fig. 1.3a). As such both a warmer crust and underlying convecting mantle are simply impossible to reconcile with a lithosphere under steady state conditions and the temperatures that allow for diamond formation (c. 1250°C; Day, 2012) in the cratonic lithosphere at depths of ~150 km since the Archean. Yet despite this clear evidence to the contrary, the assumption of similar geothermal gradients in the cratonic lithosphere remains entrenched in the petrological community, leading to the wide adoption of time-insensitive steady state geotherms and, consequently, lithosphere models with unchanged internal temperatures and thicknesses through time. Despite the assumption that the cratonic lithosphere has remained of constant thickness through time there are obvious cases where cratonic lithospheric mantle has been thinned or even thickened after earlier stages of thinning (Liu et al., 2021).

Mechanisms driving thinning and the destruction of ancient cratonic lithosphere include thermomechanical erosion via vigorous convection, basal drag or edge-driven

convection (Artemieva and Mooney, 2002; Kjarsgaard et al., 2017), rifting (e.g., Tappe et al., 2007; Larsen et al., 2009), interaction with upwelling mantle plumes (e.g., Celli et al., 2020) or refertilization by fluids/melts from subducted lithosphere (e.g., Wu et al., 2019). Combinations of the above, have destroyed the ancient cratonic lithosphere below the North China, Wyoming and Dharwar Cratons as well as parts of the Superior Craton (e.g., Darbyshire et al., 2007; An et al., 2009; Griffin et al., 2009a; Dave and Li, 2016). More localised thinning is indicated by recent seismic imaging of the Kaapvaal and Zimbabwe cratons (Celli et al., 2020), whilst rifting has split the North Atlantic Craton asunder along the Davis Straight into Greenlandic and Canadian sections (Tappe et al., 2007; Larsen et al., 2009). Almost all these mechanisms drive changes in composition (metasomatism and the introduction of H_2O) and rheology in the lithosphere that serve to further weaken the cratonic root meaning that, despite their age, cratons aren't necessarily forever. However, that the cratonic lithosphere can only experience damage and destruction since its formation has been questioned with 'plume-driven re-cratonization' of previously thinned lithosphere also argued to occur (Liu et al., 2021). Therefore, an assumption of cratons with near constant thickness through Earth's history is highly questionable.

A final assumption, that the cratonic lithospheric mantle has an internal radiogenic heat production of close to zero, is more reasonable. The formation of the cratonic lithospheric mantle as a residue of > 40 % melting of the convecting mantle precludes significant HPE contents and is a pre-requisite for the formation of thick lithosphere (Michaut et al., 2007, 2009). Even small values of internal radiogenic heat production in the mantle lithosphere can amount to a large contribution to the Moho heat flux when integrated across the whole mantle root (e.g., Chapter 4), an effect that would only increase with greater lithospheric thickness and farther back in time. The consequence of such a large contribution to the Moho heat flux from the underlying mantle lithosphere in effect impedes heat transfer from the convecting mantle through ancient continental lithosphere. When sufficiently large (a particular risk in the Archean) the integrated heat flux across the lithospheric mantle can be greater than that at the Moho producing a negative heat flux at the lithosphere-asthenosphere boundary (LAB), with the lithosphere acting to heat the underlying convecting mantle. This scenario generates 'turning' geotherms in the mantle lithosphere (i.e., a geotherm with a thermal maximum in the lithosphere rather than at its base) which is thermodynamically unstable and prone to delamination at mid-lithospheric depths (Michaut et al., 2007). Thus, an assumption of a near-zero heat production (< 0.01

μW/m^3) within the cratonic lithospheric mantle, at least at the time of its formation, seems entirely reasonable.

However, maintaining conditions of near-zero radiogenic heat production in the cratonic lithospheric requires that HPE are not reintroduced in later events (e.g., metasomatism). Metasomatism (i.e., the removal or addition of chemical constituents) is a widely documented process in the cratonic lithosphere globally and throughout Earth's history (e.g., Dawson, 1984). Enrichment of the cratonic lithosphere is most clearly demonstrated by modal metasomatism which involves the introduction of new phases and abundances (e.g.,, phlogopite, amphibole, garnet, clinopyroxene) that simply could not have remained in a residue of extreme melting. The introduction of these phases also acts to decrease the stability of the lithospheric root by increasing density and introducing H_2O potentially driving thinning and/or destruction of the lithospheric root. Perhaps the most conspicuous examples of modal metasomatism in the cratonic mantle are demonstrated by assemblages of mica-amphibole(K-richterite)-rutile-ilmenite-diopside (MARID) and the presumably related phlogopite-K-richterite-peridotite (PKP) xenolith suites common to South Africa (Dawson and Smith, 1977). It is clear from the isotopic compositions of MARID and PKP that the sampling of an ancient, enriched and probably subducted component is required in their genesis (e.g., Kramers et al., 1983; Hawkesworth et al., 1990; Banerjee et al., 2015). The concentration of HPE in MARID are *extremely* high (present-day median heat production = 0.84 μW/m^3, for ρ = 3.3 g/cm^3) larger than that of Archean lower crust (cf. Rudnick and Fountain, 1995; Fitzpayne et al., 2018a). Therefore, even a small proportion of such K-rich domains in the mantle can introduce a noticeable effect on the radiogenic heat production in the lithospheric mantle counter to the assumption of a near zero heat production in the mantle lithosphere, when calculated through time using Eq. 1.1:

$$H(t) = \left(3.48E-6 \times C_K \times e^{0.554t} + 0.0256 \times C_{Th} \times e^{0.495t} + C_U\left(0.9929 \times 0.0918 \times e^{0.1551t} + 0.0071 \times 0.576 \times e^{0.98485t}\right)\right)$$

[Eq. 1.1]

Where, H is the heat production in μW/m^3, C is the concentration of the elements K, Th and U in ppm and t is the time in the past (age) in Ga. Measurements of heat production in more refractory mantle peridotites are lower than in modally metasomatised xenoliths (Fig.

1.3), but often still high compared to the range of present-day values of 0.00 – 0.025 $\mu W/m^3$ that are thought to favour stabilization of a thick lithosphere in the Archean (Michaut and Jaupart, 2007). These values themselves are likely masked by significant contamination of the peridotite by vastly more HPE-rich kimberlites during their transport to the surface. Therefore, the actual radiogenic heat budget of the lithospheric remains poorly defined and cannot be easily defined through direct measurement. Another consideration is that of 'apparent' or pseudo heat production in the lithospheric mantle, which refers to the contribution from radiogenic heat produced earlier in Earth's cooling history but not yet lost by diffusion (Chapter 4). The radiogenic heat production of the Earth decreases by a factor of 2 in about ~ 2.5 Ga which is a similar timeframe for heat to diffuse through a 250 km thick lithosphere. As a result, thermal equilibrium is not met in the lithosphere (Michaut and Jaupart, 2004). The effect of this thermal disequilibrium is to increase the curvature of the mantle portion of lithospheric geotherm, in effect generating an 'apparent' internal heat production in the lithospheric mantle and conditions that deviate from steady state. Thus, even in circumstances where the lithospheric mantle has had zero internal heat production since its formation it can appear to have so. Collectively, these assumptions lead to a somewhat 'uniformist' lithosphere that is essentially unchanged through time. This thesis aims to investigate the validity of the assumptions made with respect to the thermal conditions within the Earth's ancient cratonic lithosphere and if or how these may have evolved through time.

Co-Author Statement and Layout of Thesis

The core chapters (2-4) of this thesis are comprised of one published paper (Chapter 3), one accepted manuscript pending revision (Chapter 2), and one manuscript draft (Chapter 4). I am the lead author of the three manuscripts, the work of which was undertaken and produced during the duration of the PhD at Trinity College Dublin. As the lead author of these manuscripts, I was responsible, where applicable, for sample preparation and analysis, mathematical modelling, data collection reduction and interpretation, and all stages of manuscript preparation through to submission. I am also second author on a publication that is in advanced stage of draft (Chapter 5). A list of other published works produced during my PhD study is also provided. The contributions from each co-author for the core chapters are outlined below in order of the published or proposed author list as are my contributions to Chapter 5:

Chapter 2: Improved Steady-State Thermal Evolution Models of the Earth's Cratonic Lithosphere Through Time

Dr Emma L. Tomlinson: Supervision, conceptualization, manuscript review and editing,
Dr Balz S. Kamber: Conceptualization, manuscript review and editing,

Chapter 3: Metasomatism of the Kaapvaal Craton During Cretaceous Intraplate Magmatism Revealed by Combined Zircon U-Pb Isotope and Trace Element Analysis

Dr Gary J. O'Sullivan: Conceptualization, PCA code for interpretation of trace element data, interpretation of trace element data, manuscript review and editing,
Dr Emma L. Tomlinson: Supervision, manuscript review and editing, interpretation of trace element data,

Chapter 4: Real or 'Apparent' Radiogenic Heat Production in the Cratonic Lithospheric Mantle

Dr Emma L. Tomlinson: Supervision, conceptualization, manuscript review and editing,
Dr Balz S. Kamber: Conceptualization, manuscript review and editing (future),

Chapter 5: Pyrope Garnet U-Pb dating: A Mantle and Kimberlite-Emplacement Chronometer

Brendan C. Hoare: Conceptualization; SEM-EDX analysis; LA-ICP-MS data collection; LA-ICP-MS data reduction (in part); Manuscript writing (in part), review and editing,

Other published works completed during the duration of the PhD:

O'Sullivan, G.J., Daly, J.S., Murray, J., Ó'Gogáin, A., Chew, D.M., Drakou, F., Guyett, P.C., Badenszki, E. and **Hoare, B.C.,** 2021. Uranium–lead phosphate chronostratigraphy: A proof of concept from the mid-Carboniferous boundary. *Sedimentary Geology, 422,* p.105961.

O'Sullivan, G.J., Thakurdin, Y., Bolhar, R., Horváth, P., **Hoare, B.C.,** and Collerson, K.D., 2021. The Great Falls Tectonic Zone after the assembly of Laurentia: evidence for long-term tectonic stability from xenolith apatite. *Lithos, 384*, p.105977.

Hoare, B.C., Tomlinson, E.L., Barnes, J.D., Tappe, S., Marks, M.A., Epp, T., Caulfield, J. and Riegler, T., 2021. Tracking halogen recycling and volatile loss in kimberlite magmatism from Greenland: Evidence from combined F-Cl-Br and δ37Cl systematics. *Lithos, 384*, p.105976.

Corbett, E.P., Simonetti, A., Shaw, P., Corcoran, L., Crowley, Q.G. and **Hoare, B.C.,** 2020. Shallow sampling by multi-shot laser ablation and its application within U-Pb zircon geochronology. *Chemical Geology, 544*, p.119568.

Tomlinson, E.L., Kamber, B.S., **Hoare, B.C.,** Stead, C.V. and Ildefonse, B., 2018. An exsolution origin for Archean mantle garnet. *Geology, 46(2),* pp.123-126.

Chapter 2: Steady-state thermal evolution models of the Earth's cratonic lithosphere

Brendan C. Hoare[1], Emma L. Tomlinson[1], Balz S. Kamber[2]

[1] Department of Geology, Trinity College Dublin, Dublin 2, Ireland

[2] School of Earth and Atmospheric Sciences, Queensland University of Technology, Brisbane, QLD, Australia

Keywords: Geotherm models; diamonds; craton; heat flow; continents

This work is currently accepted pending revision for publication in *Earth and Planetary Science Letters.*

Abstract

The presence of peridotitic (P-type) diamonds of Archean age within the cratonic lithosphere is a surprising, if not paradoxical, observation because their formation and survival required the early mantle lithosphere to have been cool and remained so to the present-day. This observation has led to the widely held concept that geothermal gradients within Archean cratons were similar to the present-day. However, the inescapable effects of secular cooling and the time-dependent decrease of radioactivity within the Earth, make it unrealistic to expect that steady state geotherms in the Archean lithosphere were the same as today. Here we model the effects of a thermally evolving Earth on lithospheric geotherms within the Kaapvaal Craton of South Africa. We modelled geotherms from the present-day conditions backward in time to 3.0 Ga under steady state by (i) calculating crustal heat production according to half-lives of the major heat producing radioisotopes; (ii) investigating the effects of secularly changing mantle potential temperature (T_p) in the underlying convecting mantle; and (iii) varying either the depth of the lithosphere-asthenosphere boundary (LAB) or the heat flow at the LAB. The computed results were evaluated with respect to pressure-temperature (*PT*) conditions recorded in mantle xenoliths of recent and Proterozoic age in addition to P-type diamond inclusions (DI). We find that geotherms in a secularly evolving lithosphere cannot be reconciled with either Proterozoic xenolith or DI *PT* conditions recorded in the Kaapvaal Craton, irrespective of the real diamond age. Rather, to explain the *PT* conditions recorded by DIs from the

Kaapvaal Craton it is required that the original early lithosphere was substantially thicker than what is preserved at the present-day. Depending on the age of diamond formation and the prevailing mantle T_p at the time the total thickness of Kaapvaal Craton could have reached up to ~350 km. If the Kaapvaal Craton is a representative analogue, it is likely that cratons attained their maximal vertical extent early in their history and that they have been variably eroded and weakened ever since.

2.1 Introduction

Diamond is stable in the Earth's mantle at elevated pressure and low to moderately high temperature. At a depth of 150 km, diamond stabilises at ~1250°C (Day, 2012), conditions that are found mostly in the present-day deep cratonic lithosphere. However, it is also apparent that peridotitic (P-type) diamond was already widely stable back in the Archean. Detrital diamond exists in 2.8 to 3.0 Ga alluvial deposits in South Africa (Robinson, 1979; Poujol et al., 2003) and in 2.7 Ga meta-lamprophyres and conglomerates in the Superior craton of Canada (e.g., Stachel et al., 2006), whilst dating of diamond inclusions (DI) has yielded mostly Archean ages in most cratonic regions (e.g., Richardson et al., 1984, 1993; Koornneef et al., 2017; Howell et al., 2020). The presence of diamond in the Archean cratonic lithosphere is surprising, if not paradoxical, because it dictates that at least some deep lithosphere must have been relatively cool at formation and remained so ever since.

This observation has led to the wide adoption of time-insensitive cratonic geotherms and, consequently, lithosphere models with unchanged internal temperatures and thicknesses through time. However, due to secular planetary cooling, temperatures within the cratonic lithosphere would be expected to have been substantially higher in the Archean. In the absence of insulation from an originally substantially thicker lithosphere during the Archean, the pressure-temperature *(PT)* conditions within the cratonic mantle should have been inhospitable for diamond formation (Ballard and Pollack, 1988). Secular cooling of the Earth is an inescapable planetary phenomenon resulting from both the decrease in the radioactive decay of radioelements and the gradual loss of any residual primordial heat left over from accretion. Most current models of terrestrial mantle evolution propose that prior to 2.7 Ga, the mantle potential temperature (T_p) was 150-200 °C hotter than today (e.g., Korenaga, 2008; e.g., Herzberg et al., 2010) in apparent contradiction of subdued temperatures within the overlying Archean mantle lithosphere.

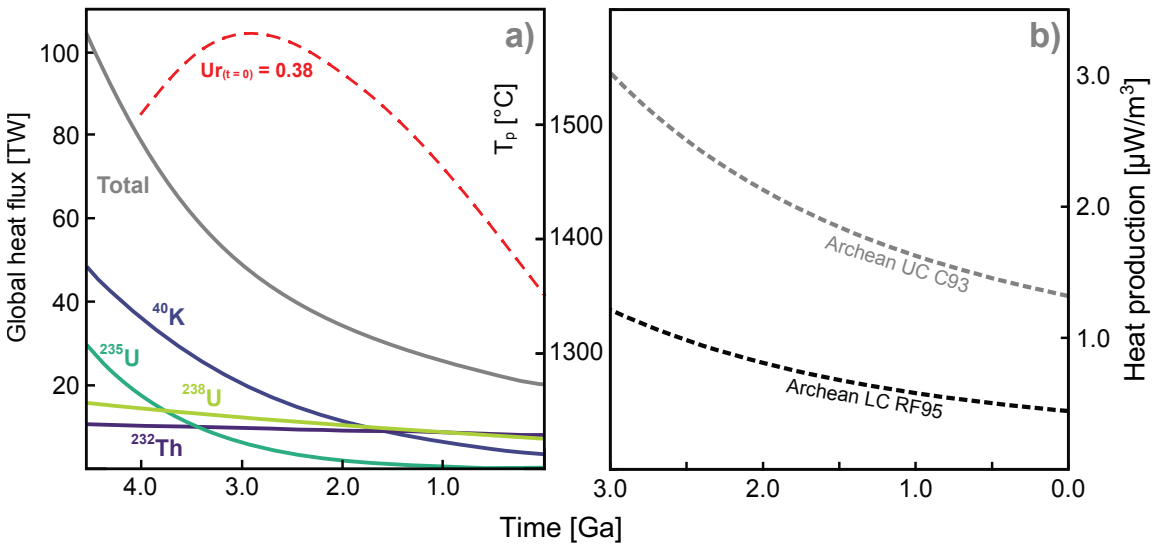

Figure 2.1: a) Global heat flux (in TW) at the Earth's surface as a function of the contribution of radioactive decay within the Earth through time from the principal heat-producing radioisotopes ^{40}K, ^{232}Th, ^{235}U and ^{238}U, adapted from Arevalo et al. (2009). Also shown is the evolution of the mantle potential temperature (T_p) as proposed by Korenaga, (2008) and Herzburg et al., (2010) for a present day convective Urey ratio (Ur$_{(t = 0)}$) of 0.38. b) The internal heat production of the upper (UC) with a ρ = 2.75 g/cm^3 of and lower crust (LC) with a ρ = 2.86 g/cm^3 as a function of radioactive decay within the Earth through time. RF95: Archean intermediate granulitic LC of Rudnick and Fountain, (1995); C93: Archean UC (exposure) of Condie, (1993).

To date, the effect of the Earth's dynamic thermal evolution has only rarely been considered with respect to thermobarometry of potentially ancient DIs (but see Ballard and Pollack, 1988). Rather, *PT* data from DIs and mantle xenoliths of significant age (e.g., Proterozoic or older) are most commonly compared to fixed geotherm 'families' of present-day heat generation with differing surface (and mantle) heat fluxes and lithospheric thicknesses (e.g., Hasterok and Chapman, 2011). However, as these geotherm families are fixed at present-day conditions in the cratonic lithosphere they do not account for the expected dynamic thermal evolution of the Earth. The backward extrapolation of geotherm families based on present-day heat generation might be justified into the Proterozoic on account of the general similarity of *PT* conditions recorded by xenoliths from Proterozoic kimberlites with those derived from much more recently erupted xenoliths. Specifically, the ~ 1.15 Ga Premier kimberlite of the Kaapvaal Craton of South Africa contains mantle xenoliths with similar apparent equilibration *PT* conditions to those emplaced much more recently elsewhere in the Kaapvaal (Viljoen et al., 2009; cf., Mather et al., 2011). However, this observation alone does not justify extrapolation of similar cratonic geotherms back into the Archean. The difference in the contribution to the surface heat flux due to heat generation from the radioactive decay of ^{40}K, ^{232}Th, ^{235}U and ^{238}U within the Earth between 1 Ga and the present-day is a relatively modest ~ 5 TW (Fig.

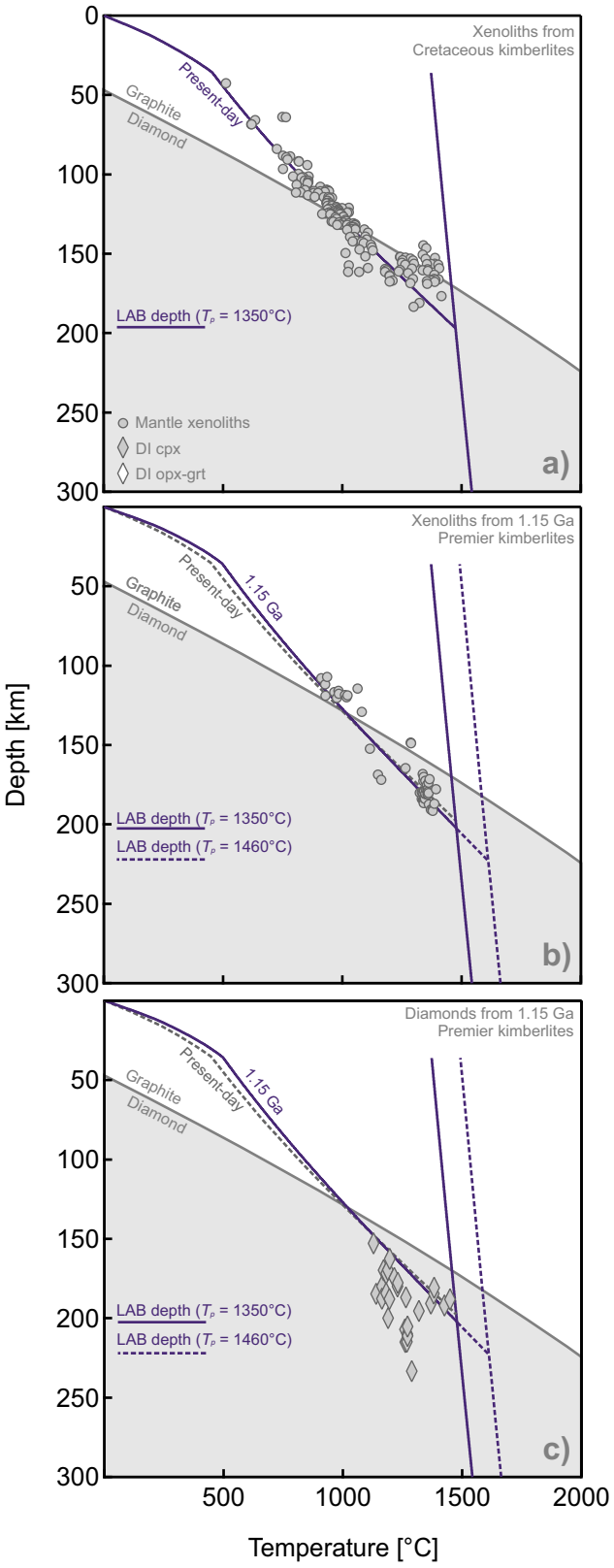

Figure 2.2: Semi-quantitative best-fitting geotherms for mantle xenoliths from Cretaceous (a) and Premier kimberlites (c), compared with diamond inclusions within Cretaceous kimberlites (b) and from the Premier kimberlite (d). For data references see the supplementary information of this article and Supplementary Figure 2. Graphite diamond transition after Day, (2012).

2.1a). However, from 1 to 3 Ga the difference in radioactive heat production is much more pronounced, with resulting contributions to the heat flow at the Earth's surface almost

doubling from 25 TW at 1 Ga to 48 TW at 3.0 Ga (Fig. 2.1a).

To appreciate just how problematic it is to not account for the secular evolution of heat generation within the Earth during the Archean, it suffices to consider heat production within cratonic crust alone. Consider a theoretical present-day cratonic crust of 35 km thickness differentiated into an upper crust of 17 km thickness with internal heat generation of 1.4 μW/m^3 and a lower crust of 18 km thickness with an internal heat generation of 0.4 μW/m^3. At the present-day this would contribute 31 mW/m^2 to surface heat flux. Using, K, Th and U abundances and K/U and K/Th ratios of 1.0 and 0.26 (where K is reported in Wt % and Th and U in ppm), derived from the global average of 3.5 to 2.5 Ga Archean upper crust (Condie, 1993), the theoretical crustal contribution to surface heat flow can be calculated back through time. From this, it can be demonstrated that the crustal contribution to the surface heat flux alone eventually surpasses typical present-day cratonic surface heat fluxes worldwide of ~ 36-50 mW/m^2 (Jaupart and Mareschal, 2007). Indeed, at 3.0 Ga the calculated crustal contribution to the surface heat flux in this example is 75.1 mW/m^2. Comparison of *PT* conditions recorded in DIs (likely of > 2 Ga age) to present-day steady-state thermal models is thus not valid, because this would require negative Moho heat fluxes in the ancient past. Motivated by the lack of more recent realistic estimates for ancient cratonic geotherms, this contribution presents modelling of the effects of a secularly cooling Earth for geotherms within the cratonic lithosphere of South Africa. We have modelled steady-state geotherms from the present-day conditions backward in time to 3.0 Ga by (i) calculating crustal heat production through time according to half-lives of the major heat producing radioisotopes (Fig. 2.1b); (ii) investigating the effects of secularly changing T_p in the underlying convecting mantle; and (iii) varying either the depth of lithosphere-asthenosphere boundary (LAB) or the heat flux at the LAB. The computed results were compared to *PT* conditions recorded in mantle xenoliths of near-modern and Proterozoic age and P-type DIs presumed to be mostly of Archean age. From this evaluation, conclusions are drawn regarding the original depth of the LAB and the chances of survival of Archean diamonds.

2.2 Methodology

Geotherm calculation

For the calculation of geotherms we followed the approach of Hasterok and Chapman (2011) as summarised below. For a specified lithospheric architecture (i.e., heat production,

layer divisions and thicknesses), thermal conductivity and surface heat flux, one dimensional steady-state geotherms can be calculated downward from the Earth's surface (T = 0°C) by solving the heat equation for the upper crust, lower crust and lithospheric mantle;

$$T_{i+1} = T_i + \frac{q_i}{\lambda_i}\Delta Z_i - \frac{A_i}{2\lambda_i}\Delta Z_i^2$$

[Eq. 2.1]

and,

$$q_{i+1} = q_i - A_i \Delta Z_I$$

[Eq. 2.2]

where A_i, λ_i, ΔZ_i, are the inter-layer heat production (in $\mu W/m^3$), inter-layer thermal conductivity (in W/m·K) and layer thickness (in km), respectively. The vertical column is divided into arbitrarily thin layers (0.1 km), for which properties can be considered constant. Temperature, T_{i+1} (°C) and the heat flux, q_{i+1} (mW/m^2) at the bottom of each layer are determined from the temperature, T_i, and heat flux, q_i at the top of each layer. The thermal conductivity model used in this study is presented in the supplementary material (Supplementary Figure 2.1).

The vertical extent of the lithosphere can either be set as an input parameter by iterating the surface and thus mantle heat flux or allowed to emerge as a result from a fixed mantle heat flux. The intercept of the calculated lithospheric geotherm and the isentrope, which is itself a reflection of T_p (Rudnick et al., 1998), provides the depth to the LAB. As explained earlier, T_p in our models was varied to explore the effect of secular cooling of the convecting mantle, for which we use a thermal model corresponding to a Urey ratio of 0.38 (from Korenaga, 2008). This thermal model has been argued to provide a good fit to petrological estimates of mantle potential temperature through Earth's past for non-arc lavas and komatiites of known age (Herzberg et al., 2010).

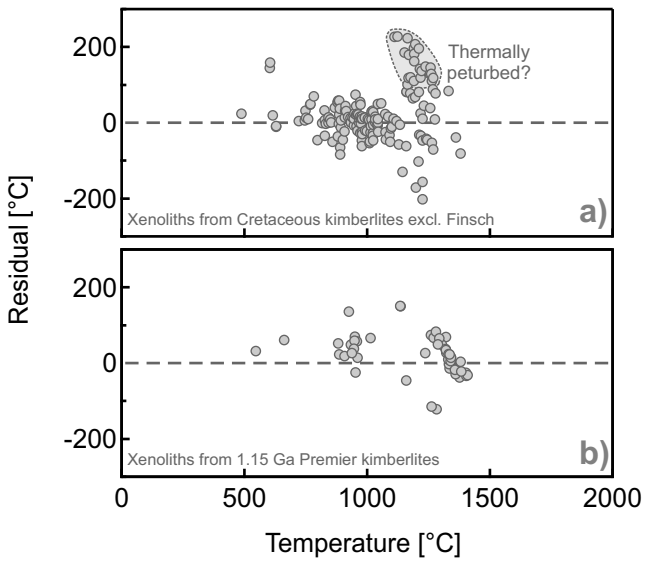

Figure 2.3: Residual plots for the semi-quantitative best fitting geotherms constructed from xenolith data for close-to-the-present-day (~ 85 Ma) and for Premier kimberlite (1.15 Ga).

In the strictest sense the geotherm/isentrope intercept does not quite coincide with the LAB because this is a projection of a purely conductive regime onto the isentrope. In reality, a thermal boundary layer exists between the lithosphere and asthenosphere (McKenzie et al., 2005) and the intercept of a purely conductive geotherm and the isentrope is therefore a minimum estimate of true lithospheric thickness. However, the resulting differences of a geotherm calculated with and without a thermal boundary layer has been argued to be minimal (McKenzie et al., 2005) and for simplicity is neglected.

Constraining the near-modern thermal state of the Kaapvaal Craton

As a starting point to secular modelling, we calculated an 'initial' geotherm that represents close-to-present-day (~ 85 Ma) thermal conditions in the Kaapvaal lithosphere. The input parameters for the calculation are listed in Table 2.1 and were selected to be consistent with what might be considered 'typical' of present-day Kaapvaal lithosphere. The internal heat production of the lithospheric mantle is the input parameter most difficult to determine due to conflicting estimates of K, Th and U concentration in mantle xenoliths. The problem derives from ubiquitous contamination of mantle xenoliths and secondary addition of heat-producing elements during ascent in host kimberlite. Such contamination explains the dichotomy in the measured heat production of mantle xenoliths sampled by basalts and kimberlites (Rudnick et al., 1998). The former have heat production values that are overwhelmingly low < 0.02 $\mu W/m^3$, compared to the much wider range and generally higher values (0 to 0.1 $\mu W/m^3$) seen in xenoliths transported by the vastly more incompatible element-rich kimberlites (Rudnick et al., 1998).

Instead of relying on arbitrary correction for contamination, we followed McKenzie et al. (2005) in working with an internal lithospheric mantle heat production of 0 $\mu W/m^3$. This dictates that the Moho heat flux is equal to that of our estimate through the LAB. With zero heat generation within the lithospheric mantle the effect of long-wavelength thermal transients (e.g., Michaut et al., 2007) is minimised in the lithosphere and thus steady state conditions can be assumed to be achieved over less than 500 Ma (Hasterok and Chapman, 2011).

The geotherm was compared to *PT* equilibration conditions in non-sheared mantle xenoliths from Cretaceous kimberlites, extracted from the database of Wu and Zhao (2011), which provides a good geographical cover of the Kaapvaal Craton (for information on thermobarometry see Supplemental Figure 2.2). The only *PT* data not considered were those of mantle xenoliths from Finsch, due to their peculiar offset towards lower temperatures. Possible causes for these anomalous data are discussed later.

The preferred near-modern geotherm (Fig. 2.2a) was obtained iteratively and yields the following parameters: a surface heat flux of 47.5 mW/m^2, a Moho and LAB heat flux of 16.4 mW/m^2 and a lithospheric thickness of 197 km. These results are defined by a modern T_p of 1350 °C (Korenaga, 2008). The model surface heat flux closely matches the independently derived 48 ± 8 mW/m^2 empirical average surface heat flux taken from 144 measurements over the geographical region of the Kaapvaal Craton. The geotherm produces a very reasonable fit to mantle xenolith *PT* data for xenoliths of < 150 km depth where a conductive steady state regime is expected to be in effect. Inspection of the residual plot between modelled and xenolith temperature (Fig. 2.3a) reveals a cluster of deep xenoliths plotting at 100-200 °C higher than the model geotherm. These most likely represent thermally perturbed xenoliths close to the LAB, widely interpreted to record transient (i.e., non-steady state) thermal conditions.

We opted to constrain the geotherm via close approximation to the known surface heat flux of the Kaapvaal Craton while achieving a semi-quantitative fit to *PT* data for xenoliths of < 150 km depth. The alternative would be to statistically minimise the misfit between the geotherm and the *PT* array from non-perturbed xenolith. This would require classifying xenoliths into pristine and thermally perturbed. This carries the risk of accidental inclusion of thermally perturbed data, which would artificially decrease the depth to the LAB. Regardless, our near-modern Kaapvaal Craton geotherm is similar to previous estimates from xenolith studies (e.g., Mather et al., 2011) and independent

estimates of LAB depth from geophysical studies (e.g., Muller et al., 2009). Therefore, we consider it to be a robust starting point, consistent with widely used earlier geotherms, for exploring fossil geotherms that were calculated back to 3.0 Ga at 0.5 Ga intervals.

Constraints from Proterozoic mantle xenolith samples and diamond inclusions

There are two key groups of empirical fossil *PT* constraints for validation of secular geotherms. The first is the ~1.15 Ga Premier kimberlite (Viljoen et al., 2009), which has brought mantle xenoliths and DIs to the surface. The xenoliths hold valuable information about the thermal state of the Kaapvaal lithosphere slightly more than 1 Ga The preferred steady state geotherm of the Kaapvaal Craton at the time of the emplacement of the Premier kimberlite at 1.15 Ga (Fig. 2.2c) was constructed analogously to the near-modern starting geotherm. Thus, the 1 Ga geotherm of our models should closely approximate the *PT* array from the 1.15 Ga Premier mantle xenoliths (Fig. 2.2c).

The second source of information are *PT* sensitive silicate DIs from the 1.15 Ga Premier kimberlite (for list of sources and method of thermobarometry is provided in the supplementary information of this submission). As such diamond inclusions from Premier must have formed, either at, or prior to 1.15 Ga. It is widely believed that the majority of Kaapvaal Craton P-type DIs have Archean entrapment ages (Richardson et al., 1984, 1993), albeit not exclusively (cf. Koornneef et al., 2017). The *PT* data available for Kaapvaal Craton DIs are therefore viewed to dominantly reflect the thermal state of the deep lithosphere in the Archean. There is a marked difference in kimberlite-hosted DI *PT* and peridotite xenoliths, with the former plotting well below both the near-modern and the 1.15 Ga Kaapvaal geotherms (Fig. 2.2b; 2.2d).

2.3 Results

Results of the geotherm calculations are presented as two classes of models. In the first, the heat flux across the Moho (and thus LAB) is fixed, allowing the lithospheric thickness to vary. In the second, the LAB depth is fixed, allowing the heat flux across the Moho (and LAB) to vary. The geotherms were generated by iteratively changing the surface heat flux until it reproduces the Moho heat flux (first class of models) or lithospheric thickness (second class of models) at each time window. All models were run for both an evolving (secularly cooling) convecting asthenosphere and for a fixed isentropic profile corresponding to the modern T_p of 1350 °C. For all models, the evolution of the 'diamond

window' (*PT* conditions in which formation of diamond can occur) is shown to afford easy assessment of compatibility with formation and preservation of diamond within cratonic lithosphere since the Archean as evidenced in many studies (see Howell et al., 2020).

Results from models with fixed LAB heat flux and variable lithospheric thickness

The fossil cratonic geotherms (in 0.5 Ga steps up to 3.0 Ga) are shown for the secularly cooling and fixed isentropes in in figures 2.4a and 2.4b, respectively. The key observation is that with the Moho/LAB heat flux held constant, the effect of increased internal heat production within the crust backward in time leads to significantly higher temperatures in the lithospheric root. This ultimately derives from the fact that, as energy transfer from the underlying mantle is constant through time, the increased heat production in the crust must be accommodated by increased temperatures in the cratonic mantle, such that at a depth of 120 km, the temperature at 3.0 Ga would have been ~ 400°C hotter than today, and this is regardless of whether the asthenosphere T_p was hotter than 1350 °C or not. In this scenario, diamond is not stable at any depth prior to ~ 2.25 Ga , in the case of secularly cooling mantle, and ~ 1.85 Ga , in the case of the fixed modern isentrope (Fig. 2.4i and 2.4ii). This prediction is in clear conflict with the ubiquity of Archean diamonds from cratonic lithosphere worldwide, including those in the Kaapvaal Craton (Richardson et al., 1984; Pearson et al., 1998; Koornneef et al., 2017).

The second clear outcome of the models with fixed Moho and LAB heat fluxes, regardless of T_p, is that the LAB is at its minimum depth in the Archean, but subsequently, in response to the decay of radioactive heat production in the crust, the lithosphere is predicted to have cooled and thickened (Table. 2.2). Secular thickening of the lithosphere since the Archean is in opposition to the vast majority of Lu-Hf and Re-Os ages found in depleted cratonic peridotites that show Archean stabilisation when unperturbed by later metasomatism (e.g., Pearson and Wittig, 2008).

A third observation is that the 1.0 and 1.5 Ga modelled lithosphere structures do a very poor job at reproducing the *PT* data from mantle xenoliths from the ~ 1.15 Ga Premier kimberlite. Firstly, because many xenoliths equilibrated at pressures corresponding to depths greater than the modelled LAB (Figs. 2.5a; b). This is particularly problematic for the model of a secularly cooling asthenosphere in which the LAB is < 185 km in the Mesoproterozoic. Secondly, even for the xenoliths that equilibrated at shallower depths

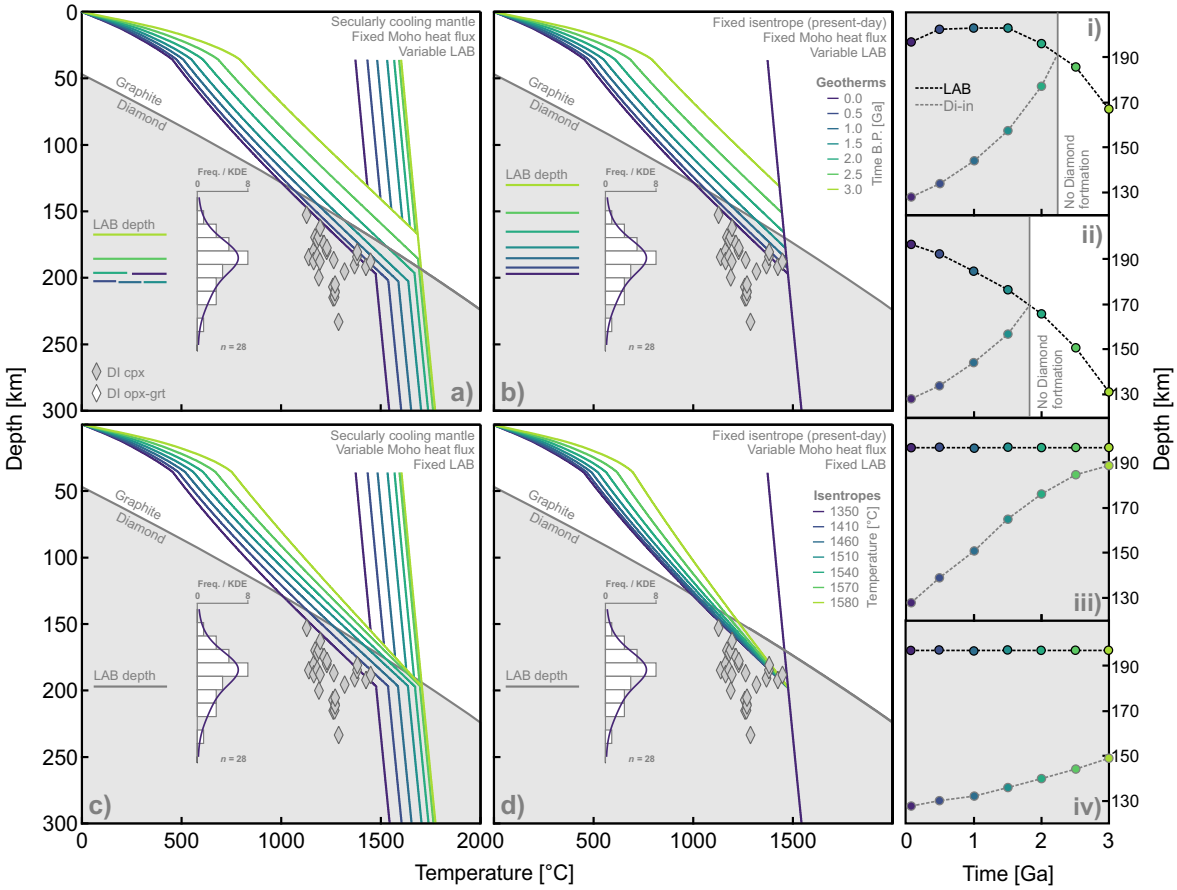

Figure 2.4: Thermodynamically modelled geotherms calculated for the Kaapvaal Craton accounting for the decrease in heat production within the Earth from 3.0 Ga to the close-to-present-day (85 Ma) under varying conditions. Models a) and b) used a fixed LAB heat flux, models c) and d) used a fixed lithospheric thickness. Models a) and c) have a secularly cooling convecting mantle temperature demonstrated by decrease in isentrope temperatures since 3.0 Ga (Korenaga, 2008). Models b) and d) have a constant convecting mantle through time demonstrated by a fixed mantle isentrope. Panels i, ii, iii and iv display the depth to LAB and graphite-diamond transition (Di-in) as a function of time for geotherm models a, b, c and d, respectively. For data references see Supplementary Figure 2. Note that in none of the models does any secular geotherm approach the position of most non-touching diamond inclusions from the Kaapvaal Craton and in the case of models a) and b) no diamond window exists prior to at least ~ 2.2 Ga

(i.e., above the modelled LAB) there is a notably poor fit of the 1.0 and 1.5 Ga modelled geotherms with the *PT* data for mantle xenoliths from Premier, apparently having equilibrated at lower temperature at any given pressure. The final observation is that none of the modelled geotherms at any time interval are at all consistent with DI thermobarometry. The recorded *PT* conditions in DIs are consistently strongly offset below the model geotherms (Figs. 2.4a; 2.4b). This observation is valid regardless of the true age of the DIs.

Results from models with fixed lithospheric thickness and variable basal heat flux

Unlike models with fixed heat transfer from the convecting mantle, those with fixed lithospheric thickness of 197 km (Figs. 2.4c; d) display more modest increases in fossil lithosphere temperature. Whether with fixed or secularly cooling convecting mantle, a diamond window persists into the Archean. At a qualitative level this is consistent with the presence of Archean diamonds in the Kaapvaal mantle lithosphere (Figs. 2.4iii; 2.4iv).

However, as before, comparison with xenolith *PT* data from the ~ 1.15 Ga Premier kimberlite cannot be reconciled with the geotherm model of a fixed LAB depth for a secularly cooling convecting mantle due to the consistently hot modelled geotherm relative to conditions recorded in the xenoliths (Fig. 2.5c). It is worth noting that the Premier kimberlite is emplaced in close proximity to the Bushveld Igneous Complex (BIC) and is known to have erupted through anomalously thick crustal architecture (~ 45 km) compared to crust in the wider Kaapvaal Craton likely due to mafic underplating in the lower crust associated with the emplacement of the BIC (Youssof et al., 2013). Such underplating could result in thermal conditions deviating from those predicted by our models which use data mostly from the Kimberley region of the Western Kaapvaal and Lesotho, which have crustal architecture ranging from ~36 to 40 km in thickness (Youssof et al., 2013). As a thicker lower crust at Premier would lead to greater temperature in the lithosphere this increase would simply make models with a fixed lithospheric thickness (or fixed Moho heat flux above) even less reconcilable with mantle xenolith *PT* data.

Thirdly, the Mesoproterozoic model geotherms at 1.0 and 1.5 Ga with a fixed isentrope and LAB depth do provide an acceptable fit to xenolith *PT* data from those Premier xenoliths that equilibrated above 200 km (Fig. 2.5d). However, there are many xenoliths that apparently derived from greater depth. In any case, the *PT* conditions recorded by Premier kimberlite DIs space invalidate the model during the Archean (Fig. 2.4d). Finally, across the entire time range explored, there is no window that would provide the temperatures low enough at the recorded depths where diamonds could have formed in the modelled Kaapvaal Craton (Fig. 2.4c), even with an optimistically 'cool' modern-day T_P (Fig. 2.4d).

Together these models demonstrate that neither a cratonic lithosphere of fixed modern-day thickness nor fixed Moho and LAB heat fluxes are compatible with the thermal evolution of the Kaapvaal Craton constrained by the presence of Archean age

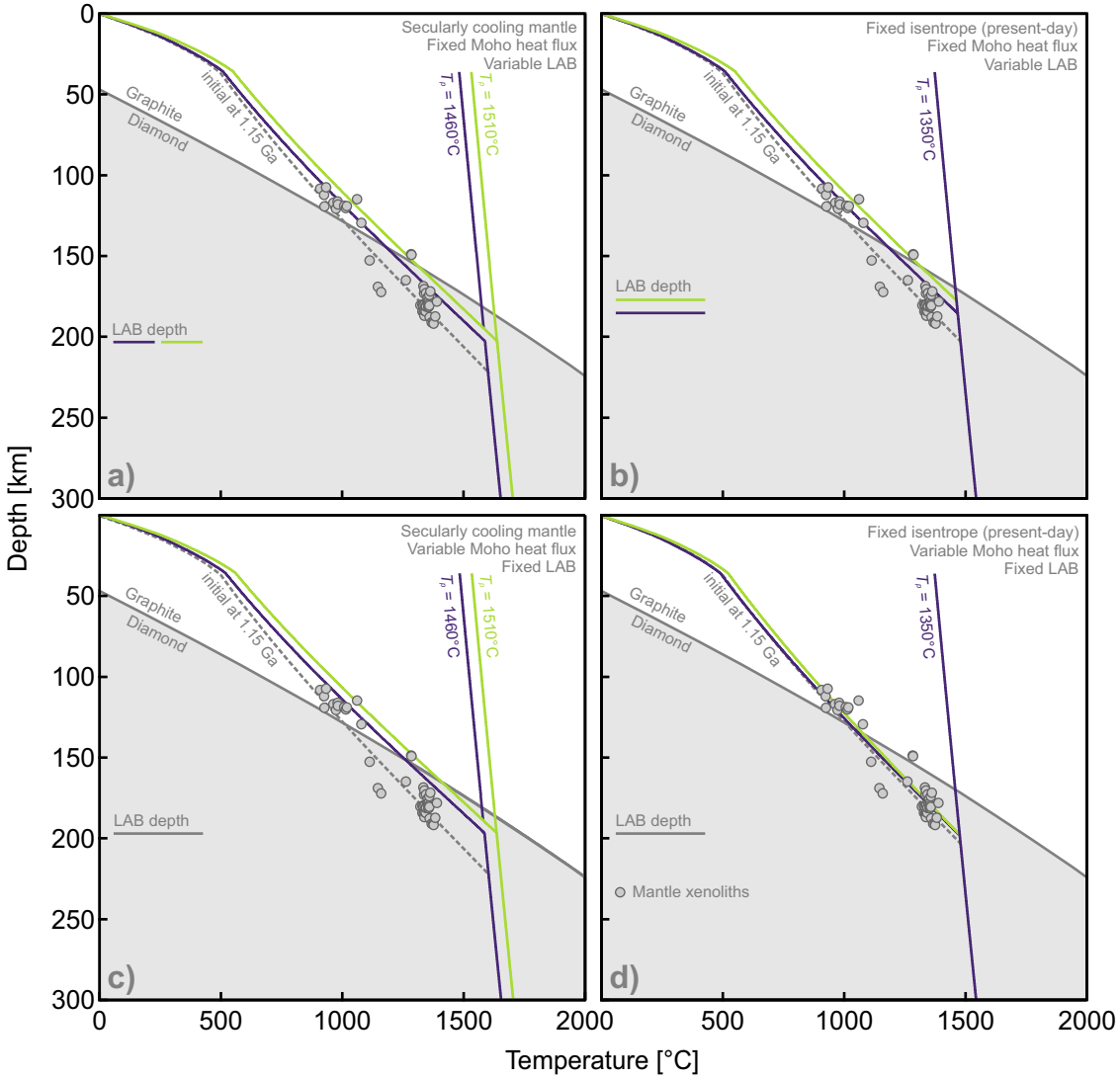

Figure 2.5: Geotherm models at 1.0 Ga and 1.5 Ga taken from Figure. 4 compared to PT conditions recorded in mantle xenoliths from the ~ 1.15 Ga Premier kimberlite. Models a) and b) comprise used a fixed LAB heat flux, models c) and d) calculated with a fixed lithospheric thickness of 199 km obtained from the best fit geotherm model from mantle xenoliths entrained within Cretaceous kimberlites. Graphite diamond transition after Day (2012).

diamond, DI *PT* equilibration, and Premier xenolith *PT* data. Their position in *PT* space is consistently below any geotherm (i.e., offset to lower T for a given P) derived from our models. This clearly indicates that the geothermal gradient must have been cooler at the time of their formation. The most straight-forward explanation for a cooler geotherm is the former existence of a thicker lithosphere consequently with a lower LAB heat flux (Ballard and Pollack, 1988). The following section explores this possibility and discusses ensuing conclusions regarding lithosphere evolution.

2.4 Discussion

There are two dominant, independent and mutually compatible means to steepen the geothermal gradient within the lithosphere at the time of diamond formation. The first is to decrease the heat-producing element inventory of the ancient crust. The second is to lower the Moho and LAB heat fluxes, and hence, thicken the lithosphere. Regarding the possibility of secular change in crustal composition, there is strong evidence that the distribution of igneous rock types in the Archean was appreciably more bimodal felsic/mafic than at later times. Yet, the inventory of radioactive heat producing elements in average continental crust has remained quite uniform (Condie, 1993). Hawkesworth and Jaupart (2021) recently argued that pre-2.8 Ga Archean crust may have been more mafic and produced less heat. For the Kaapvaal Craton, they based their mafic model on lower Kaapvaal Craton surface heat flow. However, the high heat flow Paleoproterozoic supracrustal rocks and intrusions that contribute to the average cratonic heat flow of 48 ± 8 mW/m^2 (Jones, 2017), have Archean isotope systematics (e.g., Jahn and Condie, 1995) and in our view, represent preferential incorporation of highly evolved Archean material that rose to high crustal levels due to Archean intra-crustal melting. We also note that the adjacent Zimbabwe Craton, with much less Proterozoic cover, has a similarly high (45 ± 12 mW/m^2; Jones, 2017) surface heat flow. There is thus no strong evidence to invoke significantly reduced radioactive heating as the explanation for steeper geotherms in the ancient Kaapvaal cratonic lithosphere.

Prima facie evidence for the second explanation, a lower LAB heat flux and thicker lithosphere, comes from the mantle xenoliths from Premier. For a secularly cooling convecting mantle, the LAB depth at 1.15 Ga is calculated to have been 223 km at Premier, 26 km thicker than at 85 Ma (Fig. 2.2a; 2.2c). This LAB depth corresponds to the intercept of the 1.15 Ga geotherm and an isentrope defining a mantle potential temperature of 1470°C (Fig. 2.2c). This would mean that over ca. 1 Ga alone, ~ 25 km of refractory lithosphere may have been removed from the base of Kaapvaal Craton.

A thicker lithosphere: Evidence from diamond inclusions

To further explore whether and how lower LAB heat fluxes (and greater LAB depths) could fit to the 'coolest' diamond *PT* data, we produced additional models by iterating the surface heat flux (Fig. 2.6) to achieve a reasonable coincidence of geotherm with recorded DI *PT*. Three geotherms were modelled at 1.15, 1.9 and 3.0 Ga These were chosen

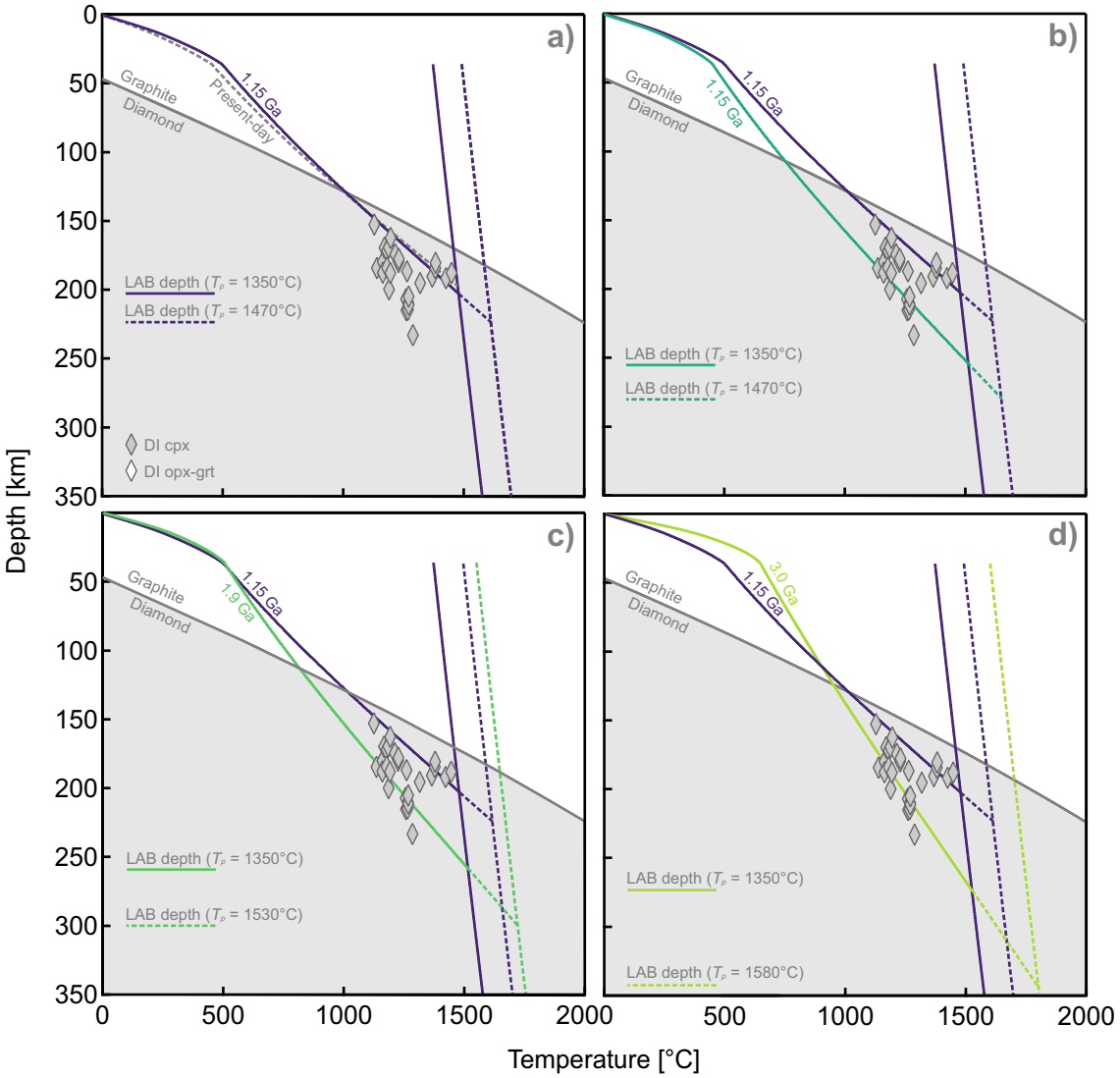

Figure 2.6: Effect of LAB depth on geotherms. Geotherms in panel a) display the semi-quantitative 'initial' geotherms chosen for close-to-the-present-day and at 1.15 Ga, fitted to mantle xenolith PT estimates. Geotherms in models b), c) and d) show geotherms from hypothetically thicker lithosphere at 1.15, 1.9 and 3.0 Ga, respectively, that provide a qualitative fit to the coolest PT conditions recorded in Premier diamonds. For data references see Supplementary Figure 2.

because they could represent potential diamond growth events in the Kaapvaal coinciding with emplacement of kimberlite (e.g., Wu et al., 2013) and the Umkondo LIP (Hanson et al., 2004), a diamond forming metasomatic event at 1.9 Ga (e.g., Richardson et al., 1993) and stabilisation of the Kaapvaal mantle lithosphere taken as the time of suturing of the western and eastern blocks (Schmitz et al., 2004). As before, the model geotherms account both for the run-down in heat producing elements in the crust and the potential for a secularly cooling mantle and one of fixed modern T_p. In all the modelled geotherms (parameters listed in Table. 2.3), the heat flux across the Moho and LAB is substantially lower than in the earlier versions and in all cases, the resulting lithosphere is also

substantially thicker than at 85 Ma: 279, 300 and 345 km, respectively. This lower Moho heat flux contrasts the assumption behind the model of Hawkesworth and Jaupart (2021) who project the modern Moho heat flux unchanged back beyond 2.8 Ga.

If the diamond that erupted at Premier formed only shortly before 1.15 Ga, a LAB at 279 km would be required (Fig. 2.6b) to explain the *PT* information contained in its DIs. This would imply very (perhaps unreasonably) substantial (ca. 50 km) and rapid removal of lithosphere to yield the shallower LAB depth required by the xenolith data (Fig. 2.2c). This seems improbable and instead, the DIs far more likely record *PT* conditions from much earlier times. It is worth noting that a subset of clinopyroxene and one orthopyroxene-garnet DIs from the Premier kimberlite yield temperatures that are substantially 'hotter' for a given depth, in closer agreement with the thermal conditions recorded by xenoliths at 1.15 Ga (Fig. 2.2d). It is possible that these DIs derived from post-Archean growth events, like a suite of DIs dated from the nearby Venetia kimberlite. The Venetia DIs yield two separate Sm-Nd isochron regression ages, one at 2.95 ± 0.07 Ga and another at 1.15 ± 0.11 Ga (Koornneef et al., 2017). The latter age overlaps emplacement of kimberlites at Premier (Wu et al., 2013), as well as the eruption of the Umkondo large igneous province (LIP) in southern Africa (Hanson et al., 2004).

More significantly, for the widely used secularly cooling mantle model of Herzberg et al. (2010), the 1.9 and 3.0 Ga geotherms best fitting the DI *PT* conditions predict that the original LAB was very deep, at 300 and 345 km, respectively (Table. 3.3). This would imply much more substantial erosion of the LAB than is generally envisaged but could be an attractive explanation for the recovery of majorite (or exsolutions thereof) in Kaapvaal Craton DIs. Majorite is not stable within the current cratonic keel and P-type majoritic garnet DIs apparently formed between 250 and 350 km depth. According to our calculation, rather than being sub-lithospheric, such DIs could thus be vestiges of the long-removed much deeper portions of the original cratonic lithosphere. The Jagersfontein kimberlite contains rare xenoliths with omphacitic exsolution lamellae in pyrope garnet with excess $Si^{[iv]}$ (i.e. majorite component) indicative of formation at between 300-400 km depth (Haggerty and Sautter, 1990). Thus, at some point in the past, the Kaapvaal Craton could have been significantly thicker. The exact constraints on early Precambrian LAB depths are, however, highly sensitive to the mantle T_p. Using the modern convecting T_p of 1350°C, more modest lithospheric thicknesses emerge at 1.9 and 3.0 Ga of 258 and 274 km, respectively. These only barely protrude into the stability field of majoritic garnet.

Whilst diamond inclusion *PT* data need be treated with more caution than those from mantle xenoliths, we suggest that the consistency in *PT* estimates is indicative of formation over a relatively narrow time interval, likely within the Archean, and more likely within a lithosphere that was substantially thicker. Exactly how deep the original Kaapvaal Craton LAB was, cannot be resolved with thermal modelling due to the strong effect of the relatively poorly constrained T_p in the convecting Archean asthenosphere. However, we argue the original LAB in the Kaapvaal Craton was deeper than today, most likely in the region of 250-350 km.

Mechanisms of lithosphere erosion

Possible mechanisms for thinning of the cratonic lithosphere include thermomechanical erosion via vigorous convection or basal drag and interaction with upwelling mantle plumes, with erosion from the former gradual and the latter likely episodic. Erosion and/or refertilization has destroyed the cratonic lithosphere below several cratons (e.g., North China, Dharwar and southern Superior) and more localised thinning is indicated by recent seismic imaging of the Kaapvaal and Zimbabwe cratons (Celli et al., 2020). In these examples, lithospheric erosion significantly post-dated craton formation and stabilisation.

The most recent episode of erosion from the base of the Kaapvaal lithosphere (between 1.15 Ga and 85 Ma) could be consistent with foundering related to mantle plume interaction over the last 200 Ma (e.g., Celli et al., 2020). Indeed, the Kaapvaal Craton has anomalously high elevation, up to ~1.5 km in the central regions, that has been argued to be at least partly dynamically supported by upwelling of hot asthenospheric mantle (Ravenna et al., 2018). Significant crustal erosion and denudation in the Kaapvaal Craton (which could imply uplift) has occurred since 120 Ma, with erosion of ~500 m of the upper crust in the Kimberley region and a further ~850 m post 85 Ma (Hanson et al., 2009). Such significant erosion clearly contrasts the generally low denudation rates of cratons worldwide (e.g., Blackburn et al., 2012). It also contrasts with evidence that the elevation of the Kaapvaal Craton prior to the Cretaceous showed limited emergence above sea-level since the Archean (Ballard and Pollack, 1988) implying uplift was recent. Substantial basal removal of cratonic lithosphere prior to the Cretaceous, perhaps related to kimberlite emplacement at 1.15 Ga and/or the nearby Umkondo LIP can be considered unlikely due to evidence of widescale subsidence on-craton at this time (Baughman and Flowers, 2020).

Recent erosion at the base of the lithosphere of the Kaapvaal Craton may also be consistent with the anomalously 'cool' *PT* estimates obtained on mantle xenoliths from the

Finsch group II kimberlite, which was emplaced at 118 ± 3 Ma, earlier than the other mantle xenoliths used in our models which are overwhelmingly from late Cretaceous (~ 85 Ma) kimberlites (e.g., Tappe et al., 2018). The position of the Finsch mantle xenoliths in *PT* space fits along a geotherm at 85 Ma of a lithosphere of 223 km thickness (deeper than the present-day thickness of 197 km) and could represent conditions prior to which erosion occurred (Supplemental Figure 3). In the case of a convecting mantle of fixed temperature (T_p = 1350°C) the variation in lithosphere thickness between 1.15 Ga and 85 Ma from the mantle xenolith data is almost identical (within 5 km), which would not provide a significant component to uplift of the Kaapvaal Craton during the Late Cretaceous.

The thicker lithosphere (up to ~350 km) implied from DIs and the lack of evidence that the Kaapvaal was substantially above sea-level prior to the Cretaceous strongly suggests that most of the erosion must have been gradual, with a possible mechanism being basal drag. If Archean plates were moving slower than today and mantle viscosities were significantly lower, it is possible that basal drag was less significant earlier in Earth's past and that, as plate velocities increased, greater erosion of the lithosphere occurred with time and secular cooling of the convecting mantle (Artemieva and Mooney, 2002). Numerical modelling of mantle convection with chemically distinct continental roots also supports a bimodality in their stability at thicknesses of 300-350 km and ~ 220 km (Doin et al., 1997). A lithosphere of > 300 km is in excess of the deepest xenoliths from ~ 240-250 km found to date from cratonic lithosphere but not in excess of seismic models for cratons globally (see Fig. 1; Artemieva and Mooney, 2002). With respect to the rarity of mantle xenoliths from >220 km depth globally, the absence of evidence alone does not disprove a thicker lithosphere (Artemieva, 2011), particularly as kimberlites seem to be sample mantle xenoliths non-randomly and generally from shallower depths than diamonds (Nimis et al., 2020). Most simply though, the rarity of xenoliths from >200 km depth globally might have resulted from the fact that kimberlites have overwhelmingly formed in the Phanerozoic (Tappe et al., 2018) long after most of the basal erosion had already occurred. Therefore, an original lithosphere of >300 km thickness in the Kaapvaal is not beyond the realm of possibility. It is currently the most parsimonious explanation for the chemistry of Archean basaltic lavas that require a high T_p, the position of DI *PT* well below a modern cratonic geotherm, and the existence of DIs and xenoliths with chemistries that could only have formed below the base of the current lithosphere.

Implications of secularly dynamic cratonic geotherms

Our calculations demonstrate that geothermal gradients within a lithosphere under steady state, of either fixed thickness or basal heat flux since the Archean is incompatible with the *PT* conditions recorded in Proterozoic mantle xenoliths and DIs. Regardless of whether the convecting asthenosphere has cooled since the Archean or not, to reconcile the position of Proterozoic mantle xenolith and DI data (irrespective of age) in *PT* space, the vertical extent of the lithosphere should have been substantially greater during Earth's past. Despite any remaining uncertainties, one firm conclusion from this study is that it is not valid to project DI temperature estimates from assemblages with no pressure control onto present-day geotherm families. Although a common practice, this type of projection should be discontinued as it is likely to produce erroneous depth and temperature information. Likewise, given the potential for an originally deeper LAB, present-day Moho heat flux cannot necessarily be used to calculate the composition and heat production in Archean crust.

While the new geotherms calculated here are more realistic proxies for the early continental lithosphere, they still do not capture the full dynamism of cratonic thermal and LAB evolution. A first element to keep in mind is that the temperature of the cratonic crust continually evolved as could T_p in the underlying convecting mantle take time to permeate the root. Two factors contribute to the secularly dropping Moho temperature and heat flow. Firstly, the predictable reduction in crustal radioactive heat production (Fig. 2.1b) and secondly, the upward chemical distillation of radioactive elements into the upper crust. Crustal re-organisation events concentrate heat production into shallow depths, leading to lower Moho temperature. Thus, once a craton is established, the mantle lithosphere will always be caught up in a state of thermal re-equilibration. Our instantaneous models therefore slightly underestimate the true temperature at depth at any given time in the past and more so if the mantle T_p changed through time.

The new geotherms confirm predictions of earlier proposals (notably Ballard and Pollack, 1988 and Artemieva and Mooney, 2002) that the vertical extent of the cratonic lithosphere should have been substantially greater in the past. If the LAB depth was dominantly a function of the intercept of the geotherm with the isentrope, cratons formed within specific time windows are predicted from DI to have started out being quite uniformly deep. This would have made early Archean cratons particularly strong and could help to explain the survival of yet older Hadean material on them. The common

observation of deep Archean lithosphere would then be the expected consequence of the cooling of the Earth's asthenosphere and the surviving cratons would be representative of the early continents rather than being a biased picture of survival of the tectonically fittest.

This consideration does not, however, involve the strong geological evidence for complex magmatic histories experienced by cratons. These require multiple melt extraction events, including from the mantle lithosphere itself, that in the case of the Kaapvaal Craton, occurred episodically and over 0.75 Ga (cf., Lazarov et al., 2009; Shu et al., 2013). Many Archean greenstone belts contain komatiites of quite variable Al- and Ti-content. These chemistries have long been known to require repeated melting of quite refractory mantle and the latest models show that interaction of deep melts with residual cratonic harzburgite was common (Tomlinson and Kamber, 2021). On the one hand, the repeated exposure of the deep cratonic lithosphere to heating events will make the remaining residues less dense and stronger, but on the other hand, they may also have caused LAB erosion (Artemieva, 2011). Finally, the depth-dependent distribution of cratonic peridotite and pyroxenite shows that over time, the originally highly refractory deep cratonic lithosphere has become weakened and partly re-enriched in the process of long-term exposure to thermal and metasomatic events (e.g., Gibson et al., 2013).

In summary, whilst cratons may have attained their maximal vertical extent early in their history, most likely during the Archean at a time culminating with their greatest mechanical stability, they have been gradually eroded and weakened ever since.

Tables

Initial model input parameters		Comment	Reference
Q_s	47.5 mW m^{-2}	Fixed from fit to mantle xenolith P/T data (see text)	-
H_{uc} (τ = 0.085)	1.34 µW m^{-3}	Calculated from ^{40}K, ^{232}Th, ^{235}U and ^{238}U concentrations from average 2.5-3.5 Ga exposed cratonic upper crust worldwide	[1]
H_{lc} (τ = 0.085)	0.45 µW m^{-3}	Calculated from ^{40}K, ^{232}Th, ^{235}U and ^{238}U concentrations of average Archean intermediate lower crust xenoliths worldwide	[2]
$k_{uc\_initial}$	2.8 W m^{-1} k^{-1}	Weighted average of thermal conductivities of exposed cratonic upper crustal rocks worldwide	[1] and [3]
$k_{lc\_initial}$	2.54 W m^{-1} k^{-1}	Weighted average of thermal conductivities of granulite	[3]
k_{uc} (T= 0°C)	2.94 W m^{-1} k^{-1}	Thermal conductivity projected to 0°C	[4]
k_{lc} (T= 0°C)	2.61 W m^{-1} k^{-1}	Thermal conductivity projected to 0°C	[4]
ρ_{uc}	2.75 Kg m^{-3}	Density of granite	-
ρ_{lc}	2.86 Kg m^{-3}	Calculated from teleseismic functions from the Kimberley region of the Kaapvaal Craton	[5]
T_p	1350 °C	Present-day mantle potential temperature	[6]
T_p (τ = 0.5 Ga)	1410 °C	Mantle potential temperatrue at 0.5 Ga	[6]
T_p (τ = 1.0 Ga)	1460 °C	Mantle potential temperatrue at 1.0 Ga	[6]
T_p (τ = 1.5 Ga)	1510 °C	Mantle potential temperatrue at 1.5 Ga	[6]
T_p (τ = 2.0 Ga)	1545 °C	Mantle potential temperatrue at 2.0 Ga	[6]
T_p (τ = 2.5 Ga)	1570 °C	Mantle potential temperatrue at 2.5 Ga	[6]
T_p (τ = 3.0 Ga)	1580 °C	Mantle potential temperatrue at 3.0 Ga	[6]

Table. 2.1: Input parameters for initial geotherm model at close-to-the-present-day (~ 85 Ma) for the Kaapvaal Craton used as the start point for secular geotherms: Where Q_s is the surface heat flux, H_{uc} and H_{lc} is the internal heat production in the upper and lower crust, respectively, K_{uc_inital} and $K_{lc\_initial}$ are the thermal conductivities of the estimated for upper and lower crust and K_{uc} and K_{lc} are the same values projected to T = 0°C. ρ_{uc} and ρ_{lc} are the densities of the upper and lower crust, respectively. T_p is the mantle potential temperature as demonstrated by an isentrope at specific time intervals (τ) in Ga. References: [1] Condie (1993); [2] Rudnick and Fountain (1995); [3] Jennings et al. (2019); [4] Rolandone et al. (2002); [5] James et al. (2003); [6] Korenaga (2008a).

Model parameters (a)	Time (τ)	Q_s (mW m^{-2})	Q_{LAB} (mW m^{-2})	H_{uc} (μW m^{-3})	H_{lc} (μW m^{-3})	T_p (°C)	LAB (km)	Di-in (km)	Window (km)
Fixed LAB heat flux	0.085	47.5	16.4	1.33	0.45	1350	197	128	69
Cooling mantle	0.5	50.3	16.4	1.44	0.5	1410	202	134	68
	1	54.7	16.4	1.61	0.58	1460	203	144	59
	1.5	60.1	16.4	1.82	0.68	1510	203	157	46
	2	67.5	16.4	2.11	0.81	1545	196	177	19
	2.5	77	16.4	2.48	0.98	1570	186	-	-
	3	90.2	16.4	2.99	1.22	1580	167	-	-
Model parameters (b)									
Fixed LAB heat flux	0.085	47.5	16.4	1.33	0.45	1350	197	128	69
Constant mantle	0.5	50.3	16.4	1.44	0.5	1350	193	134	59
	1	54.7	16.4	1.61	0.58	1350	185	144	41
	1.5	60.1	16.4	1.82	0.68	1350	177	157	20
	2	67.5	16.4	2.11	0.81	1350	166	-	-
	2.5	77	16.4	2.48	0.98	1350	151	-	-
	3	90.2	16.4	2.99	1.22	1350	131	-	-
Model parameters (c)									
Fixed LAB depth	0.085	47.5	16.4	1.33	0.45	1350	197	128	69
Cooling mantle	0.5	50.7	16.8	1.44	0.5	1410	197	139	58
	1	55.1	16.8	1.61	0.58	1460	197	151	46
	1.5	60.5	16.8	1.82	0.68	1510	197	165	32
	2	67.5	16.3	2.11	0.81	1545	197	176	21
	2.5	76.3	15.6	2.48	0.98	1570	197	185	12
	3	88.2	14.3	2.99	1.22	1580	197	189	8
Model parameters (d)									
Fixed LAB depth	0.085	47.5	16.4	1.33	0.45	1350	197	128	69
Constant mantle	0.5	50	16.1	1.44	0.5	1350	197	130	67
	1	53.9	15.6	1.61	0.58	1350	197	132	65
	1.5	58.8	15.1	1.82	0.68	1350	197	136	61
	2	65.4	14.3	2.11	0.81	1350	197	140	57
	2.5	73.9	13.3	2.48	0.98	1350	197	144	53
	3	85.7	11.9	2.99	1.22	1350	197	149	48

Table. 2.2: Model results for secular models with fixed LAB heat fluxes or fixed lithospheric thickness both with and without a secularly cooling underlying convecting mantle. Where Qs is the surface heat flux, Huc and Hlc is the internal heat production in the upper and lower crust, respectively0°C. Tp is the mantle potential temperature as demonstrated by an isentrope at specific time intervals (τ) in Ga. LAB = our defined lithosphere-asthenosphere boundary (see text for discussion). Di-in marks the intersection of the geotherm and the diamond stability field in the lithospheric mantle after Day (2013) and window corresponds to the thickness of lithospheric mantle hospitable for diamond stability.

Model parameters (variable T_p)	Time (τ = Ga)	Q_s (mW m^{-2})	Q_{LAB} (mW m^{-2})	H_{uc} (μW m^{-3})	H_{lc} (μW m^{-3})	T_p (°C)	LAB (km)	Di-in (km)	Window (km)
Best-fitting Premier emplacement geotherm	1.15	55	15.1	1.67	0.61	1470	223	130	93
	1.15	52.5	12.6	1.67	0.61	1470	279	107	172
Thicker lithosphere	1.9	61	11.6	2.04	0.78	1530	300	112	188
	3.0	83	9.2	2.99	1.22	1580	345	124	221
Model parameters (fixed T_p)									
Best-fitting Premier emplacement geotherm	1.15	55	15.1	1.67	0.61	1350	202	130	72
	1.15	52.5	12.6	1.67	0.61	1350	254	107	147
Thicker lithosphere	1.9	61	11.6	2.04	0.78	1350	258	112	146
	3.0	83	9.2	2.99	1.22	1350	274	124	150

Table. 2.3: Model results for hypothetically thicker lithosphere at differing times in Earth's history. Abbreviations as used in Table. 2.

Acknowledgements

This project was funded through support from a Government of Ireland Postgraduate Scholarship from the Irish Research Council held by BCH (GOIPG/2017/1132). BCH would like to warmly thank T. Stachel and P. Nimis for graciously providing their major element diamond inclusion data. The authors have no competing interests to declare.

Supplementary data

Thermal conductivity model

We used a temperature dependent thermal conductivity model similar to that implemented in the *FITPLOT* software (Mather et al., 2011), adapted from McKenzie et al. (2005). This is a common approach to fitting geotherms to mantle xenolith *PT* data. Our thermal conductivity model only differs from *FITPLOT* by working with a temperature dependency to thermal conductivity in the crust, which is more realistic but in effect has only minor consequences for the resulting Archaean geotherms. Assuming that thermal conductivity in the crust only decreases as a result of lattice conductivity, which decreases with increasing temperature (i.e., there is no radiative contribution), thermal conductivity at T_i can be calculated in the crust using the expression of Rolandone et al. (2002);

$$\lambda_T = 2.26 - \frac{618.241}{T} + \lambda_0 \left(\frac{3.55.576}{T} - 0.30247 \right)$$

[Eq. 2.S1]

Where, T is temperature in K and λ_0 is the thermal conductivity at T = 0°C. As thermal conductivity experiments are conducted at room temperature, empirical thermal conductivities used in our modelling are projected to T = 273 K or 0°C. Thermal

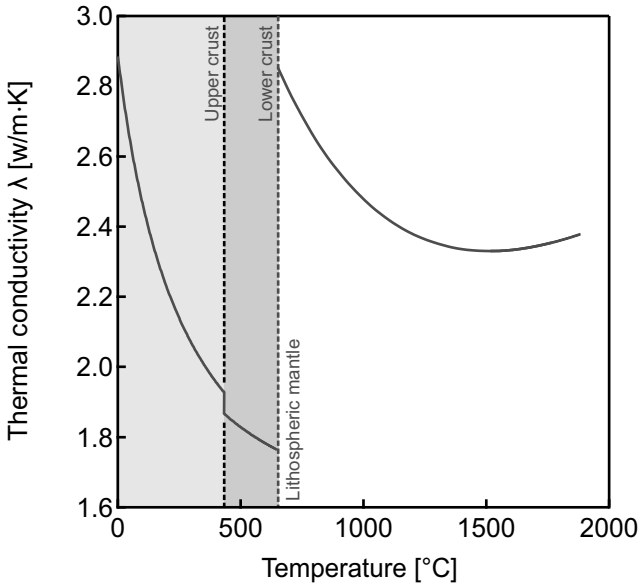

Figure. 2S.1: Thermal conductivity model used in this study. Thermal conductivity in the crust calculated from the expression of Rolandone et al. (2002), assuming only lattice contribution to thermal conductivity (i.e., no radiative contribution). Lattice contribution to thermal conductivity in the mantle calculated after McKenzie et al. (2005) from Hofmeister (1999). Radiative contribution to the thermal conductivity in the mantle from Hofmeister (1999).

conductivity in the mantle is calculated for T_i with both lattice and radiative contributions. The lattice contribution to thermal conductivity is calculated using the simplified expression of Hofmeister (1999), adapted by McKenzie et al. (2005);

$$\lambda_T = \frac{b}{1 + cT} + \sum_{m=0}^{3} d_m \, (T + 273)^m$$

[Eq. 2S2]

Where, the values used as constants are b = 0.053, c = 0.0015, $d_0 = 1.753 \times 10^{-2}$, $d_1 = -1.0365 \times 10^{-4}$, $d_2 = 2.2451 \times 10^{-7}$, $d_3 = -3.4071 \times 10^{-11}$. The radiative contribution to thermal conductivity is calculated according to Hofmeister (1999):

$$\lambda_T = 0.01753 - 0.00010365T + 2.2451T^2 \, x \, 10^7 - 3.407T^3 \, x \, 10^{11}$$

[Eq. 2S3]

Where, T is temperature in K and λ_T is the radiative contribution to the thermal conductivity at a specified temperature. The depth-dependency of thermal conductivity is illustrated in Supplemental Fig. 2S.1. As we use a temperature dependent thermal conductivity model, a Newton-Raphson iterative scheme is employed to solve for

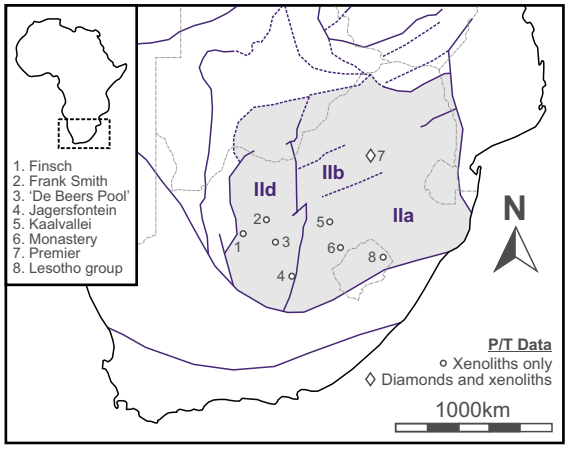

Figure. 2S.2: Map of localities from which PT data for mantle xenoliths diamond inclusions are used in this study. Tectonic domains after Griffin et al. (2003). Numbers 1-8 (inset) are the kimberlite sampling localities.

temperature T_{i+1} and the intra-layer thermal conductivity K_{i+1} moving downward in 0.1 km increments from T = 0°C at the Earth's surface.

Mantle xenolith and diamond inclusion PT data

Mantle xenolith data from the database of Wu and Zhou (2011) and diamond inclusion data from the Premier kimberlite (n= 26; Nimis, 2002; Viljoen et al., 2014). Mantle xenoliths in the database were used selected according to these criteria: (i) presence of granoblastic or equigranular textures displaying ubiquitous 120° mineral contacts; (ii) no reaction textures or chemical zoning of minerals that would be likely for chemical disequilibrium between mineral species were used for *PT* calculations; (iii) all other minerals were 'fresh' and no alteration is found; (iv) orthopyroxene with < 0.4 wt.% Al_2O_3 were discarded in order to limit significant transference of *PT* errors propagated from analytical errors. Nonetheless, as is clearly demonstrated in Figures 2.2 and 2.3, mantle xenoliths that pass the above criteria still provide anomalous *PT* estimates that most likely derive from either mineral disequilibrium or simply record conditions that deviate from steady state (i.e., transient conditions). Therefore, as there is no way to exclude these data based on defined criteria the qualitative method described in the methodology was preferred. All data used is provided in Tables 2S.1 and 2S.2.

Eclogitic DIs were not used as they there is no reliable barometer to calculate P from the major element compositions of commonly included species and because their relationship to the formation of the peridotitic lithosphere is unclear. Equilibrium *PT* estimates of lherzolite mantle xenoliths were obtained from the two-pyroxene thermometer of Taylor (1998) combined with the Al-in-orthopyroxene of Nickel and Green (1985). Only

single (clinopyroxene) were selected for comparison with geotherms due to the possibility of temperature re-equilibration in diamonds with touching species (Phillips et al., 2004). *PT* conditions for clinopyroxene DIs were obtained with the most recent single crystal thermobarometer of Sudholtz et al. (2021) after Nimis and Taylor (2000).

Supplementary Table. S2.1

Location	ID	P(kbar)	T(°C)	Thermobarometer
Premier	FB1325	14.9	579	TA98-NG85
Premier	PR90-9	48.4	1287	TA98-NG85
Premier	PR90-57	37.3	1062	TA98-NG85
Premier	PR89-1	48.3	1286	TA98-NG85
Premier	PR90-6	42.0	1080	TA98-NG85
Premier	PHN5267	57.9	1391	TA98-NG85
Premier	FRB930B/2	22.2	724	TA98-NG85
Premier	RVD100	54.7	1335	TA98-NG85
Premier	RVD101	59.9	1337	TA98-NG85
Premier	RVD106	58.7	1347	TA98-NG85
Premier	RVD112	60.7	1340	TA98-NG85
Premier	RVD119	56.1	1346	TA98-NG85
Premier	RVD120	59.8	1345	TA98-NG85
Premier	RVD121	59.8	1332	TA98-NG85
Premier	RVD123	58.6	1335	TA98-NG85
Premier	RVD126	57.9	1350	TA98-NG85
Premier	RVD128	61.9	1377	TA98-NG85
Premier	RVD132	58.6	1323	TA98-NG85
Premier	RVD136	62.0	1370	TA98-NG85
Premier	RVD149	57.0	1353	TA98-NG85
Premier	RVD155	34.9	935	TA98-NG85
Premier	RVD158	58.4	1331	TA98-NG85
Premier	RVD159	57.8	1357	TA98-NG85
Premier	RVD161	58.3	1341	TA98-NG85
Premier	RVD164	55.3	1339	TA98-NG85
Premier	RVD175	39.2	975	TA98-NG85
Premier	RVD181	49.6	1114	TA98-NG85
Premier	RVD186	58.8	1346	TA98-NG85
Premier	RVD190	55.8	1364	TA98-NG85
Premier	RVD197	37.7	982	TA98-NG85
Premier	RVD401	58.9	1358	TA98-NG85
Premier	RVD413	57.9	1356	TA98-NG85
Premier	RVD416	58.4	1357	TA98-NG85
Premier	RVD417	38.6	1021	TA98-NG85
Premier	RVD419	35.1	910	TA98-NG85
Premier	RVD422	58.9	1356	TA98-NG85
Premier	RVD424	55.9	1162	TA98-NG85
Premier	RVD437	53.5	1263	TA98-NG85
Premier	RVD441	59.7	1341	TA98-NG85

Location	ID	P(kbar)	T(°C)	Thermobarometer
Premier	RVD442	56.5	1360	TA98-NG85
Premier	RVD500	39.1	1016	TA98-NG85
Premier	RVD501	58.6	1360	TA98-NG85
Premier	RVD502	62.2	1378	TA98-NG85
Premier	RVD503	38.6	1009	TA98-NG85
Premier	RVD504	38.7	928	TA98-NG85
Premier	RVD505	36.4	927	TA98-NG85
Premier	RVD506	38.3	984	TA98-NG85
Premier	RVD507	56.2	1338	TA98-NG85
Premier	RVD508	60.9	1362	TA98-NG85
Premier	RVD509	54.8	1148	TA98-NG85
Premier	RVD510	38.0	965	TA98-NG85
Premier	PKSV-4	60.8	1384	TA98-NG85
Eastern Kaapvaal/Lesotho	1359	42.3	1006	TA98-NG85
Eastern Kaapvaal/Lesotho	1361	42.5	1046	TA98-NG85
Eastern Kaapvaal/Lesotho	1362	45.2	1097	TA98-NG85
Eastern Kaapvaal/Lesotho	1363	42.7	1054	TA98-NG85
Eastern Kaapvaal/Lesotho	1870/2.	29.8	816	TA98-NG85
Eastern Kaapvaal/Lesotho	2125	43.8	1054	TA98-NG85
Eastern Kaapvaal/Lesotho	2012	43.3	1042	TA98-NG85
Eastern Kaapvaal/Lesotho	2573	53.8	1385	TA98-NG85
Eastern Kaapvaal/Lesotho	2575/2.	51.9	1357	TA98-NG85
Eastern Kaapvaal/Lesotho	2575/3.	52.2	1359	TA98-NG85
Eastern Kaapvaal/Lesotho	PHN1569	38.3	934	TA98-NG85
Eastern Kaapvaal/Lesotho	PHN1591	54.9	1356	TA98-NG85
Eastern Kaapvaal/Lesotho	FRB1	50.6	1250	TA98-NG85
Eastern Kaapvaal/Lesotho	PHN1611	53.0	1386	TA98-NG85
Eastern Kaapvaal/Lesotho	LBM9	43.7	1038	TA98-NG85
Eastern Kaapvaal/Lesotho	LBM11	43.2	1034	TA98-NG85
Eastern Kaapvaal/Lesotho	LBM12	45.8	1102	TA98-NG85
Eastern Kaapvaal/Lesotho	LBM16	42.9	1053	TA98-NG85
Eastern Kaapvaal/Lesotho	LBM18	46.8	1119	TA98-NG85
Eastern Kaapvaal/Lesotho	LBM32	40.4	972	TA98-NG85
Eastern Kaapvaal/Lesotho	LBM33	43.7	1092	TA98-NG85
Eastern Kaapvaal/Lesotho	LBM36	48.0	1128	TA98-NG85
Eastern Kaapvaal/Lesotho	LBM37	44.4	1108	TA98-NG85
Eastern Kaapvaal/Lesotho	BD1355	46.5	1090	TA98-NG85
Eastern Kaapvaal/Lesotho	11102	47.4	1123	TA98-NG85
Eastern Kaapvaal/Lesotho	1643	20.7	748	TA98-NG85
Eastern Kaapvaal/Lesotho	1654	43.8	1021	TA98-NG85

Location	ID	P(kbar)	T(°C)	Thermobarometer
Eastern Kaapvaal/Lesotho	1660	52.4	1070	TA98-NG85
Eastern Kaapvaal/Lesotho	BD2501	49.4	1243	TA98-NG85
Eastern Kaapvaal/Lesotho	AJE62	45.3	1050	TA98-NG85
Eastern Kaapvaal/Lesotho	JJG703	52.0	1242	TA98-NG85
Eastern Kaapvaal/Lesotho	JVS73-149	20.8	763	TA98-NG85
Eastern Kaapvaal/Lesotho	JVS73-152	37.4	946	TA98-NG85
Eastern Kaapvaal/Lesotho	JVS73-154B	41.5	976	TA98-NG85
Eastern Kaapvaal/Lesotho	JVS73-155B	49.2	1097	TA98-NG85
Eastern Kaapvaal/Lesotho	JVS73-164	34.3	854	TA98-NG85
Eastern Kaapvaal/Lesotho	JVS73-165	37.2	942	TA98-NG85
Eastern Kaapvaal/Lesotho	JVS73-172A	47.8	1072	TA98-NG85
Eastern Kaapvaal/Lesotho	PHN1567	29.4	770	TA98-NG85
Eastern Kaapvaal/Lesotho	PHN1568	39.4	946	TA98-NG85
Eastern Kaapvaal/Lesotho	PHN1569	37.3	956	TA98-NG85
Eastern Kaapvaal/Lesotho	PHN1570	43.7	1043	TA98-NG85
Eastern Kaapvaal/Lesotho	PHN1572	29.9	818	TA98-NG85
Eastern Kaapvaal/Lesotho	PHN1573	35.7	844	TA98-NG85
Eastern Kaapvaal/Lesotho	PHN1592	35.9	907	TA98-NG85
Eastern Kaapvaal/Lesotho	PHN1596	49.6	1388	TA98-NG85
Eastern Kaapvaal/Lesotho	PHN1611	50.8	1354	TA98-NG85
Eastern Kaapvaal/Lesotho	PHN1925	48.9	1337	TA98-NG85
Eastern Kaapvaal/Lesotho	PHN2549	43.7	1034	TA98-NG85
Eastern Kaapvaal/Lesotho	FRB135	39.4	976	TA98-NG85
Eastern Kaapvaal/Lesotho	PHN1611	54.1	1390	TA98-NG85
Eastern Kaapvaal/Lesotho	PHN1925	47.6	1352	TA98-NG85
Eastern Kaapvaal/Lesotho	BD2501	49.4	1242	TA98-NG85
Eastern Kaapvaal/Lesotho	FRB140	52.6	1276	TA98-NG85
Eastern Kaapvaal/Lesotho	1595	35.8	881	TA98-NG85
Eastern Kaapvaal/Lesotho	1567	36.1	926	TA98-NG85
Eastern Kaapvaal/Lesotho	1569	40.5	995	TA98-NG85
Eastern Kaapvaal/Lesotho	1568	35.9	944	TA98-NG85
Eastern Kaapvaal/Lesotho	Mothae1917	46.2	1044	TA98-NG85
Eastern Kaapvaal/Lesotho	Mothae1559B	41.8	1014	TA98-NG85
Eastern Kaapvaal/Lesotho	Mothae2001	53.9	1296	TA98-NG85
Eastern Kaapvaal/Lesotho	1591	54.4	1355	TA98-NG85
Eastern Kaapvaal/Lesotho	E3	54.2	1374	TA98-NG85
Eastern Kaapvaal/Lesotho	Mothae1924	49.8	1349	TA98-NG85
Eastern Kaapvaal/Lesotho	Mothae1925	47.0	1339	TA98-NG85
Eastern Kaapvaal/Lesotho	1610	50.8	1374	TA98-NG85
Eastern Kaapvaal/Lesotho	1566	50.8	1387	TA98-NG85

Location	ID	P(kbar)	T(°C)	Thermobarometer
Eastern Kaapvaal/Lesotho	1596	51.0	1402	TA98-NG85
Eastern Kaapvaal/Lesotho	1597	51.7	1406	TA98-NG85
Eastern Kaapvaal/Lesotho	PHN1569	38.4	935	TA98-NG85
Eastern Kaapvaal/Lesotho	M2	34.0	858	TA98-NG85
Eastern Kaapvaal/Lesotho	M9	41.2	972	TA98-NG85
Eastern Kaapvaal/Lesotho	M13	42.1	955	TA98-NG85
Eastern Kaapvaal/Lesotho	LET29	39.4	999	TA98-NG85
Eastern Kaapvaal/Lesotho	M1	41.1	1004	TA98-NG85
Kaalvaalai	13-52-106	34.6	809	TA98-NG85
Kaalvaalai	13-54-8	32.4	816	TA98-NG85
Kaalvaalai	13-54-25	36.2	806	TA98-NG85
Kaalvaalai	13-54-26	36.1	825	TA98-NG85
Kaalvaalai	13-52-8	42.7	996	TA98-NG85
Kaalvaalai	13-52-13	52.4	1179	TA98-NG85
Kaalvaalai	13-52-14	53.9	1404	TA98-NG85
Kaalvaalai	13-52-26	57.3	1416	TA98-NG85
Kaalvaalai	13-52-27	51.1	1027	TA98-NG85
Kaalvaalai	13-52-109	54.8	1285	TA98-NG85
Kaalvaalai	13-52-110	40.3	945	TA98-NG85
Kaalvaalai	13-53-70	51.8	1180	TA98-NG85
Kaalvaalai	13-54-3	54.5	1387	TA98-NG85
Kaalvaalai	13-54-9	40.6	916	TA98-NG85
Kaalvaalai	13-54-24	52.1	1185	TA98-NG85
Kaalvaalai	13-54-27	52.4	1236	TA98-NG85
Kaalvaalai	13-54-102	40.5	931	TA98-NG85
Kaalvaalai	13-54-103	48.6	1014	TA98-NG85
Monastery	rom194	32.9	859	TA98-NG85
Monastery	rom198	21.3	634	TA98-NG85
Monastery	rom210	35.0	908	TA98-NG85
Monastery	rom302	35.7	940	TA98-NG85
Monastery	rom68	42.8	989	TA98-NG85
Monastery	rom377lh 111	28.6	752	TA98-NG85
Frank Smith	JVS73-105	53.2	1199	TA98-NG85
Frank Smith	JVS73-106	54.4	1198	TA98-NG85
Frank Smith	FRB76	58.8	1323	TA98-NG85
Kimberley	1140	33.0	835	TA98-NG85
Kimberley	1149	39.8	985	TA98-NG85
Kimberley	BT7	40.0	967	TA98-NG85
Kimberley	BD2384	42.0	1016	TA98-NG85
Kimberley	EJB4	40.2	986	TA98-NG85

Location	ID	P(kbar)	T(°C)	Thermobarometer
Kimberley	EJB48	38.3	944	TA98-NG85
Kimberley	MB3	38.7	953	TA98-NG85
Kimberley	MB4	43.2	1049	TA98-NG85
Kimberley	MB7	40.4	986	TA98-NG85
Kimberley	MB12	40.7	991	TA98-NG85
Kimberley	MB13	39.1	974	TA98-NG85
Kimberley	PHN2762	39.6	939	TA98-NG85
Kimberley	Bo-01	36.2	880	TA98-NG85
Kimberley	Bo-05	33.1	829	TA98-NG85
Kimberley	Bo-08	46.3	1081	TA98-NG85
Kimberley	Bo-13	54.2	1211	TA98-NG85
Kimberley	Bo-26	33.8	857	TA98-NG85
Kimberley	DC0203	59.6	1299	TA98-NG85
Kimberley	DC0207	42.8	1020	TA98-NG85
Kimberley	DC0212	46.1	1058	TA98-NG85
Kimberley	DC0213	40.0	978	TA98-NG85
Kimberley	DC0215	39.3	1027	TA98-NG85
Kimberley	DC0333	36.7	856	TA98-NG85
Kimberley	DC0345	45.3	1032	TA98-NG85
Kimberley	FB1301	52.1	1337	TA98-NG85
Kimberley	JVS73-64	42.3	987	TA98-NG85
Kimberley	JVS73-76	27.3	725	TA98-NG85
Kimberley	FRB348	37.8	938	TA98-NG85
Kimberley	FRB350	35.6	933	TA98-NG85
Kimberley	BD2379	36.3	898	TA98-NG85
Kimberley	BD2421	40.3	1021	TA98-NG85
Kimberley	BD2425	30.6	853	TA98-NG85
Kimberley	BD2358	28.8	781	TA98-NG85
Kimberley	BD2426	40.2	1027	TA98-NG85
Kimberley	Kim21	42.5	1026	TA98-NG85
Kimberley	Kim36	37.1	923	TA98-NG85
Kimberley	Kim37	38.9	938	TA98-NG85
Kimberley	Kim46	51.6	1107	TA98-NG85
Kimberley	Kim71	38.9	956	TA98-NG85
Kimberley	Kim80	42.8	978	TA98-NG85
Kimberley	Kim91	41.2	1004	TA98-NG85
Kimberley	FRB838	37.1	885	TA98-NG85
Kimberley	K1	40.7	950	TA98-NG85
Kimberley	FRB347	39.6	983	TA98-NG85
Jagersfontein	JJG859	51.7	1292	TA98-NG85

Location	ID	P(kbar)	T(°C)	Thermobarometer
Jagersfontein	JAG90-8	22.2	620	TA98-NG85
Jagersfontein	JAG90-12	29.0	765	TA98-NG85
Jagersfontein	JAG90-19	50.1	1296	TA98-NG85
Jagersfontein	JJG 1773	50.7	1300	TA98-NG85
Jagersfontein	JAG90-1	22.2	618	TA98-NG85
Jagersfontein	JAG90-10	40.5	953	TA98-NG85
Jagersfontein	JAG90-13	49.5	1265	TA98-NG85
Jagersfontein	JJH35	53.1	1199	TA98-NG85
Jagersfontein	JJH10	50.0	1253	TA98-NG85
Jagersfontein	JJH13	51.0	1263	TA98-NG85
Jagersfontein	JJG1713	49.7	1286	TA98-NG85
Jagersfontein	JAG89-5.	33.7	843	TA98-NG85
Jagersfontein	JAGK7-244	13.8	512	TA98-NG85
Jagersfontein	Jag90-72	52.4	1024	TA98-NG85
Jagersfontein	Jag93-8	42.2	962	TA98-NG85
Jagersfontein	UX497	31.4	751	TA98-NG85
Jagersfontein	FRB1009	32.9	793	TA98-NG85
Finsch	F05JM1	54.7	1173	TA98-NG85
Finsch	F05JM2	53.3	1178	TA98-NG85
Finsch	F05JM4	54.8	1171	TA98-NG85
Finsch	F05JM7	53.7	1179	TA98-NG85
Finsch	BD3692	46.0	1066	TA98-NG85
Finsch	BD3693	45.9	1073	TA98-NG85
Finsch	BD3697A	45.8	1064	TA98-NG85
Finsch	F-1	52.3	1172	TA98-NG85
Finsch	F-3	54.0	1146	TA98-NG85
Finsch	F-4	55.8	1177	TA98-NG85
Finsch	F-5	55.0	1159	TA98-NG85
Finsch	F-6	54.1	1194	TA98-NG85
Finsch	F-8	56.5	1181	TA98-NG85
Finsch	F-10	49.7	1127	TA98-NG85
Finsch	F-11	54.6	1191	TA98-NG85
Finsch	F-12	58.3	1151	TA98-NG85
Finsch	F-13	53.1	1189	TA98-NG85
Finsch	F-14	59.8	1217	TA98-NG85
Finsch	F-15	52.4	1155	TA98-NG85
Finsch	F-16	51.8	1168	TA98-NG85
Finsch	F-25b	54.0	1197	TA98-NG85
Finsch	F-25c	54.4	1196	TA98-NG85
Finsch	F-26	54.4	1190	TA98-NG85

Location	ID	P(kbar)	T(°C)	Thermobarometer
Finsch	695	56.1	1177	TA98-NG85
Finsch	XM46	66.9	1270	TA98-NG85
Finsch	XM48	60.1	1209	TA98-NG85

Supplementary Table. S2.2

Location	Mineral	ID	T(°C)	P(kbar)	Thermobarometer
Premier	DI-CPX	P240	1128	49.6	NT00*
Premier	DI-CPX	P261	1138	59.9	NT00*
Premier	DI-CPX	P252	1163	58.5	NT00*
Premier	DI-CPX	P250	1163	61.0	NT00*
Premier	DI-CPX	P203	1170	55.1	NT00*
Premier	DI-CPX	P271	1181	55.8	NT00*
Premier	DI-CPX	P224	1181	59.8	NT00*
Premier	DI-CPX	P280	1187	55.1	NT00*
Premier	DI-CPX	P231	1189	64.9	NT00*
Premier	DI-CPX	P243	1194	61.0	NT00*
Premier	DI-CPX	P201	1196	52.8	NT00*
Premier	DI-CPX	P249	1215	56.7	NT00*
Premier	DI-CPX	P215	1228	58.4	NT00*
Premier	DI-CPX	P211	1229	57.7	NT00*
Premier	DI-CPX	P251	1260	67.2	NT00*
Premier	DI-CPX	P067	1261	69.8	NT00*
Premier	DI-CPX	P220	1264	60.7	NT00*
Premier	DI-CPX	P212	1267	69.7	NT00*
Premier	DI-CPX	P210	1269	68.2	NT00*
Premier	DI-CPX	P219	1271	68.6	NT00*
Premier	DI-CPX	P070	1271	66.6	NT00*
Premier	DI-CPX	P204	1288	75.7	NT00*
Premier	DI-CPX	P103	1318	63.4	NT00*
Premier	DI-CPX	P071	1368	61.9	NT00*
Premier	DI-CPX	P282	1380	59.9	NT00*
Premier	DI-CPX	P221	1382	58.7	NT00*
Premier	DI-CPX	P205	1425	62.3	NT00*
Premier	DI-CPX	P075	1449	61.1	NT00*

Chapter 3: Metasomatism of the Kaapvaal Craton during Cretaceous intraplate magmatism revealed by combined zircon U-Pb isotope and trace element analysis

Brendan C. Hoare[1], Gary O'Sullivan[2], Emma L. Tomlinson[1]

[1] Department of Geology, Trinity College Dublin, Dublin 2, Ireland

[2] School of Earth Sciences, University College Dublin, Belfield, Dublin 4, Ireland

Keywords: Zircon U-Pb; trace elements; Kaapvaal; metasomatism; mantle; LA-ICP-MS

This work is published in *Chemical Geology*, Volume 578, 120302 and forms part of a special issue dedicated to J.D Kramers: '*Geochemical and isotopic constraints on the dynamics of the Earth: A celebration of the contributions by Jan Dirk Kramers'*.

Abstract

The origins of the mica-amphibole(K-richterite)-rutile-ilmenite-diopside (MARID) and the, presumably related, phlogopite-K-richterite-peridotite (PKP) mantle xenolith suites remain enigmatic. For instance, it is unclear if MARID represents pervasively metasomatised peridotite, or veins of magmatic material. In the Kaapvaal Craton, previous studies employing zircon U-Pb dating in MARID and PKP xenoliths demonstrated that ages of zircon are broadly coincident with nearby expressions of Cretaceous kimberlite and orangeite magmatism, implying a genetic link. However, the use of typically small sample sizes (i.e. few analysed grains) in previous studies may mask complexities in the growth history of zircon in mantle lithologies, as key populations may remain undetected. In this paper, we analyse the isotopic (U-Pb) and trace element composition of zircon ($n > 40$) from three MARID/PKP rocks from the Kaapvaal Craton, to reveal not just the timing, but the tempo of metasomatism. This protocol takes its inspiration from studies of detrital zircon in clastic sedimentary rocks, in which large numbers of grains are typically dated, so that no important parts of the zircon U-Pb record are missed.

Our data show that zircon growth is broadly coincident with nearby expressions of late-Cretaceous kimberlite magmatism and mid-Cretaceous orangeite magmatism. While the range of zircon U-Pb ages we detect mirrors the range detected by previous workers,

the addition of larger sample sizes means we can detect that zircon growth was episodic. By integrating trace element data with zircon ages, we demonstrate that older zircon, generally has greater geochemical affinity to lamproitic zircon. By contrast, most zircons with ages coincident with peak kimberlite magmatism have trace-element compositions similar to megacrystic zircon - a suite of zircon crystals thought to be connected to early high-pressure proto kimberlitic liquids/fluids.

These data strongly indicate that MARID and PKP rocks form during localized and recurrent melting of enriched lithosphere. The metasomatizing effects of the passage of varying magmas at shallow depth in the lithosphere may also contribute to their complex age and geochemical signatures. The presence of zircon with U-Pb ages that span the entire range of Cretaceous intra-cratonic Kaapvaal magmatism, and trace element compositions that derive from both major phases of intra-cratonic magmatism in a single MARID xenolith, necessitates a more complex origin for the MARID suite than that of a simple magmatic cumulate. This observation argues for a complex metasomatic origin for zircon in MARID and presumably PKP rocks.

3.1 Introduction

Archean peridotitic xenoliths demonstrate that the depleted cratonic lithospheric mantle formed as the residue of > 40 % melt extraction (Boyd and Mertzman, 1987; Boyd, 1989) and has since been widely refertilized via metasomatism (e.g., Dawson and Smith, 1977; Kramers et al., 1983; Waters and Erlank, 1988; Grégoire et al., 2002; Fitzpayne et al., 2018b, 2019). Metasomatism of the continental lithosphere is thought to be intimately related to the emplacement of diamond hosting intraplate magmas such as orangeite and kimberlite in continental regions. Metasomatism is also implicated in both the precipitation and destruction of diamond in the cratonic lithosphere (Stachel and Harris, 2008; Creighton et al., 2009; Shirey et al., 2013; Weiss et al., 2015). Therefore, constraining the timing of metasomatism in the cratonic lithosphere is critical to understanding the formation, destruction and surface-emplacement of its mineral resources, which are sampled by intraplate magmas.

Modal metasomatism of the cratonic lithosphere results in the addition of new phases, including hydrous minerals (phlogopite, K-richterite), ilmenite, apatite, rutile and zircon, as well as exotic oxides and sulphides. Metasomatised mantle xenoliths, it is argued, can be divided into distinct suites based both on their mineralogy and also their

geochemical and isotopic compositions (Kramers et al., 1983; Grégoire et al., 2000, 2002; Bell et al., 2005; Fitzpayne et al., 2018b, 2019). Nonetheless, the potential origins of the agents responsible for cratonic lithospheric metasomatism are extremely varied. Potential sources include fluids or melts released from recycled lithosphere (Bell et al., 2005; Simon et al., 2007; Broadley et al., 2016; Wang et al., 2016; Hoare et al., 2021b), fluids or melts derived from mantle plumes and/or large igneous provinces (Giuliani et al., 2014; Howarth et al., 2014; Barry et al., 2015) and low-degree carbonate-rich fluids or melts from the asthenosphere (Yaxley et al., 1991; Rudnick et al., 1993; Grégoire et al., 2002; Aulbach et al., 2013; le Roex and Class, 2016).

The phlogopite-ilmenite-clinopyroxene (PIC) xenolith suite recognized by Grégoire et al. (2002) is perhaps the best example of a product of metasomatism by low-degree asthenospheric melts. A growing body of chemical and isotopic data link PIC to metasomatism associated with kimberlite magmatism in cratonic regions (Grégoire et al., 2002; Fitzpayne et al., 2018b, 2019). The origin of K-richterite- and phlogopite-bearing xenolith suites is more problematic. It is clear from the isotopic compositions of some mantle xenoliths, such as the mica(phlogopite)-amphibole(K-richterite)-rutile-ilmenite-diopside (MARID) and the phlogopite-K-richterite peridotites (PKP) suites, that sampling of ancient, recycled crustal material is required in their genesis (Kramers et al., 1983; Hawkesworth et al., 1990; Fitzpayne et al., 2019).

The processes by which MARID rocks form remains unclear; are they magmatic veins or do they represent intensely metasomatised peridotite (cf. Fitzpayne et al., 2018a)? And further, what relationship do they have with the intraplate magmas that transport them to the Earth's surface? A magmatic origin for MARID can be supported by their cumulate-like textures, as originally described by Dawson and Smith (1977) and later workers (e.g., Erlank et al., 1987; Waters, 1987). However, the direct derivation of MARID from small-degree potassic silicate melts at ~ 3 GPa depth would require the melts to retain temperatures of ~1300°C (Sweeney et al., 1993) during their passage through the comparatively cool lithosphere (~800°C at 3 GPa; Mather et al., 2011). Alternatively, the MARID suite may form via intense metasomatism of peridotite as a result of interaction with alkali-rich hydrous fluid, which could percolate through the lithosphere at substantially lower temperatures (Sweeney et al., 1993). However, it is unclear how such metasomatism could generate the cumulate textures seen in MARID rocks (Sweeney et al., 1993). In contrast to the debatable origins of MARID rocks, PKP are demonstrably

metasomatised peridotites. In their initial study of MARID rocks, Dawson and Smith, (1977) also reported a metasomatised peridotite with similar phases to those seen in MARID, which led the authors to suggest PKP formed as a wall-rock product of MARID crystallization. Subsequent studies have supported a genetic link between the suites, with similar major element compositions of shared phases and isotopic trends common to both rock types (Hawkesworth et al., 1990; Grégoire et al., 2002; Fitzpayne et al., 2019).

In this paper, we have analysed the isotopic (U-Pb) and trace element compositions of zircon from three MARID and PKP mantle xenoliths entrained from kimberlites from the Kimberley region of the Kaapvaal Craton, South Africa, to better investigate the origins of the MARID and PKP suites. We have employed significantly more analyses of individual zircon crystals ($n \geq 40$) to complement previous smaller high-precision datasets (Konzett et al., 1998, 2000, 2013; Giuliani et al., 2015).

3.2 Previous studies of mantle-derived zircon

Zircon has only been used to date PKP and MARID rocks in the Kaapvaal craton in a handful of studies (Konzett et al., 1998, 2000, 2013; Giuliani et al., 2015), all employing high-precision techniques (e.g., sensitive high-resolution ion microprobe). However, as a consequence of the techniques employed, only relatively few grains, with limited trace element data (e.g., Th and U) have been reported. In those previous studies, zircon commonly exhibits U-Pb ages that significantly predate the emplacement of the kimberlite in which they are sampled (Konzett et al., 1998, 2000). This is likely because of the high closure temperature of the U-Pb system in zircon (Cherniak and Watson, 2001), which is higher than the typical sampling interval of these suites, which are generally confined to depths of < 100 km (Waters and Erlank, 1988), corresponding to temperatures of ~ 800°C along the cratonic mantle geotherm of the Kimberley region (Mather et al., 2011). Even from the relatively small pre-existing datasets of mantle xenolith zircon from Kaapvaal (Konzett et al., 1998, 2000, 2013; Giuliani et al., 2015), it can be determined that zircon records complex metasomatic histories on cm-scales, which we consider likely to yield multi-modal age distributions. For this reason, we propose that chronology on zircon in xenoliths from the lithospheric mantle should be treated more similarly to multimodal populations of detrital zircon in clastic sedimentary rocks, rather than non-inherited zircon in crustal igneous rocks.

In provenance studies of clastic sediments, it is necessary to analyse large a number of zircons in order to accurately characterise the variety of rocks of different age which are sampled by sediments. Given an unbiased sampling procedure, the size of a population that will be detected with a high probability can thus be defined statistically (e.g., Andersen, 2005). However, perhaps in part due to the expectation of scarcity of zircon in mantle peridotites, or low yields, typical sample sizes employed in the study of mantle zircon are small (n = ~10; Konzett et al., 1998; 2000) and/or the zircon contain a contribution of common lead (Konzett et al., 2000; Giuliani et al., 2015). Consequently, in these small high-precision datasets, there is a high probability that significant zircon population(s) might be missed. For instance, for a discrete zircon population to be detected 95 % of the time with a sample size of n = 10, the population would have to comprise between 20-30% of the zircon within the rock (Anderson, 2005). Perhaps, in part, due to the high probability that critical information remains undetected, it is unclear from existing datasets whether zircon crystallization reflects an episodic or continuous process of modification of the Kaapvaal mantle lithosphere underlying Kimberley or how the MARID and PKP suites might be related to wider tectonic and magmatic events.

3.3 Materials and Methods

Materials and petrography

The selected samples comprise three variably metasomatised K-richterite- and phlogopite-bearing xenoliths (Fig. 3.1). Samples PKP001 and PKP003 were obtained from spoils from the Kimberley kimberlite which was emplaced at 87 Ma (age from database of Tappe et al., 2018). Sample MAR010 was obtained from the Boshoff Road dumps nearby to Kimberley, which mostly comprise material mostly from the historical mining of the Bultfontein kimberlite emplaced at 84 Ma (Kramers et al., 1983).

Sample MAR010 is a classic example of a MARID xenolith (Dawson and Smith, 1977). The original recognition of the MARID suite by Dawson and Smith, (1977) encompasses xenoliths of a very unique petrology that is totally dominated by K-bearing phases (phlogopite and K-richterite), which commonly display compositional layering and cumulate-like textures. Sample MAR010 displays foliation with preferential alignment of phlogopite and modal layering of both phlogopite and K-richterite into discrete bands. Accessory phases seen in thin section include clinopyroxene, apatite, ilmenite, barite and zircon.

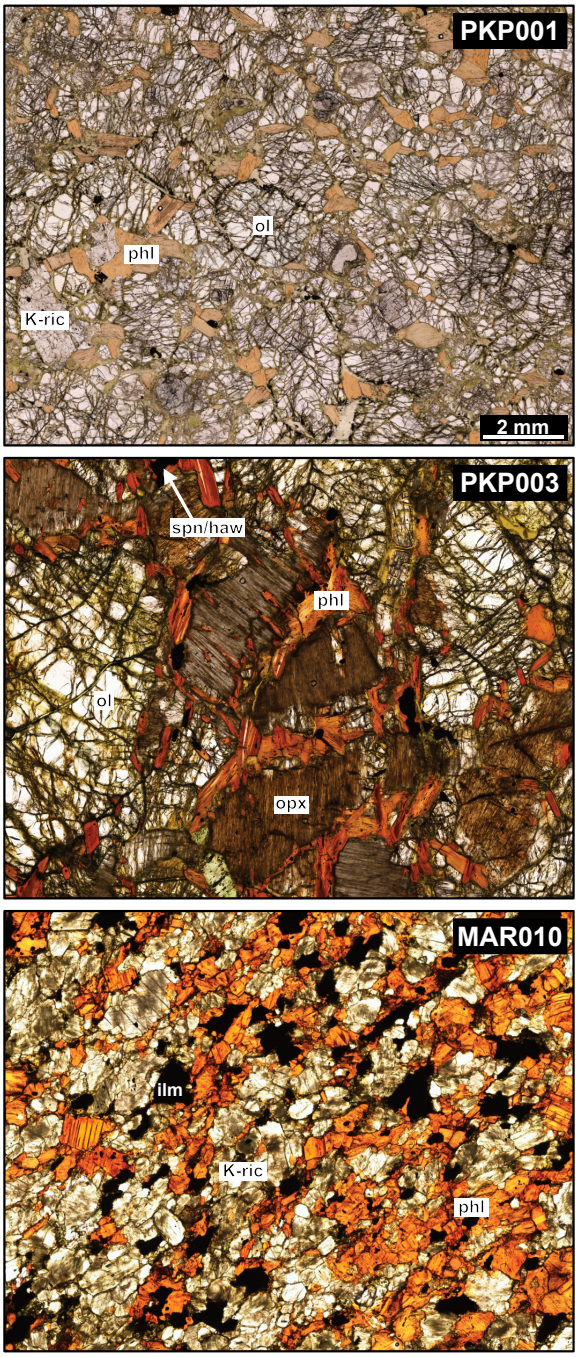

Figure 3.1: Photomicrographs of the three metasomatised xenoliths of this study. K-ric - K-richterite, phl – phlogopite, ol – olivine, opx – orthopyroxene, ilm – ilmenite, spn/haw – complex spinel and hawthornite intergrowths.

Samples PKP001 and PKP003 are examples of PKP (Erlank et al., 1987). Sample PKP001 is a phlogopite-rich granular spinel harzburgite. Alteration and growth of metasomatic phases in the harzburgite occurs preferentially along grain boundaries and through areas of particularly fractured and altered (i.e., serpentinized) olivine. Phlogopite is by far the most common metasomatic phase present, with K-richterite occurring at lower abundance. Accessory rutile, where present, forms as extremely poorly defined 'aggregates'

intergrown with ilmenite. Sample PKP003 is a granular spinel harzburgite. Secondary metasomatic phases comprise (Fe-rich) orthopyroxene, K-richterite and phlogopite, which are distributed somewhat evenly throughout the rock. Phlogopite is spatially associated with both K-richterite and orthopyroxene, whist the others are not commonly found in close association. Hawthorneite ($Ba[Ti_3Cr_4Fe_4Mg]O_{19}$; Haggerty et al., 1989) occurs as an alteration product of Cr-spinel found within phlogopite and/or orthopyroxene. As in sample PKP001, olivine is commonly partially serpentinized along fractures. None of the sampled xenoliths can provide either pressure or temperature estimates from thermobarometry due to the absence of appropriate phase assemblages or mineral compositions.

Methods

Phlogopite and K-richterite within each xenolith were analysed by energy-dispersive X-ray spectroscopy via scanning electron microscopy (SEM-EDX) at the iCRAG laboratory, Trinity College Dublin. Analyses were carried out using a Tescan TIGER MIRA3 field emission SEM, equipped with two Oxford XMax^n 150 mm^2 EDS detectors. The TIGER MIRA3 instrument uses the Oxford Instruments AZtec X-ray microanalysis software suite. The setup used a beam current of ~ 230 pA an accelerating voltage of 15 kV and an acquisition time varied to obtain a minimum of 4,000,000 counts to ensure adequate counting statistics and lower detection limits. Beam current drift was restricted by frequent analysis of pure cobalt. The instrument was calibrated using a suite of appropriate mineral standards from the Smithsonian Institute and in-house reference materials (Jarosewich et al., 1980; Jarosewich, 2002).

Zircon was extracted through standard separation techniques. For separation, rock samples were crushed using a disc mill, washed, passed through a 200 µm mesh sieve and a Frantz magnetic separator. Heavy liquid separation was not required, as the non-magnetic residue was easily picked for zircon. Zircon crystals were mounted in epoxy resin and polished to approximately half-thickness. Zircon were imaged in using back-scatter electron (BSE) and cathodoluminescence (CL) detectors using the same Tescan TIGER MIRA3 instrument used for SEM-EDX analysis.

Zircon was analysed for U-Pb isotope and trace element compositions by laser-ablation inductively-coupled-plasma mass-spectrometry (LA–ICP–MS) at the iCRAG laboratory at Trinity College Dublin. The analytical setup comprised a Teledyne Photon Machines G2 laser-ablation system with a 193 nm ArF excimer laser and a Helex II active

two-volume ablation cell, coupled to an Agilent Technologies 7900 quadrupole-ICP-MS. Analyses were conducted using a 30 µm spot size with a ~ 3 s washout time. Oxide production rates were below 0.02%. The analysed masses were ^{29}Si, ^{89}Y, ^{93}Nb, ^{175}Lu, ^{178}Hf, ^{181}Ta, ^{206}Pb, ^{207}Pb, ^{232}Th, ^{238}U.^{137}Ba was used to screen for any contamination from fractures; ^{29}Si was used as an index mass (Paton et al., 2011). For U-Pb geochronology the integration times for individual mass scans were 50 ms for mass 238, 20 ms for mass 232, 10 ms for masses 208 and 204, 150 ms for mass 207, 70 ms for mass 206 and 5 ms for mass 202. Data reduction was completed using the 'VizualAge' data reduction scheme of Petrus and Kamber, (2012), which makes use of the Iolite software package of Paton et al. (2011). Data visualization was aided with the use of the IsoplotR package of Vermeesch, (2018).

The analytical procedure for zircon U-Pb geochronology and trace element geochemistry utilized repeated blocks of zircon reference materials followed by 20 unknown samples using standard-sample bracketing. The zircon reference materials for U-Pb geochronology comprised: three analyses of the primary reference material Temora-2 (^{206}Pb/^{238}U TIMS age of 416.78 ± 0.33 Ma; Black et al., 2004) followed by three analyses of secondary reference materials WRS 1348 zircon (^{206}Pb/^{238}U TIMS age of 526.26 ± 0.70 Ma; Pointon et al., 2012) and FC-1 (^{206}Pb/^{238}U TIMS age of 1099.9 ± 1.1 Ma; Paces and Miller, 1993). At the beginning and end of the analytical session the bracket was expanded to five analyses per reference material. Weighted mean ^{206}Pb/^{238}U ages for WRS 1348 zircon and FC-1 were 526.5 ± 2.3 Ma (MSWD = 0.9) and 1100.8.1 ± 4.5 (MSWD = 1.1), respectively (Fig. S1). Rutile was analysed in situ within thin sections. Rutile geochronology used the same method as zircon above. The rutile reference materials for U-Pb geochronology comprised: three analyses of the primary reference material R10 (intercept age of 1095.2 Ma ± 4.7; Luvizotto et al., 2009), followed by three analyses of secondary reference materials R19 (^{206}Pb/^{238}U TIMS age of 489.5 ± 0.9 Ma; Zack et al., 2011). The lower intercept Tera-Wasserburg age of R19 was 500 Ma ± 25 Ma (MSWD = 0.3).

For trace element analysis, NIST612 was used as the calibration material. Natural zircon 91500 (Wiedenbeck et al., 1995, 2004) was analysed as an unknown during analytical runs and returned values within the range of those previously reported (Table. S3.1). To investigate inter- and intra- sample variability in the trace element composition of zircon we enact a methodology that replicates the steps taken by O'Sullivan et al. (2020)

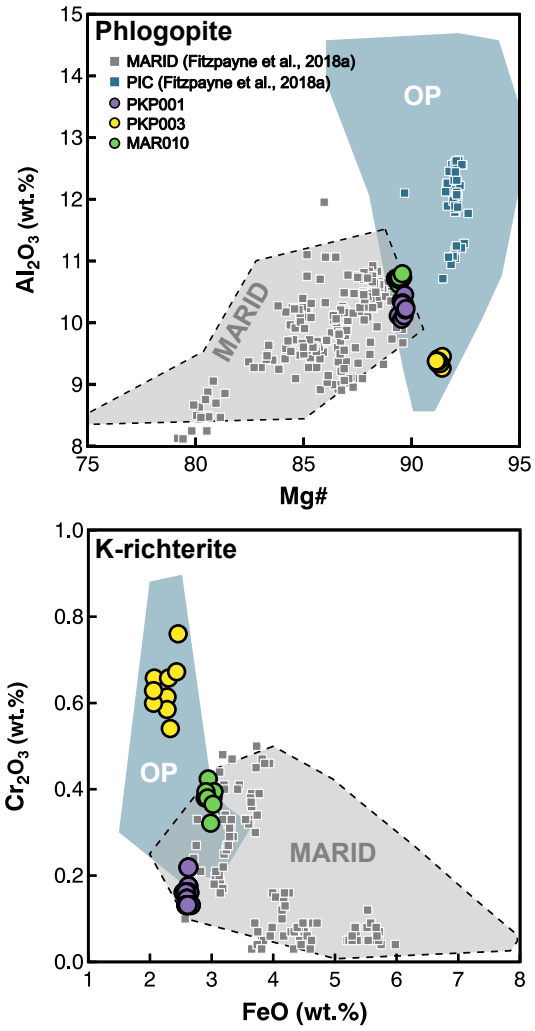

Figure 3.2: Major element plots for K-richterite and phlogopite from xenoliths of this study. Mg# = [Mg/(Mg+Fe2+) x 100]. Fields from Fitzpayne et al., (2018a). MARID – mica-amphibole(K-richterite)-rutile-ilmenite-diopside. PIC – phlogopite-ilmenite-clinopyroxene. 'OP' other K-richterite or phlogopite bearing peridotites.

and Dornan et al. (2020), with principal Component Analysis (PCA) used to determine element pairs or ratios that are useful for separating zircons of different origin.

3.4 Results

Major element compositions of phlogopite and K-richterite

K-richterite and phlogopite from MARID sample MAR010, as expected, plot close to previous analyses of MARID rocks from the Kimberley area (Fig. 3.2). Phlogopite from Sample PKP001, albeit technically not of the MARID suite, also plots within the MARID field. Whilst in the strictest sense the classification is generally restricted to the unusual and extremely phlogopite and K-richterite-rich MARID mantle xenoliths, and not to metasomatised peridotites, a genetic link between MARID and phlogopite and K-richterite

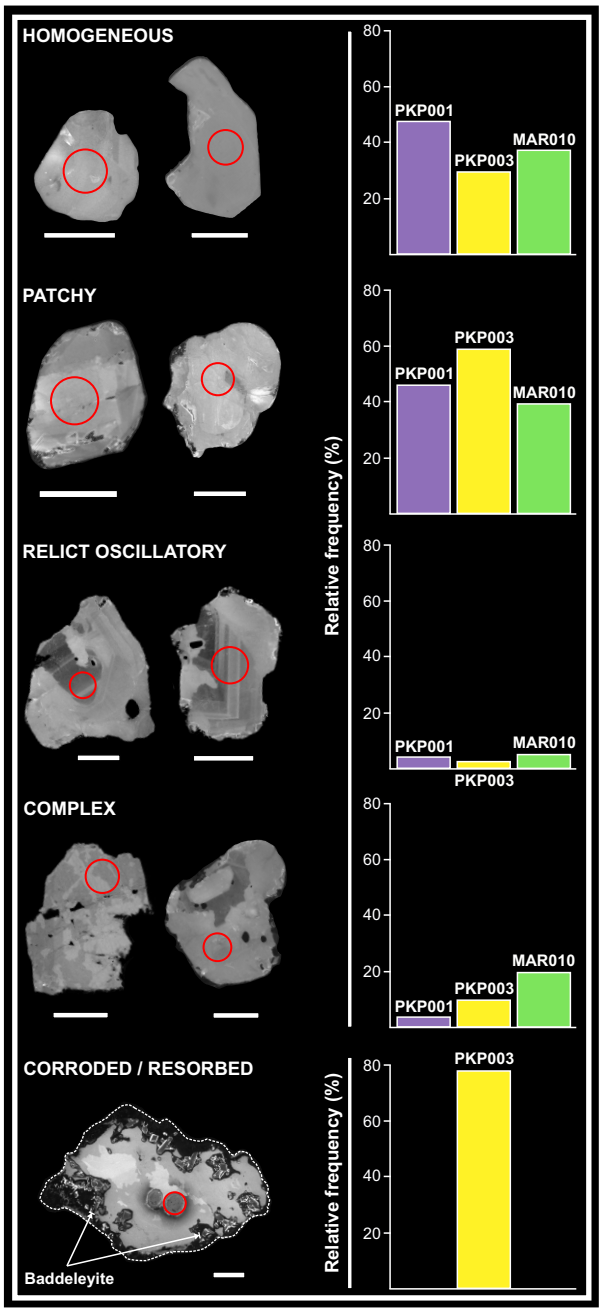

Figure 3.3: Typical cathodoluminescence (CL) images of the non-homogeneous textures observed in zircon of this study. Also shown are the relative frequencies of each texture in each of the analysed xenoliths. Red circle represents the spot placement. All scale bars correspond to 50 µm distance. Dashed outline around the example of the corroded texture demonstrates the grain edge and the growth of CL-poor phases as a corona on the zircon.

bearing peridotites has been suggested since the first recognition of the suite (Dawson and Smith, 1977). Phlogopite and K-richterite in sample PKP003, by contrast, do not overlap with the MARID suite, with phlogopite displaying distinctly elevated Mg# at relatively low Al_2O_3 contents (Fig. 3.2). These characteristics are common to peridotites that do not host K-richterite (e.g., PIC). K-richterite is also relatively enriched in Cr_2O_3 and depleted in FeO compared to K-richterite characteristic of the MARID suite.

Zircon imaging and U-Pb geochronology

Zircon imaging

Backscatter electron imaging shows most zircon is mostly texturally homogeneous. However, samples show occasional veinlets or patches of 'lighter' BSE response. In cathodoluminescence (CL) images, the observed textures are similar for zircon in all three xenolith samples, with either homogeneous, patchy, relict zoned CL or more complex textures observed (Fig. 3.3). The most common textures were either homogeneous or patchy with the latter a common texture seen in other mantle zircon, such as the megacryst suite (Belousova et al., 1998; Corfu et al., 2003). Homogeneous zircon textures under CL are most common in metamorphic rocks. In rare cases where our zircon display igneous zonation, the zoning is overprinted, crosscut or mantled by patchy or featureless CL regions similar to those seen in high grade metamorphic zircon in crustal rocks (Hoskin and Schaltegger, 2018). Uniquely, zircon crystals from sample PKP003 commonly show corrosion toward the grain rims, with occasional overgrowths of baddeleyite (Fig. 3). Inclusions are commonly found in zircon from each xenolith and are K-richterite and phlogopite.

U-Pb Geochronology

U-Pb isotope data are provided in Table. S3.2. Kernel density plots of zircon age distributions and ranked age plots are shown in figures 4-6. Zircon in the studied samples spans 120-80 Ma. In two of the three analysed xenoliths, PKP001 and MAR010, zircon ages are clearly inconsistent with growth in a single event (Fig. 3.4 and 3.6). Zircon ages are not linked to any specific texture under CL or BSE. Of the limited set of relict zircons with oscillatory textures under CL (n = 4), all are <102 Ma. However, geological observations can't be made from such a small subset with any certainty. The zircon age distributions of each sample can be summarised as follows:

- PKP001 has a major mode at ~92.5 Ma and a long tail of older ages to ~120 Ma on kernel density plots (Fig. 3.4c). When plotted as cumulative age distributions (CAD) brief hiatuses are observed in zircon growth from the onset of growth ~120 Ma until kimberlite emplacement, which could be indicative of episodic zircon growth over this period (Fig. 3.4b).
- PKP003 has a unimodal zircon age distribution (Fig. 3.5c). A weighted mean $^{206}Pb/^{238}U$ age for zircon from PKP003 provides an age of 87.3 ± 1.1 Ma (n = 41,

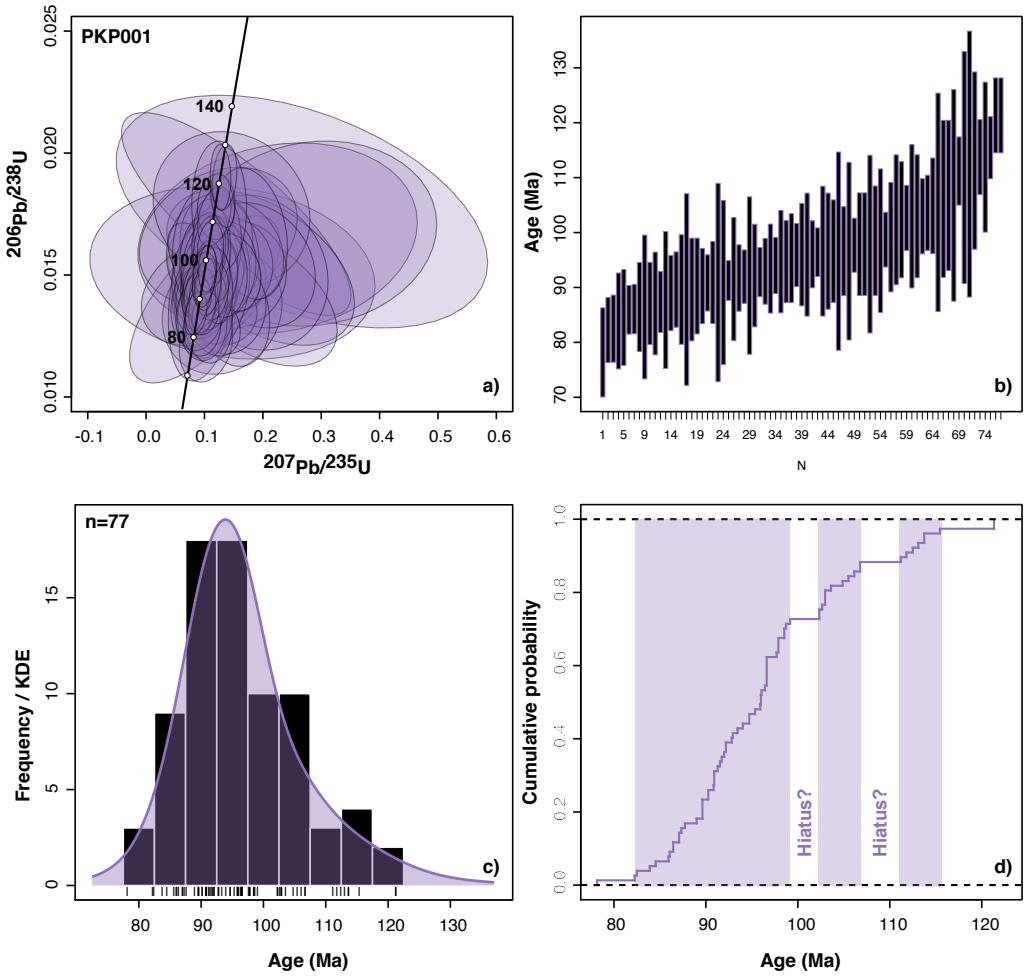

Figure 3.4: Wetherill Concordia diagrams (a), $^{206}Pb/^{238}U$ ranked age plots (b), $^{206}Pb/^{238}U$ age kernel density estimation (KDE) diagrams (c) and cumulative $^{206}Pb/^{238}U$ age distribution diagrams (d) of PKP001 zircon from this study.

MSWD = 1.1). A one sample Anderson-Darling test (Anderson and Darling, 1952) indicates the age data follows a normal distribution expected for zircon derived from a single event at a 95% confidence level.

- Sample MAR010 has three clear zircon age modes visible in kernel density plots (Fig. 3.6c) suggesting that three major peaks of activity are recorded by zircon. The dominant mode is at ~87.5 Ma, shortly prior to kimberlite emplacement of the Bultfontein kimberlite at 84 ± 0.9 Ma (Kramers and Smith, 1983), and there are two earlier modes at ~102.5 Ma and ~112-120 Ma. No time-integrated signal aberrations, nor systematic age differences, were observed between regions showing veinlets or patchy textures under BSE (Fig. S2).

In addition, U-Pb discordia projected through rutile analysed from sample PKP001 from the Kimberley pipe provides a lower intercept age of 89.1 ± 8.3 Ma (Fig; 3.7, n = 11,

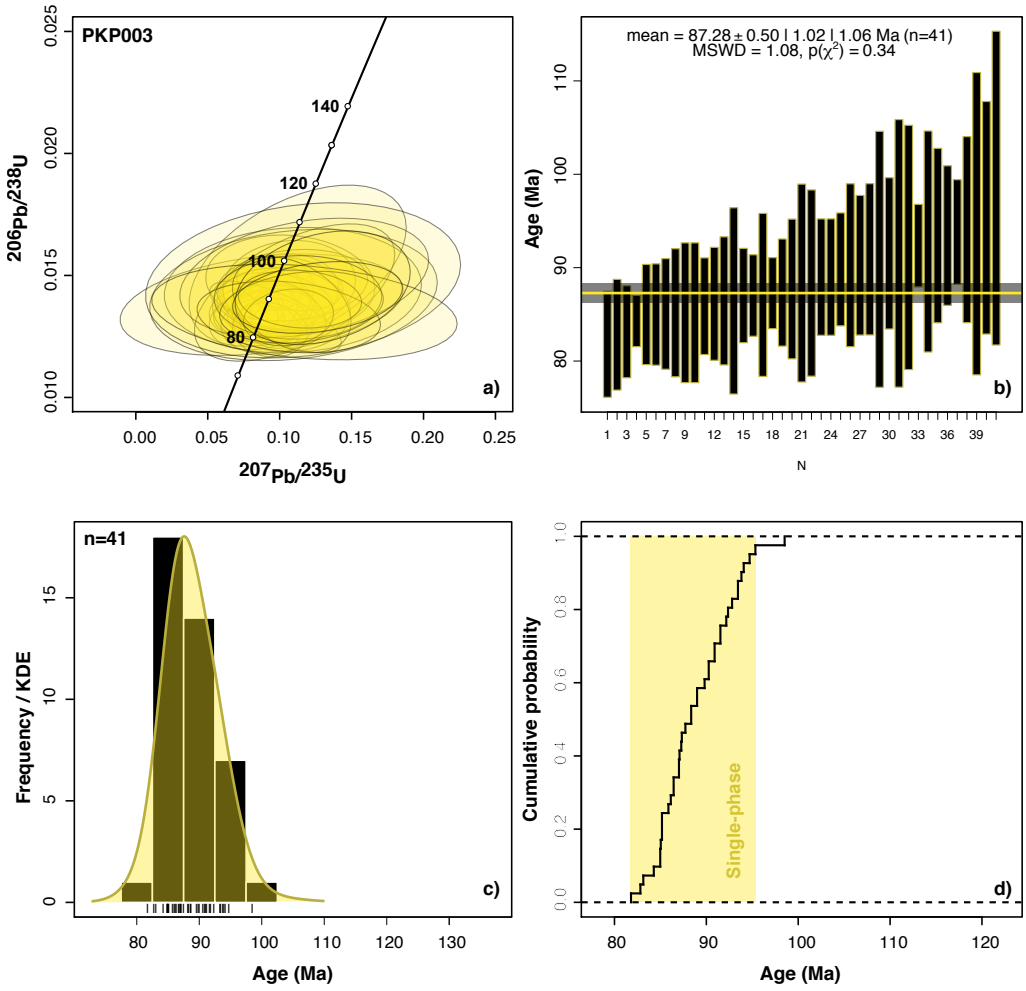

Figure 3.5: Wetherill Concordia diagrams (a), $^{206}Pb/^{238}U$ ranked age plots (b), $^{206}Pb/^{238}U$ age kernel density estimation (KDE) diagrams (c) and cumulative $^{206}Pb/^{238}U$ age distribution diagrams (d) of PKP003 zircon from this study.

MSWD = 0.7), adding another data point to chronology of the Kimberley pipe that is dated to 87 Ma (age from the database of Tappe et al., 2018). Rutile was not observed in either of the other two samples.

Zircon trace elements

The trace element compositions of zircon from the studied samples are displayed on multi-element primitive mantle normalized ('spidergram') plots in Figure 3.8. Trace element abundances for each grain are provided in Table. S3.3. In samples PKP001 and PKP003, trace element compositions of zircon are relatively uniform. Contrastingly, zircon in MAR010 may be subdivided into four compositional populations based on variations in Ta; Lu; Nb; and Y contents (type-I to type-IV, Fig. 3.8), and from plots of Th/Y vs Ta (Fig. 3.9), which were determined to be potentially useful discriminant factors through the use of a PCA biplot (Fig. 3.10).

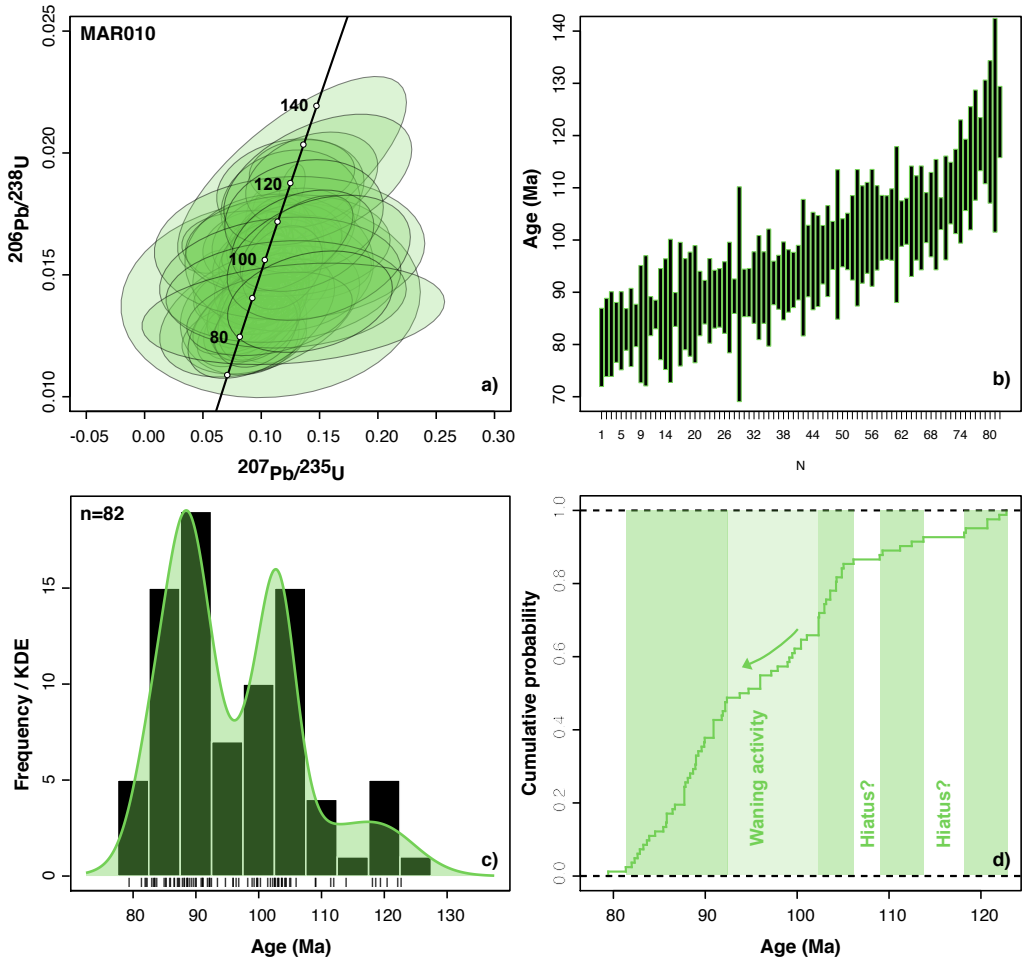

Figure 3.6: Wetherill Concordia diagrams (a), $^{206}Pb/^{238}U$ ranked age plots (b), $^{206}Pb/^{238}U$ age kernel density estimation (KDE) diagrams (c) and cumulative $^{206}Pb/^{238}U$ age distribution diagrams (d) of MAR010 zircon from this study.

In Th/U space zircon from samples PKP001 and MAR010 span a range of U and Th compositions. By contrast, zircon from sample PKP003 have a far narrower range in concentration, spanning the range of Th and U contents typical of megacrystic zircon (Fig. 11a-c; Belousova et al., 1998). Overall, Th/U ratios in zircons from the three xenoliths range from 0.04 to 5.54, similar to values seen in zircons from mantle peridotites (Fig. 3.11d-f; Konzett et al., 2000; Liati et al., 2004; Giuliani et al., 2014; Wang et al., 2020) and lamproites (Fig. 11g-I; Santosh et al., 2018 albeit from relatively few analyses) to megacrystic zircon from kimberlite. Thorium is systematically higher in zircons from sample PKP001 (e.g., Fig. 3.11a-c). As a result, zircon in this sample display Th/U ratios (~1.5) which are systematically higher than the other zircon analysed in this study; similar to igneous zircon in other rocks (Th/U > 0.5; Hoskin and Schaltegger, 2018).

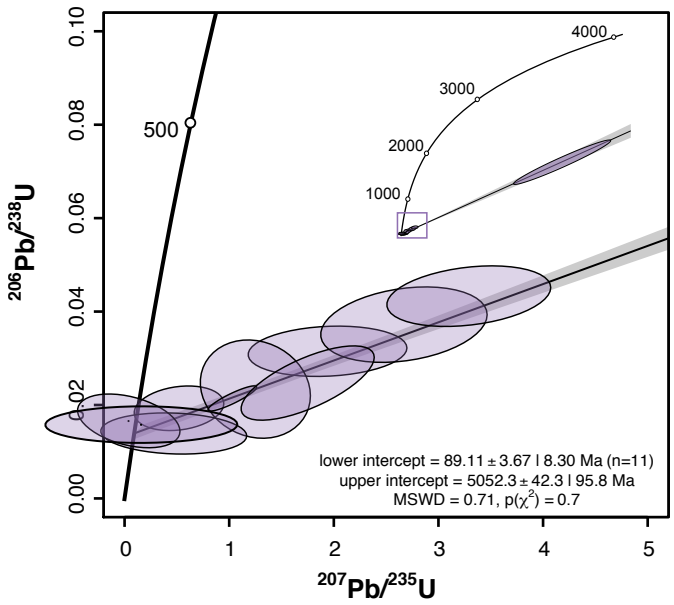

Figure 3.7: Wetherill Concordia diagram from rutile from sample PKP001.

Zircon from both PKP001 and PKP003 have relatively consistent trace element compositions, as illustrated by the distinguishable compositional groups seen on a PCA biplot (Fig. 3.10). Similar to the multi-element plots (Fig. 3.8), on a PCA biplot (Fig. 3.10) zircon from sample MAR010 plots over a much wider area, indicating large compositional variation. Generally, types-I and IV display concentrations of Y, Th, and U contents most like lamproitic zircon and trend toward cratonic crustal compositions (Fig. 3.12; Belousova et al., 2002; Wu et al., 2016; Zhou et al., 2018; Mitra et al., 2019). Type-III zircon form MAR010 have trace element compositions very similar to zircon in sample PKP003 (Fig. 8). The similarities of the trace element compositions seen in zircon from PKP003 and type-III zircon from MAR010 are mirrored by similarities in their age distributions (Fig. 3.13). Lastly, type-II zircon displays an anomalous trend, clearly seen in Th and Y space, unlike either megacrystic or lamproitic zircon (Fig. 3.12). No specific trace element composition is linked to any of the homogeneous, patchy, or complex textures seen in the zircons here. However, the limited examples of relict oscillatory-zoned zircon with generally provide the highest trace element compositions of this study. As with the ages of this subset, no useful observations can be made with any reliability with regards to their trace element compositions.

3.5 Discussion

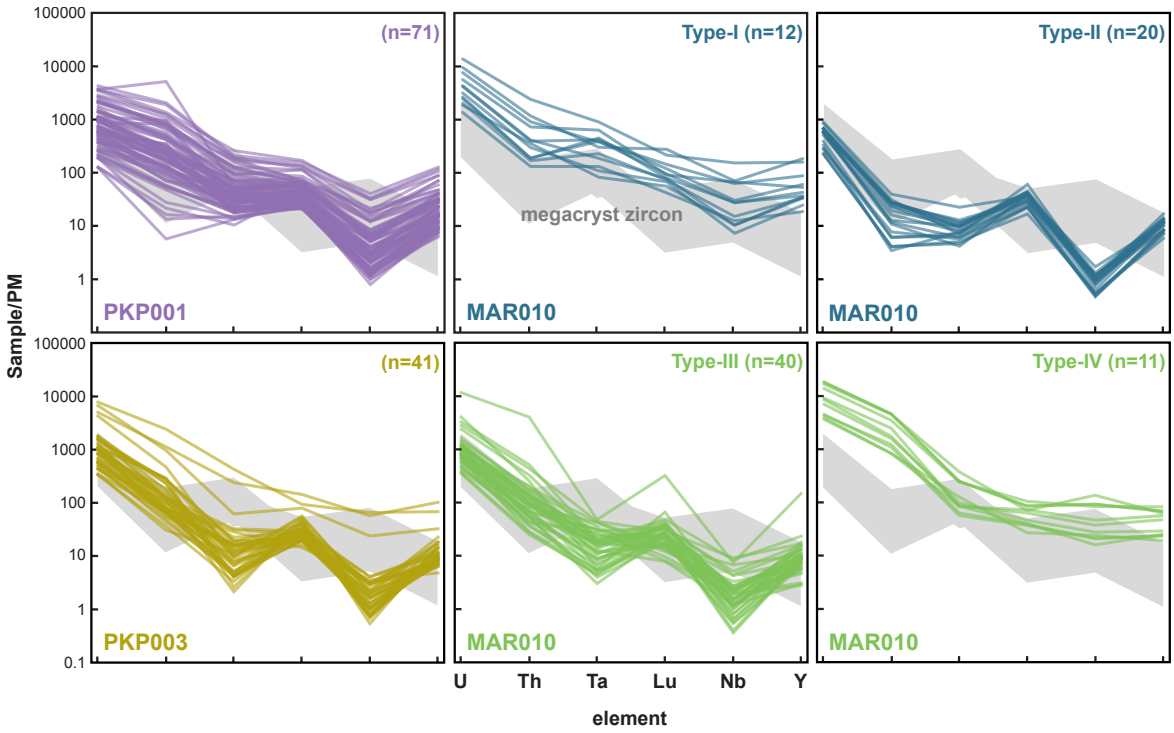

Figure 3.8: Primitive mantle (PM) normalized (McDonough and Sun, 1995) trace element spider diagrams for samples PKP001, PKP003 and MAR010. Megacryst zircon data from Belousova et al., (1998) and Agashev et al., (2020).

Pb-loss in mantle zircon from Kimberley region?

In previous studies of zircon in mantle xenoliths from the Kimberley region of the Kaapvaal craton, Pb-loss is commonly considered a risk; with reported ages considered minimum ages (Konzett et al., 1998, 2000; Giuliani et al., 2015). However, we consider Pb loss to be unlikely for the following reasons. Pb-loss in zircon occurs in four ways: volume diffusion in pristine zircon, volume diffusion in metamict zircon, leaching from metamict zircon and recrystallization of metamict zircon (e.g., Mezger and Krogstad, 1997). The latter three cases are all facilitated by radiation damage and metamictisation, which can be considered extremely unlikely in this instance because zircon (PKP) bearing rocks from Kimberley were resident at mantle temperatures (755-890°C; Waters and Erlank, 1988) that are in excess of the lower-limits of self-annealing behaviour (Geisler et al., 2001). Additionally, the zircons themselves have extremely low U-contents, which is not conducive for metamictisation (Table. S3.2). This leaves only the possibility of the first case, diffusion of Pb in pristine zircon. However, the estimated residence temperature of PKP rocks from Kimberley is lower than 900°C, the temperature below which Pb diffusion in pristine zircon becomes insignificant (Cherniak and Watson, 2001), implying minimal Pb loss via diffusion at least under steady state conditions (Waters and Erlank, 1988). In any

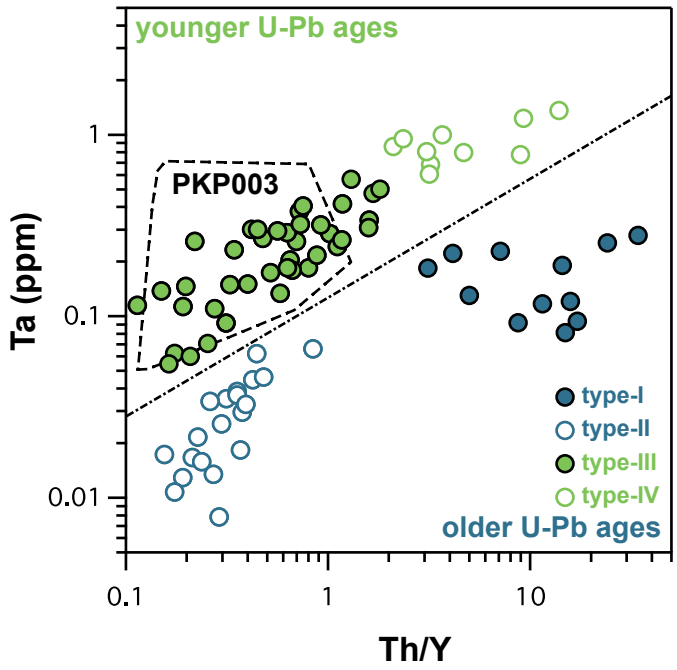

Figure 3.9: Ta vs Th/Y biplot for zircon from MAR010 for distinguishing sub-populations.

case we would argue that slow cooling of zircon from temperatures in excess of U-Pb closure in transient conditions deviating from steady-state in the lithosphere is unlikely to be viable in such volumetrically insubstantial mantle domains, such as those we have studied. Furthermore, the retention of concordant U-Pb in mantle zircon at mantle temperatures over byr timescales is already demonstrated by two suites of megacrystic zircon from the Timber Creek Kimberlites from Australia (Belousova et al., 2001). The first and 'younger' suite provides a single mean-squared weighted age, presumed to coincide with the kimberlite emplacement, of 179 ± 2 Ma, whilst a second 'older' suite provides a substantially older single population age of 1462 ± 53 Ma. Whilst both the suites analysed by Belousova et al. (2001) display morphologies and trace element compositions typical of megacrystic zircons they have distinct trace element compositions that defy origins from a common source. Rather, the older suite must have been sampled from a distinct mantle domain (potentially formed with earlier magmatic activity) and clearly must have experienced minimal Pb-loss. This story is potentially similar to that also seen megacrystic zircon in the Permian Jwaneng kimberlite from the Kaapvaal craton, which seems to preserve an Archean megacryst population (Kinny et al., 1989), suggesting negligible Pb-loss in mantle zircon over yet longer timescales. Experimental evidence simulating recycled zircon in the mantle at extremely high temperatures (1300-1500°C) also show limited possibility for diffusion of Pb in zircon (Bea et al., 2018), albeit with the

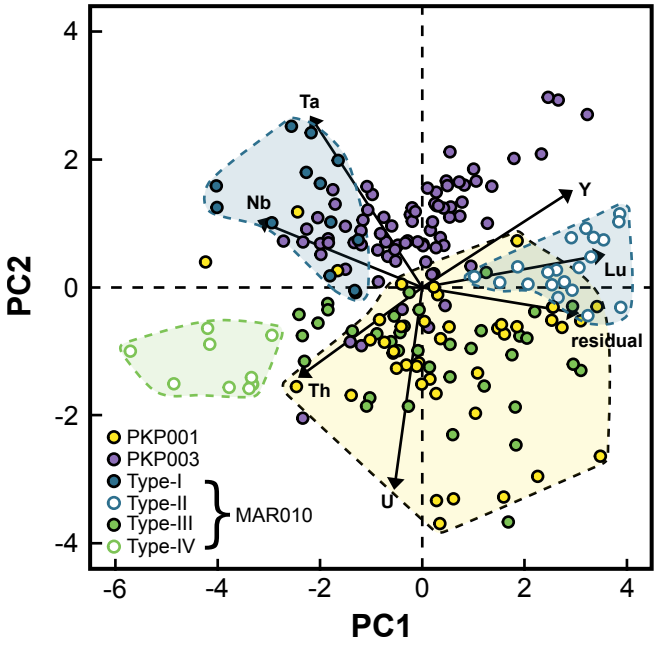

Figure 3.10: Zircon PCA plot by xenolith samples and sub-populations of this study. Note that the stippled fields are a visual aid and have no statistical meaning. PC1 - principal component 1, PC2 – principal component 2.

assumption that zircon would be effectively sealed by minerals with extremely low diffusivity (e.g., olivine; orthopyroxene), which may not be directly applicable to PKP and MARID rocks. Nonetheless, these examples demonstrate that Pb loss should not be assumed *a priori* for in zircon residing at mantle temperatures, potentially over byr timescales.

Based on the observed textures of zircon in CL and BSE we propose that recrystallization is a far more likely to have occurred rather than Pb-loss, which also explains the homogeneous and more complex transgressive CL patterns and resorption seen in these zircons. In this respect, the U-Pb ages, particularly the homogeneous and patchy textured zircon, actually represent the timing of crystallization. This means that they can be treated similarly to igneous zircon, with the caveats that multiple age zones may occur in a single zircon (e.g., Konzett et al., 1998; 2000), and that highly complex grains may yield mixed and/or multiple ages. We note that multiple analyses of complex textured zircon reported by Giuliani et al. (2015) displayed almost no intragrain age variation. In zircon from MAR010 Pb-loss cannot adequately explain the observed temporal control on their trace element composition (see below). We argue that it is hard to envisage the selective age-resetting of just a single population of zircon within sample MAR010 (a fragment of rock <15 cm in size) due to any thermal perturbations in the

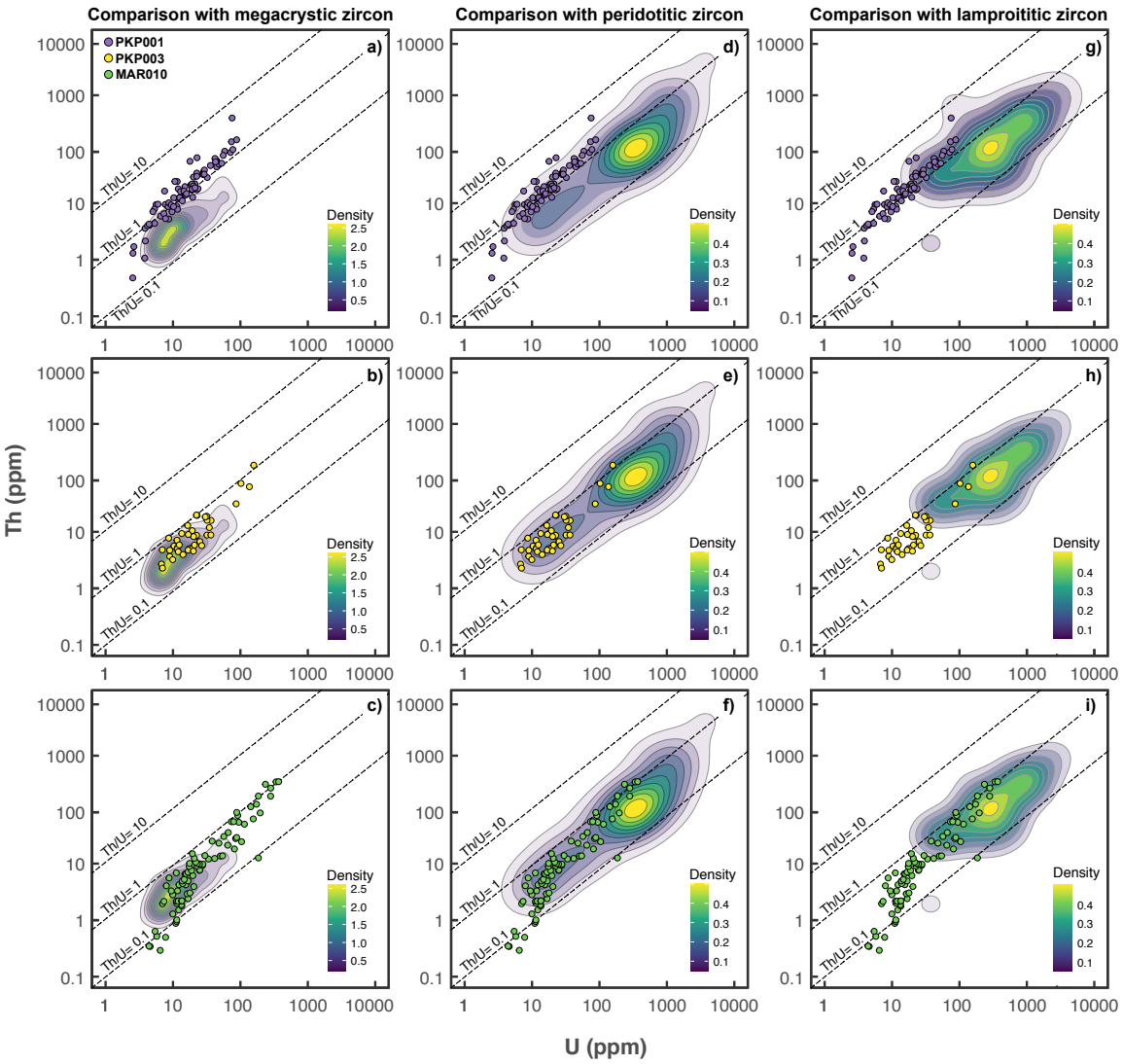

Figure 3.11: Th vs U biplots of zircon from this study compared to densities of literature data. Megacrystic zircon (a-c) from kimberlite (Kinny et al., 1989; Belousova et al., 1998; Griffin et al., 2000), peridotitic zircon (d-f; Konzett et al., 2000; Liati et al., 2004; Giuliani et al., 2014; Wang et al., 2020) and non-xenocrystic lamproite zircon (g-i; Santosh et al., 2018).

lithosphere coinciding with Cretaceous kimberlite and/or orangeite magmatism. Given the existing evidence, we consider that radiogenic Pb was retained by the analysed self-annealing low-U zircon in this study.

Comparison of zircon U-Pb ages and trace elements with Mesozoic intraplate magmatism in Southern Africa

U-Pb dates recorded by zircon in the xenoliths analysed in this study span from ca. 120 to 80 Ma (Figs. 3.4-3.6), similar to the range reported for zircon in other MARID/PKP mantle xenoliths from the Kimberley region of the Kaapvaal Craton (Konzett et al., 1998, 2000, 2013; Giuliani et al., 2015). The range of zircon U-Pb dates from these xenoliths

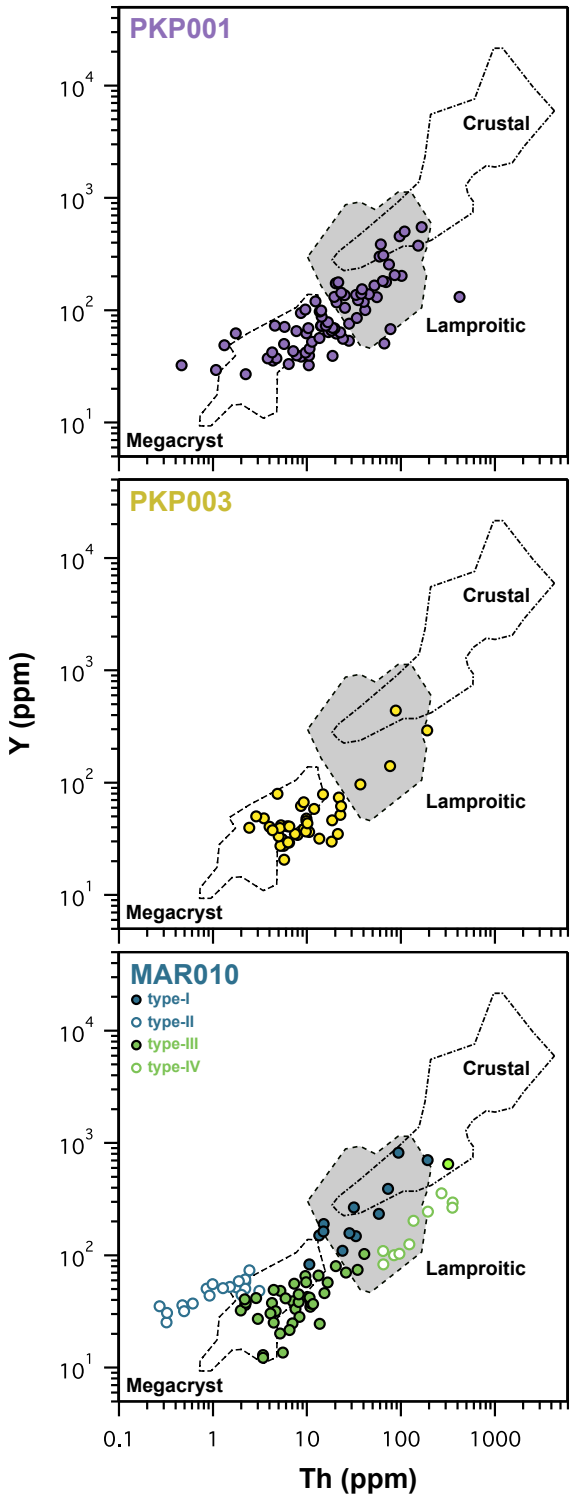

Figure 3.12: Y vs Th biplot, adapted from Belousova et al. (2002), for comparison of xenolithic zircon with cratonic crustal zircon (Wu et al., 2016; Zhou et al., 2018; Mitra et al., 2019), lamproitic zircon (Belousova et al., 2002) and megacrystic zircon (Belousova et al., 1998; Agashev et al., 2020).

closely aligns with kimberlite and orangeite activity in Southern Africa, and particularly those magmas in close proximity to the Kimberley region of the Kaapvaal craton (Griffin

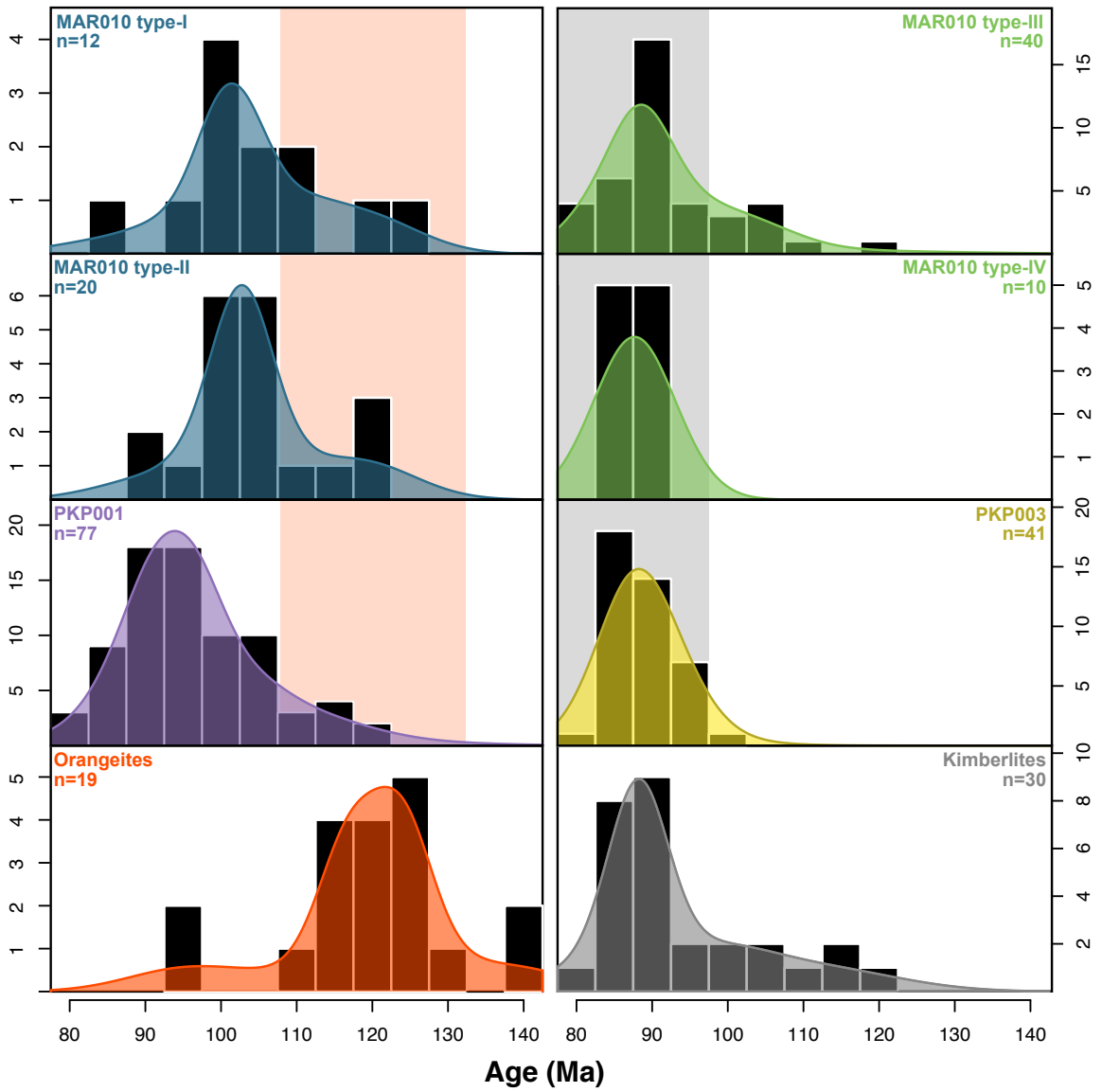

Figure 3.13: $^{206}Pb/^{238}U$ kernel density estimation (KDE) plots each sample (and sub population) compared with orangeite and kimberlite magmatism in the near vicinity (<300 km) of the Kimberley region of the Kaapvaal, South Africa. Distance from Kimberley was calculated assuming a spherical Earth using the Haversine formula. Orangeite and kimberlite emplacement age data taken from combined databases of Griffin et al., (2014) and Tappe et al., (2018).

et al., 2014; Tappe et al., 2018; Fig. 3.13). The large numbers of grains analysed in this study reveal a complex metasomatic history.

Zircon associated with kimberlite magmatism

The unimodal age distribution population of zircon in PKP003 (87.3 ± 1.1 Ma, n= 41, MSWD = 1.1) coincides with the emplacement of its host kimberlite (Griffin et al., 2014; Tappe et al., 2018). Unlike zircons from the other samples in this study, those from sample PKP003 commonly (though not always) display significant corrosion at the grain rim and in rare cases baddeleyite coronas (Fig. 3.3). We suggest that this corrosion results from

partial resorption of the zircon by interaction with a kimberlite-like melt or metasomatic agent into the xenolith. Baddeleyite coronas have also been seen in other mantle xenoliths from the Kimberley cluster and have been argued to result from kimberlite-related metasomatism of the lithosphere at the time of kimberlite emplacement (Konzett et al., 2013; Giuliani et al., 2015). Thus, it is likely that the unimodal age distribution in PKP003 provides the age of the kimberlite emplacement, the age being derived from resetting of the U-Pb system during resorption/recrystallization and baddeleyite-forming reactions. The action of kimberlite metasomatism in sample PKP003 is supported by the major element composition of coexisting phlogopite and K-richterite, which are dissimilar to equivalent phases in other MARID/PKP rocks and more comparable to PIC xenoliths thought to derive from kimberlite metasomatism (Fig. 3.2). Evidence from zircon of kimberlite metasomatism in PKP003 is somewhat supported by their trace element compositions, which are similar (albeit depleted in Nb and Ta) in composition to megacrystic zircon (Figs. 3.8 and 3.12) which are argued to form within kimberlite or in the final stages of crystallization from fractionated kimberlite liquids/melts at mantle depths (Gurney et al., 1979; Mitchell, 1987; Moore et al., 1992). Combining the rock-forming phase and zircon trace element data, we suggest that zircon from PKP003 equilibrated with a kimberlite melt or kimberlitic metasomatic agent in the lithosphere during, or shortly prior to, its host kimberlite's emplacement.

The trace element composition of zircon from sample PKP003 is very similar to the type-III sub population identified MAR010 (Fig. 3.8). The similarity in the trace element compositions of these zircons is matched by a coincidence of their recorded ages. However, unlike PK003 the ages in type-III zircons are not consistent with a single unimodal age suggesting these zircons formed over a more prolonged timeframe albeit one mainly encompassing peak kimberlite activity in the Kimberley region of the Kaapvaal (Griffin et al., 2014; Tappe et al., 2018; Fig. 3.13). These similarities in the trace element compositions and age distributions suggest a common origin and support a genetic link between the MARID and PKP suites, i.e., both are modified or partly formed by common metasomatic agents. As neither MARID or PKP are consistent with direct derivation from kimberlite by any mechanism at mantle depths (Grégoire et al., 2002) our samples demonstrate that PKP or MARID rocks can be either partially (MAR010; see below) or totally (PKP003) overprinted by kimberlite-type metasomatism.

Zircon of lamproite-like affinity

Unlike zircon inferred to derive from kimberlite-metasomatism, zircon from PKP001 and types-I and IV from MAR010 have trace element compositions distinct from those seen in PKP003 or type-III of MAR010. Rather, these zircons have trace element compositions more alike to lamproitic zircon, whilst type-II zircon has anomalous Th depletion, which apparently shares no affinity with any pre-existing data for mantle-derived zircon (Fig. 3.12). The trace element compositions of zircon sub-populations in sample MAR010 can be linked by their U-Pb ages to discrete periods of time (Fig. 3.13), indicating that up to three distinct sources were responsible for zircon growth in the rock. Type-I and type-II zircon in MAR010, and a significant proportion of zircon in PKP001, yield ages that are systematically older than kimberlite emplacement, with age distributions that peak shortly after orangeite magmatism (Griffin et al., 2014; Tappe et al., 2018) and a tail of ages that trend toward the expressions of orangeite magmatism in the Kimberley region (Fig. 3.13). Unusually, type-IV zircon provides ages that coincide with the main phase of kimberlite magmatism in the Kimberley region. A mean-squared weighted age of type-IV zircon provides an age of 87.2 ± 2.1 Ma (n = 10; MSWD = 2.33). The MSWD of this population is in excess of an acceptable MSWD of 1.9 at 2σ (n = 10) that could be indicative of a single age (Spencer et al., 2016), so these zircon are not totally restricted to formation concomitant with the host kimberlite emplacement in which the xenolith was sampled.

Cretaceous magmatic activity recorded by zircon

With the geochemical similarities of some of these zircons to lamproitic zircon and ages predating the main expression of kimberlite magmatism, it is feasible that these zircons share a genetic link with orangeite magmatism, which also shares some geochemical similarities with lamproite magmas (Mitchell, 1995). Clearly the age distributions of these zircons belie a simple model whereby they formed directly as a result of the passage of orangeite magmas through the Kaapvaal lithosphere. In fact, the majority of activity, at least that recorded by lamproite-like zircon, in samples PKP001 and MAR010 marks the transition between waning orangeite magmatism and the onset of the main pulse of kimberlite magmatism in the region (Griffin et al., 2014; Tappe et al., 2018; Fig. 3.13). To explain this, we favour a scenario in which, from about 130 Ma, low-degree carbonate rich asthenospheric mantle melts were channelled along pre-existing MARID-like or phlogopite-rich vein assemblages and zones of weakness near the craton root (Griffin et al., 2014). The mutual exclusivity in the stability of carbonate with phlogopite and K-richterite

at depth in the lithosphere (Ulmer and Sweeney, 2002) favours melting of these veined assemblages forming hybrid vein-plus-wall-rock (e.g., Foley, 1992) and asthenospheric components leading to the generation of orangeite magmatism. Such a mechanism can explain the high Mg#, CO_2 and compatible element (e.g., Ni and Cr) contents of orangeite juxtaposed with their extreme incompatible element enrichment and high H_2O contents (Becker and Le Roex, 2006; Giuliani et al., 2015). On ascent through the lithosphere, these melts drive metasomatism and generation of melt veins in shallower portions of the lithosphere and the oldest zircon crystallization seen in our PKP and MARID samples. From 110 Ma, diminishing melt productivity from the asthenospheric mantle and/or exhausting of the metasomatic assemblage near the craton root (e.g., Griffin et al., 2014) led to a termination of surface expressions of orangeite magmatism. However, at shallow depths in the lithosphere, as sampled in our xenoliths, localized melting continued leading to recurrent (re-?) crystallization of zircon with lamproite-like affinity. Recurrent recrystallization of zircon in these PKP and MARID rocks is also consistent with their CL textures, which most commonly mirror those seen in high-grade metamorphic crust.

Finally, late-Cretaceous kimberlite magmatism of South Africa, derived principally of asthenospheric origin (Smith, 1983; Nowell et al., 2004; Tappe et al., 2020), was channelled along the pre-existing mantle weaknesses formed through earlier orangeite magmatism. At depth these zones of weakness were now highly refractory with the purging of the pre-existing metasomes during orangeite magmatism and therefore have little influence on the composition of passing kimberlite magmas. Similarly, at higher levels in the lithosphere remnants of MARID and PKP rocks, as sampled here, would also have little influence on the composition on passing kimberlites due to the rapid ascent of the magmas (Griffin et al., 2014). Nonetheless, passage of kimberlitic melts through the lithosphere produced a final phase of zircon growth at shallow depths that we presume to have been in equilibrium with a kimberlite-type melt or agent. In the case of sample PKP003, total overprinting of major element compositions of phlogopite and K-richterite also occurred and possibly a total reset of the zircons U-Pb isotope compositions.

We argue the complexity and extremely localized isotopic disequilibria seen in MARID rocks cannot be explained in terms of a simple cumulate magmatic origin. The scenario we present also implies that MARID and PKP rocks are not the source of orangeite magmas (cf., Giuliani et al., 2015), but rather are products of the generation, passage and metasomatic effects of multiple and localized low-degree melts from depth. By

analogy MARID and PKP rocks could be compared to migmatised lower crustal rocks that undergo multiple phases of metamorphism and anatexis. Collectively, the zircon age and trace element evidence suggest that PKP and MARID xenoliths are hybrid rocks and that no single source can be attributed to their formation. Rather, it appears that MARID/PKP rocks more likely form as a direct result of the metasomatic effects of the passage of *both* kimberlite and orangeite magmatism through the lithosphere, as originally suggested by Konzett et al. (2000). Therefore, the assignment of xenolith to a specific suite (e.g., PIC or MARID) may not capture the full metasomatic history of the rock and such divisions, whilst demonstrably useful, cannot reflect the extremely complex and hybrid nature of these rocks.

A hybrid origin for the formation of PKP and MARID rocks is supported by studies that document conflicting isotope systematics. It is apparent that MARID (Kramers et al., 1983; Fitzpayne et al., 2019) and PKP xenoliths (Hawkesworth et al., 1990) have variable $^{87}Sr/^{86}Sr$ and $^{143}Nd/^{144}Nd$ compositions that belie a simple one component origin, ranging from those similar to the convecting upper mantle, as sampled by kimberlite, to the 'enriched' compositions of orangeites and certain ocean island basalts (e.g., enriched mantle I or enriched mantle II endmembers; Zindler and Hart, 1986). The kimberlite-like endmember radiogenic compositions seen in some MARID rocks suggest at least partial influence of kimberlite-like melts in their formation, as supported by this study. The influence of kimberlite-type melts in their formation is supported by thallium isotope analysis of MARID rocks, which demonstrates that their isotopic composition mirrors that of the convecting upper mantle (Fitzpayne et al., 2020). In contrast the enriched 'endmember' of compositions seen in MARID, PKP and orangeite require long-term isolation from the homogenizing effects of convection in the asthenospheric mantle, which is presumed to reside in the lithospheric mantle (e.g., Fraser et al., 1985). When this enriched component was introduced into the lithosphere remains unclear. The volatile composition of MARID xenoliths are in agreement with the sampling of a recycled subducted component with enriched $\delta^{15}N$ compositions relative to the typical depleted convecting upper mantle (Banerjee et al., 2015) that could be linked to ancient subduction metasomatism. Alternatively, isotopically enriched MARID veined assemblages at depth could have been introduced during previous magmatic activity in the region; such as the Karoo LIP (Giuliani et al., 2015), and possibly as a result of the impingement of a plume on the South African lithosphere (Celli et al., 2020).

The scenario we present for the generation of complex lithospheric domains with localised and recurrent melting of both asthenospheric and enriched mantle components is probably not restricted to the Kaapvaal Craton nor the generation of orangeite magmatism. Similarly enriched continental lithosphere is seen in other cratonic regions (e.g., North Atlantic Craton) and is thought to be a key component in the formation of other ultrapotassic rocks such as ultramafic lamprophyre (Foley et al., 2002; Tappe et al., 2006, 2008, 2011). Furthermore, K-rich mantle xenoliths of thick oceanic lithosphere intimate that this type of scenario might not be restricted to the continental realm with potential implications for OIB genesis (Smart et al., 2019).

3.6 Conclusions

- Through the use of larger zircon sample sizes from metasomatised mantle xenoliths than have previously been employed (n > 40) and fully integrating trace element and U-Pb isotope data in those analyses, we establish a methodology to document and trace complex metasomatism of cratonic lithosphere through time.
- Zircon growth in PKP and MARID xenoliths was recurrent, with multiple metasomatic compositions that correspond to discrete time periods. In the zircon record, metasomatism appears intimately linked with Cretaceous intra-cratonic magmatism in South Africa. At ca. 120 Ma new zircon is lamproite like in composition and is coincident with orangeite magmatism on the Kaapvaal Craton. In contrast, most zircon with late Cretaceous U-Pb ages (ca. <100 Ma), corresponding to peak kimberlite magmatism, have trace-element compositions more similar to that seen in megacrystic zircon - a suite thought to derive from fractionated kimberlitic liquids/fluids at mantle depths.
- We infer MARID and PKP rocks form during localized and recurrent melting of lithospheric and asthenospheric components. The metasomatizing effects of the passage of varying magmas at shallow depth in the lithosphere contribute to their complex age and geochemical signatures.
- The presence of zircon grown from opposing metasomatic agents within a single xenolith (MAR010) demonstrates both trace element and isotopic disequilibria on cm-scales. This further supports a hybrid multiphase metasomatic origin is required to form MARID and probably PKP rocks.

- Large-n zircon datasets are thus an ideal method to trace complex metasomatism and the passage of ultrapotassic and kimberlitic melts in the lithosphere, as the high closure temperature of the U-Pb system in zircon means that zircon can act as a capsule of former agents in pervasively overprinted rocks.

Acknowledgements

This project was funded through support from a Government of Ireland Postgraduate Scholarship from the Irish Research Council held by BCH (GOIPG/2017/1132). GOS acknowledges support from a Government of Ireland Postdoctoral Fellowship from the IRC (GOIPD/2019/906). The TCD iCRAG laboratory is supported by SFI grant SFI/RI/3227. We thank David Chew and Eoghan Corbett for several productive conversations concerning experiment design and for helping us to better develop our ideas. We warmly thank Chris Hawkesworth and Sebastian Tappe for their thoughtful and constructive reviews and additional comments from Thomas Pettke, which we believe improved the clarity of this submission. We also thank Thomas Pettke and Balz Kamber for the editorial handling of this contribution. The authors have no competing interests to declare.

Supplemental information

Discordance and data filtering

As the majority of zircon analysed in this study are relatively young and low in U (and thus Pb) contents we argue that absolute age discordance cut-off criteria are inappropriate (typically -1 to 5-10% difference in absolute age, where positive concordance represents the plotting of grains below concordia). Absolute age discordance cut-off unfairly punishes young, lower precision analyses as the enlarged error (particularly in measurements of $^{207}Pb/^{206}Pb$ ratios) is such that the analysis could be 'concordant' within 2SE but removed by absolute discordance filters. We apply a simpler, less punishing criteria of accepting grains as concordant if their error ellipses overlap within 2SE of the U-Pb concordia. We retain a negative -5% discordance filter as positive discordances in this study derive from grains with extremely low ^{207}Pb contents and thus provide more questionable ages. Positively discordant zircon filtered out of the dataset fall along a mixing line toward 'common' Pb, rather than any instances of lead loss of older grains. No obvious texture is typical of zircon that is discordant, so our removal is likely justified.

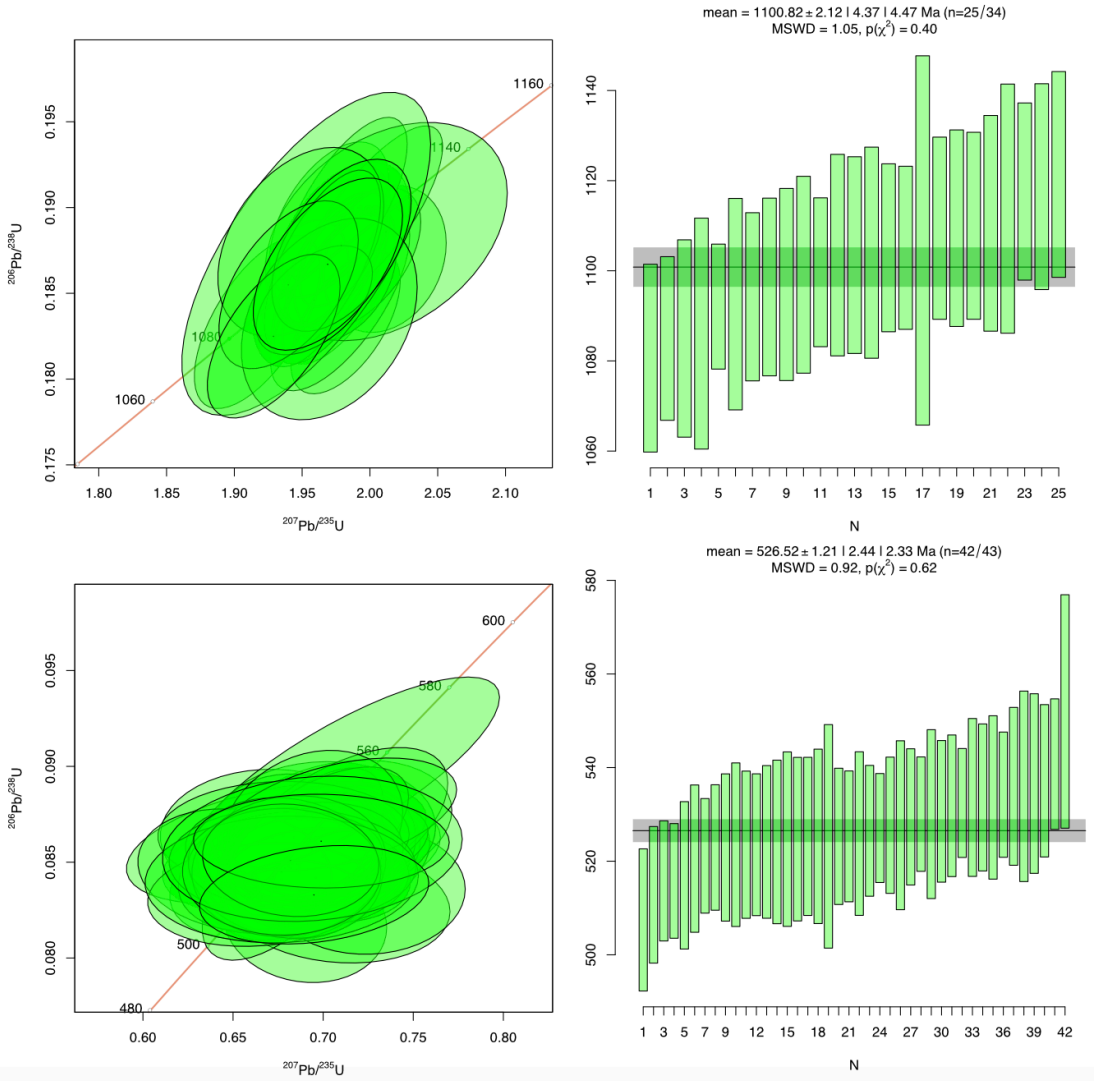

Figure. S3.1: MAll values reported in µg/g. U-Pb concordias and $^{206}Pb/^{238}U$ mean-squared weighted ages and standard data for FC-1 and WRS1348

U-Pb geochronology of 'light' and 'normal' BSE in singular zircon grains

Prior to the analytical session of which all geochronological data presented in the paper were completed a short analytical session to ascertain if any there was any systematic age variation between light and dark BSE regions. We utilized the same analytical setup as stated in Section 3, but using a Thermo iCAPQc ICP-MS. The zircon reference materials for U-Pb geochronology comprised; three analyses of the primary reference material Plešovice ($^{206}Pb/^{238}U$ TIMS age of 337.13 ± 0.37 Ma; Sláma et al., 2008) followed by three analyses of secondary reference materials WRS 1348 zircon ($^{206}Pb/^{238}U$ TIMS age of 526.26 ± 0.70 Ma; Pointon et al., 2012) and Fish Canyon Tuff (astronomically calibrated

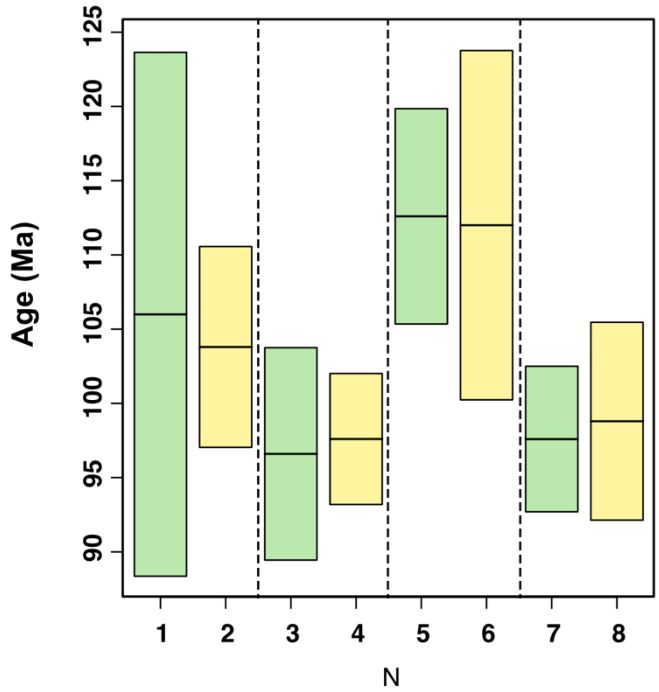

Figure. S3.2: $^{206}Pb/^{238}U$ ages of zircon with 'light' (green) and normal BSE regions (yellow).

age of 28.201 ± 0.012 Ma; Kuiper et al., 2008). Weighted mean $^{206}Pb/^{238}U$ ages for Fish Canyon Tuff and WRS 1348 zircon were 28.16 Ma (MSWD= 0.27, n=6) and 523.1 ± 3.9 (MSWD=0.5, n=5), respectively. We saw no age systematic age difference between light and normal BSE regions (Fig. S3.1). We infer that these anomalous BSE regions were formed during their growth via interaction with surrounding fluids/melts.

element	measured 91500	reported 91500	measured Temora	reported Temora-2
Y	62.6 ± 0.68	114-193	740 ± 140	828
Nb	0.58 ± 0.02	0.73 - 6.71	0.55 ± 0.07	no data
Lu	6.66 ± 0.08	6.75 - 21.7	55.3 ± 5.9	56
Ta	0.33 ± 0.01	no data	0.25 ± 0.02	no data
Th	12.6 ± 0.1	12.7 - 42.9	39.7 ± 6.4	19-294
U	46.9 ± 0.6	42.8 - 113.4	110 ± 14	45-755

Table S3.1: Measured and reported trace element data for 91500 zircon and Temora-2. Data from GEOREM archive and Wiedenbeck et al., (2004). All values reported in ppm.

Supplementary Table. S3.2

Grain	$^{207}Pb/^{235}U$	2SE	$^{206}Pb/^{238}U$	2SE	ρ	$^{207}Pb/^{235}U$ Age	2SE	$^{206}Pb/^{238}U$ Age	2SE
PKP001_2	0.119	0.068	0.0151	0.0029	-0.0052	139.9	88.4	96.6	9.2
PKP001_4	0.111	0.032	0.01288	0.00098	-0.0437	114.1	15.7	82.5	3.1
PKP001_5	0.129	0.057	0.0136	0.0012	-0.1119	118.4	24.5	87.1	3.8
PKP001_6	0.106	0.043	0.0148	0.0015	0.1824	104.2	18.4	94.7	4.8
PKP001_7	0.1	0.047	0.0144	0.0023	0.1054	108.8	24.1	92.2	7.3
PKP001_8	0.175	0.086	0.0153	0.0026	-0.1462	181.8	55.8	97.9	8.3
PKP001_9	0.19	0.15	0.0165	0.0032	-0.1523	206.2	81.1	105.5	10.1
PKP001_10	0.155	0.079	0.0135	0.0021	0.1465	124.3	37.7	86.4	6.7
PKP001_11	0.13	0.11	0.0177	0.0026	-0.3024	138.7	48.6	113.1	8.2
PKP001_13	0.093	0.019	0.01364	0.00089	0.2475	93	8.9	87.3	2.8
PKP001_14	0.105	0.042	0.0148	0.0012	0.0913	104.2	22.1	94.7	3.8
PKP001_15	0.095	0.032	0.014	0.0015	-0.0775	100.6	16.5	89.6	4.8
PKP001_16	0.106	0.026	0.0164	0.0014	-0.1158	108.7	11.9	104.9	4.4
PKP001_17	0.086	0.015	0.01344	0.00072	0.178	83.7	7	86.1	2.3
PKP001_18	0.108	0.017	0.01605	0.00095	0.1368	106.3	8.4	102.6	3
PKP001_19	0.115	0.045	0.016	0.0019	0.0579	120.2	24.9	102.3	6
PKP001_21	0.092	0.017	0.014	0.0011	0.1139	93.5	8.6	89.6	3.5
PKP001_22	0.086	0.04	0.0153	0.0015	-0.2008	94	22.6	97.9	4.8
PKP001_23	0.139	0.047	0.0154	0.0016	-0.0193	136.9	26.4	98.5	5.1
PKP001_24	0.16	0.13	0.0175	0.0034	0.0459	145.8	70.7	111.8	10.8
PKP001_25	0.094	0.026	0.0145	0.00072	-0.0879	93	12.5	92.8	2.3
PKP001_26	0.105	0.042	0.0151	0.0017	0.2578	123.2	21.7	96.6	5.4
PKP001_27	0.102	0.028	0.0149	0.0013	0.4387	93.6	13.4	95.3	4.1
PKP001_28	0.104	0.036	0.0155	0.0016	0.1431	97.1	16.2	99.2	5.1
PKP001_29	0.118	0.022	0.01499	0.00092	0.037	113	9.8	95.9	2.9
PKP001_31	0.107	0.019	0.01543	0.0008	0.0267	104.9	8.2	98.7	2.5
PKP001_33	0.096	0.013	0.01426	0.00058	-0.0351	92.6	6.1	91.3	1.8
PKP001_34	0.124	0.05	0.0144	0.0015	0.3327	116	28.1	92.2	4.8
PKP001_35	0.117	0.026	0.0178	0.0011	0.0524	115.3	12	113.7	3.5
PKP001_37	0.13	0.016	0.019	0.0011	-0.0981	121.9	6.4	121.3	3.5
PKP001_38	0.121	0.079	0.0143	0.0018	-0.0021	95.4	40.3	91.5	5.7
PKP001_39	0.093	0.028	0.0153	0.0015	0.1282	94	13.9	97.9	4.8
PKP001_42	0.1	0.014	0.01469	0.00082	0.3043	97.5	6.6	94	2.6
PKP001_44	0.087	0.024	0.0135	0.0013	0.0142	90.3	15.9	86.4	4.1
PKP001_46	0.092	0.027	0.0131	0.0014	0.094	102.8	15.4	83.9	4.5
PKP001_47	0.108	0.025	0.0161	0.0011	0.0788	106.8	11.2	103	3.5
PKP001_48	0.106	0.061	0.0161	0.0018	0.1837	104.8	27.7	103	5.7
PKP001_49	0.118	0.023	0.0174	0.001	0.3565	112.2	10.6	111.2	3.2

Grain	$^{207}Pb/^{235}U$	2SE	$^{206}Pb/^{238}U$	2SE	ρ	$^{207}Pb/^{235}U$ Age	2SE	$^{206}Pb/^{238}U$ Age	2SE
PKP001_50	0.125	0.016	0.01807	0.00091	-0.3193	124.8	7.5	115.5	2.9
PKP001_51	0.092	0.022	0.01419	0.00082	0.0672	91.1	10.9	90.8	2.6
PKP001_54	0.133	0.052	0.0136	0.0015	0.1988	135.2	22.8	87.1	4.8
PKP001_55	0.101	0.02	0.01342	0.00071	0.1587	98.4	8.8	85.9	2.3
PKP001_56	0.21	0.11	0.0176	0.0039	0.0234	240	104	112.5	12.4
PKP001_58	0.178	0.073	0.0151	0.0026	0.1059	174.3	43.5	96.6	8.3
PKP001_60	0.11	0.023	0.0162	0.0011	0.0949	103.4	10.8	103.6	3.5
PKP001_62	0.137	0.072	0.0154	0.0021	0.211	175.7	35.3	98.5	6.7
PKP001_63	0.143	0.045	0.0167	0.0022	-0.0715	165.7	22.8	106.8	7
PKP001_66	0.2	0.13	0.0167	0.0031	-0.0254	256.7	67.7	106.8	9.8
PKP001_67	0.13	0.029	0.0151	0.0013	-0.1928	139.9	17.6	96.6	4.1
PKP001_68	0.128	0.033	0.0151	0.0015	-0.0123	125.1	15.4	96.6	4.8
PKP001_69	0.104	0.016	0.01452	0.00096	0.103	102.7	8.1	92.9	3.1
PKP001_70	0.143	0.057	0.016	0.0017	-0.1279	149.6	27.5	102.3	5.4
PKP001_71	0.146	0.056	0.0137	0.002	0.1789	136.2	24.7	87.7	6.4
PKP001_72	0.132	0.016	0.019	0.0011	0.2154	128.2	7.7	121.3	3.5
PKP001_73	0.131	0.064	0.0151	0.0019	-0.0709	102.4	23.3	96.6	6
PKP001_74	0.163	0.074	0.015	0.0018	0.2154	142.7	32.3	96	5.7
PKP001_75	0.138	0.071	0.0142	0.0024	-0.0134	169.8	51	90.9	7.6
PKP001_76	0.116	0.026	0.0146	0.0013	-0.0457	113.9	11.1	93.4	4.1
PKP001_77	0.099	0.016	0.01501	0.00098	0.1787	97.1	7.9	96	3.1
PKP001_78	0.121	0.038	0.0178	0.0022	0.1683	119.7	17.3	113.7	7
PKP001_79	0.103	0.011	0.01527	0.00079	0.1168	101.2	5.7	97.7	2.5
PKP001_80	0.113	0.021	0.01433	0.00097	0.226	110.1	9.9	91.7	3.1
PKP001_81	0.103	0.045	0.0161	0.0021	0.0882	100.7	22.2	103	6.7
PKP001_82	0.105	0.017	0.01507	0.00071	0.112	97.6	7.4	96.4	2.3
PKP001_83	0.107	0.07	0.014	0.0028	0.3603	97.1	48.5	89.6	8.9
PKP001_85	0.095	0.042	0.014	0.0016	0.0949	95.3	21.1	89.6	5.1
PKP001_86	0.102	0.027	0.01437	0.00078	-0.0244	99.5	12.5	92	2.5
PKP001_87	0.089	0.032	0.0132	0.0014	-0.1422	93.5	16.1	84.5	4.5
PKP001_88	0.108	0.036	0.015	0.0015	-0.0004	105.6	17.5	96	4.8
PKP001_89	0.131	0.092	0.0166	0.0023	0.285	118.3	50	106.1	7.3
PKP001_90	0.087	0.029	0.0122	0.0013	0.0296	99.1	17.2	78.2	4.1
PKP001_91	0.094	0.029	0.0141	0.0011	-0.0893	97.7	14.5	90.3	3.5
PKP001_92	0.093	0.026	0.01284	0.00095	0.0562	92.7	12.1	82.3	3
PKP001_95	0.09	0.018	0.0139	0.0011	0.5106	87.2	8.9	89	3.5
PKP001_96	0.098	0.028	0.0142	0.0012	0.376	93	12.5	90.9	3.8
PKP001_97	0.094	0.034	0.0141	0.0014	0.0773	95.9	18.2	90.3	4.5
PKP001_98	0.097	0.057	0.0142	0.0029	0.021	94.8	22.6	90.9	9.2

Grain	$^{207}Pb/^{235}U$	2SE	$^{206}Pb/^{238}U$	2SE	ρ	$^{207}Pb/^{235}U$ Age	2SE	$^{206}Pb/^{238}U$ Age	2SE
PKP003_2	0.109	0.042	0.0145	0.0019	0.2045	124	22.3	92.8	6
PKP003_4	0.108	0.09	0.0148	0.0026	0.1311	111.7	40.7	94.7	8.3
PKP003_5	0.101	0.036	0.0146	0.0012	-0.03	104.7	19.6	93.4	3.8
PKP003_6	0.089	0.022	0.01277	0.00091	-0.0318	90.6	9.9	81.8	2.9
PKP003_7	0.097	0.015	0.01443	0.00071	-0.0234	94.8	6.8	92.4	2.3
PKP003_8	0.092	0.023	0.01364	0.00092	0.0888	93	10.1	87.3	2.9
PKP003_9	0.104	0.044	0.0141	0.0014	-0.0754	108.4	21.7	90.3	4.5
PKP003_11	0.107	0.055	0.0149	0.002	0.1343	112.4	32.1	95.3	6.4
PKP003_13	0.095	0.033	0.0139	0.001	-0.1962	94.7	15	89	3.2
PKP003_16	0.114	0.09	0.0135	0.0016	-0.2573	112.5	39.4	86.4	5.1
PKP003_17	0.0888	0.0077	0.01316	0.00044	0.2188	87.1	3.6	84.3	1.4
PKP003_18	0.094	0.025	0.0135	0.0011	-0.3362	97.2	11.9	86.4	3.5
PKP003_19	0.089	0.034	0.0136	0.0014	-0.0915	97.9	18.1	87.1	4.5
PKP003_21	0.113	0.051	0.0154	0.0027	0.1547	108.2	28.1	98.5	8.6
PKP003_22	0.095	0.024	0.01359	0.00081	0.1657	92.6	10.7	87	2.6
PKP003_23	0.095	0.014	0.01359	0.0007	0.2046	92.8	6.3	87	2.2
PKP003_24	0.103	0.068	0.0142	0.0022	-0.005	105.6	37.4	90.9	7
PKP003_26	0.087	0.016	0.01298	0.00079	-0.0225	90.3	8.1	83.1	2.5
PKP003_27	0.105	0.061	0.0144	0.0021	0.2262	105.2	33.5	92.2	6.7
PKP003_28	0.114	0.044	0.0137	0.0012	0.1511	110.7	21.2	87.7	3.8
PKP003_31	0.111	0.034	0.01403	0.00097	-0.072	109.7	16	89.8	3.1
PKP003_33	0.109	0.035	0.0138	0.0016	-0.0526	104.5	15.4	88.4	5.1
PKP003_36	0.127	0.045	0.0141	0.0012	0.2682	120.8	21.7	90.3	3.8
PKP003_37	0.088	0.022	0.01327	0.00087	0.0681	88.8	10.5	85	2.8
PKP003_41	0.091	0.033	0.0133	0.0012	-0.2279	94.1	17.3	85.2	3.8
PKP003_42	0.087	0.025	0.01293	0.00095	0.0961	88.3	12.1	82.8	3
PKP003_46	0.1	0.028	0.01466	0.0009	-0.1313	103.3	13.8	93.8	2.9
PKP003_47	0.104	0.025	0.01328	0.00095	0.2069	102.4	11.7	85	3
PKP003_49	0.102	0.079	0.0138	0.0017	0.0041	85.2	37.6	88.4	5.4
PKP003_54	0.108	0.048	0.0147	0.0016	0.0185	103.6	22	94.1	5.1
PKP003_55	0.098	0.049	0.0133	0.0012	-0.0299	102.6	23.9	85.2	3.8
PKP003_56	0.099	0.03	0.0146	0.0015	0.0464	102.9	17.3	93.4	4.8
PKP003_61	0.092	0.022	0.0139	0.001	0.1289	91.1	10.4	89	3.2
PKP003_62	0.087	0.027	0.0133	0.0011	0.0738	85.6	14.1	85.2	3.5
PKP003_65	0.102	0.046	0.0143	0.0023	0.8982	106.3	26	91.5	7.3
PKP003_67	0.0902	0.0088	0.01363	0.00061	0.1162	88.9	4.3	87.3	1.9
PKP003_69	0.091	0.018	0.01327	0.00086	-0.1616	82.7	7	85	2.7
PKP003_70	0.092	0.029	0.0142	0.0013	0.3644	87.5	12.7	90.9	4.1
PKP003_73	0.094	0.029	0.01341	0.00083	-0.0153	88	13.9	85.9	2.6

Grain	$^{207}Pb/^{235}U$	2SE	$^{206}Pb/^{238}U$	2SE	ρ	$^{207}Pb/^{235}U$ Age	2SE	$^{206}Pb/^{238}U$ Age	2SE
PKP003_74	0.104	0.033	0.0143	0.0013	0.0755	97.2	15.3	91.5	4.1
PKP003_78	0.086	0.029	0.01345	0.00097	-0.0782	86.5	14.5	86.1	3.1
MAR010a_1	0.108	0.012	0.0162	0.00071	0.37469	104.6	4.66	103.6	2.25
MAR010a_2	0.111	0.03	0.0164	0.0013	0.1894	110.8	14.2	104.86	4.12
MAR010a_3	0.098	0.045	0.0137	0.0019	0.61668	84.6	17.4	87.72	6.04
MAR010a_4	0.089	0.0045	0.01339	0.00044	0.1773	87.04	2.41	85.74	1.4
MAR010a_5	0.098	0.013	0.01465	0.00084	-0.16617	97.1	6.92	93.75	2.67
MAR010a_10	0.088	0.044	0.0131	0.0018	0.19605	82.7	20.8	83.9	5.73
MAR010a_13	0.092	0.019	0.01385	0.00089	0.12541	90.79	8.95	88.67	2.83
MAR010a_15	0.1112	0.0061	0.01643	0.00049	-0.03107	107.25	3.87	105.05	1.55
MAR010a_16	0.093	0.023	0.01389	0.0009	-0.13862	96.4	14	88.92	2.86
MAR010a_17	0.0922	0.0065	0.01394	0.00053	0.35518	89.92	2.89	89.24	1.68
MAR010a_18	0.132	0.034	0.0192	0.0011	0.11717	128.5	16.5	122.6	3.48
MAR010a_19	0.125	0.0077	0.01853	0.00082	0.18914	120.87	4.14	118.36	2.59
MAR010a_20	0.099	0.028	0.0157	0.0013	-0.072685	104.3	16.7	100.42	4.13
MAR010a_22	0.111	0.035	0.0161	0.0011	-0.17774	112.9	19.1	102.96	3.49
MAR010a_24	0.089	0.062	0.0135	0.0022	-0.19525	95.5	32.4	86.44	7
MAR010a_27	0.116	0.011	0.01705	0.00095	0.26632	109.59	4.66	108.98	3.01
MAR010a_29	0.136	0.053	0.0185	0.0017	0.057107	119.5	23.3	118.17	5.38
MAR010a_30	0.089	0.025	0.0129	0.0012	-0.088045	93.1	14.2	82.63	3.82
MAR010a_31	0.107	0.015	0.01555	0.00074	0.38599	102.37	5.72	99.47	2.35
MAR010a_32	0.132	0.045	0.0189	0.0016	-0.031884	135.9	20.6	120.7	5.06
MAR010a_33	0.114	0.049	0.016	0.0014	0.16245	102.2	21	102.33	4.44
MAR010a_34	0.11	0.029	0.016	0.0018	0.29428	108.2	12.7	102.33	5.71
MAR010a_35	0.134	0.062	0.0191	0.0033	-0.56574	120.8	36.2	122	10.4
MAR010a_36	0.108	0.011	0.01601	0.00098	0.10483	106.26	6.41	102.39	3.11
MAR010a_37	0.121	0.067	0.0161	0.0024	0.13147	118.9	42.8	102.96	7.61
MAR010a_38	0.13	0.059	0.0174	0.0019	0.10822	130.1	24.8	111.2	6.02
MAR010a_39	0.149	0.058	0.0157	0.0021	-0.020976	141.3	28.4	100.42	6.66
MAR010a_40	0.079	0.065	0.014	0.0033	0.16796	104.2	48.1	89.6	10.5
MAR010a_42	0.103	0.028	0.015	0.0014	0.23455	101.8	12.1	95.98	4.45
MAR010b_1	0.099	0.047	0.0134	0.0014	-0.13596	103.3	26.6	85.81	4.45
MAR010b_2	0.109	0.016	0.01631	0.00077	0.2759	105.07	7.03	104.29	2.44
MAR010b_3	0.0901	0.0072	0.01354	0.00052	-0.063692	88.32	4.41	86.7	1.65
MAR010b_4	0.104	0.02	0.01559	0.00087	0.04713	101.05	9.82	99.72	2.76
MAR010b_5	0.112	0.017	0.0176	0.0011	0.20856	108.29	7.74	112.47	3.48
MAR010b_7	0.092	0.01	0.01404	0.00073	-0.17625	91.98	6.38	89.88	2.32
MAR010b_8	0.096	0.03	0.0144	0.0012	0.075553	96.1	14.9	92.17	3.81
MAR010b_9	0.114	0.063	0.0162	0.0017	0.07201	117.6	32.4	103.6	5.39

Grain	$^{207}Pb/^{235}U$	2SE	$^{206}Pb/^{238}U$	2SE	ρ	$^{207}Pb/^{235}U$ Age	2SE	$^{206}Pb/^{238}U$ Age	2SE
MAR010b_13	0.088	0.025	0.0128	0.0013	0.074199	92.4	13.5	81.99	4.14
MAR010b_15	0.134	0.046	0.0189	0.0022	-0.21741	140.6	29.1	120.7	6.96
MAR010b_16	0.098	0.022	0.01436	0.00083	0.0019865	97.6	11.3	91.91	2.64
MAR010b_19	0.109	0.026	0.016	0.001	0.59138	112.2	11.4	102.33	3.17
MAR010b_20	0.093	0.026	0.0138	0.0013	0.17012	92.2	11.5	88.35	4.13
MAR010b_22	0.093	0.028	0.01372	0.00099	-0.23464	86.5	13.4	87.84	3.15
MAR010b_25	0.09	0.011	0.01306	0.00065	-0.098048	87.67	6.1	83.65	2.07
MAR010b_26	0.099	0.028	0.0142	0.0011	0.34853	93	11.1	90.9	3.5
MAR010b_27	0.093	0.038	0.0142	0.0011	-0.096192	91.2	19.7	90.9	3.5
MAR010b_29	0.098	0.022	0.015	0.0011	0.10642	96.1	10.7	95.98	3.49
MAR010b_30	0.115	0.025	0.0153	0.0014	0.11881	113.3	12.8	97.88	4.44
MAR010b_31	0.112	0.043	0.0166	0.0016	-0.052505	114.1	22.7	106.13	5.07
MAR010b_32	0.095	0.041	0.0132	0.002	-0.24872	96.8	23.7	84.54	6.36
MAR010b_33	0.103	0.015	0.01547	0.00074	0.15401	100.11	6.99	98.96	2.35
MAR010b_36	0.09	0.025	0.0137	0.0016	-0.45468	96.8	22.1	87.72	5.09
MAR010b_37	0.123	0.029	0.0163	0.0016	-0.30214	124.4	17.7	104.23	5.07
MAR010b_38	0.113	0.026	0.0171	0.0013	0.391	108.17	9.7	109.3	4.12
MAR010b_40	0.108	0.076	0.0134	0.0017	-0.087459	121.8	47.8	85.81	5.41
MAR010b_41	0.118	0.077	0.0158	0.0015	0.3701	108.9	30.3	101.06	4.76
MAR010b_43	0.107	0.01	0.01613	0.0007	0.13833	103.76	4.78	103.15	2.22
MAR010b_45	0.098	0.027	0.0144	0.00096	0.028077	97.9	13.1	92.17	3.05
MAR010b_49	0.11	0.075	0.0148	0.0021	0.040723	111.7	38.5	94.71	6.67
MAR010b_51	0.112	0.034	0.0163	0.0013	0.019732	116.3	17.8	104.23	4.12
MAR010b_52	0.097	0.011	0.01443	0.00085	0.23464	93.86	5.13	92.36	2.7
MAR010b_54	0.089	0.043	0.0124	0.0012	-0.018678	83.3	20.4	79.44	3.82
MAR010b_55	0.131	0.045	0.0139	0.0017	0.027502	134.6	25.7	88.99	5.4
MAR010b_56	0.094	0.026	0.0139	0.0011	0.060321	96.4	13.5	88.99	3.5
MAR010b_59	0.119	0.062	0.0155	0.0023	0.25628	110.9	30.1	99.15	7.3
MAR010b_61	0.134	0.039	0.0164	0.0017	-0.022262	129.1	22.3	104.86	5.39
MAR010b_62	0.124	0.041	0.0178	0.0019	0.16144	119.7	22	113.74	6.02
MAR010b_65	0.095	0.012	0.01434	0.00067	0.30314	96.41	6.09	91.79	2.13
MAR010b_66	0.111	0.037	0.016	0.0013	0.21838	108.2	15.7	102.33	4.12
MAR010b_67	0.101	0.034	0.015	0.0015	0.30489	96.1	15.5	95.98	4.76
MAR010b_68	0.087	0.021	0.01285	0.00092	-0.23088	87.8	12.6	82.31	2.93
MAR010b_69	0.094	0.025	0.0137	0.0018	-0.050959	98.6	14.7	87.72	5.72
MAR010b_70	0.095	0.021	0.01376	0.00067	0.065672	93.7	10.6	88.1	2.13
MAR010b_71	0.088	0.012	0.01334	0.0006	-0.27789	90.83	7.52	85.43	1.91
MAR010b_72	0.095	0.019	0.01519	0.0009	-0.22089	103	13.4	97.18	2.86
MAR010b_73	0.0852	0.0069	0.01294	0.00064	0.20676	84.23	3.65	82.88	2.04

Grain	$^{207}Pb/^{235}U$	2SE	$^{206}Pb/^{238}U$	2SE	ρ	$^{207}Pb/^{235}U$ Age	2SE	$^{206}Pb/^{238}U$ Age	2SE
MAR010b_74	0.087	0.025	0.013	0.0012	-0.16285	82.1	12.9	83.26	3.82
MAR010b_75	0.086	0.03	0.0127	0.0012	-0.17822	80.3	14.2	81.35	3.82
MAR010b_76	0.117	0.085	0.0142	0.0018	0.086515	116.3	38.1	90.9	5.72
MAR010b_77	0.091	0.026	0.0137	0.0014	-0.15996	93.3	16.2	87.72	4.45
MAR010b_78	0.103	0.013	0.01405	0.00074	0.050708	100.27	6.69	89.94	2.35
MAR010b_79	0.093	0.016	0.0142	0.0016	0.4881	91.71	6.29	90.9	5.08

Supplementary Table S3.3

Grain	Y	2SE	Nb	2SE	Lu	2SE	Hf	2SE	Ta	2SE	Th	2SE	U	2SE	Th/U	Texture	R?	Spot placement	Type
MAR010b-40	83	15	8.5	2.3	2.89	0.4	13000	720	5	1.3	10.8	2.8	28.4	5.5	0.38	Homogenous	no	-	Type-1
MAR010a-18	157	42	7	2.2	3.88	0.81	12400	1000	3.12	0.93	28.9	9.9	39	10	0.74	Patchy	no	-	Type-1
MAR010b-4	150	11	10.3	1.2	5.08	0.37	12870	950	8.7	0.81	13.8	1.1	42.4	3.2	0.33	Patchy	no	-	Type-1
MAR010b-5	163	18	18.8	2.9	5.49	0.63	13000	1300	17.1	2.1	15.3	2.2	51.5	6.6	0.3	Homogenous	no	-	Type-1
MAR010b-2	190	16	18.5	1.5	6.54	0.52	14460	870	14.9	1.3	15.4	1.2	55.5	3.5	0.28	Patchy	no	-	Type-1
MAR010b-33	109.6	8.9	4.96	0.61	4.71	0.46	13730	920	4.14	0.45	24.3	1.6	66.2	5	0.37	Complex	no	Mixed	Type-1
MAR010a-1	267	21	20.4	1.8	8.24	0.7	12050	930	15.8	1.1	32.2	2	86.6	5.2	0.37	Patchy	no	-	Type-1
MAR010a-31	148	14	7	0.88	5.38	0.49	12200	1200	7.11	0.94	33.7	3.1	89.8	8.8	0.38	Patchy	no	-	Type-1
MAR010a-36	234	29	45.2	6.3	6.36	0.75	12900	1500	24.1	3.1	59.4	7.1	117	12	0.51	Relict oscillatory	no	zoned area of grain	Type-1
MAR010a-27	390	52	42.3	5.4	10	1.2	11900	1500	14.4	1.8	74.3	9.5	158	18	0.47	Patchy	no	-	Type-1
MAR010a-5	820	120	47.2	5.5	19.1	2.3	9590	930	11.5	1.4	96	13	200	22	0.48	Patchy	no	-	Type-1
MAR010a-19	704	57	103	8	14.9	1.1	10290	680	34.2	2.6	196	16	285	16	0.69	Complex	no	-	Type-1
MAR010b-41	30.7	2.5	0.32	0.094	1.53	0.18	12600	970	0.174	0.027	0.33	0.041	4.55	0.32	0.07	Homogenous	no	-	Type-2
MAR010b-76	25.3	2	0.37	0.14	1.15	0.14	13230	870	0.191	0.036	0.326	0.033	4.73	0.27	0.07	Patchy	no	-	Type-2
MAR010a-37	37.2	4.2	0.31	0.12	1.53	0.21	11400	1300	0.213	0.043	0.62	0.14	5.59	0.75	0.11	Homogenous	no	-	Type-2
MAR010b-9	31.7	2.3	0.35	0.1	1.59	0.15	12700	1100	0.237	0.038	0.501	0.074	5.92	0.48	0.08	Patchy	no	-	Type-2
MAR010a-40	35.2	3.8	0.34	0.13	2	0.29	14500	1400	0.289	0.08	0.276	0.045	6.66	0.58	0.04	Patchy	no	-	Type-2
MAR010b-59	35.8	4.5	0.62	0.2	1.79	0.25	12600	770	0.271	0.049	0.481	0.077	8	0.81	0.06	Patchy	no	-	Type-2
MAR010b-61	50.9	3.3	0.54	0.14	2.58	0.17	13700	950	0.297	0.034	1.3	0.11	10.23	0.58	0.13	Patchy	no	-	Type-2
MAR010a-39	50.3	5	0.42	0.13	2.62	0.26	13100	1400	0.155	0.036	0.87	0.13	11.3	1.1	0.08	Patchy	no	-	Type-2
MAR010a-29	43.6	5.1	0.63	0.17	2.2	0.25	11700	1600	0.227	0.053	0.94	0.11	11.6	1.5	0.08	Homogenous	no	-	Type-2
MAR010b-38	36	5.2	0.81	0.17	1.92	0.3	12400	1300	0.444	0.096	2.24	0.26	11.6	1.1	0.19	Complex	no	Mixed	Type-2
MAR010a-32	55.2	5.9	0.51	0.14	2.98	0.33	12170	970	0.369	0.064	1.01	0.13	11.7	1.5	0.09	Patchy	no	-	Type-2
MAR010b-62	44.4	5.5	0.77	0.15	2.14	0.23	13800	1300	0.48	0.097	2.05	0.18	11.7	1.1	0.18	Patchy	no	-	Type-2
MAR010b-51	58.2	4.3	0.57	0.11	2.81	0.21	13870	950	0.355	0.039	2.24	0.15	12.23	0.67	0.18	Homogenous	no	-	Type-2
MAR010a-33	52.1	6.8	0.71	0.17	2.8	0.28	12200	1400	0.377	0.065	1.54	0.21	12.5	1.4	0.12	Homogenous	no	-	Type-2
MAR010b-15	58.8	4.5	0.87	0.2	3.01	0.31	12900	1300	0.392	0.061	1.92	0.19	13.71	0.99	0.14	Homogenous	no	-	Type-2
MAR010a-2	60.8	5.5	0.76	0.2	2.84	0.24	11570	990	0.355	0.052	2.24	0.2	13.8	1.1	0.16	Patchy	no	-	Type-2
MAR010b-31	50.3	5.4	0.79	0.24	2.45	0.29	15300	1900	0.425	0.056	2.25	0.25	13.8	1.5	0.16	Patchy	no	-	Type-2
MAR010b-66	37.8	3.1	0.267	0.075	1.85	0.17	13820	950	0.208	0.034	2.27	0.32	13.9	1.4	0.16	Patchy	no	-	Type-2
MAR010a-20	73.3	9.1	0.68	0.16	4.15	0.45	12000	1200	0.261	0.052	2.49	0.35	17.2	2.1	0.14	Homogenous	no	-	Type-2

Grain	Y	2SE	Nb	2SE	Lu	2SE	Hf	2SE	Ta	2SE	Th	2SE	U	2SE	Th/U	Texture	R?	Spot placement	Type
MAR010b-19	48.1	2.4	1.13	0.13	2.44	0.18	10900	620	0.841	0.076	3.18	0.26	18.3	1.1	0.17	Complex	no	Mixed	Type-2
MAR010b-36	32.2	2.4	0.44	0.16	1.6	0.17	12770	840	0.174	0.032	2.01	0.29	7.21	0.5	0.28	Homogenous	no	-	Type-3
MAR010a-38	40.6	4.1	0.43	0.14	1.93	0.25	12200	1100	0.163	0.037	2.22	0.24	7.57	0.62	0.29	Homogenous	no	-	Type-3
MAR010b-1	37.5	4	0.24	0.12	1.67	0.19	12300	1600	0.114	0.03	4.31	0.63	8.2	1.1	0.53	Complex	no	homogenous area of grain	Type-3
MAR010b-49	41.3	5.9	0.54	0.16	1.66	0.24	12900	1400	0.198	0.06	6.02	0.92	9	1.3	0.67	Homogenous	no	-	Type-3
MAR010b-54	12.91	0.86	0.81	0.15	0.535	0.071	12030	820	0.476	0.044	3.47	0.29	9.7	1	0.36	Complex	no	homogenous area of grain	Type-3
MAR010b-55	41.5	3.2	0.55	0.21	1.85	0.2	12150	920	0.254	0.038	2.94	0.3	10.21	0.91	0.29	Homogenous	no	-	Type-3
MAR010b-32	55.9	5.1	1.03	0.45	2.76	0.35	11600	1700	0.58	0.17	7.47	0.86	11.5	1.7	0.65	Homogenous	no	-	Type-3
MAR010b-13	12.2	0.91	1.29	0.21	0.557	0.059	11130	600	1.02	0.081	3.48	0.27	12.02	0.7	0.29	Patchy	no	-	Type-3
MAR010b-8	25.1	2	0.83	0.18	1.04	0.12	12100	690	0.664	0.079	4.5	0.31	12.61	0.76	0.36	Patchy	no	-	Type-3
MAR010b-67	51.8	5.3	0.65	0.19	2.69	0.31	14800	1200	0.314	0.068	1.82	0.23	13.9	1.6	0.13	Homogenous	no	-	Type-3
MAR010b-29	20.1	2.1	1.42	0.19	0.959	0.099	11990	660	1.17	0.11	5.29	0.48	14.1	1	0.38	Homogenous	no	-	Type-3
MAR010b-75	31.7	2.7	0.8	0.18	1.59	0.14	12360	710	0.327	0.045	4.74	0.63	14.3	1.2	0.33	Homogenous	no	-	Type-3
MAR010a-3	13.6	2.9	1.35	0.45	0.66	0.15	10700	1900	1.18	0.19	5.66	0.66	15.1	2.5	0.37	Patchy	no	-	Type-3
MAR010b-45	24.7	2	1.05	0.19	0.983	0.088	11880	800	0.628	0.068	7.13	0.59	15.5	1.2	0.46	Complex	no	Mixed	Type-3
MAR010a-35	49	12	0.67	0.27	2.67	0.62	12200	2000	0.313	0.079	4.5	1.4	15.9	3.6	0.28	Complex	no	Mixed	Type-3
MAR010a-24	38.9	6	1.82	0.78	1.85	0.33	12600	1700	0.8	0.15	7.2	1.2	16	2.2	0.45	Homogenous	no	-	Type-3
MAR010a-42	27.1	2.7	0.36	0.13	1.23	0.14	12100	1200	0.192	0.042	3.06	0.35	16.7	1.5	0.18	Homogenous	no	-	Type-3
MAR010b-69	33.2	5	0.77	0.18	1.34	0.15	12400	1400	0.343	0.067	7.7	1.3	17.1	2.1	0.45	Complex	no	Mixed	Type-3
MAR010b-22	48.2	4.9	0.81	0.2	2.47	0.27	12410	880	0.275	0.046	5.3	1.2	17.2	2.5	0.31	Homogenous	no	-	Type-3
MAR010b-27	65.2	9	1.28	0.2	2.73	0.36	11600	1300	0.4	0.12	9.8	1.1	17.9	1.5	0.55	Patchy	no	-	Type-3
MAR010b-74	37.2	2.5	1.1	0.24	1.58	0.17	11410	740	0.419	0.047	11.2	1.8	18.08	0.9	0.62	Patchy	no	-	Type-3
MAR010b-26	38.3	4.4	1.53	0.27	1.4	0.21	11280	850	0.88	0.12	8.31	0.95	19.3	1.5	0.43	Patchy	no	-	Type-3
MAR010a-22	57.2	7.2	2.93	0.54	2.47	0.37	11700	1300	0.562	0.097	16.9	3.6	19.9	2.5	0.85	Patchy	no	-	Type-3
MAR010b-37	21.6	2.7	1.66	0.34	0.89	0.13	12300	1400	1.59	0.2	6.64	0.7	20.2	2	0.33	Patchy	no	-	Type-3
MAR010a-10	30.3	4.2	0.37	0.16	1.24	0.23	10900	1500	0.15	0.08	4.17	0.55	20.9	3.3	0.2	Homogenous	no	-	Type-3
MAR010b-72	24.5	2.3	2.2	0.46	0.821	0.096	10880	890	1.3	0.15	13.9	1.9	21.2	2	0.66	Complex	no	Mixed	Type-3
MAR010a-34	36.7	5.6	1.47	0.28	1.74	0.26	11900	1400	0.73	0.11	11.8	1.4	22.3	2.8	0.53	Homogenous	no	-	Type-3
MAR010b-77	57.4	9.8	1.5	0.42	2.44	0.35	12600	1600	0.52	0.12	10	2.1	23.2	3.2	0.43	Homogenous	no	-	Type-3
MAR010a-30	34.8	3.8	2.82	0.5	1.51	0.21	13300	1700	0.92	0.13	11.1	1.4	23.6	2.5	0.47	Homogenous	no	-	Type-3
MAR010b-30	44.9	6.3	1.54	0.33	1.71	0.21	11600	1200	0.63	0.11	8.3	1.7	25.3	3.1	0.33	Homogenous	no	-	Type-3
MAR010b-56	42	4	1.8	0.27	1.58	0.15	11300	1000	0.697	0.077	10.87	0.9	25.3	2.1	0.43	Patchy	no	-	Type-3
MAR010b-70	28.2	2	0.97	0.17	1.17	0.12	11290	640	0.448	0.052	8.48	0.59	25.6	1.5	0.33	Complex	no	Mixed	Type-3

Grain	Y	2SE	Nb	2SE	Lu	2SE	Hf	2SE	Ta	2SE	Th	2SE	U	2SE	Th/U	Texture	R?	Spot placement	Type
MAR010a-13	42.3	4	1.69	0.24	2.31	0.21	12110	960	1.11	0.11	10.25	0.83	28.1	2.3	0.36	Homogenous	no	-	Type-3
MAR010b-16	46	11	4.5	1.1	1.09	0.13	10850	930	1.6	0.26	15.6	3.5	30.5	5.2	0.51	Patchy	no	-	Type-3
MAR010b-20	66.1	9.4	0.68	0.27	3.04	0.55	10000	1100	0.65	0.14	13.5	2.1	34.4	3.7	0.39	Homogenous	no	-	Type-3
MAR010b-68	70.2	9.8	3.44	0.56	2.22	0.27	11630	970	0.721	0.082	26.5	3.2	49	4.9	0.54	Complex	no	Mixed	Type-3
MAR010b-79	74	16	6.1	1.4	1.99	0.39	12600	1100	1.67	0.24	35.2	9.1	58	13	0.61	Patchy	no	-	Type-3
MAR010b-7	102.8	6.3	5.64	0.59	3.32	0.27	12060	580	0.752	0.056	41.6	3.4	67.4	4.4	0.62	Relict oscillatory	no	zoned area of grain	Type-3
MAR010b-43	80	12	0.92	0.18	4.53	0.59	10950	570	0.219	0.039	20.7	4.1	83.1	4.3	0.25	Homogenous	no	-	Type-3
MAR010a-15	649	42	4.98	0.39	22.1	1.1	11330	760	1.81	0.13	325	21	239	13	1.36	Homogenous	no	-	Type-3
MAR010a-16	109	22	10.5	2.6	2.69	0.39	11000	1500	3.17	0.44	66	13	75	12	0.88	Complex	no	Mixed	Type-4
MAR010b-65	82.9	9.6	15.8	1.9	1.82	0.23	10790	780	4.68	0.5	66.2	8.3	81	10	0.82	Relict oscillatory	no	zoned area of grain	Type-4
MAR010b-78	103	14	13.6	2	2.61	0.36	10400	1100	2.35	0.38	98	13	90	10	1.09	Patchy	no	-	Type-4
MAR010b-71	100	19	14.2	3.6	2.48	0.35	11180	680	2.1	0.38	86	20	93	17	0.92	Complex	no	Mixed	Type-4
MAR010b-73	125	12	18.2	1.9	3.13	0.26	10760	850	3.67	0.47	125	11	145	11	0.86	Complex	no	Mixed	Type-4
MAR010b-25	203	29	24.5	4.5	4.28	0.29	9700	1200	3.21	0.46	139	19	176	20	0.79	Homogenous	no	-	Type-4
MAR010b-52	244	58	30.5	3.5	4.93	0.51	11600	1400	3.07	0.44	197	25	188	25	1.05	Complex	no	Mixed	Type-4
MAR010a-17	356	26	54.6	5.4	7.1	0.62	9240	810	8.97	0.82	276	16	286	16	0.97	Homogenous	no	-	Type-4
MAR010b-3	265	28	89.3	8.8	4.8	0.49	10060	770	13.89	0.99	360	25	343	27	1.05	Relict oscillatory	no	zoned area of grain	Type-4
MAR010a-4	295	21	60.5	6.4	5.78	0.49	10310	890	9.26	0.76	363	24	374	27	0.97	Homogenous	no	-	Type-4
PKP003_2	36.4	2.7	0.6	0.13	1.7	0.14	12130	710	0.285	0.056	10.59	0.67	13.49	0.76	0.79	Homogenous	yes	-	-
PKP003_4	41.7	3.1	0.49	0.18	2.17	0.28	13000	1200	0.156	0.057	5.31	0.63	6.93	0.58	0.77	Patchy	yes	-	-
PKP003_5	78.8	6.1	1.3	0.26	3.79	0.32	12030	660	0.363	0.055	14.9	1.4	16.51	0.81	0.9	Patchy	yes	-	-
PKP003_6	38.4	2.6	1.05	0.17	1.39	0.11	11300	600	0.42	0.05	9.28	0.7	21.6	1.2	0.43	Homogenous	yes	-	-
PKP003_7	438	32	37.7	3.5	9.7	0.71	9730	640	8.81	0.62	88.8	5	102.1	5.4	0.87	Homogenous	yes	-	-
PKP003_8	47.9	5.3	2.06	0.54	1.82	0.17	11490	550	0.84	0.29	9.9	1.3	31.9	2.9	0.31	Patchy	yes	-	-
PKP003_9	40.9	2.8	0.67	0.18	1.8	0.17	13800	1000	0.24	0.04	6.21	0.39	10.33	0.63	0.6	Patchy	yes	-	-
PKP003_11	62	3.1	0.51	0.12	2.95	0.21	12000	620	0.249	0.03	8.7	0.51	8.64	0.47	1.01	Homogenous	no	-	-
PKP003_13	29.9	2.4	0.68	0.2	1.33	0.22	11690	950	0.159	0.042	18.4	1	36.7	2	0.5	Complex	yes	homogenous area of grain	-
PKP003_16	40.5	3.3	0.88	0.25	1.75	0.15	13150	910	0.156	0.04	4.02	0.4	8.93	0.76	0.45	Patchy	yes	-	-
PKP003_17	292	16	43.1	2.6	6.27	0.37	12100	720	15.83	0.82	192	11	157.7	7.6	1.22	Homogenous	yes	-	-
PKP003_18	46.1	4.8	0.48	0.13	2.16	0.18	12580	840	0.151	0.04	18.6	1.9	32	2.2	0.58	Homogenous	yes	-	-
PKP003_19	34.3	1.8	1.1	0.21	1.69	0.11	12950	520	0.355	0.048	7.96	0.38	11.46	0.51	0.69	Homogenous	yes	-	-
PKP003_21	48.1	3.4	0.48	0.11	2.17	0.26	12560	700	0.181	0.039	3.5	0.25	9.91	0.54	0.35	Patchy	yes	-	-
PKP003_22	45.6	4	2.68	0.36	1.99	0.16	10030	520	1.2	0.13	9.94	0.52	36.5	2	0.27	Patchy	yes	-	-

Grain	Y	2SE	Nb	2SE	Lu	2SE	Hf	2SE	Ta	2SE	Th	2SE	U	2SE	Th/U	Texture	R?	Spot placement	Type
PKP003_23	140.3	8.9	15.6	2.1	5.38	0.24	9210	450	2.28	0.18	77.1	7.8	136	10	0.57	Relict oscillatory	yes	spot placed in zoned area of grain	-
PKP003_24	50.2	3.1	0.44	0.19	2.48	0.29	12330	780	0.122	0.03	2.89	0.5	6.75	0.61	0.43	Homogenous	yes	-	-
PKP003_26	73.6	4.9	1.95	0.3	2.62	0.18	11690	590	0.689	0.081	22	1.1	31.7	1.7	0.69	Patchy	yes	-	-
PKP003_27	58.4	6.2	2.09	0.33	2.14	0.24	11200	930	0.56	0.12	11.94	0.96	19.3	1.4	0.62	Homogenous	yes	-	-
PKP003_28	20.6	1.2	2.34	0.25	0.97	0.11	10490	430	1.048	0.095	5.75	0.34	11.59	0.53	0.5	Homogenous	yes	-	-
PKP003_31	30.2	1.9	0.72	0.14	1.29	0.13	11060	560	0.177	0.035	5.6	0.28	17.58	0.83	0.32	Homogenous	yes	-	-
PKP003_33	27.4	1.7	1.11	0.24	1.32	0.12	10770	750	0.275	0.041	5.67	0.43	19.5	1.5	0.29	Complex	yes	homogenous area of grain	-
PKP003_36	31.4	2.4	1.99	0.24	1.33	0.14	11040	570	0.566	0.067	5.46	0.32	11.51	0.6	0.47	Homogenous	yes	-	-
PKP003_37	34.9	2.4	1.98	0.32	1.76	0.18	10410	630	1.14	0.11	7.52	0.47	25.1	1.5	0.3	Homogenous	yes	-	-
PKP003_41	27.4	1.8	1.39	0.23	1.1	0.1	11260	510	0.317	0.055	5.24	0.33	16.78	0.84	0.31	Complex	yes	homogenous area of grain	-
PKP003_42	36.8	1.9	2.07	0.31	1.57	0.14	11790	770	0.69	0.1	9.78	0.8	22.4	1.9	0.44	Homogenous	yes	-	-
PKP003_46	67	4.9	0.35	0.1	3.17	0.2	12620	750	0.079	0.015	9.29	0.5	20.2	1.1	0.46	Homogenous	no	-	-
PKP003_47	33.2	2.3	1.93	0.28	1.42	0.1	10590	550	0.616	0.069	5.02	0.28	20.1	0.95	0.25	Homogenous	yes	-	-
PKP003_49	39.7	2	0.71	0.11	1.89	0.17	12760	590	0.407	0.051	2.44	0.14	6.98	0.33	0.35	Homogenous	no	-	-
PKP003_54	39.5	2.8	0.84	0.22	1.66	0.14	12160	680	0.195	0.03	5.2	0.3	8.95	0.47	0.58	Homogenous	yes	-	-
PKP003_55	79.4	4.5	0.66	0.11	3.35	0.26	13130	800	0.181	0.027	4.89	0.33	11.99	0.62	0.41	Homogenous	no	-	-
PKP003_56	43.5	2.5	1.19	0.22	1.88	0.12	13320	790	0.489	0.056	10.15	0.59	16.87	0.86	0.6	Patchy	no	-	-
PKP003_61	35	3.1	1.88	0.33	1.33	0.13	11830	540	0.732	0.082	21.5	1.7	30.1	1.5	0.71	Patchy	yes	-	-
PKP003_62	29.3	1.7	1.43	0.22	1.32	0.11	11080	590	0.471	0.064	6.49	0.41	20.8	1.1	0.31	Homogenous	yes	-	-
PKP003_65	40.7	2.8	1.26	0.32	1.53	0.12	12930	610	0.548	0.06	6.52	0.45	12.4	0.61	0.53	Homogenous	yes	-	-
PKP003_67	96.6	5.9	1.44	0.28	3.58	0.24	11140	570	0.361	0.047	37.3	2	86.4	5.1	0.43	Complex	no	homogenous area of grain	-
PKP003_69	51.7	3.4	2.66	0.27	2.25	0.17	13230	680	0.444	0.058	22.8	1.3	22.8	1.1	1	Homogenous	no	-	-
PKP003_70	29.4	1.9	0.84	0.21	1.35	0.18	10670	630	0.614	0.057	6.34	0.41	26.7	1.4	0.24	Patchy	no	-	-
PKP003_73	61.7	4.4	0.54	0.15	2.81	0.22	10580	530	0.096	0.024	23.2	1.6	22.3	1.3	1.04	Patchy	no	-	-
PKP003_74	37.7	2.7	1.6	0.21	1.69	0.19	11360	670	0.603	0.071	4.33	0.28	14.12	0.77	0.31	Homogenous	yes	-	-
PKP003_78	31.8	2.2	1.05	0.24	1.41	0.16	11230	660	0.148	0.035	13.63	0.74	34.6	1.8	0.39	Homogenous	yes	-	-
PKP001_2	37.5	2.4	0.86	0.18	1.78	0.12	710	0.58	0.498	0.046	3.81	0.33	3.87	0.24	1.51	Patchy	no	-	-
PKP001_4	50.8	2.4	1.67	0.31	1.97	0.15	670	0.41	0.959	0.08	66.1	3.6	17.91	0.92	0.27	Patchy	no	-	-
PKP001_5	50.5	2.4	1.38	0.21	1.71	0.12	760	0.39	1.1	0.1	5.67	0.29	8.67	0.35	3.79	Homogenous	no	-	-
PKP001_6	56	4.2	1.79	0.34	2.56	0.22	1100	0.44	0.98	0.13	24	2.2	18.4	2	0.45	Homogenous	no	-	-
PKP001_7	76.4	3.9	0.94	0.31	3.63	0.42	650	0.47	0.87	0.13	28	2.8	10.7	0.55	0.31	Patchy	no	-	-
PKP001_8	35.8	1.9	0.8	0.15	1.46	0.13	560	0.25	0.778	0.078	4.33	0.18	4.51	0.22	4.32	Patchy	no	-	-
PKP001_9	27.1	1.7	0.92	0.28	1.5	0.2	920	0.17	0.55	0.11	2.22	0.25	3.91	0.29	2.2	Homogenous	no	-	-

Grain	Y	2SE	Nb	2SE	Lu	2SE	Hf	2SE	Ta	2SE	Th	2SE	U	2SE	Th/U	Texture	R?	Spot placement	Type
PKP001_10	45.7	2.4	1.06	0.28	2.01	0.29	1000	0.15	0.78	0.091	10.63	0.87	6.01	0.36	0.9	Patchy	no	-	-
PKP001_11	53.7	4.5	0.94	0.33	2.67	0.37	1300	0.17	0.69	0.14	27.9	2.6	11.6	1.1	0.27	Homogenous	no	-	-
PKP001_13	68.4	3	2.62	0.26	2.24	0.14	540	0.11	1.072	0.096	76.9	3.9	22.8	1	0.27	Homogenous	no	-	-
PKP001_14	98.2	7.8	2.15	0.33	2.9	0.34	860	0.12	1.5	0.15	13.6	1.2	12.64	0.96	1.25	Homogenous	no	-	-
PKP001_15	123.7	7.5	3.77	0.37	3.9	0.3	700	0.13	1.78	0.13	34.9	2	22.6	1	0.89	Patchy	no	-	-
PKP001_16	178	12	4.04	0.45	5.36	0.39	750	0.12	2.59	0.23	21.4	1.4	21.3	1.1	1.85	Patchy	no	-	-
PKP001_17	132	11	4.77	0.78	4.22	0.27	880	0.14	2.01	0.19	418	39	75.5	6.7	0.05	Patchy	no	-	-
PKP001_18	179	11	9.83	0.81	4.53	0.35	720	0.12	4.31	0.27	69.2	3.7	44.1	2.4	1.16	Patchy	no	-	-
PKP001_19	62.6	6.7	1.87	0.32	1.88	0.2	960	0.13	1.44	0.16	9.8	1	11.4	1	1.44	Patchy	no	-	-
PKP001_21	138	10	5.16	0.7	3.92	0.36	850	0.12	3.6	0.35	33.1	2.9	32.3	2.3	1.24	Homogenous	no	-	-
PKP001_22	73	14	2.4	0.69	2.04	0.31	660	0.45	1.02	0.18	14	3.2	10.3	1.5	0.32	Patchy	no	-	-
PKP001_23	69.7	3.6	1.43	0.23	2.24	0.21	660	0.49	1.19	0.11	10.3	0.54	9.43	0.4	2.2	Homogenous	no	-	-
PKP001_24	62.8	5.2	0.76	0.12	3.36	0.33	630	0.46	0.39	0.049	1.744	0.095	2.64	0.11	4.11	Homogenous	no	-	-
PKP001_25	310	17	8.01	0.97	7.72	0.59	770	0.57	3.43	0.29	64.7	4.1	42.9	2	0.84	Patchy	no	-	-
PKP001_26	57	4.9	2.12	0.41	2.26	0.16	780	0.49	1.1	0.16	13.5	3	11.7	2	0.37	Homogenous	no	-	-
PKP001_27	144.2	8.6	4.07	0.48	4.46	0.35	820	0.52	1.96	0.16	23.1	1.9	20.1	1.4	1.03	Homogenous	no	-	-
PKP001_28	73.5	7.1	2.58	0.43	2.3	0.25	1200	0.52	1.33	0.15	15.8	1.7	15.5	1.5	0.78	Patchy	no	-	-
PKP001_29	140	12	5.67	0.61	4.09	0.34	780	0.53	2.64	0.21	45.6	2.9	29.3	2.2	0.91	Patchy	no	-	-
PKP001_31	302	24	10.73	0.97	7.77	0.78	1200	0.53	4.79	0.44	58.9	5.6	48	4.2	0.86	Relict oscillatory	no	homogenous area of grain	-
PKP001_33	554	31	27.1	1.8	10.73	0.8	780	0.55	7.89	0.47	165.4	6.7	88.1	4.2	1.18	Homogenous	no	-	-
PKP001_34	39.6	3.3	1.4	0.27	1.82	0.17	870	0.72	0.746	0.076	10.5	1.7	7.73	0.75	0.44	Patchy	no	-	-
PKP001_35	88.1	4.8	2.15	0.31	2.93	0.24	600	0.72	1.77	0.13	14.28	0.83	19.65	0.85	2.13	Homogenous	no	-	-
PKP001_37	504	34	22.2	1.4	11.64	0.83	780	0.74	9.76	0.58	109.1	7.3	77.5	4.6	1.34	Patchy	no	-	-
PKP001_38	32.5	2	0.77	0.17	1.45	0.13	710	0.72	0.868	0.071	10.43	0.96	5.63	0.36	0.9	Homogenous	no	-	-
PKP001_39	78.9	4.4	2.7	0.3	2.72	0.18	540	0.71	1.332	0.092	16.64	0.93	15.88	0.71	1.43	Complex	no	Mixed	-
PKP001_42	207	13	12.1	1	4.9	0.32	720	0.74	5.92	0.38	85.2	4.5	55.8	3.3	1.32	Patchy	no	-	-
PKP001_44	64.4	4.5	2.76	0.35	1.83	0.2	860	0.7	1.28	0.11	16.8	1.3	14.57	0.8	0.98	Patchy	no	-	-
PKP001_46	73.2	4.5	1.39	0.2	2.41	0.21	900	0.66	1.23	0.11	14.2	1.1	13.65	0.8	1.12	Relict oscillatory	no	Spot placed on zoned area of grain	-
PKP001_47	105.5	8.8	3.59	0.47	3.07	0.29	780	0.66	1.89	0.16	25.3	2	21.2	1.5	0.95	Patchy	no	-	-
PKP001_48	101.8	8.4	1.79	0.27	2.8	0.26	1100	0.7	1.36	0.13	9.59	0.83	10.23	0.86	1.64	Homogenous	no	-	-
PKP001_49	388	43	13.2	2.3	9.1	1.2	970	0.7	6.38	0.72	60.8	9.7	52.9	7	0.66	Patchy	no	-	-
PKP001_50	458	20	21.3	1.4	9.5	0.6	630	0.67	7.02	0.41	96.4	4	71.4	3.3	1.76	Homogenous	no	-	-
PKP001_51	155	8.4	4.83	0.49	4.43	0.32	670	0.67	2.82	0.21	38.3	1.8	29.1	1.1	1.57	Patchy	no	-	-

Grain	Y	2SE	Nb	2SE	Lu	2SE	Hf	2SE	Ta	2SE	Th	2SE	U	2SE	Th/U	Texture	R?	Spot placement	Type
PKP001_54	39.4	2.6	0.8	0.15	1.77	0.16	680	0.25	0.711	0.085	18.6	1.7	7.54	0.47	0.42	Patchy	no	-	-
PKP001_55	131.3	9.1	8.12	0.8	3.6	0.29	760	0.25	3.24	0.22	55.2	3.8	36	2.2	0.85	Complex	no	homogenous area of grain	-
PKP001_56	49.1	3.3	0.98	0.16	2.45	0.19	740	0.26	0.511	0.056	1.315	0.095	2.56	0.14	5.38	Complex	no	homogenous area of grain	-
PKP001_58	39.9	2.8	0.53	0.16	1.84	0.15	820	0.26	0.661	0.076	7.74	0.88	5.06	0.33	0.75	Homogenous	no	-	-
PKP001_60	174.8	9.7	3.29	0.43	4.58	0.37	710	0.25	2.24	0.2	20.2	1.3	19.3	1.1	1.72	Homogenous	no	-	-
PKP001_62	38.9	2.9	0.83	0.14	1.92	0.15	660	0.26	0.74	0.062	8.62	0.53	5.34	0.27	1.4	Homogenous	no	-	-
PKP001_63	43.4	4.4	1.11	0.18	1.41	0.14	770	0.26	0.893	0.096	7.1	0.46	7.36	0.55	1.94	Patchy	no	-	-
PKP001_66	32.6	2.1	0.65	0.16	1.64	0.13	890		0.493	0.057	0.461	0.048	2.54	0.18	10.27	Patchy	no	-	-
PKP001_67	100.2	6.5	2.03	0.34	2.9	0.29	910		1.47	0.12	14.07	0.79	12.61	0.76	1.86	Patchy	no	-	-
PKP001_68	95	8	2.1	0.29	2.94	0.25	820		1.62	0.11	8.6	0.68	11.72	0.82	2.38	Patchy	no	-	-
PKP001_69	101.2	6.6	4.7	0.78	2.92	0.25	690		2.29	0.17	41.5	3.1	28.4	2	0.74	Patchy	no	-	-
PKP001_70	42.2	2.6	1.22	0.22	1.55	0.13	680		0.834	0.082	9.6	1	8.47	0.55	0.83	Homogenous	no	-	-
PKP001_71	33.4	2.7	0.99	0.24	1.49	0.12	630		0.677	0.069	6.39	0.8	6.58	0.5	0.85	Homogenous	no	-	-
PKP001_72	257	28	11.7	1.5	5.87	0.5	800		3.75	0.26	74.4	7.3	42.1	3.6	0.51	Patchy	no	-	-
PKP001_73	65.5	5.2	1.61	0.23	2.5	0.18	800		1.08	0.12	7.7	1.2	9.7	1.4	0.9	Homogenous	no	-	-
PKP001_74	37.5	2.3	1.08	0.2	1.77	0.13	830		0.66	0.086	4.7	0.35	5.36	0.3	1.89	Homogenous	no	-	-
PKP001_75	29.6	2.1	0.67	0.16	1.49	0.15	740		0.578	0.059	1.07	0.084	3.83	0.2	6.88	Homogenous	no	-	-
PKP001_76	119.6	8.6	4.26	0.37	4.04	0.29	650		1.65	0.14	40	2.2	22.6	1.2	0.75	Patchy	no		-
PKP001_77	183	12	8.65	0.85	4.62	0.38	890		4.57	0.33	64	3.6	45.6	2.5	1.27	Homogenous	no	-	-
PKP001_78	70.1	6.9	3.68	0.54	2.22	0.21	1100	0.57	1.87	0.23	18.6	1.9	14.6	1.3	0.98	Patchy	no	-	-
PKP001_79	204	17	14.4	1.4	4.81	0.42	880	0.51	6.8	0.62	101.5	9.2	58.7	4.9	0.74	Patchy	no	-	-
PKP001_80	137	13	5.7	0.71	3.21	0.25	660	0.47	2.5	0.22	25.1	2.3	19.2	1.6	1.09	Homogenous	no	-	-
PKP001_81	71.4	3.7	1.76	0.21	2.48	0.21	820	0.48	1.56	0.14	5.76	0.36	7.79	0.39	4.33	Patchy	no	-	-
PKP001_82	167	14	8.06	0.93	4.28	0.35	960	0.48	4.78	0.38	52.1	4.5	44.6	3.2	1.06	Homogenous	no	-	-
PKP001_83	42.5	3.9	0.87	0.21	1.54	0.16	1000	0.53	0.76	0.12	4.25	0.38	4.2	0.38	2	Homogenous	no	-	-
PKP001_85	66.4	4.8	1.53	0.22	2.42	0.2	880	0.5	1.04	0.11	18.2	1.5	13	0.9	0.69	Homogenous	no	-	-
PKP001_86	118.4	6.7	4.18	0.52	3.45	0.31	780	0.49	2.66	0.23	20.6	1.5	23.6	1.4	1.77	Patchy	no	-	-
PKP001_87	86	14	3.35	0.55	2.67	0.39	1100	0.47	1.23	0.2	33.8	3.9	20.2	2.6	0.32	Patchy	no	-	-
PKP001_88	120.7	8	2.23	0.31	3.48	0.26	660	2	1.84	0.15	12.29	0.8	13.81	0.66	2.3	Patchy	no	-	-
PKP001_89	73.2	6.5	0.77	0.22	3.15	0.4	1400	2.1	0.668	0.097	4.55	0.47	4.43	0.39	1.42	Homogenous	no	-	-
PKP001_90	64.1	6.3	3.54	0.48	2	0.21	830	2	1.62	0.18	22.5	2.3	15.1	1.3	0.7	Relict oscillatory	no	Spot placed on zoned area of grain	-
PKP001_91	132	11	3.79	0.49	3.84	0.3	760	2	2	0.17	19.4	1.3	19.1	1	1.54	Homogenous	no	-	-
PKP001_92	69.5	5.3	1.91	0.29	2.93	0.24	960	2.1	0.721	0.082	19.6	1.4	22.6	1.4	0.52	Homogenous	no	-	-

Grain	Y	2SE	Nb	2SE	Lu	2SE	Hf	2SE	Ta	2SE	Th	2SE	U	2SE	Th/U	Texture	R?	Spot placement	Type
PKP001_95	379	33	20.7	2.6	8.3	1.1	1000	2.5	7.26	0.89	152	13	73.9	5.5	0.56	Homogenous	no	-	-
PKP001_96	141	12	3.82	0.58	4.07	0.38	890	2.3	1.92	0.18	37.7	3.1	28	2.1	0.62	Homogenous	no	-	-
PKP001_97	62.4	4.7	1.49	0.23	2.54	0.23	770	2.1	0.811	0.097	20.4	1.3	12.01	0.94	0.62	Homogenous	no	-	-
PKP001_98	52.7	5.9	1.36	0.44	2.14	0.31	1300	2.8	0.72	0.13	11.3	1.6	8.7	1.3	0.45	Patchy	no	-	-

Chapter 4: Real or 'Apparent' Radiogenic Heat Production in the Cratonic Lithospheric Mantle

Brendan C. Hoare[1], Emma L. Tomlinson[1], Balz S. Kamber[2*]

[1] Department of Geology, Trinity College Dublin, Dublin 2, Ireland

[2] School of Earth and Atmospheric Sciences, Queensland University of Technology, Brisbane, QLD, Australia

Keywords: Geotherms; heat flow; continents; heat production; mantle heat production

This work is presented as an advanced manuscript draft, which is aimed to be submitted to G[3].

* Author yet to receive manuscript draft

Abstract

The internal heat production (H_m) of the cratonic lithospheric mantle is assumed to be zero. That the H_m of cratons is assumed, rather than known to be zero, results from the inaccessibility of the lithospheric mantle and the difficulty in analysing the heat-producing elements (HPE) within mantle xenoliths that are carried to the Earth's surface due to contamination from their host kimberlites. This contribution attempts to circumvent the problem of directly measure HPE in mantle xenoliths by presenting thermodynamic modelling of the Kaapvaal and Slave lithospheres using *PT* data from mantle xenoliths and the heat equation to assess the potential for a non-zero internal radiogenic heat production of the cratonic lithospheric mantle.

Our analysis suggests that both the Slave and Kaapvaal Cratons appear to have a relatively high internal heat production (H_m) of between 0.04 and 0.05 μW/m^3 near to the present-day (i.e., < c.170 Ma). Similarly, mantle xenoliths from the 1.15 Ga Premier kimberlite suggest similarly high values of H_m (~ 0.04 μW/m^3) earlier in the Kaapvaal Craton's history. In the Archean such values would not allow for either the stabilization of a strong mechanical lithosphere (Michaut and Jaupart, 2007) or an extensive diamond-hosting root much earlier than 2.5 Ga. The first possibility is that the high H_m values

modelled for the Slave Cratons and Kaapvaal Cratons, derives from an 'apparent' heat production resulting from the thermal disequilibrium of the crust and lithospheric mantle. A second scenario is that the H_m reflects the real radiogenic heat production in the mantle lithosphere through the later metasomatic refertilization of the cratonic mantle with K, Th and U. Irrespective of the 'source' of this internal heat generation an assumption of a lithosphere with zero H_m will likely lead to severe underestimations of the depth to the lithosphere-asthenosphere boundary (LAB) and the thermal contribution of heat generation in the cratonic lithosphere to the overall thermal heat loss of the Earth.

4.1 Introduction

Radiogenic heat production within the ancient lithospheric mantle, created through the decay of the radioisotopes ^{40}K, ^{232}Th, ^{235}U and ^{238}U, must be low for the formation and long-term stability of Earth's cratons. This results from the increased effect of radioactivity earlier in Earth's history, which becomes substantially higher when projected backward in time to the mid to late Archean, when most cratonic mantle stabilized (Pearson and Wittig, 2008) (Fig. 4.1a). Using estimates of present-day radiogenic heat production in the crust and assuming a lithospheric thickness equal to modern day (e.g., ~ 200 km), it is possible to demonstrate the effect of projecting high, modern-day heat production (e.g., 0.04 $\mu W/m^3$) back into the Archean by making assumptions with regards to the ratios of K/U and U/Th in the lithospheric mantle (Fig. 4.2). It is readily apparent that such high heat generation in the lithosphere is incompatible with the widespread formation of diamond in the Archean, as the geotherm only barely descends into the diamond stability field at 2.5 Ga (Fig. 4.2). The problem of a high heat generation within the mantle lithosphere during the Archean is further amplified where the lithosphere exceeds 200 km thickness. In extreme examples (i.e., thick lithospheres with significant internal heat generation) modelled geotherms either fail to intercept with the isentrope or 'turn', meaning that the temperature initially increases with depth, before decreasing with greater depth – such conditions are indicative of thermodynamically unstable lithosphere that is likely to delaminate at mid-lithospheric depths (Michaut and Jaupart, 2007).

Yet, firm estimates on the present-day internal heat production within the cratonic mantle lithosphere remain poorly constrained despite its importance for the computation of

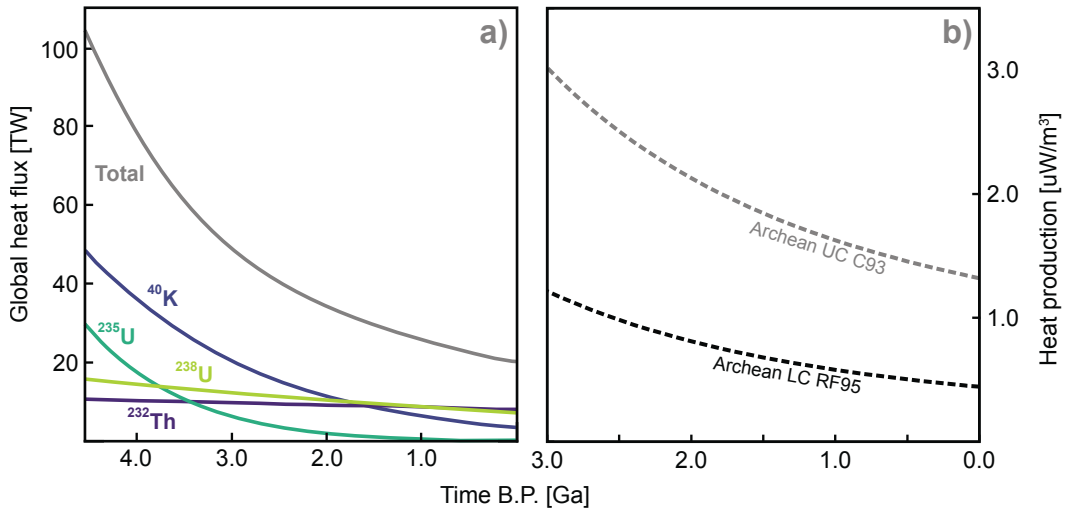

Figure 4.1: a) Global heat flux (in TW) at the Earth's surface as a function of the contribution of radioactive decay within the Earth through time from the principal heat-producing radioisotopes ^{40}K, ^{232}Th, ^{235}U and ^{238}U, adapted from Arevalo et al. (2009). b) The internal heat production of the upper (UC) with a ρ = 2.75 g/cm^3 of and lower crust (LC) with a ρ = 2.86 g/cm^3 as a function of radioactive decay within the Earth through time. RF95: Archean intermediate granulitic LC of Rudnick and Fountain, (1995); C93: Archean UC (exposure) of Condie, (1993).

geotherms that can be used to infer the internal temperatures and thickness of the lithospheric mantle. That the internal heat production of the cratonic lithosphere remains poorly constrained is partly due to its inaccessibility and our scarcity of samples, but also because of the mechanism by which samples of the ancient deep lithosphere reach the Earth's surface. Most cratonic mantle xenoliths are transported to the surface by kimberlite magmas, which are some of the most extreme low-degree and incompatible element enriched rocks found on Earth. It is argued that mantle xenoliths experience ubiquitous contamination and secondary addition of heat-producing elements during transport to the Earth's surface in the host kimberlite (Eggins et al., 1998). Indeed cratonic mantle xenoliths in less incompatible element enriched intraplate magmas (e.g., alkali basalts) display lower abundances of HPE compared to the wider range and higher values seen in xenoliths transported by the vastly more incompatible element-rich kimberlites (Rudnick et al., 1998). This supports a notion that the K, Th and U contents of mantle xenoliths reflect contamination and melt infiltration from their host magmas. This leads to an assumption that all almost all HPE measure in cratonic peridotites simply derives from contamination and that the H_m of the mantle must be zero. Support of this assumption is shown by careful direct measurements of K, Th and U from constituent minerals of cratonic peridotites and

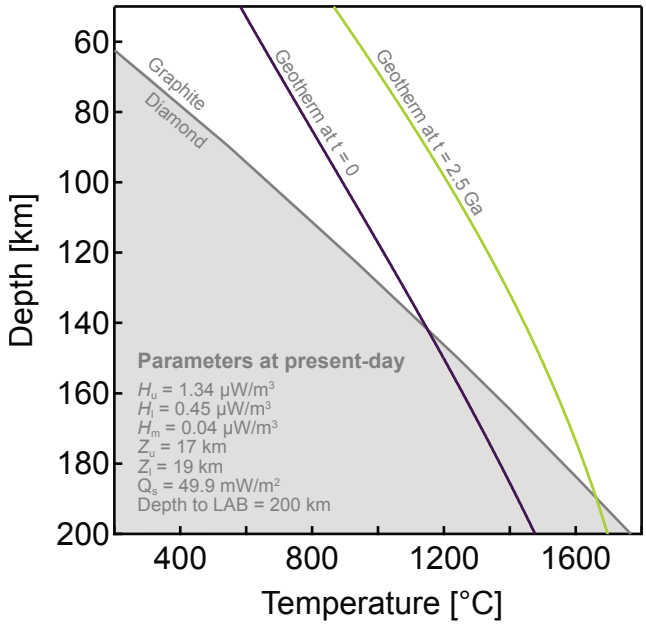

Figure 4.2: Mantle geotherms the present-day (T = 0 Ga) and (T = 2.5 Ga) with Hm at present-day of 0.04 µW/m3 in the lithospheric mantle for lithosphere of 200 km thickness. Hm projected back to 2.5 Ga using K/U and Th/U of 10,000 and 4, respectively for a mantle density of 3.3 kg/m3. Note that the 2.5 Ga geotherm barely protrudes into the diamond stability field and fails to at 3.0 Ga, which is clearly in opposition to 3.0 Ga aged diamonds found globally (see Howell et al., 2020 for ages).

the application of reconstitution approaches which equate to negligible heat production values of 0.0004 to 0.006 µW/m³ in refractory mantle peridotites (McIntyre et al., 2021).

Nonetheless, it is apparent that the cratonic mantle has undergone varying degrees of refertilization via metasomatism. An example driving metasomatism being the passage of kimberlite and related magmas (e.g., orangeite) through the mantle, with the process exemplified by the extremely modally metasomatised phlogopite-ilmenite-clinopyroxene (PIC) and *extremely* HPE-rich (radiogenic heat productions that exceed continental lower curst) mica-amphibole (K-richterite)-ilmenite-diopside (MARID) suites of mantle xenoliths common in South African kimberlites (e.g., Dawson and Smith, 1977; Grégoire et al., 2002). At the other end of the spectrum is cryptic metasomatism by percolating fluids or melts (e.g., Dawson, 1984), which may introduce heat producing elements without affecting a change in modal mineralogy. Accordingly, the high HPE values measured in mantle peridotites entrained in kimberlite could simply reflect wider metasomatism of the lithosphere at mantle depths, perhaps long after the cratons formation, rather than secondary addition during their transport to the Earth's surface.

Another consideration is that of 'apparent' or pseudo heat production in the lithospheric mantle, which refers to the contribution of radiogenic heat produced earlier in

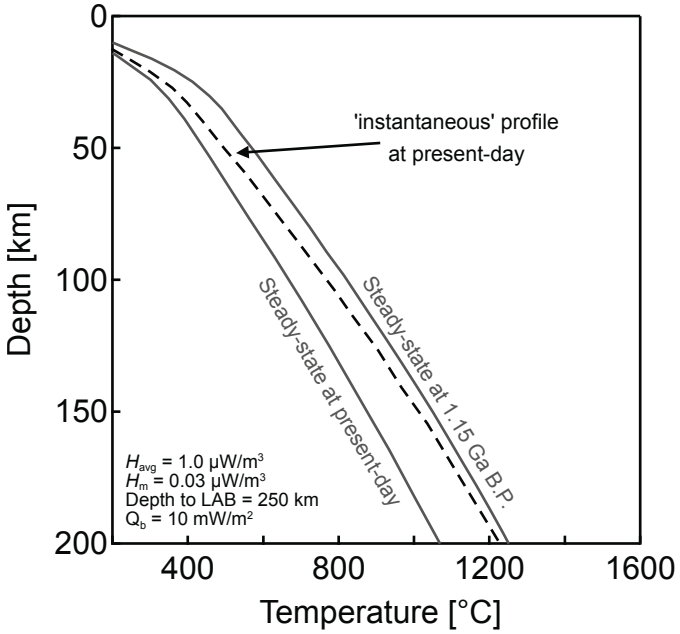

Figure 4.3: Example of 'instantaneous' vs. steady state geotherms (Michaut and Jaupart, 2004).

Earth's cooling history but not yet lost by diffusion in the mantle root. Radiogenic heat production decreases within the Earth by a factor of 2 in about ~ 2.5 Ga (Fig. 4.1a). However, the time for that same heat to diffuse through and permeate a 250 km thick lithosphere is ~ 1.9 Ga, based on the relationship Z^2/k where Z and k correspond to the thickness and thermal diffusivity, respectively (Michaut and Jaupart, 2004). Therefore, a thick cratonic lithosphere cannot be in thermal equilibrium with instantaneous heat production in the coupled crust and/or mantle lithosphere (Michaut and Jaupart, 2004), even in circumstances where the lithospheric mantle has had zero internal heat production since its formation. The effect of this thermal disequilibrium is to increase the curvature of the mantle portion of lithospheric geotherm (Fig. 4.3), in effect generating an 'apparent' internal heat production in the lithospheric mantle and conditions that will deviate from steady state.

Unfortunately, the 'instantaneous' solutions that account for this disequilibrium suggested by Michaut and Jaupart, (2004) most likely cannot be realistically applied to the cratonic lithosphere. This results from the fact that the heat flux (or temperature) at the base of the a lithosphere of constant thickness is required as a boundary condition. Whilst either the heat flux or temperature at the LAB can be specified it is unlikely they have simply decreased through time as is assumed in these solutions. In the Kaapvaal Craton, this result is demonstrated via thermobarometry of diamond inclusions that suggest significant erosion (up to c.150 km), and thus significant changes in the heat flux at the LAB, of the cratonic lithospheric mantle since its formation (Hoare et al., in review). It also

remains unclear precisely when this erosion occurred (due to the non-existence of diamond inclusion *PT* data that can provide host diamond age estimates), or over how long of a timeframe, such that the evolution of the basal heat flux or temperature at the LAB cannot be modelled. Significant changes in basal heat flux resulting from basal erosion of the lithosphere is also not limited to the Kaapvaal Craton with both thinning (e.g., Superior and Zimbabwe Cratons; Darbyshire et al., 2007; Celli et al., 2020) and in extreme cases near total destruction of the cratonic mantle lithosphere (e.g., North China and Wyoming Cratons; An et al., 2009; Dave and Li, 2016) seen elsewhere on Earth. A yet further complication derives from relatively poor constraints on the secular evolution of the T_p in the underlying mantle (see Kamber, 2015 for discussion). Both complications are such that the assumption of either the heat flux or the temperature at the LAB as a boundary condition is, at present, totally impractical. Therefore, whilst steady state formulations may not truly reflect true thermal conditions in the lithosphere they remain the best approach for estimating the internal heat production in the lithospheric mantle (real and/or otherwise 'apparent').

In this contribution, we test the accepted assumption of near-zero internal heat production within the cratonic mantle (real or apparent) to investigate the effects of a non-zero heat mantle heat production on the heat loss of the Earth and the thermal conditions of the Kaapvaal and Slave mantle lithospheres. We model the thermal structure of the Kaapvaal and Slave lithospheres assuming steady state conditions by varying input parameters in heat equation to find a range of permissible geotherms that provide a best fit to the *PT* array recorded in mantle xenoliths that record near present-day conditions. Further model comparisons are made between mantle xenoliths that record thermal conditions in the near present-day Kaapvaal lithosphere and mantle xenoliths from the 1.15 Ga Premier kimberlite, which records thermal conditions earlier in Earth's history. The resulting range of best fitting parameters provides limits on the amount of heat production in the close-to-present-day lithospheric mantle, but also estimates of the heat production in the crust, surface, mantle and basal heat fluxes, Moho temperatures and lithospheric thicknesses. In the case of the Kaapvaal Craton, it is also possible to see how these parameters may have changed through time.

4.2 Methods and results

We focus on constraining the thermal structure using mantle xenolith *PT* data from the Kaapvaal and Slave cratons that were sampled in kimberlites from c.170 Ma, which we

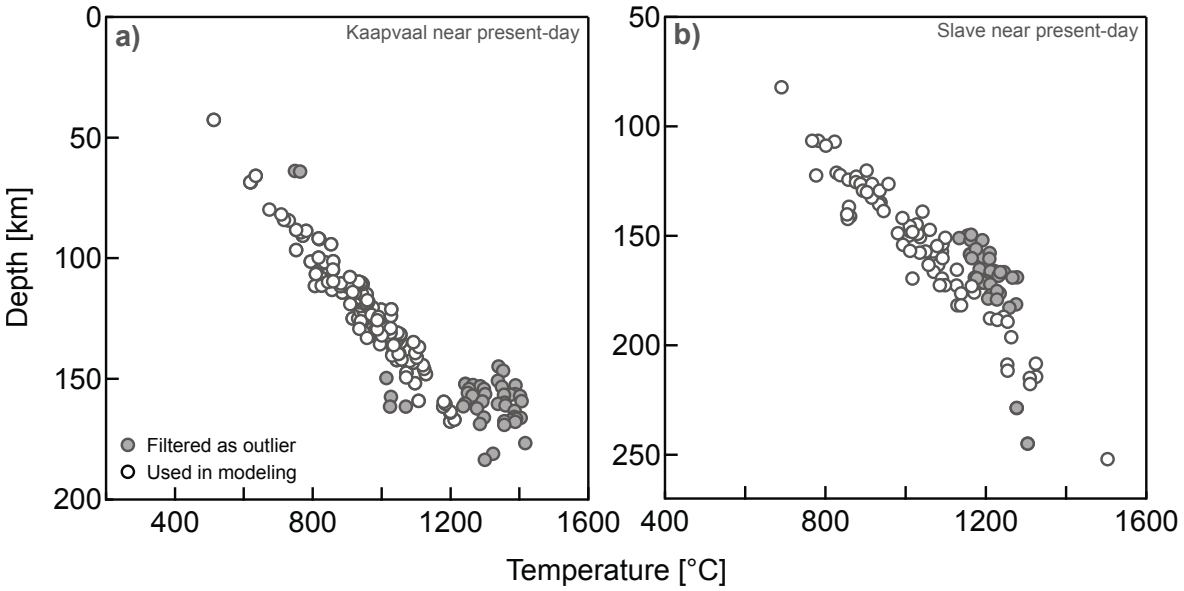

Figure 4.4: Filtered P/T data of mantle xenoliths used for modelling. Note the removal of mantle xenoliths that appear to record thermally perturbed conditions. For data sources see supplementary text.

argue approximate the near present-day thermal structure of the cratons. For the Kaapvaal Craton we also investigate the thermal structure using xenoliths sampled by kimberlite in the Proterozoic at 1.15 Ga (Table. 4.1). Mantle xenolith samples from the Kaapvaal cover most of the geographical region of the Kaapvaal Craton (Griffin et al., 2003), from the Western (Bultfontein, Frank Smith, Jagersfontein and Kimberley kimberlites), South-Eastern (Kaalvaalei, 'Lesotho group' and Monastery kimberlites) and Central Terranes (Premier kimberlites), erupted during the Mesozoic between 84 -114 Ma (see Field et al., 2008) and 1.15 Ga (Wu et al., 2013). Mantle xenoliths from the Slave Craton were emplaced in the central Slave (Domain-III) at Diavik and the Ekati properties (Arnie, Grizzly, Panda, Pidgeon and Sable kimberlites) near Lac de Gras and northern (Domain-IV) Slave at Jericho (Heaman et al., 2003), between ~ 50-55 Ma (Graham et al., 1999; Creaser et al., 2004; Sarkar et al., 2015a) and 172 Ma (Heaman et al., 2006), respectively. Mantle xenolith *PT* data were mostly acquired through the database of Wu and Zhao, (2011) supplemented by data from Liu et al., (2021). Only *PT* data from lherzolites were used for modelling, where possible as two-pyroxene thermometry is the 'gold-standard' for calculating *PT* conditions from mantle xenoliths (Nimis and Grütter, 2010). *PT* data for lherzolites were obtained using the TA98-NG85 thermobarometer combination, whilst those from harzburgites used the HAR84-NG85 combination (Nickel and Green, 1985; Taylor, 1998). The data used in this modelling is provide in Table 2S.1 of this thesis.

The method for the computation of the lithospheric geotherms from the heat equation is outlined in Hoare et al., (in review) and follows the approach of Hasterok and

Chapman, (2011). The only fixed parameters were the thicknesses of layers in a three-layer crust (see below) and their corresponding densities (ρ_u, ρ_{mid}, ρ_l), the temperature dependent thermal conductivity of the crust and mantle (k_u, k_l, where k_u corresponds to both the upper and mid crust) and the mantle potential temperature (T_p). These parameters are listed in Table. 4.2. The crust was stratified into 6 km upper, 11 km middle and 19 km lower divisions. Rather than define the surface (q_s) heat flux, heat production in the upper (H_u), middle (H_{mid}) and lower crusts (H_l), heat production in the mantle lithosphere (H_m) and the mantle potential temperature (T_p), used in the heat equation for the calculation of geotherms, these parameters were randomly selected across the range of a plausible parameter space outlined in Table. 4.2. The parameter space differs slightly for models at the near present-day and models at 1.15 Ga due to the anticipated effects of the higher radiogenic heat production earlier in Earth history and differing T_p. We used the Monte Carlo method to iterate each set of input parameters for 1,000,000 separate model iterations. From these parameters, the heat flux at the Moho (q_M) and heat flux at the base of the lithosphere (q_b) can also be calculated by subtracting the crustal contribution to the surface heat flux and any mantle contribution to the Moho heat flux, respectively. Additionally, the average heat production across the bulk crust (H_{avg}) can be calculated from the heat production values from each of the crustal divisions. From these crustal input parameters, a differentiation index (D_i) can also be calculated. The D_i is calculated by the ratio of heat production at the Earth's surface to the average heat production of the bulk crust (Perry et al., 2006a, 2006b). The D_i measures the degree of upward concentration of HPE within the crust with a value of 1 undifferentiated, (i.e., heat production of the bulk crust is equal to that at the Earth's surface). Values > 1 show greater enrichment of HPE at higher levels in the Earth's crust.

Each geotherm model was quantitively compared with mantle xenolith *PT* data from the Kaapvaal and Slave Cratons. The quality of fit of a modelled geotherm was assessed by means of the mean absolute error (MAE) of the residuals of the mantle xenolith *PT* data to the modelled geotherm. Any solution that displayed correlation of the residuals (R^2) > 0.2 was discarded. Using MAE for model evaluation is preferred to other metrics (e.g., root mean squared error; RMSE) due to it being less sensitive to outliers. Nonetheless, effort was taken to remove clearly anomalous data, particularly mantle xenoliths that appear to record heightened and likely transient thermal conditions (Fig. 4.4), so-called high temperature or 'sheared' peridotites (e.g., Finnerty and Boyd, 1987; Finnerty, 1989).

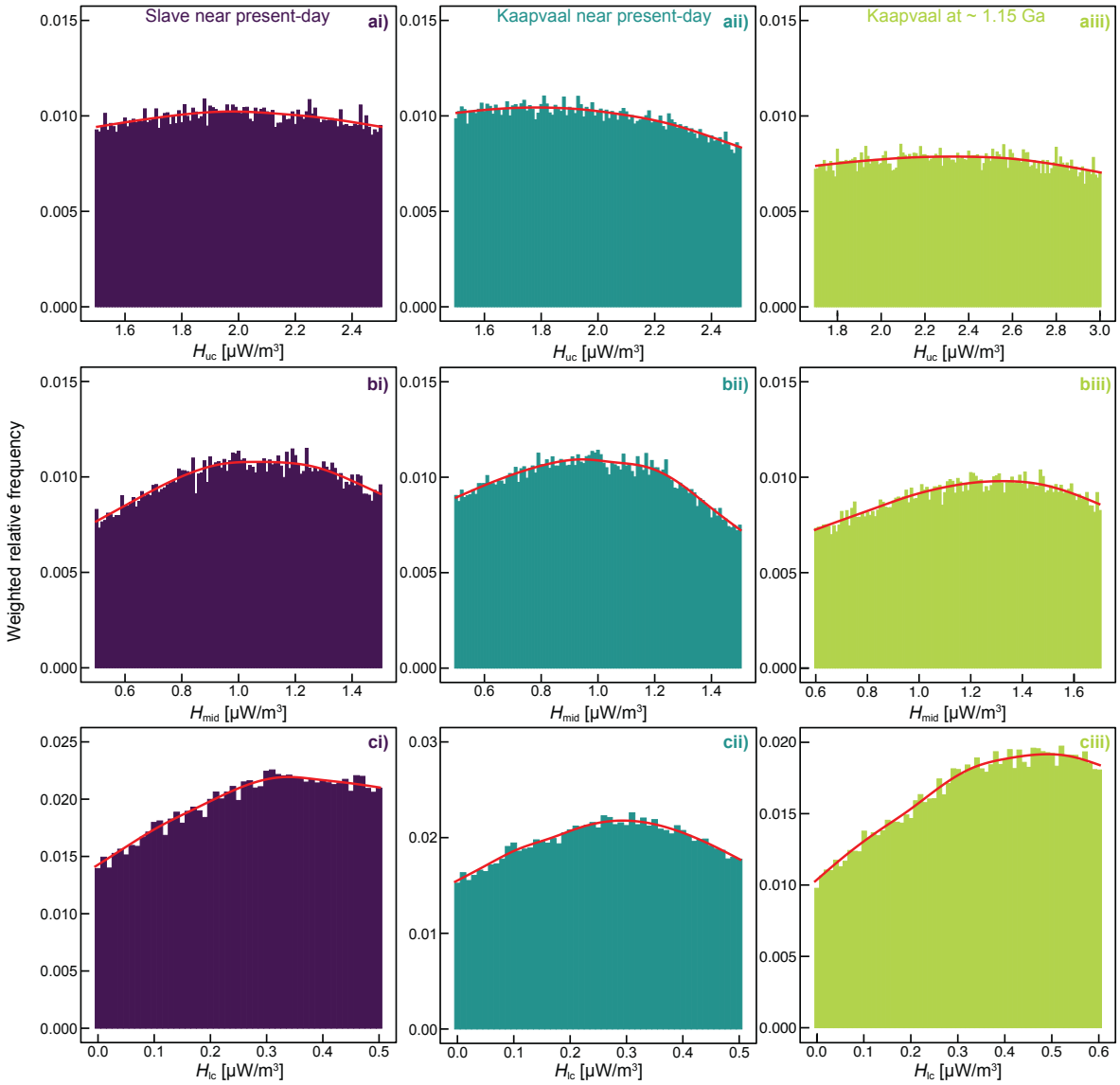

Figure 4.5: Weighted relative frequency of the 'accepted' (see text) parameters that provide the best fits to geotherms modelled by our Monte Carlo approach. a) Heat production in the upper crust, b) heat production in the middle crust, c) heat production in the lower crust, d) average heat production of the whole crust, e) differentiation index (Perry et al., 2006a; 2006b), f) heat production, g) surface heat flux, h) Moho heat flux, i) basal heat flux, j) temperature at the Moho and k) depth to lithosphere-asthenosphere boundary (LAB). i) close-to-present-day Slave Craton, ii) close-to-present-day Kaapvaal Craton and iii) Kaapvaal Craton at 1.15 Ga B.P. Also shown is the weighted median (dashed line) and a non-parametric fit to the weighted relative frequency obtained from a general additive model (GAM). Weighted medians not shown for a-c due to weak dependence.

Models were filtered to include only those that were consistent with constraints on the thickness of the lithosphere. Model solutions with a depth to the LAB of < 170 km were discarded as these geotherms fail to intersect the present day position of the diamond stability field (Day, 2012), which is required for the diamondiferous roots of the Slave and Kaapvaal Cratons. For models using mantle xenoliths from the 1.15 Ga Premier kimberlite, the depth at which geotherms intersect the diamond stability is ~ 183 km, due

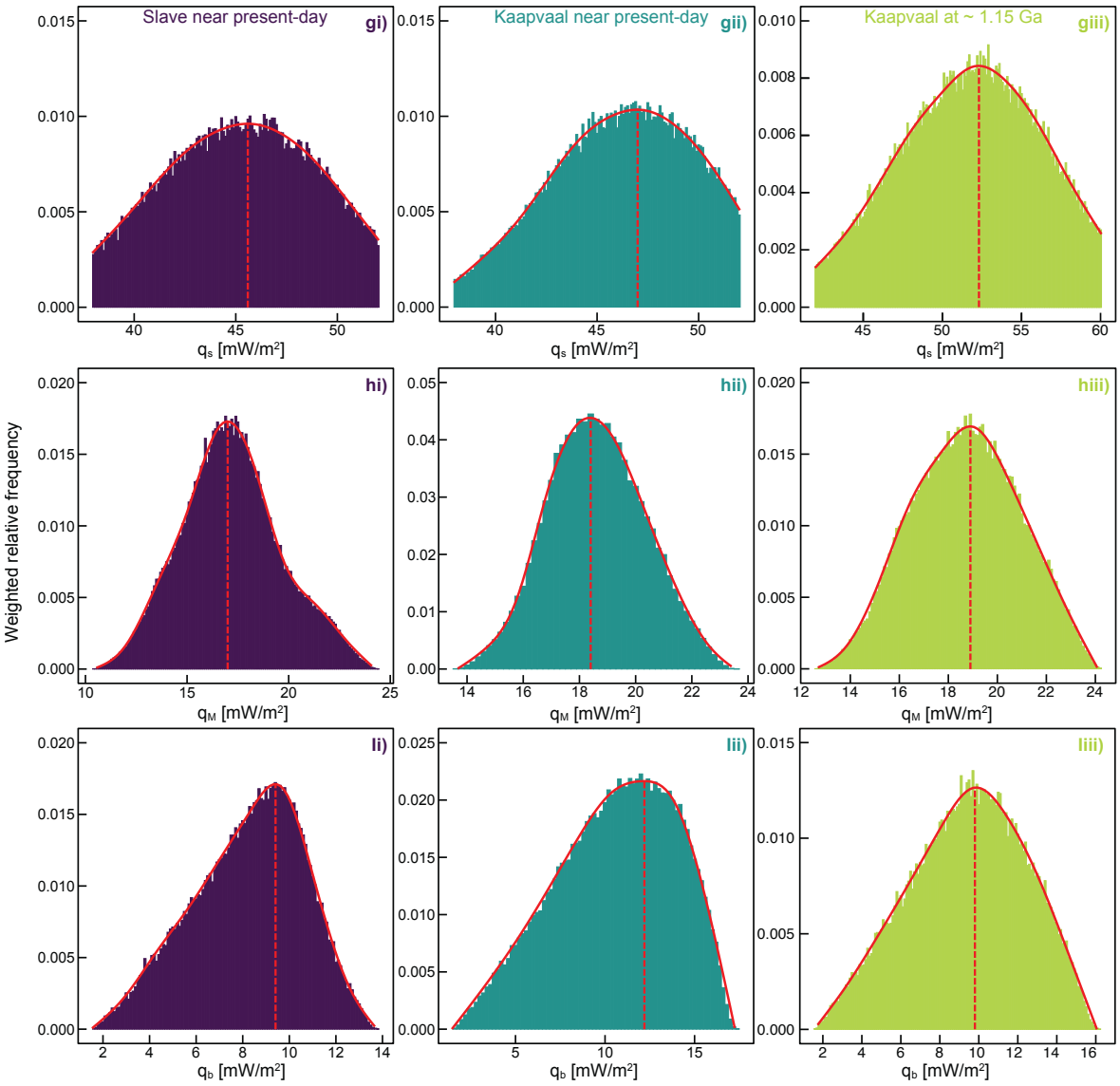

Figure 4.5: *(cont.)*

to an increased mantle potential temperature (T_p) of 1470°C compared to the 1350°C T_p of the near present-day. As a result, for models at 1.15 Ga, solutions with a depth to LAB of < 183 km were discarded. Model geotherms with a depth to LAB in > 350 km were also discarded in all models as these are far in excess of the present-day Slave and Kaapvaal Craton thicknesses estimated from geophysical models (e.g., Moorkamp et al., 2007; Ravenna et al., 2018) and maximum xenolith sampling depth. The total number of model solutions that passed these criteria for the near present-day Kaapvaal and Slave Cratons was n = 149,243 and n = 117,313, respectively. The total number of solutions that passed the criteria for the Kaapvaal Craton at 1.15 Ga, modelled from mantle xenoliths from the Premier kimberlite, was n = 147,477.

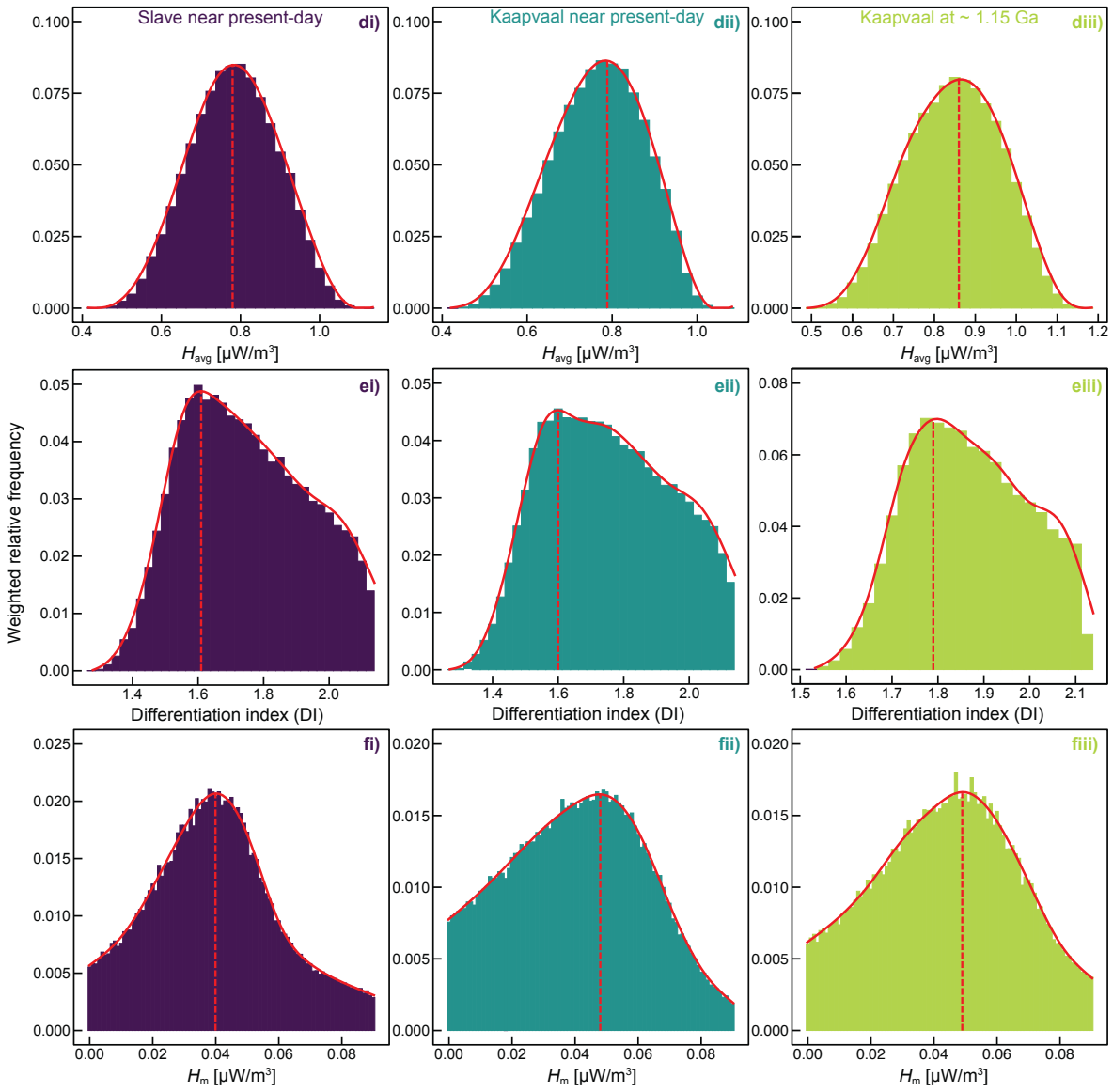

Figure 4.5: *(cont.)*

Rather than give all solutions that pass these criteria equal weight, the likelihood of a given model solution is obtained by weighting the MAE of the residuals of xenolith *PT* data to the modelled geotherm to provide a probability of model fit to each input parameter. Weighted relative frequency histograms for the values of input parameters of acceptable models are shown in Figure. 4.5. We do not report the 'best-fitting' model parameters (i.e., those parameters that generate the geotherm with the lowest MAE) as these values could be misleading due to the non-uniqueness of model solutions that results from multiple theoretical solutions existing across a parameter space. To demonstrate why the selection of a 'best' fitting geotherm should be avoided we selected the 1000 best fitting models based on their MAE from the Slave Craton, equating to less than 1% of the total modelled solutions. The difference in the MAE between the 1st (MAE = 34.74°C) and

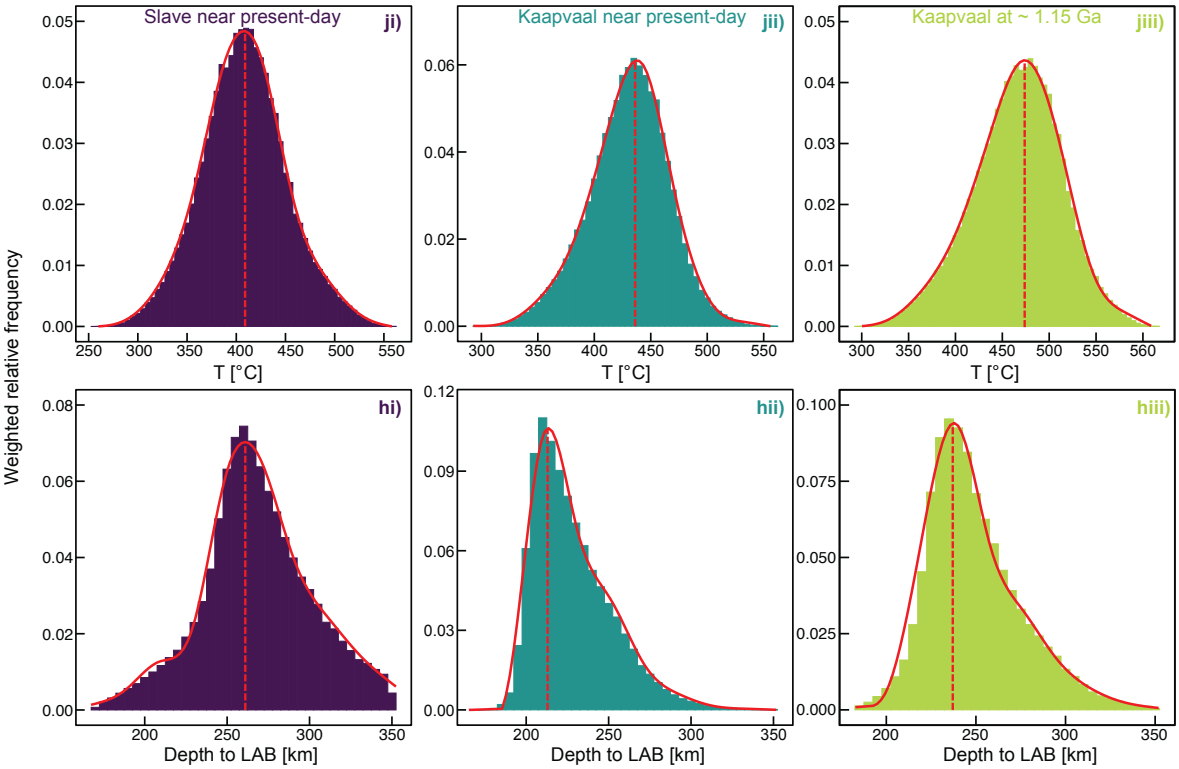

Figure 4.5: *(cont.)*

1000th best-fitting model (MAE = 35.29°C) is negligible at only ~ 1.5 %. Yet the total range of parameter space utilized by the 1000 models in between is total for all input parameters. This clearly demonstrates that for a negligible change in MAE vastly differing input parameters can satisfy a well-fitting model. It is for this reason we prefer to weight the model input parameter fits as outlined above. This contrasts with previous thermal modelling approaches in which model solutions are equally weighted and are only required to pass through (seemingly arbitrarily) defined temperature windows at specific depths in the lithosphere (e.g., Michaut et al., 2007) or within 95 % confidence limits obtained from linear regression of *PT* data from xenoliths (e.g., Rudnick et al., 1998). We argue that equally weighting all models, irrespective of their fit to mantle xenolith *PT* data, will result in too much importance being assigned to relatively poorly fitting model parameters, as is *clearly* illustrated in Figure. 4.6.

Best-fitting input parameters

Crustal heat production (H_u, H_{mid}, H_l, H_{ave})

The individual internal radiogenic heat productions in layers of the stratified upper, middle, and lower crusts are only weakly (H_{mid} and H_{lc}) or seemingly not at all (H_{uc}) dependent on generating well-fitting models for any of our models (Fig. 4.5a-c). Rather,

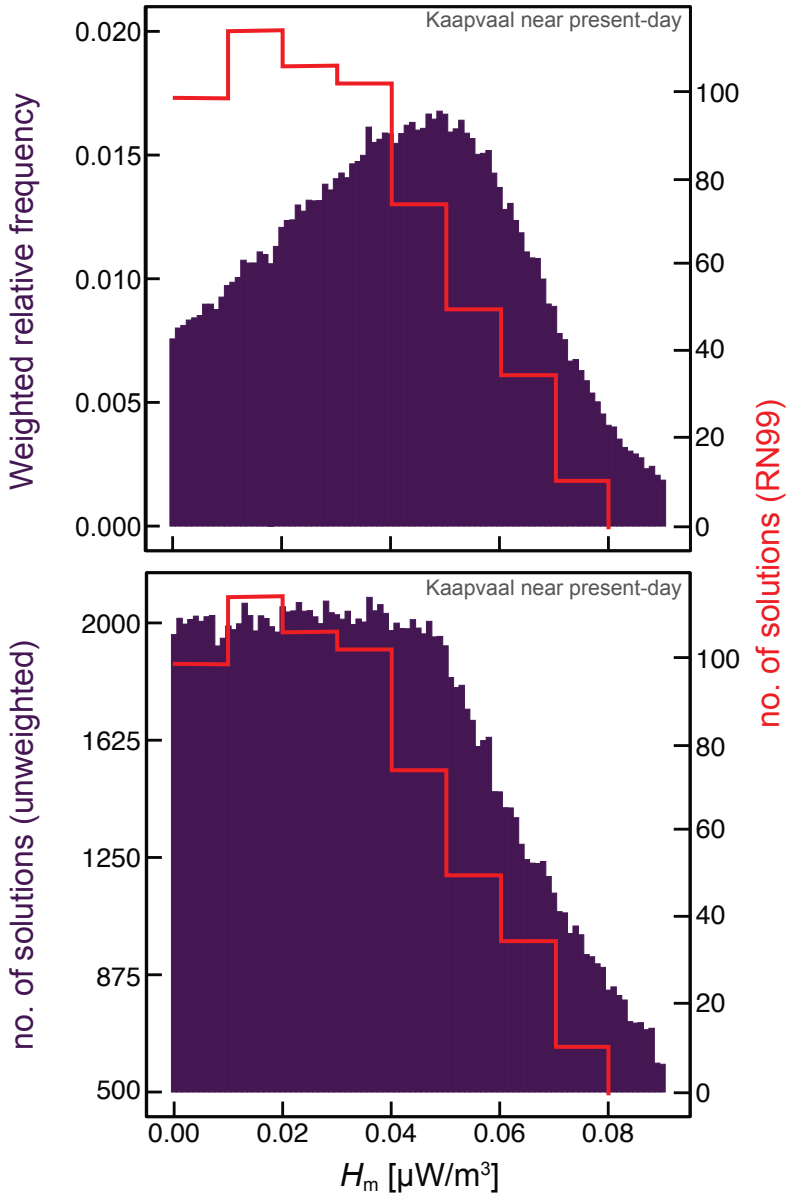

Figure 4.6: Comparison of weighted (a) and unweighted (b) frequency histograms for the Hm parameter from models from the Kaapvaal Craton at close-to-the-present-day, with a comparison to model results (red line) from Rudnick and Nyblade, 1999 (RN99). Note the similarities of our unweighted result and that of Rudnick and Nyblade, (1999).

well-fitting models are dependent on the average composition of the total crust (H_{avg}) and the degree of upward differentiation of heat production as defined by the differentiation index D_i. The best fitting D_i of ~ 1.6-1.8 (Fig. 4.4e) and overall shape of the distributions are very similar, irrespective of whether the models were generated for either of the modelled cratons, or between different ages from the same craton. The best fitting H_{avg} of models from near the present-day in both the Slave and Kaapvaal Cratons is, as with the D_i, almost identical at ~ 0.8 μW/m^3 (Fig. 4.4d). Best-fitting H_{avg} for the Kaapvaal Craton

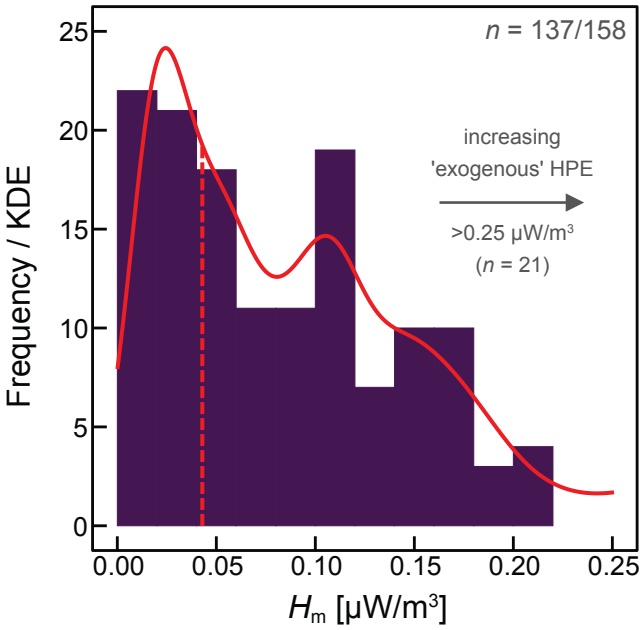

Figure 4.7: Comparison of H_m from direct measurement of HPE from mantle xenoliths and from the best-fitting H_m parameters of our modelling. Data taken from the GEOROC database (http://georoc.mpch-mainz.gwdg.de/georoc/) and Liu et al., (2021). KDE: kernel density estimation (Vermeesch, 2018). Exogeneous heat-producing elements (HPE) defined as that unsupported by major constituent minerals that comprise cratonic peridotites.

at 1.15 Ga slightly higher at 0.86 μW/m^3. The best-fitting D_i of the Kaapvaal crust is identical at 1.15 Ga than at the near present-day (Fig. 4.4e).

Internal heat production in the lithospheric mantle (H_m)

From our analysis in both the close-to-present-day Slave and Kaapvaal Cratons it is apparent that the best fitting H_m model parameter is non-zero with values of 0.040 and 0.048 μW/m^3, respectively (Fig. 4.5f). A similar H_m of 0.049 is also modelled for the Kaapvaal Craton at 1.15 Ga (Fig. 4.f) a value comparable to the present-day.

Surface (q_s), Moho (q_M) and basal heat fluxes (q_b)

The best fitting surface heat fluxes for the Slave craton approximates a normal distribution centred at 45.6 mW/m^2, whilst for the near present-day Kaapvaal slightly higher heat fluxes are observed approximating a normal distribution centred at 47 mW/m^2 (Fig. 4.4g). The most probable Moho heat fluxes from the Slave Craton approximate a normal distribution centred at 17 mW/m^2 compared to the similarly distribution for the Kaapvaal Craton centred at 18.4 mW/m^2 (Fig. 4.4h). Due to the similarity of D_i, (see above) the crustal contribution (surface minus the Moho heat fluxes) to the overall heat flux from both cratons at the near present-day is almost identical, with the minor variation between each

cratons surface heat fluxes reflected simply by slightly lower modelled Moho and basal heat fluxes in the Slave Craton. Both the best fitting surface heat flux for the Kaapvaal Craton at 1.15 Ga of 52.3 mW/m^2 and a Moho heat flux of 18.9 mW/m^3, are slightly higher than those modelled at the near present-day (Fig. 4.4g-h), most likely a result of a slightly warmer Earth interior at 1.15 G. Due to the internal heat production in the mantle lithosphere (H_m) the best fitting basal heat fluxes are substantially smaller than the Moho heat fluxes for all our models. The probability distributions for the basal heat fluxes are both left-skewed centred at 9.5 mW/m^2 and 12.2 mW/m^2 for the near present-day Slave and Kaapvaal Cratons, respectively (Fig. 4.4i). The best approximated basal heat flux for the Kaapvaal Craton at 1.15 Ga is slightly lower at 9.8 mW/m^2 than that measured at the near present-day also following a similar left-skewed distribution (Fig. 4,4i). The thicker lithospheric mantle of the Slave Craton coupled with a non-negligible internal lithospheric heat production is such that the Slave lithosphere on the whole transfers less energy from the underlying convecting mantle than the Kaapvaal Craton, either at the close-to-the-present-day or at 1.15 Ga.

Best-fitting output parameters

Depth to the lithosphere-asthenosphere boundary (LAB)

The most probable depth to the LAB (a minimum estimate see Hoare et al., in review), defined here as the interception of the geotherm and the present-day mantle adiabat of a mantle potential temperature (T_p) of 1350°C (Korenaga, 2008), for the Kaapvaal and Slave cratons is 213 km and 261 km (Fig. 4.4h), respectively, with both following skewed distributions. The most probable LAB depth of the Kaapvaal at 1.15 Ga from the intersection of the geotherm and a higher T_p of 1470°C for models for the Kaapvaal at 1.15 Ga is 235 km (Fig. 4.4h), with the weighted relative frequency following an approximate normal distribution.

4.3 Discussion

Our modelled surface fluxes are higher than is commonly assigned for Earth's cratons (Jaupart and Mareschal, 1999; Hasterok and Chapman, 2011). The surface heat flux of cratons is assumed to be relatively constant and taken to be low at 41 ± 0.8 mW/m^2 (Nyblade and Pollack, 1993). Indeed there is an almost blanket assumption of low (38 – 44 mW/m^2) surface heat fluxes for Earth's cratons, despite the, now increasingly apparent, wide variation in surface heat fluxes from Archean lithosphere (36 - 50 mW/m^2; Jaupart

and Mareschal, 2007). That this assumption pervades the petrological community most likely derives from the practice of making qualitative (often by eye) comparisons of with mantle xenolith *PT* data with 'geotherm families' of differing surface heat fluxes (e.g., Hasterok and Chapman, 2011). These comparisons have utility in that one can quickly assess whether xenoliths or diamonds (via thermobarometry of suitable inclusions) from one region or craton differ in terms of their equilibrium temperatures and/or depth of origin (Nimis et al., 2020). However, the most commonly used geotherm families are generalized and have a very low upper crust internal heat production of 1 $\mu W/m^3$ (Hasterok and Chapman, 2011). This upper crust heat production generates geotherm families with substantially lower modelled surface heat fluxes than is calculated when using higher and more realistic average upper and middle crust heat production of 1.25 – 1.5 $\mu W/m^3$, as constrained by exposed Archean upper crustal sections (e.g., Vredefort; Nicolaysen et al., 1981) or average compilations of exposed Archean upper crust (Condie, 1993). As a result these geotherm families are likely to significantly underestimate cratonic surface heat fluxes, a view that is supported by the wide range of, and frequently higher, surface heat flux data in Archean domains (Jaupart and Mareschal, 2007) found since the work of earlier work of Nyblade and Pollack, (1993).

In perhaps Earth's most well-studied craton the Kaapvaal, the direct measurement of the average surface heat flux is 48 ± 8 mW/m^2 taken from 144 measurements over the whole geographical region of the Kaapvaal Craton (Jones, 2017). This value is far higher than the commonly used value of 38 – 42 mW/m^2 for Archean domains. The 48 ± 8 mW/m^2 surface heat flux average for the Kaapvaal Craton closely matches our best fitting value of 47.0 mW/m^2 (Fig. 4.5), which is also similar to those of previous studies (Mather et al., 2011). By comparison, surface heat flux measurements are scarce for the Slave Craton. Two surface heat flux readings of 43 ± 5 and 48 ± 8 mW/m^2 from the Lac de Gras region of the Slave Craton provide (at best) a qualitative estimate of the surface heat flux of the region which averages at 46 ± 6 mW/m^2 (Mareschal et al., 2004). Nonetheless, a surface heat flux of 46 ± 6 mW/m^2 is consistent with our best-fitting modelled surface heat flux of 45.6 mW/m^2.

The most probable LAB depths for both the close to present-day Slave and Kaapvaal Cratons are also consistent with seismological estimates of the LAB that, despite measuring differing phenomena, are argued to provide similar estimates to petrological studies (e.g., Eaton et al., 2009). Seismological estimates for the depth of the LAB for the

former extend to depths of ~ 200-300 km, the wide range being a reflection of localized thinning (e.g., Jones et al., 2003; Moorkamp et al., 2007; Pedersen et al., 2009), and the later ~ 200-220 km (e.g., Muller et al., 2009; Priestley and McKenzie, 2013; Ravenna et al., 2018). These estimates are consistent with the estimates from our models. The similarity of these independent and empirically measured surface heat flux measurements and estimations of LAB depths from both cratons, the former particularly so, suggest our model results appear robust.

The modelling results from both the Slave and Kaapvaal Cratons at the near present-day are strikingly similar with respect to the overall heat production in the whole lithosphere. Indeed, the best-fitting average heat production and differentiation of heat producing elements towards the surface within the crust is almost identical in models from both the Slave and Kaapvaal Cratons (Fig. 4.5). On the one hand, the similarities of both the Kaapvaal and Slave crust, at least with respect to their heat producing elements, is perhaps surprising on account of the fundamental differences in the evolution of individual cratons that demonstrate varying tectonic histories (particularly the Slave and Kaapvaal Cratons) and thus potentially the conditions (i.e., stratification of HPE in the crust) with respect to their formation (e.g., Bleeker, 2003). On the other hand, the consistency in D_i is perhaps not such a surprising result. The upward stratification of heat-producing elements in the crust during the Archean is crucial for depressing temperatures in the lower crust below that of the solidus and hence allowing for stabilization of the cratonic crust (Michaut et al., 2009). In this scenario heat producing elements could be somewhat decoupled from the tectonics operating in the early Archean crust irrespective of the mechanism of their formation. Put another way, the Archean crust could be thought of as simply striving to redistribute its heat producing elements upward (driving by melting in the lower crust), this occurring to a point where melting in the lower crust no longer occurs due to suitably low HPE contents, at which point the D_i and H_{avg} becomes effectively fixed forever more. That the D_i of cratonic crust was established and unchanged in Earth's cratons at the time of their stabilization is consistent with the indistinguishable D_i of the Kaapvaal crust obtained from modelling at 1.15 Ga (Fig. 4.5). An unchanged D_i can also be supported by the position of lower crustal xenoliths in *PT* space with Archean age systematics that are trapped at granulite facies between c.700-850°C (Huang et al., 1995; Davis et al., 2003; Semprich and Simon, 2014) at temperatures far in excess of those expected at the Moho now (Fig. 4.5). Collectively, once the lower cratonic crust stabilized (during the Archean) it

seems to have remained unchanged ever since, irrespective of where or how the craton formed.

The low thermal contribution to lithospheric temperatures from the vertical stratification of HPE contrasts with non-zero internal lithospheric heat production of 0.04 – 0.05 μW/m^3 (Fig. 4.5). If these values are reliable, even at 1.15 Ga, they could not have been during the Archean, as they do not allow for stabilization of a diamond-hosting cratonic mantle earlier than 2.5 Ga (Fig. 4.2). Below, we examine the extent to which non-zero mantle heat production can be attributed to 'apparent' heat production resulting from the thermal disequilibrium of the crust and lithospheric mantle (Michaut and Jaupart, 2004; Michaut et al., 2009) or the metasomatic refertilization of the cratonic mantle with K, Th and U after 2.5 Ga.

Real or 'apparent' heat production in the cratonic lithospheric mantle?

Due to the characteristic time for heat diffusion in a thick lithosphere and the time taken for radioactive decay to occur within the Earth it is expected that the coupled crust and mantle are in a state of thermal disequilibrium (Michaut and Jaupart, 2004). As a result of the time lag between radiogenic heating and heat removal, steady-state models (such as those employed here) tend to overestimate mantle heat fluxes. By contrast, instantaneous solutions (e.g., Michaut and Jaupart, 2004, 2007; Michaut et al., 2007, 2009) that account for the time-dependent diffusion of heat through the lithosphere tends to increase the curvature of a geotherm. Thus, due to the expectation of disequilibrium between the crust and lithospheric mantle, steady state formulations (that fail to take such thermal disequilibrium take into account) will provide an 'apparent' heat production due to this increased curvature, even in circumstances where the lithospheric mantle has had zero internal heat production since its formation. As such the H_m parameter of the steady state heat equation will provide estimates that can be > 0 when the absolute radiogenic heat production is actually 0.

We suggest that a generalization of a constant or averaged H_m that would be produced by steady state formulations is the best approach to producing accurate lithospheric geotherms. This approach is not dissimilar to our modelling of heat production in the crust, which is most likely a gross simplification of the real geological complexities of the distribution of the HPE. It follows that the 'apparent' contribution to the H_m parameter will be both overestimated and underestimated in differing region of the lithospheric mantle. Unfortunately, as instantaneous solutions cannot reasonably be applied to the

cratonic lithosphere due to the uncertainties in both the physical evolution of the cratonic lithosphere and the thermal evolution of the underlying mantle e.g., Hoare et al., in review). We suggest that, however imperfect, steady state formulations are the only practical methodology for the estimation of the thermal conditions in the lithosphere, at least until better constraints on the secular cooling of the Earth's convecting mantle the timing of erosion that have thinned Earth's cratons occurred.

Due to the uncertainties associated with 'apparent' heat generation in the lithospheric mantle it becomes unclear whether there is a genuine heat production in the root derived from the decay of K, Th and U. Tentative support of a scenario of later re-enrichment of the cratonic lithosphere with K, Th and U could derive from direct whole-rock estimates of the H_m of cratonic peridotites themselves, which resemble the best-fitting H_m derived from our modelling albeit tailing to far higher values (Fig. 4.7). In the Kaapvaal the similarity in H_m between the near present-day and at 1.15 Ga would require that any re-enrichment in HPE of the cratonic lithosphere happened at (which is unlikely as time is required to permeate the root), or prior, to 1.15 Ga perhaps concomitant with either the emplacement of the ~ 1.15 Ga Umkondo igneous province (Hanson et al., 2004) or the earlier Bushveld igneous province at ~ 2.06 Ga (Zeh et al., 2015). If metasomatism occurred at 2.0 Ga the diffusion of heat would have only now permeated the whole lithospheric root, which could explain the slightly higher H_m observed at the present-day. Evidence of metasomatism in the lithospheric root at ~2.0 Ga in the Kaapvaal Craton is well documented from the dating of sulphide and silicate inclusions in diamond erupted in kimberlites (Richardson et al., 1993, 2004; Richardson and Shirey, 2008) as are earlier events between 1.0 and 1.7 Ga (Smith et al., 1991; Pearson et al., 1998; Aulbach et al., 2009a; Koornneef et al., 2017).

However, the remarkably similar H_m values from the Slave would require somewhat similar metasomatic histories to that seen in the Kaapvaal, which we argue is probably unlikely, as is testified by their substantially differing tectonic histories. Evidence of from the Slave Craton from diamond inclusions, while less abundant, also suggests a differing metasomatic history in the mantle lithosphere (see Howell et al., 2020). Furthermore, geochronology of modally metasomatised rocks from the Kaapvaal produce ages that are exclusively young < 140 Ma and seemingly related to the Cretaceous kimberlite and orangeite bloom of the region or the emplacement of the Karoo LIP (e.g., Konzett et al., 1998; Giuliani et al., 2014; Hoare et al., 2021a). A high internal radiogenic

heat production in the lithospheric mantle, irrespective of when it could have been introduced, is also at odds with the near zero heat production of mantle peridotites derived from recent in-situ measurements of K, Th and U in minerals that constitute cratonic peridotite (McIntyre et al., 2021), that can be used to estimate the overall heat production from reconstitution approaches (e.g., Emo and Kamber, 2021).

Based on the current evidence; principally the need for low H_m to stabilize the cratonic lithosphere in the Archean (e.g., Michaut et al., 2009) and the low HPE abundances in 'reconstituted' cratonic peridotites (McIntyre et al., 2021), it is probably simpler for the majority, of the H_m modelled for the cratonic lithospheric mantle of the Slave and Kaapvaal cratons derives from apparent heat production resulting from the thermal disequilibrium of the crust and mantle. This is because the apparent H_m at the time of craton formation would be 0 and subsequently increase reaching a maximum value later, in the specific case of a 250 km thick root (of constant thickness) 1.9 Ga later. However, we do not, or rather cannot, rule out a metasomatic (i.e., real) component, particularly in light of the *extreme* HPE enrichment seen in some mantle xenolith suites (e.g., MARID; Fitzpayne et al., 2018) and the increasing acceptance that the cratonic mantle is a significant reservoir of elements previously assumed to be highly depleted (Gibson, 2021). As such, the H_m parameter modelled here can be considered in two scenarios:

$$H_{m(absolute)} > 0 \Rightarrow H_m \approx H_{m(absolute)} + H_{m(apparent)} \quad \text{[Eq. 4.1]}$$

or

$$H_{m(absolute)} = 0 \Rightarrow H_m \approx H_{m(apparent)} \quad \text{[Eq. 4.2]}$$

where $H_{m(absolute)}$ is any real contribution to heat production in the mantle root from the internal decay of K, Th and where U and $H_{m(apparent)}$ refers to the contribution of radiogenic heat to the lithospheric mantle produced earlier from the Earth's crust and convecting mantle earlier in its cooling history, but not yet lost by diffusion.

Implications for the heat loss from the Earth

Irrespective of the ultimate 'source' of heat production in the cratonic lithospheric mantle its contribution to the Moho heat flux and its inhibiting effect for the transfer of heat through the lithosphere is significant. Where the $H_m = 0 \Rightarrow$ Moho heat flux ≈ basal heat flux. Yet, in the case of the Slave craton at near the present-day, the difference between the

Moho and basal heat fluxes equates to 7.5 mW/m^3, with the lithospheric mantle contributing ~ 44 % of the Moho heat flux. Near present-day conditions in the Kaapvaal are similar with the difference between the Moho and basal heat fluxes equating to 6.2 mW/m^3, contributing ~ 34 % of the Moho heat flux, slightly less than seen in the Slave most likely due to the thinner lithospheric mantle seen in the Kaapvaal. As such, these values represent a not negligible component of Earth's own present-day internal heat generation and a significant insulator for heat loss from the Earth which should be accounted for in parametrized convection models of the upper mantle (e.g., Grigné and Labrosse, 2001; Lenardic et al., 2011). If certain assumptions are made (Table. 4.3) it is possible to estimate the contribution a non-zero value of H_m would make to the total energy loss of the Earth. The total contribution of a continental mantle with an internal heat production of 0.05 μW/m^3 (in this case also including a non-cratonic continental component) to the total heat loss of the Earth or the continental lithosphere can be calculated from eq. 3-10 where:

$$Q_m = \frac{A_c \times q_{mt}}{1E + 15}$$

[Eq. 4.3]

and

$$q_{mt} = (q_{m1} \times F_1) + (q_{m2} \times F_2)$$

[Eq. 4.4]

and

$$q_{m1} = (Z_1 - Z_c) \times H_{m1}$$

[Eq. 4.5]

and

$$q_{m2} = (Z_2 - Z_c) \times H_{m2}$$

[Eq. 4.6]

and

$$Q_E = \frac{A_T \times q_E}{1E + 15}$$

[Eq. 4.7]

and

$$q_E = (q_o \times F_o) + (q_{ct} \times F_c)$$

[Eq. 4.8]

and

$$q_{ct} = (q_{c1} \times F_1) + (q_{c2} \times F_2)$$

[Eq. 4.9]

and

$$Q_c = \frac{A_c \times q_{ct}}{1E + 15}$$

[Eq. 4.10]

Where, Q_E, Q_c, Q_m is the total heat loss from the Earth, continental and continental lithospheric mantle in TW, respectively, q_{mt} is the total contribution of the continental lithospheric mantle to the surface heat flux from the continents (q_{ct}) in mW/m^2, A_c is the total area of the continental lithosphere in km^2, q_{m1} and q_{m2} are the contributions of heat flux from the cratonic and non-cratonic lithospheric mantle to the continental surface heat flux in mW/m^2, respectively, z_c, z_1 and z_2 are the cratonic and non-cratonic lithospheric and average continental crust thicknesses in km, respectively, and H_{m1} and H_{m2} are the internal heat production of the cratonic and non-cratonic lithospheric mantle in μW/m^3, respectively. F_1 and F_2 are the fractions of "cratonic" taken here as lithosphere of > 150 km thickness (Pearson et al., 2021) and F_o and F_{ct} are the fractions of the Earth that are oceanic and continental, lithosphere respectively. These calculations (Table. 4.4) show that a continental lithospheric mantle with an internal heat generation of 0.05 μW/m^3 could be responsible for 1.2 TW of heat loss from the Earth's surface or 3.1 % of the total energy budget of the Earth or 11.4 % of the total energy lost through the continents, values that would be not so insignificant that should be neglected.

Concluding remarks

- Our thermodynamic modelling results from both the Slave and Kaapvaal Cratons at near present-day are strikingly similar with respect to the overall heat production in the lithosphere. In the crust, irrespective of the fact that the Slave and Kaapvaal cratons have very different tectonic histories the heat production and thus stratification of the HPE is almost identical. We suggest that this ultimately results from melting in the lower cratonic crust driving upward migration of HPE through the crust. Due to the similarity of this value in cratons with substantially differing histories the upward stratification of HPE could be independent of the tectonic processes that form a craton.

- Both the Slave and Kaapvaal cratons have a non-zero internal heat generation in the mantle, the latter also through time. It is unclear whether this heat generation is real (i.e., actual radioactive decay of K, Th and U in the cratonic mantle) or 'apparent' (i.e., that resulting from the thermal disequilibrium between the lithospheric crust and mantle).
- It follows that the blanket assumption of a lithospheric mantle with zero heat production (real or otherwise) is not consistent with *PT* data from mantle xenoliths, and may lead to the underestimation of LAB depths in Earth's cratons. A non-negligible H_m (~ 0.05 μW/m^3) in the continental lithosphere could also contribute to a significant (3.1 %) portion of the global heat loss budget of the Earth.

Tables

Models near present-day

Input parameters	range	stepsize (h)		Reference
q_s	38-52	0.1	$mW\ m^{-2}$	-
H_{uc}	1.5-2.5	0.01	$\mu W\ m^{-3}$	-
H_{mid}	0.5-2.5	0.01	$\mu W\ m^{-3}$	-
H_{lc}	0-0.5	0.01	$\mu W\ m^{-3}$	-
H_m	0-0.09	0.001	$\mu W\ m^{-3}$	-
$k_{uc\_initial}$	2.8	-	$W\ m^{-1}\ k^{-1}$	see [1]
$k_{lc\_initial}$	2.54	-	$W\ m^{-1}\ k^{-1}$	see [1]
k_{uc} (T= 0°C)	2.94	-	$W\ m^{-1}\ k^{-1}$	see [1]
k_{lc} (T= 0°C)	2.61	-	$W\ m^{-1}\ k^{-1}$	see [1]
ρ_{uc}	2.75	-	$Kg\ m^{-3}$	-
ρ_{lc}	2.86	-	$Kg\ m^{-3}$	[2]
T_p	1350	-	°C	[3]

Models at 1.15 Ga

Input parameters	range	stepsize (h)		Reference
q_s	42-60	0.1	$mW\ m^{-2}$	-
H_{uc}	1.7-3.0	0.01	$\mu W\ m^{-3}$	-
H_{mid}	0.6-1.7	0.01	$\mu W\ m^{-3}$	-
H_{lc}	0-0.6	0.01	$\mu W\ m^{-3}$	-
H_m	0-0.09	0.001	$\mu W\ m^{-3}$	-
$k_{uc\_initial}$	2.8	-	$W\ m^{-1}\ k^{-1}$	see [1]
$k_{lc\_initial}$	2.54	-	$W\ m^{-1}\ k^{-1}$	see [1]
k_{uc} (T= 0°C)	2.94	-	$W\ m^{-1}\ k^{-1}$	see [1]
k_{lc} (T= 0°C)	2.61	-	$W\ m^{-1}\ k^{-1}$	see [1]
ρ_{uc}	2.75		$Kg\ m^{-3}$	-
ρ_{lc}	2.86		$Kg\ m^{-3}$	[2]
T_p (τ = 1.15 Ga)	1470	-	°C	[3]

Table. 4.1: Input parameters for geotherm construction at the near present-day Kaapvaal and Slave Cratons. Also shown are the input parameters at 1.15 Ga for further modelling in the Kaapvaal Craton. Where qs is the surface heat flux, Huc, Hmid and Hlc is the internal heat production in the upper, middle, and lower crust, respectively, Kuc_inital and Klc_initial are the thermal conductivities of the estimated for upper and lower crust and Kuc and Klc are the same values projected to T = 0°C (a value chosen for the Earth's surface). ρuc and ρlc are the densities of the upper, and middle and lower crust, respectively. Tp is the mantle potential temperature as demonstrated by an isentrope at specific time intervals (τ) in Ga. References: [1] Hoare et al., in review; [2] James et al., (2003); Korenaga, (2008b).

Xenoliths		near present-day				1.15 Ga B.P.		
		Slave Craton		Kaapvaal Craton		Kaapvaal Craton		
Accepted for modeling	Diavik	*(n = 23)*		Bultfontein	*(n = 27)*	Premier	*(n = 90)*	
	Ekati	*(n = 9)*		Frank Smith	*(n = 2)*			
	Jericho	*(n = 43)*		Jagersfontein	*(n = 10)*			
				Kaalvaalei	*(n = 11)*			
				Kimberley	*(n = 15)*			
				Lesotho group	*(n = 48)*			
				Monastery	*(n = 6)*			
	total		*75*	total	*119*	total		*90*
Rejected as outliers	Diavik	*(n = 23)*		Bultfontein	*(n = 0)*	Premier	*(n = 0)*	
	Ekati	*(n = 6)*		Frank Smith	*(n = 1)*			
	Jericho	*(n = 6)*		Jagersfontein	*(n = 8)*			
				Kaalvaalei	*(n = 7)*			
				Kimberley	*(n = 2)*			
				Lesotho group	*(n = 27)*			
				Monastery	*(n = 0)*			
	total		*45*	total	*45*	total		*0*

Table. 4.2: Mantle xenolith data used in modelling. For references see text.

Table. 4.3

Input parameters	value	unit	Comments and/or assumptions	Reference
Assumed craton thickness (ζ_1)	200	km	That all here termed cratonic lithosphere is of equal thickness	-
Assumed non-cratonic continental thickness (ζ_2)	75	km	Midpoint estimate of Phanerozoic lithospheric thickness, assumes equal thickness	O'Reilly and Griffin 2006
Assumed continental crust thickness (ζ_c)	40	km	Average of all continental crust, does not take into account secular changes in thickness nor overthickened crust (e.g., mountain ranges)	Rudnick and Gao, 2003
Heat production cratonic lithospheric mantle (H_{m1})	0.05	$\mu W/m^3$	Assumes that all cratons have the same H_m relationship as inferred from this study for the Slave and Kaapvaal cratonic lithospheric mantle	this study
Heat production non-cratonic lithospheric mantle (H_{m2})	0.05	$\mu W/m^3$	Assumes that all non-cratonic lithosphere has the same H_m relationship as inferred from this study for the lithospheric mantle of the Slave and Kaapvaal cratons. This value could be higher, particularly if U-rich (up to 200 ppm) apatite found from non-cratonic lithosphere is widespread (O'Reilly and Griffin, 2000).	-
Oceanic lithosphere area (A_o)	3E+14	m^2		Jaupart and Mareschal, 2007
Continental area (A_c)	2.1E+14	m^2		Jaupart and Mareschal, 2007
Total Earth surface area (A_T)	5.1E+14	m^2		Jaupart and Mareschal, 2007
Fraction of oceanic lithosphere (F_o)	0.59	-		Jaupart and Mareschal, 2007
Fraction of continental lithosphere (F_c)	0.41	-		Jaupart and Mareschal, 2007
Fraction of continetal lithopshere that is cratonic (F_1)	0.63	-	Craton here defined seismically as cool, dense regions at depths > 150 km (i.e., not necessarily Archean), in this case only 9 % might comprise 'traditional' (Archean) cratons with the remainder Proterozoic (e.g., mobile belts)	Jaupart and Mareschal, 2007; Pearson 2021
Fraction of continetal lithopshere that is non-cratonic (F_2)	0.37	-		Pearson 2021
Cratonic heat flux (q_{c1})	45	mW/m^2	Midpoint between low heat flux cratons (e.g., Dharwar, Yilgarn, Superior) and high heat flux cratons (e.g., Kaapvaal, Zimbabwe, Slave) also matches the mid-point of Proterozic rocks	Jaupart and Mareschal, 2007
Non-cratonic heat flux (q_{c2})	58	mW/m^2	Heat flux reported for Phanerozoic rocks	Jaupart and Mareschal, 2007
Total continental heat flux (q_c)	50	mW/m^2		Jaupart and Mareschal, 2007
Oceanic heat flux (q_o)	94	mW/m^2		Jaupart and Mareschal, 2007
Total earth heat flux (q_E)	76	mW/m^2	Weighted average of continental (cratonic and non-cratonic) and oceanic heat fluxes	-

Table. 4.3: Assumptions made in calculations for the contribution of the continental lithospheric mantle to the total energy budget of the Earth and Urey ratio

Table. 4.4

Resulting calculations			Comments and/or assumptions
Contribution of craton H_m to cratonic heat flux (q_{m1})	8	mW/m^2	
Contribution of non-craton H_m to non-cratonic heat flux (q_{m2})	1.75	mW/m^2	
Total contribution of continental H_m to continental heat flux (q_m)	5.69	mW/m^2	
Heat loss from continental crust (Q_c)	10.5	TW	
Heat loss from continental lithopsheric mantle (Q_m)	1.2	TW	Assumption of no vertical changes in area of the contintal lithosphere
Heat loss total Earth (Q_E)	38.7	TW	
Proportion of heat loss from H_m in the continental mantle from Earth's total heat loss	3.1	%	
Proportion of heat loss from H_m in the continental mantle from the total continental heat loss	11.4	%	

Table. 4.2: Calculations of the contribution of a continental lithosphere with internal heat production to the total heat budget of the Earth.

Chapter 5: Pyrope Garnet U-Pb dating: A Mantle and Kimberlite-Emplacement Chronometer

Gary J. O'Sullivan[1], Brendan C. Hoare[2], Chris Mark[1], Foteini Drakou[2], Emma L. Tomlinson[2]

[1] UCD School of Earth Sciences, University College Dublin, Dublin 4, Ireland

[2] Department of Geology, Trinity College Dublin, Dublin 2, Ireland

Keywords: U-Pb; Geochronology; Garnet; Pyrope; mantle

This work is presented as an advanced manuscript draft, which is aimed to be submitted to *Nature Scientific Reports.*

Abstract

Kimberlite emplacement ages are needed to better constrain the timing and tempo of kimberlite magmatism and so understand the origin and geodynamic setting of kimberlite genesis and the evolution of mantle sources.. Kimberlite emplacement ages are most often obtained from U-based decay systems in perovskite and zircon, or Rb- or K-based systems in phlogopite, but each of these approaches has limitations that hinder determinations in certain settings. For example, groundmass perovskite is not always found in kimberlite, nor is it typically preserved as an indicator mineral in soil or sediment. Here, we present U-Pb ages of peridotitic pyrope garnet from heavy mineral concentrate from the Roberts Victor kimberlite, and from mantle xenoliths recovered from Bultfontein, to date emplacement. Despite low U-concentrations (mostly < 0.1 ppm), sub-concordant garnets can be dated using very large laser- ablation spots (130 μm) measured by quadrupole ICPMS. In both locations, the U-Pb lower-intercept discordia ages of garnet, 84.1 ± 7.1 Ma at Bultfontein and 116.3 ± 15.8 Ma at Roberts Victor, reproduce previous emplacement ages obtained from other mineral-isotope systems (chiefly Rb-Sr in phlogopite). These ages imply that the garnet U-Pb system was open during mantle residence due to high ambient temperatures, and this inference is reinforced by Ni-thermometry data which indicate high equilibration temperatures (950 - 1075 °C). A discordia fit through garnets from the Roberts Victor

separate also yields an upper-intercept age of 2560 ± 490 Ma, indicating that some ancient information was retained. Again, this interpretation may be supported by Ni-thermometry data, which indicate much lower equilibration temperatures for some Roberts Victor garnet (~ 850°C). Our analytical protocol is not complex and uses widely available analytical methods. If applied to pyrope-rich garnet inclusions in diamond, it may be possible to provide ages of garnet-entrapment and thus diamond-growth if the U-Pb system remains undisturbed.

5.1 Introduction

Kimberlites are volatile-rich, silica-poor ultramafic mantle-derived magmas that are rapidly and violently erupted onto the Earth surface. They are of scientific interest as they provide rare glimpses into the composition and evolution of the Earth's lithospheric mantle. Kimberlites transport mantle xenoliths and xenocrysts, including diamond, to the surface. They thus provide a wealth of information on the chemical, thermal and geodynamic evolution of the lithosphere. Timing kimberlite emplacement can constrain critical processes such as craton erosion, ancient plume activity, and the Earth's tectonic evolution and deep volatile cycles (e.g., Janney et al., 2010; Tappe et al., 2018). Constraining kimberlite emplacement may also aid detrital diamond prospecting, and models of the genesis of plume-associated metallogenic provinces (Fiorentini et al., 2020).

Kimberlites are dated by a range of methods, but for various reasons not all may be dated using the same method. The majority of kimberlites appear to have been emplaced during the Phanerozoic and there have been several periods of enhanced kimberlite magmatism (e.g., Tappe et al., 2018; Heaman et al., 2019). Kimberlites are most commonly dated using U-Pb perovskite (Tappe and Simonetti, 2012; Sarkar et al., 2015b), U-Pb zircon (e.g. Davis, 1977) or more recently by perovskite (U/Th)-He (e.g. Stanley and Flowers, 2016). Rb-Sr phlogopite and $^{40}Ar/^{39}Ar$ phlogopite are also employed to date kimberlites and can yield precise determinations. However, despite advancements, even current state-of-the-art methods for dating of kimberlite do not always yield accurate and precise ages. U-Pb analysis of perovskite can be complicated by high common-Pb contents and multiple age populations (Griffin et al., 2014), and is not applicable to detrital prospecting. U-Pb dating of kimberlite zircon can be complicated by the fact that zircon crystallization may predate kimberlite magmatism and thus preserve ages that predate emplacement by up to several billion years (e.g. Kinny et al., 1989; Zartman and Richardson, 2005). (U/Th)-He dating applied to zircon and perovskite circumvents some

sources of error in kimberlite dating by analysing a daughter product retained only at low-temperatures, however the system is susceptible to resetting (Stanley and Flowers, 2016), and additionally may not always provide precise age constraints amongst other issues (Reich et al., 2007). Phlogopite is more susceptible to alteration after emplacement than some other components of kimberlite (amongst other complicating factors, see Heaman et al., 2019), and thus application of the Rb-Sr and $^{40}Ar/^{39}Ar$ phlogopite methods to date kimberlite dating may be challenging. Furthermore, all of the described methods rely upon the occurrence of the mineral phase, which is not guaranteed. Thus, the addition of other methods to complement these existing methods is desirable with, for example, U-Pb dating of rutile in mantle xenoliths entrained in kimberlite having been applied successfully to trace emplacement (Tappe et al., 2014).

U-Pb dating of xenolithic garnet is an appealing prospect for dating kimberlite emplacement. An abundant phase in the mantle, it is easy to identify and separate from the groundmass and is chemically and mechanically robust. Additionally, garnet-bearing xenoliths in kimberlite are most typically entrained at ambient lithospheric temperatures in excess (> 1000°C) of the inferred closure temperatures of the almandine-pyrope U-Pb system (> 800°C; Mezger et al., 1989). Therefore, the determined garnet U-Pb age can most likely be attributed to magmatic emplacement rather than garnet formation. If it can be demonstrated that garnet provides accurate emplacement ages for kimberlite, logically, U-Pb garnet could be applied to garnet inclusions in diamond, in order to date inclusion entrapment and therefore diamond growth. Detrital garnet is also used as a key indicator mineral in diamond exploration in both proximal and distal settings (Shchukina and Shchukin, 2018), and its dating is thus appealing as a potential method to acquire more characteristic provenance-specific information. Therefore, the ability to determine kimberlite emplacement ages from garnet from xenoliths hosted within them is a novel opportunity to provide chronology for these processes.

U-Pb geochronology of garnet (using solution chemistry and thermal ionisation mass spectrometry [TIMS]) has been applied since the late 1980s (Mezger et al., 1989, 1991; Jung and Mezger, 2003). Despite evidence that - subject to composition - garnet lattice can incorporate U at the trace, minor, and even major-element level (e.g., Rák et al., 2011) such bulk analytical techniques have been hampered by uncertainty over whether U is hosted within the garnet lattice, or within inclusions (e.g., DeWolf et al., 1996). Modern *in-situ* analytical approaches and greater availability of characterised garnet reference

materials (e.g., Seman et al., 2017; Salnikova et al., 2018, 2019; Stifeeva et al., 2019) combined with non-destructive sample pre-characterisation and co-monitoring of garnet and likely inclusion major element masses during analysis, mean that this obstacle can be surmounted.

Here, we employ coupled EDX-SEM and LA-Q-ICPMS analysis together with several garnet U-Pb age reference materials for which high-precision TIMS ages are available (Salnikova et al., 2019, 2018; Stifeeva et al., 2019). We have analysed garnet from four separate peridotite xenoliths collected from the Bultfontein pans near Kimberley and two kimberlite garnet mineral separates; one (peridotitic) from Roberts Victor and one (eclogitic) from Jagersfontein, South Africa (Fig. 5.1). Information about previous chronology performed on these kimberlites is provided on Figure 5.1. The emplacement of the Bultfontein kimberlite has been previously dated by the Rb-Sr method, yielding dates of 90 ± 3 Ma (Allsopp and Barrett, 1975) and 85.6 ± 1.0 Ma (Smith et al., 1985) determined from kimberlite matrix phlogopite. Phlogopite from entrained mantle xenoliths yielded a date of 84 ± 0.9 Ma (Kramers and Smith, 1983). These age are generally typical of Group-I kimberlites in the wider 'Kimberley cluster' (Allsopp and Barrett, 1975). U-Pb zircon ages from the Bultfontein kimberlite range from 83.8 for xenolith-hosted zircon to 91.2 Ma in kimberlite zircon (Davis, 1977). Age estimates for emplacement of the Bultfontein kimberlite thus range between approximately 83 and 93 Ma, though the most precise estimates cluster around the younger part of the age range. Emplacement ages for Roberts Victor kimberlites are 127 ± 3 Ma (Allsopp and Barrett, 1975) and 128 ± 15 Ma (Smith et al., 1985), established using the Rb-Sr method on kimberlite matrix phlogopite.

5.2 Materials and methods

Materials

Garnet was analysed from four peridotite xenoliths prepared as 200 μm thick sections, and also from kimberlite garnet within heavy mineral separates (i.e. xenocrysts hosted in the kimberlite) mounted in epoxy. Peridotite xenoliths were collected from the Bultfontein pans (28.739155°S, 24.818094°E), spoils derived from mining of the Bultfontein kimberlite pipe

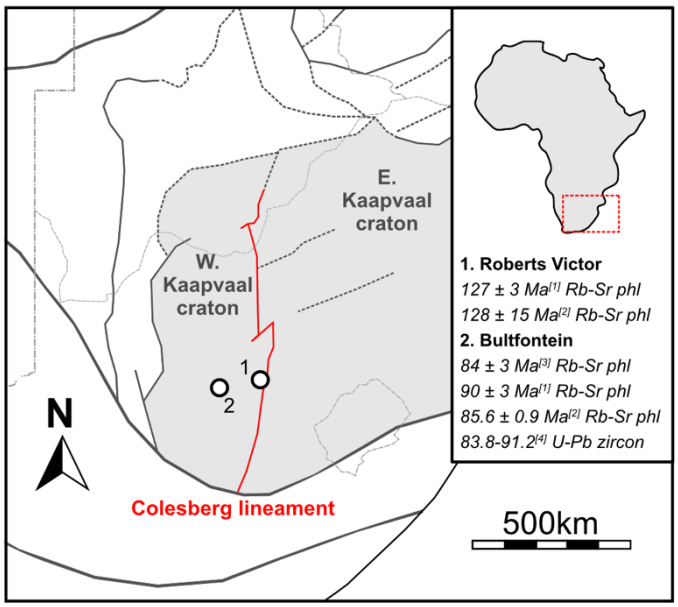

Figure 5.1: Kimberlite locations from which mantle xenoliths and garnet separates were sampled in this study. Tectonic divisions of the Kaapvaal craton after Griffin et al., (2003). References on the key are [1] Allsop and Barrett (1975); [2] Smith et al. (1985); [3] Kramers and Smith (1983); [4] Davis et al. (1977); phl = phlogopite.

in South Africa. Samples BSK064; CLA-51 and BP002 (Tomlinson et al., 2018) are from typical coarse-grained granular harzburgite (specifically, they are taken from garnet exsolution lamellae in orthopyroxene megacrysts). CLA-13 is a typical course-grained granular garnet lherzolite. Xenoliths were selected on the basis of minimal secondary metasomatic alteration (phlogopite absent). Peridotitic and eclogitic garnet xenocryst separates were analysed from the Roberts Victor and Jagersfontein kimberlites respectively (Fig. 5.1).

Methods

Garnet crystals were imaged using a Tescan TIGER MIRA3 Variable Pressure FE-SEM. Cathodoluminescence (CL) detectors were used to inspect for the presence of mineral inclusions. Major elements were obtained via calibrated energy-dispersive X-ray spectroscopy (EDS) at the iCRAG laboratory, Trinity College Dublin. For SEM-EDS analysis a beam current of ~ 380 pA and an accelerating voltage of 20 kV was utilized, with acquisition time varied to obtain a minimum of 4 million counts. Beam current drift was restricted by frequent analysis of pure Co. The instrument was calibrated using a suite of appropriate mineral standards from the Smithsonian Institute (Jarosewich et al., 1980; Jarosewich, 2002) following the method of Ubide et al., (2017). Typical analytical uncertainties of < 3 % can be obtained utilizing this analytical setup.

For U-Pb analysis, garnet crystals were directly analysed by LA-Q-ICP-MS, at Trinity College Dublin. The analytical set-up comprises a Teledyne-Cetac Analyte Excite 193nm excimer laser, with a rapid-washout HelEx 2-volume ablation cell, coupled via an in-house adjustable-volume mixing-device to an Agilent Technologies 7900 quadrupole ICP-MS. The analysed masses were ^{29}Si, ^{43}Ca,^{137}Ba, ^{206}Pb, ^{207}Pb, ^{208}Pb, ^{232}Th, ^{238}U. ^{137}Ba was used to screen for kimberlite contamination along fractures, with spots yielding significant baseline-corrected counts on ^{137}Ba (~ > 200 Counts per second) being excluded from age calculations; ^{29}Si was used as the index mass to correct for variation in signal intensity (Paton et al., 2011). A large spot size of 130 µm diameter was used in order to optimise counts on U and Pb masses from the unknown garnets, while retaining reference material signal intensity below the pulse-analogue threshold on this instrument. NIST614 standard glass was run as the primary standard for U-Pb analysis (Woodhead and Hergt, 2000), and to calculate the semi-quantitative trace element concentrations in the unknowns. Data reduction employed the VizualAge data reduction scheme (DRS) for Iolite (Paton et al., 2011; Petrus and Kamber, 2012), and age calculation and concordia plot generation employed IsoplotR (Vermeesch, 2018). A U-Pb fractionation correction factor was obtained from Odikhincha garnet (Salnikova et al., 2019; 250 ± 1 Ma) and applied to secondary references and garnet unknowns for the same analytical sessions. The secondary reference materials Afrikanda garnet (Salnikova et al., 2019 TIMS age 378 ± 3 Ma; our fractionation-corrected weighted mean age 382.62 ± 1.78 Ma, MSWD = 1.19, n = 17), Dashkesan garnet (Stifeeva et al., 2019 TIMS age 147 ± 2 Ma; our fractionation-corrected weighted mean age 145.7 ± 1.0 Ma, MSWD = 1.07, n = 24), and Chikskii garnet (Salnikova et al., 2018 TIMS age 492 ± 2 Ma; our fractionation-corrected weighted mean age 480.35 ± 2.25 Ma, MSWD = 1.71, n = 16) were employed after U-Pb fractionation correction and treated as unknowns. Uncertainties are fully propagated and reported at the 2σ-level here and throughout. Chikskii garnet appears to exhibit significant isotopic variation, demonstrated by its high MSWD even after outlier rejection, resulting in mismatch between the published TIMS age and our obtained age. We reproduce the published TIMS ages of the other two garnet secondary reference material ages within uncertainty. Mud Tank zircon (Black and Gulson, 1978; 736 ± 3 Ma, our age 735 ± 2.5 Ma, MSWD = 0.36, n = 14) was also run as a secondary reference material, without using a U-Pb correction factor. Further details of our analytical protocol are provided in a supplementary document (MMC1). Note that garnet reference materials were not run for the experiment in which Roberts Victor garnet was analysed. Instead, an unknown sample

from another session (BSK064) was used to check for reproducibility after a U-Pb fractionation correction from the other sessions was applied to the experiment, the result (BSK = 90 ± 8 Ma for this experiment vs 82 ± 12 Ma in the session using TIMS-dated garnet standards) was considered to be satisfactory. For Ni-in-garnet thermometry, the masses ^{29}Si, ^{60}Ni, ^{90}Zr, ^{232}Th and ^{238}U were analysed in a separate session under the same analytical conditions as above with BHVO-2G as the primary reference material with BCR-2G employed as a secondary reference material (Jochum et al., 2005). For this experiment ^{29}Si was again used as the index mass. The Trace Elements DRS for Iolite® was used for data reduction (Paton et al., 2011).

5.3 Results

Analysed garnet lack inclusions under cathodoluminescence-imaging (CL; Fig. 5.2). In each sample the concentrations of U and Zr, if displayed as a time-series, are stable throughout ablation (MMC2), indicating that U is resident in garnet itself, and not in another unobserved included phase (e.g., Zircon or rutile) that also eluded detection during CL imaging (Fig. 5.2). As further evidence that U in these garnets is not inclusion-hosted, linear and monotonic correlation between U and Zr concentration, or ^{238}U/^{206}Pb ratio and Zr concentration, are statistically insignificant (MMC2). Thus, the most credible model of U distribution in these peridotitic garnet is that it is lattice-bound at very low concentrations (c. 5 - 750 ppb). Conversely, contamination of some ablations by ^{137}Ba *was* encountered (MMC2), and we have excluded those spots from age calculations. This included most spots in sample BP002, but only a handful across the other samples. Excluded spots, including the specific reason they were excluded, are listed in the supplementary U-Pb data table (MMC1). Lastly, attempts to utilize the U-Pb system to date eclogitic garnet xenocrysts obtained from the Jagersfontein kimberlite were unsuccessful, owing to extremely low U concentrations (c. 8 ppb median U), so we will not discuss this sample any further.

Garnet major element compositions are uniform within each Bultfontein xenolith sample (BSK064; BP002; CLA13; CLA51), displaying insignificant major-element chemical variation. The major element compositions of garnet mineral separate from

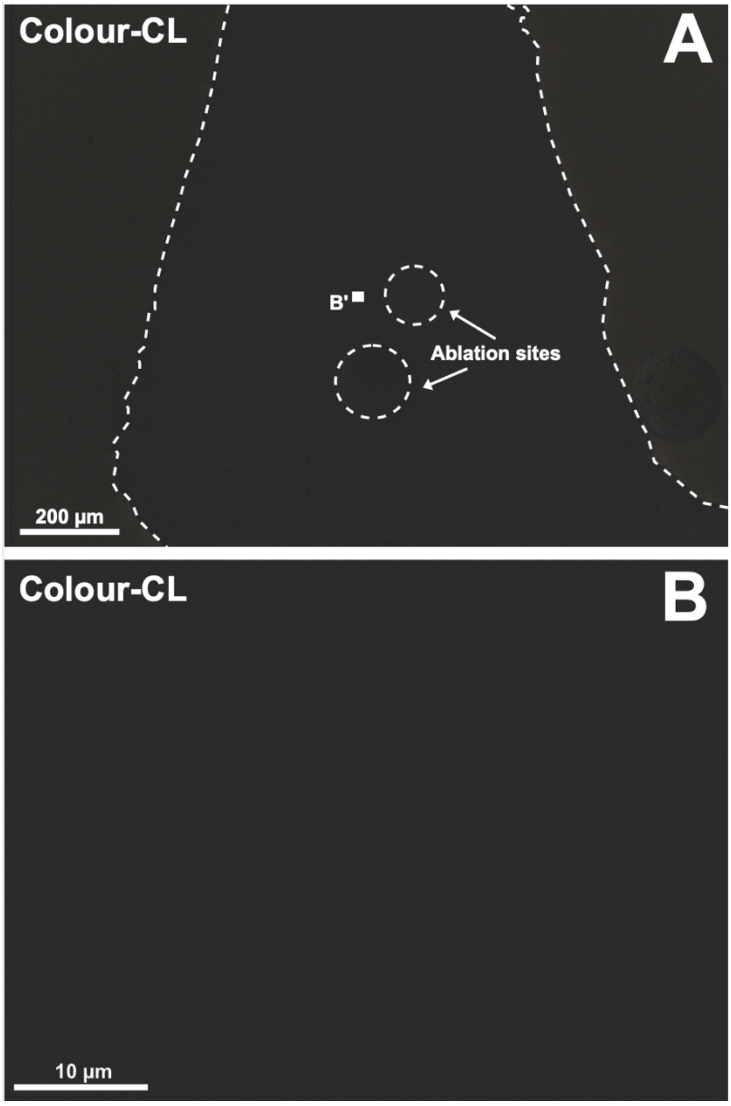

Figure 5.2: Garnet are featureless under CL, the grain analysed is highlighted by a dotted white outline (a), and a selected area on the image is zoomed-in upon in (b). Garnet does not produce a CL-response. The method highlights no features of note and the images could be considered rather uninformative; however, they serve to highlight the lack of any high CL-response inclusions (e.g. zircon) whatsoever.

Roberts Victor are more varied, as these garnets are xenocrysts hosted within the kimberlite, and thus represent a mix of material from different xenoliths of different peridotite lithologies (Fig. 5.3). Representative major element compositions for garnet xenoliths are provided in Table 5.1, and per grain for Roberts Victor separate in Table 5.2. Average Ni, Zr, U and Th concentrations are also provided. Classification of garnet separates from Roberts Victor identifies them as pyrope-rich, with a range of compositions from depleted harzburgite to fertile lherzolite (Griffin et al., 1998).

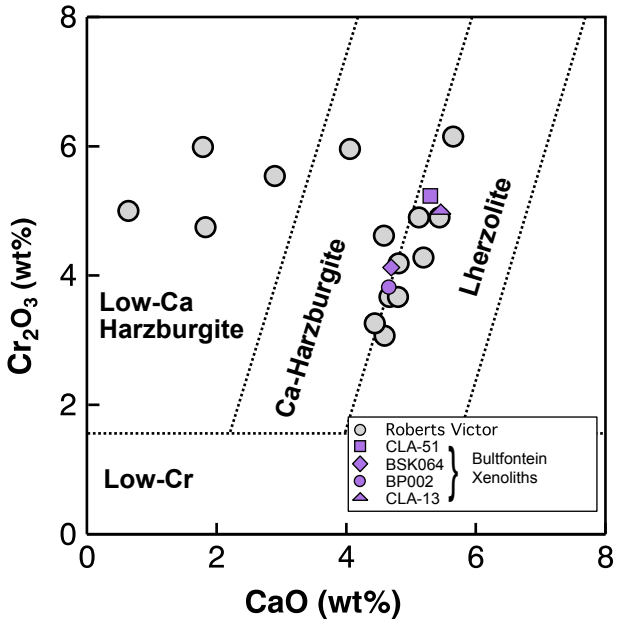

Figure 5.2: Cr_2O_3-CaO plot with fields for harzburgite, lherzolite and low-Cr garnet. After Griffin et al., (1998). No garnet plot in the low-Cr field.

Equilibration temperature was calculated using the empirical Ni-in-grt thermometer of Ryan et al (1996). The results indicate that harzburgite xenoliths from Bultfontein (BSK064; BP002; CLA51) were sampled from an extremely narrow temperature interval of 966 to 981°C. A lherzolite xenolith from Bultfontein (CLA13) is derived from higher temperature conditions, estimated at 1057°C (Table. 5.1). Temperatures calculated for xenocryst garnet from Roberts Victor garnet separate vary from 867 to 1101°C (Table 5.2). Note these temperatures represent conditions on the geotherm prior to entrainment in kimberlite melt and are unlikely to record transient heating during entrainment in kimberlite.

Bultfontein

U-Pb ages of garnet analysed from Bultfontein xenoliths are provided on Wetherill concordia on figure 5.4a. Four different xenoliths were analysed. As all xenoliths provide age information that overlap within uncertainty we present all xenolith samples simultaneously on Wetherill Concordia, yielding a more precise overall emplacement age (Fig. 5.4a). Our U-Pb garnet age for the Bultfontein kimberlite is 84.1 ± 7.1 Ma. The $^{207}Pb/^{206}Pb$ ratio of the upper intercept of this discordia is 0.895 ± 0.050 (Fig. 5.4a). Contrastingly, the $^{207}Pb/^{206}Pb$ ratio of the host kimberlite is 0.818 ± 0.002 (Kramers and Smith, 1983); kimberlite magmas in South Africa typically have radiogenic compositions of common Pb due to interaction with HIMU sources (Collerson et al., 2010). The isotopic

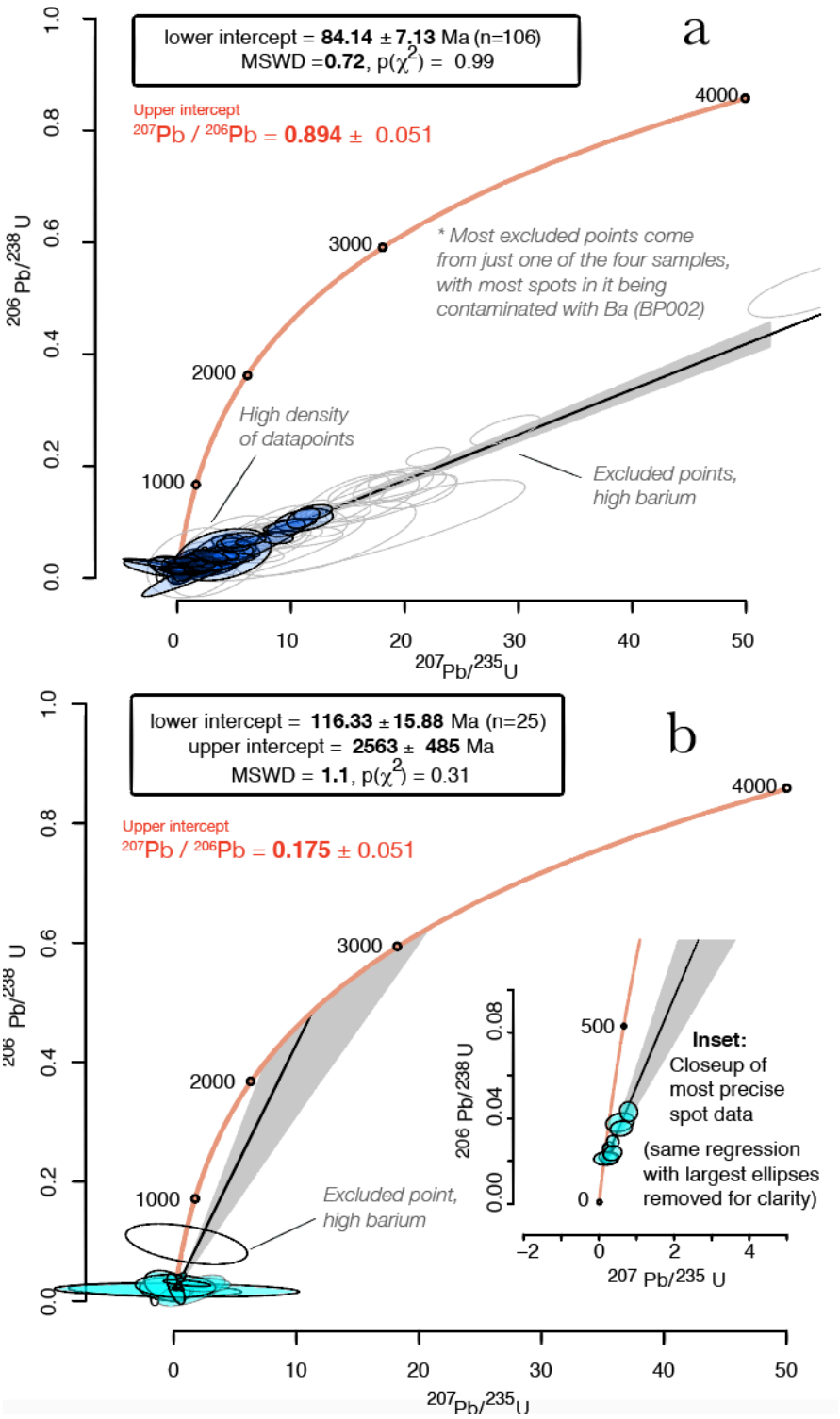

Figure 5.4: $^{207}Pb/^{206}Pb$ vs $^{206}Pb/^{238}U$ garnet U-Pb discordia ages of a) Bultfontein xenolith garnet and b) Roberts Victor garnet separate. Garnet ages are consistent with derivation from a single geological event within uncertainty. Notice the radically different upper intercepts. Age calculations employed the independently measured $^{207}Pb/^{206}Pb$ and $^{206}Pb/^{238}U$ ratios; but are here transformed for display on Wetherill concordia for convenience.

composition of common-Pb in these garnets is not within error of the host kimberlite magma, this indicates that the common-Pb hosted in xenolithic garnet is sampled from a

portion of the crystalline lower lithospheric mantle that has not interacted with a HIMU source.

Roberts Victor

U-Pb ages of garnet analysed from the Roberts Victor garnet separates are provided on Wetherill concordia on figure 4b. Our U-Pb lower intercept discordia ages for the garnet separates from Roberts Victor is 116.3 ± 15.8 Ma. A relatively imprecise upper intercept discordia age is also obtained from Roberts Victor garnet of 2563 ± 485 Ma (Fig. 5.4b).; corresponding to a highly radiogenic upper intercept $^{207}Pb/^{206}Pb$ ratio of 0.175 ± 0.051.

5.4 Discussion

Interpretation of garnet ages and comparison to previous results

Garnets from peridotite xenoliths hosted in (Group I) Bultfontein kimberlite and (Group II) Roberts Victor kimberlite yield age information that reproduce measurements from previous methods of their respective host-kimberlite emplacement ages. Our peridotitic garnet age of 84.1 ± 7.1 Ma for the Bultfontein kimberlite is in agreement with ages determined from Rb-Sr phlogopite (84 ± 0.9 Ma, MSWD unavailable; Kramers and Smith, 1983) and U-Pb zircon from peridotitic xenoliths (83.8 Ma, uncertainty and MSWD unreported; Davis, 1977). Our obtained ages are towards the younger end of the age-range reported from Rb-Sr on matrix phlogopite from kimberlite (90 + 3 Ma, MSWD unreported; Allsop and Barret, 1975), and zircon (91.8 Ma, uncertainty and MSWD unreported; Davis, 1977). Likewise, our garnet separate from Roberts Victor yields an age of 116.3 ± 15.8 Ma, which is consistent with emplacement ages previously reported from Rb-Sr phlogopite of 127 ± 3 Ma (Allsopp and Barrett, 1975) and 128 ± 15 Ma (Smith et al., 1985).

Ni-thermometry data (Tables. 5.1 and 5.2) reflect the conditions of garnet equilibration in the lithosphere prior to entrainment in erupting kimberlite. These data strongly indicate that *most* garnet (see section 5.2), including all Bultfontein garnet, was resident at ambient temperatures well above the closure temperature of the pyrope-almandine U-Pb system whilst within the lithospheric mantle. Radiogenic-Pb was consequently able to rapidly diffuse out of garnet until the garnet U-Pb system cooled below its closure temperature (a temperature thought to be in excess of 800°C; Mezger et

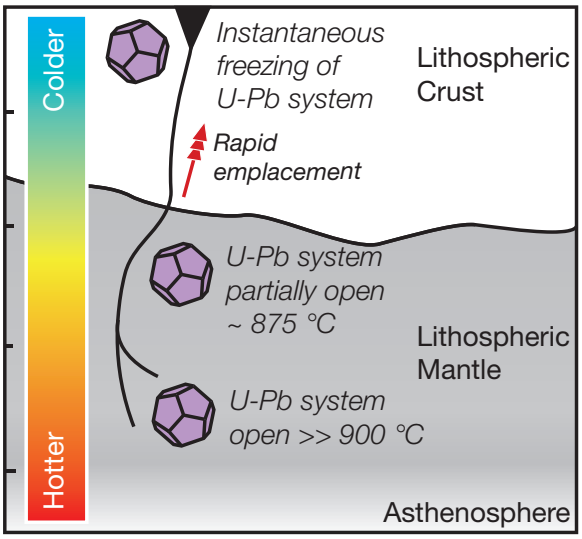

Figure 5.5: Conceptual model of the behaviour of the U-Pb system in xenolith and xenocryst pyrope-rich garnet sampled in this study. Garnet yielding low equilibration temperatures may retain some pre-emplacement age information, whereas ages of garnet sampled from very high temperatures should commonly only reflect emplacement.

al., 1989). This would have occurred at, or *en-route* to, the Earth's surface (Fig. 5.5). Open diffusion of Pb from garnet in the lithospheric mantle is supported by the contrastingly ancient > 2.5 Ga ages commonly obtained for xenoliths from the Kaapvaal Craton (and cratons worldwide) using the Lu-Hf and Re-Os methods (Pearson et al., 1995a; Lazarov et al., 2009; Shu et al., 2013). An alternative explanation for these ages, as being a product of recrystallisation of garnet *en-route* to the surface, is not a credible mechanism, as garnet compositions are clearly derived from the peridotitic mantle (Fig. 5.3). Additionally, garnet in at least one xenolith sample (BP002) formed by exsolution in equilibrium with Mg-enstatite at 4.4 GPa (Al-in-opx) and 975°C (Tomlinson et al., 2018).

Pb-isotope composition of the peridotitic garnets

In our garnet from Bultfontein xenoliths, the calculated upper $^{207}Pb/^{206}Pb$ intercept of xenolith garnet lie on a mixing line towards compositions that are typical for lower lithospheric common-Pb. Contrastingly, upper intercept Pb ratios in garnet xenocryst separates from Roberts Victor are highly radiogenic, with an upper $^{207}Pb/^{206}Pb$ intercept ratio of c. 0.17, corresponding to an ancient upper intercept age of 2560 ± 490 Ma (Fig. 5.4b). Ni-in-Grt thermometry for Roberts Victor separate indicates ambient temperatures before emplacement as low as 870°C (Table. 5.2), lower than at Bultfontein where xenolith temperatures are all in excess of 950°C. These differences may relate to different depth ranges for sampling of material. Lower temperatures may have facilitated the retention of some ancient radiogenic Pb in colder garnet sampled by the Roberts Victor kimberlite vs

hotter garnet sampled by Bultfontein kimberlite (Fig. 5.5). Previous estimates for the activation of diffusion of Pb in the almandine-pyrope system place it at temperatures > 800 °C (Mezger et al., 1989). Further study of peridotitic garnet will be required to determine whether it is a diffusion-controlled thermochronometer at ambient mantle temperatures. Regardless of the relationship between temperature and age, geologically, the obtained Roberts Victor garnet separate upper-intercept age (2560 ± 490 Ma) could be linked to the stabilization of the eastern and western blocks of the Kaapvaal craton in the Archean. This is supported by a ~ 2.9 Ga garnet Lu-Hf isochron age is obtained from mantle peridotites from Roberts Victor (Shu et al., 2013) which coincides with the collision of the eastern and western terranes of the Kaapvaal along the Colesberg lineament between 2.93 and 2.88 Ga (Schmitz et al., 2004). This age is also consistent with mantle depletion during the stabilization of the sub-cratonic lithosphere in the Archean. Such events occurred in the western block of the Kaapvaal as late as ~ 2.6 Ga (Lazarov et al., 2009).

Advantages and potential applications of U-Pb dating for mantle garnet

Pyrope-rich peridotitic garnet is a common constituent of the lithospheric mantle (5 to 10 % modal abundance in garnet-bearing xenoliths; Tomlinson et al., 2018), is easy to chemically differentiate from crustal garnet, has an analytically convenient grain size (individual grains are typically half a cm in size, much larger than required for ablation), and is relatively resistant to weathering (though not to deep burial diagenesis; Morton and Hallsworth, 1999). Peridotitic garnet sourced by kimberlites is already used to track mineral detritus derived from kimberlite provinces (e.g. Grütter et al., 2004) and could now be further identifiable to specific kimberlite fields by their single-grain U-Pb ages. U-Pb dating of peridotitic garnet may thus constitute a useful mining vector in diamond exploration.

As pyrope-rich garnet is not a rare component in xenoliths, U-Pb dating of pyrope-rich garnet should be applicable globally, and there are several possible research avenues for future work. Firstly, as demonstrated at Roberts Victor, it is possible that U-Pb dates from pyrope-rich garnet may not always characterise emplacement ages, as garnet resident at lower ambient temperatures (~ 900 °C), presumably at shallower mantle depths, may preserve older ages dependent on the thermal conditions of the lithosphere since its formation (Fig. 5.4). Secondly, it should also be possible to double-date peridotitic garnet (using Sm-Nd and/or Lu-Hf in concert with U-Pb) to reveal the formation and metasomatism of the Earth's sub-continental lithospheric mantle. Lastly, it may be possible

to obtain the age at which peridotitic garnet hosted in diamond inclusions were included by their host diamond. Retention of inclusion ages would rely on garnet having no communication with the surrounding environment after inclusion by diamond, a reasonable assumption, as diamond is shown to have among the slowest diffusivities of any solid material measured (Koga et al., 2005). Dating of such ancient garnet may be possible using smaller spot sizes than we have employed here, due to the longer timescales over which radiogenic Pb could accumulate.

5.5 Conclusions

- U-Pb dating of garnet from Earth's mantle is made possible using available TIMS-dated garnet standards and very large laser ablation spots (130 μm). Mantle garnet yields emplacement ages for entraining kimberlite magmas, as garnet lower-intercept ages are likely thermally controlled, mostly being above the closure of the U-Pb system in garnet at ambient mantle temperatures. Despite low U concentrations, on the order of 5 – 750 ppb, the ratio of radiogenic to common Pb in peridotitic garnet is very high, which aids their precise dating.
- The calculated initial isotopic composition of Pb in garnet from the mantle sampled by the Roberts Victor kimberlite is extremely radiogenic, yielding an ancient (c. 2560 Ma) upper-intercept age. Contrastingly, samples of garnet from xenoliths hosted in a kimberlite at Bultfontein yield calculated initial $^{207}Pb/^{206}Pb$ isotope compositions typical for cratonic common Pb, and which do not match the Pb-isotopic composition of the host kimberlite. This indicates that garnet from Roberts Victor may partially retain radiogenic Pb accumulated since they last communicated with the surrounding lithospheric mantle in the Archean. The temperatures of Roberts Victor garnet retaining significant ancient Pb (~ 850 °C) correspond to previous estimates (Mezger et al. 1989) of the activation temperature of Pb in the almandine-pyrope system (> 800 °C),and are lower than temperatures of garnet hosting no ancient radiogenic Pb in xenoliths sampled by the Bultfontein kimberlite (> 950 °C), where diffusion must have been rapid.
- An attempt to use eclogitic garnet from Jagersfontein for U-Pb dating was not successful, as the concentrations of uranium (c. 8 ppb) and its daughter products were too low to precisely determine U-Pb ratios. Tentatively, this may point to peridotitic garnet being an inherently better target for garnet U-Pb dating than eclogitic garnet.

- Potential applications of pyrope U-Pb dating may include its use as a detrital kimberlite exploration tool and to provide diamond-formation ages, though proof of concept is still required for this use of the method described here. The method could also be applied to any igneous rocks containing garnet xenoliths.

Tables

	BP002 (n= 11)		CLA-13 (n= 9)		CLA-51 (n= 19)		BSK064 (n= 12)	
SiO_2	41.97 ±	0.15	41.48 ±	0.13	41.83 ±	0.17	42.24 ±	0.12
TiO_2	LOD		LOD		LOD		LOD	
Al_2O_3	21.22 ±	0.17	19.96 ±	0.11	19.88 ±	0.19	20.94 ±	0.16
Cr_2O_3	3.82 ±	0.23	4.99 ±	0.1	5.23 ±	0.18	4.13 ±	0.2
MgO	21.35 ±	0.11	20.14 ±	0.13	21.04 ±	0.11	22.03 ±	0.11
FeO	6.43 ±	0.05	7.24 ±	0.05	6.7 ±	0.04	6.33 ±	0.04
MnO	0.24 ±	0.01	0.27 ±	0.02	0.25 ±	0.02	0.23 ±	0.01
CaO	4.66 ±	0.07	5.46 ±	0.05	5.3 ±	0.07	4.71 ±	0.06
Total	99.69		99.55		100.22		100.61	
Ni (ppm)	41 ±	2.3	54.1 ±	3.2	40.3 ±	2	42.5 ±	1
T (°C)	971 ±	17	1057 ±	20	966 ±	15	981 ±	7
Th (ppm)	0.075 ±	0.068	0.014 ±	0.009	0.016 ±	0.015	0.063 ±	0.068
U (ppm)	0.076 ±	0.027	0.059 ±	0.015	0.038 ±	0.011	0.086 ±	0.017
Zr (ppm)	67.6 ±	2.1	20.4 ±	5.7	59 ±	10	66.6 ±	1.6

Table. 5.1: Representative major (SEM-EDX) and trace element (LA-Q-ICPMS). LOD = below limits of detection.

Grain: (RV-)	9	10	12	13	14	16	19	20	22	25	27	31	33	37	39
SiO_2	41.84	41.84	41.39	41.86	41.31	41.93	41.86	41.65	41.52	41.18	41.48	41.39	41.54	42.25	41.56
TiO_2	0.18	LOD	0.18	0.42	0.08	LOD	LOD	0.17	0.08	0.22	0.17	0.15	0.25	LOD	LOD
Al_2O_3	21.77	21.54	20.22	21.22	19.84	21.18	20.09	20.63	21.73	19.73	20.37	20.75	20.9	21.16	19.61
Cr_2O_3	3.26	3.67	4.9	3.67	5.96	4.75	5.99	4.62	3.07	5.54	4.9	4.28	4.19	5	6.15
MgO	20.86	20.68	20.31	21.41	20.73	23.5	22.98	20.76	19.83	20.16	19.63	20.16	20.08	24.31	20.4
FeO	7.62	7.4	7.38	6.61	7.36	6.47	6.88	7.2	8.81	9.91	7.65	7.68	7.96	6.5	6.65
MnO	0.36	0.32	0.31	0.3	0.44	0.32	0.36	0.35	0.35	0.39	0.37	0.31	0.36	0.32	0.3
CaO	4.44	4.8	5.12	4.67	4.06	1.83	1.79	4.58	4.59	2.9	5.44	5.19	4.81	0.64	5.65
Total	100.33	100.25	99.82	100.16	99.78	99.98	99.96	99.96	99.99	100.02	100.02	99.92	100.1	100.18	100.33
#Mg	79.1	79.5	79.2	81.7	79.6	83.4	82.2	79.9	75.7	73.8	78	78.4	77.7	83.8	80 .9
Ni (ppm)	35.5	28	48.3	55	30.8	NA	28.6	31.1	34	28	27.8	61.4	32.8	30.8	36.8
2SE	1.2	1.1	2.3	1.9	1.5	NA	1.3	1.5	1.3	1.5	1.5	3.1	1.6	1.4	3.5
T (°C)	930	868	1020	1063	892	NA	874	895	918	868	867	1101	909	892	940
Th (ppb)	16.4	119.8	6	8.8	26	NA	62.5	14.8	7.5	70.1	160	15.7	6.6	31.6	21.2
2SE	2.1	6.3	1.3	1.6	2.7	NA	4.1	2	2	3.8	12	1.7	1.2	3.3	3.2
U (ppb)	49.2	340	18.4	18.4	63.1	NA	87	30.4	28.2	115.6	152.7	24.6	25.3	97.6	35
2SE	2.4	14	1.2	1.1	3.2	NA	4	2	1.7	5.5	9.1	1.5	1.4	4.8	4.1
Zr (ppm)	17.52	4.52	18.77	31.5	121.8	NA	7.56	29.8	15.43	19.79	42.3	27	19.6	1.814	5.04
2SE	0.6	0.19	0.79	1.2	5.6	NA	0.34	1.5	0.57	0.97	2.1	1.4	0.83	0.08	0.46

Table. 5.2: Major (SEM-EDX, in oxide Wt%) and trace element (LA-Q-ICPMS) concentrations and Ni-in-grt thermometry (Ryan et al., 1996) for each garnet analysed in Roberts Victor garnet separate. LOD = below limits of detection.

Acknowledgements

The Authors would like to thank Paul Guyett and Cora McKenna for their assistance during analysis and maintenance of lab facilities to an exceptional standard; Clare Stead and Balz S. Kamber for providing the sample materials and additionally for several productive conversations; and David M. Chew for helping us to develop our ideas. GO'S[1] thanks J. Stephen Daly for his mentorship. Lastly, we warmly thank Ekaterina Salnikova and Maria Stifeeva (Institute of Precambrian Geology and Geochronology, St. Petersburg, Russian Federation) for supplying the garnet reference materials.

Funding

This project has received support from two Irish Research Council grants: a *Government of Ireland Postdoctoral Fellowship* held by GJO'S (GOIPD/2019/906), and a *Government of Ireland Postgraduate Scholarship* held by BCH (GOIPG/2017/1132). CM is supported by a *Starting Investigator Research Grant* from Science Foundation Ireland (18/SIRG/5559). The iCRAG geochronology facility is supported by SFI award 13/RC/2092.

Supplemental information

Supplemental data MMC1 and MMC2 are provided below:

Grain	U-Pb fractionation correction factor	207/235 ratio	Prop 2SE	206/238 ratio	Prop 2SE	Rho 6/38 vs 7/35	238/206 ratio	Prop 2SE	207/206 ratio	Prop 2SE	Rho 38/6 vs 7/6	Rejected from discordia = x	Rejection Reason
CLA13_1	1.0725	1.4679	1.0092	0.0229	0.0101	-0.1280	43.60	19.18	0.80	0.69	-0.0306		
CLA13_2	1.0725	1.3394	0.7798	0.0236	0.0089	-0.3149	42.41	16.01	-0.25	0.91	0.8737		
CLA13_3	1.0725	0.2110	0.3394	0.0124	0.0044	-0.0563	80.74	28.71	0.22	0.33	0.1962		
CLA13_4	1.0725	0.3394	0.3945	0.0184	0.0050	-0.2510	54.23	14.84	0.30	0.44	0.5137		
CLA13_5	1.0725	0.4862	0.4404	0.0184	0.0045	0.0849	54.23	13.22	0.24	0.34	0.5026		
CLA13_6	1.0725	0.3394	0.6330	0.0136	0.0056	-0.1434	73.65	30.36	0.31	0.73	0.1998		
CLA13_7	1.0725	0.3670	0.3853	0.0143	0.0060	-0.3001	69.87	29.11	0.21	0.67	0.4241		
CLA13_8	1.0725	0.2936	0.2936	0.0158	0.0043	-0.1446	63.37	17.32	0.27	0.24	0.2795		
CLA13_9	1.0725	0.3119	0.3486	0.0162	0.0060	0.2752	61.58	22.61	0.21	0.24	0.2294		
CLA13_10	1.0725	0.6422	0.4312	0.0194	0.0049	-0.0391	51.66	12.98	0.01	0.28	0.2368		
CLA13_11	1.0725	0.6330	0.3761	0.0206	0.0061	-0.1199	48.66	14.34	0.19	0.37	0.3870		
CLA13_12	1.0725	0.8991	0.5138	0.0204	0.0051	0.0556	49.10	12.39	0.39	0.31	-0.1713		
CLA13_13	1.0725	0.1743	0.3394	0.0129	0.0039	-0.2611	77.30	23.03	0.12	0.53	0.5291		
CLA13_14	1.0725	0.2569	0.4220	0.0147	0.0047	-0.0399	68.13	21.71	0.01	0.51	0.2438		
CLA13_15	1.0725	0.0642	0.2569	0.0138	0.0043	0.0853	72.67	22.77	-0.11	0.28	0.0030		
CLA13_16	1.0725	0.1560	0.3028	0.0144	0.0046	-0.0659	69.43	22.11	-0.07	0.33	-0.1365		
CLA13_17	1.0725	1.9541	0.8624	0.0339	0.0092	-0.1020	29.46	7.96	0.71	0.59	0.0461		
CLA13_18	1.0725	1.3211	0.4679	0.0286	0.0064	-0.1039	34.94	7.84	0.21	0.25	0.4523		
CLA13_19	1.0725	2.3670	0.6147	0.0297	0.0041	0.0527	33.64	4.67	0.74	0.27	0.8424		
CLA13_20	1.0725	0.7615	0.3578	0.0199	0.0058	0.0809	50.23	14.58	1.05	0.65	0.0591		
CLA13_21	1.0725	0.0917	0.2569	0.0161	0.0044	0.0498	62.29	17.08	-0.01	0.24	0.0691		
CLA13_22	1.0725	0.4954	0.4862	0.0150	0.0050	-0.3662	66.46	21.88	-0.06	0.55	0.5849		
CLA13_23	1.0725	0.6881	0.4220	0.0194	0.0054	0.2252	51.66	14.44	-0.01	0.28	0.1935		
CLA13_24	1.0725	0.1835	0.3578	0.0117	0.0050	0.0184	85.83	37.17	0.13	0.51	0.1666		
CLA13_25	1.0725	0.5596	0.4862	0.0140	0.0048	0.1314	71.24	24.21	0.27	0.48	0.1157		
CLA13_26	1.0725	0.7156	0.5413	0.0190	0.0059	-0.1725	52.66	16.28	0.78	0.64	0.3546		
CLA13_27	1.0725	1.3119	0.4037	0.0258	0.0060	0.4531	38.79	8.97	0.69	0.3	0.7613		
CLA13_28	1.0725	2.5505	0.8991	0.0408	0.0072	-0.2216	24.49	4.29	0.67	0.29	0.5793		
CLA13_29	1.0725	5.2294	1.2844	0.0679	0.0110	0.1317	14.73	2.39	0.59	0.15	0.3872		
CLA13_30	1.0725	0.8624	0.4679	0.0230	0.0038	0.3217	43.43	7.09	0.23	0.16	0.3673		
CLA13_31	1.0725	0.3211	0.3394	0.0149	0.0036	0.1276	67.28	16.20	0.19	0.24	0.4248		

Grain	U-Pb fractionation correction factor	207/235 ratio	Prop 2SE	206/238 ratio	Prop 2SE	Rho 6/38 vs 7/35	238/206 ratio	Prop 2SE	207/206 ratio	Prop 2SE	Rho 38/6 vs 7/6	Rejected from discordia = x	Rejection Reason
CLA13_32	1.0725	2.8165	0.5229	0.0388	0.0067	0.1194	25.77	4.45	0.56	0.13	0.5323	x	High Ba CPS
BSK064_2	1.0725	2.4312	0.4128	0.0332	0.0046	-0.0277	30.11	4.16	0.59	0.13	0.6307		
BSK064_3	1.0725	0.1651	0.3028	0.0172	0.0047	-0.0503	58.29	15.90	0.12	0.18	-0.1014		
BSK064_4	1.0725	0.3578	0.2936	0.0146	0.0037	-0.1788	68.55	17.25	0.33	0.33	0.1028		
BSK064_5	1.0725	0.2661	0.3028	0.0153	0.0042	-0.0353	65.27	17.98	0.05	0.32	0.3999		
BSK064_6	1.0725	0.4128	0.3670	0.0149	0.0048	0.2009	67.28	21.60	0.14	0.35	0.1477		
BSK064_7	1.0725	0.2202	0.2385	0.0131	0.0053	0.2673	76.22	30.92	0.01	0.3	0.1041		
BSK064_8	1.0725	3.6697	1.3761	0.0394	0.0092	0.4875	25.35	5.90	0.54	0.32	0.7781		
BSK064_9	1.0725	1.6606	0.5688	0.0261	0.0049	0.1954	38.25	7.11	0.48	0.19	0.1383		
BSK064_10	1.0725	6.6055	1.1927	0.0669	0.0072	0.3820	14.95	1.60	0.70	0.11	0.2299		
BSK064_11	1.0725	0.3211	0.2661	0.0168	0.0041	-0.1456	59.56	14.65	0.52	0.44	0.6613		
BSK064_12	1.0725	0.2202	0.3761	0.0166	0.0047	-0.2058	60.22	16.97	0.29	0.36	0.6316		
BSK064_13	1.0725	1.7431	0.4954	0.0298	0.0065	0.4727	33.54	7.33	0.47	0.11	-0.3147		
BSK064_14	1.0725	1.5688	0.5138	0.0282	0.0055	0.1001	35.50	6.94	0.55	0.26	0.7605		
BSK064_15	1.0725	8.2569	1.1927	0.0713	0.0081	-0.1093	14.03	1.59	0.89	0.16	0.6691		
BSK064_16	1.0725	28.8991	2.5688	0.2642	0.0220	0.5829	3.78	0.32	0.79	0.053	0.3424	x	High Ba CPS
BSK064_17	1.0725	10.5505	2.0183	0.1037	0.0165	0.0898	9.65	1.54	0.78	0.15	0.4509		
BSK064_18	1.0725	0.2569	0.2569	0.0148	0.0040	-0.0958	67.70	18.50	0.22	0.28	-0.0002		
BSK064_19	1.0725	0.3028	0.3028	0.0192	0.0051	-0.0379	52.15	13.97	0.19	0.18	0.1383		
BSK064_20	1.0725	0.5963	0.2936	0.0189	0.0048	0.0825	52.91	13.36	0.31	0.21	0.3109		
BSK064_21	1.0725	4.4587	0.9083	0.0450	0.0110	0.5141	22.24	5.45	0.86	0.22	0.6638		
BSK064_22	1.0725	9.7248	1.6514	0.0945	0.0101	0.7456	10.58	1.13	0.76	0.11	-0.1406		
BSK064_23	1.0725	5.0459	1.3761	0.0596	0.0092	0.0739	16.77	2.58	0.60	0.18	0.5882		
BSK064_24	1.0725	9.4495	1.6514	0.0899	0.0128	0.3218	11.12	1.59	0.77	0.12	0.5367		
BSK064_25	1.0725	56.1468	5.4128	0.5165	0.0413	0.6687	1.94	0.15	0.79	0.05	0.2611	x	High Ba CPS
BSK064_26	1.0725	11.5596	1.2844	0.1174	0.0110	0.4508	8.52	0.80	0.74	0.083	0.3961		
BSK064_27	1.0725	0.4128	0.3578	0.0176	0.0044	0.2610	56.77	14.19	0.27	0.19	0.5679		
BSK064_28	1.0725	21.8349	1.6514	0.2165	0.0138	0.4739	4.62	0.29	0.74	0.049	0.3953	x	High Ba CPS
BSK064_29	1.0725	10.9174	1.4679	0.1073	0.0147	0.4026	9.32	1.27	0.75	0.098	0.6860		
BSK064_30	1.0725	2.6422	0.7982	0.0320	0.0053	0.2406	31.23	5.19	0.64	0.27	0.7613		
BSK064_31	1.0725	1.3853	0.6422	0.0244	0.0067	0.6604	40.98	11.25	0.43	0.29	0.4064		
BSK064_32	1.0725	1.8349	0.5413	0.0259	0.0053	0.0278	38.65	7.95	0.70	0.29	0.1976		
BSK064_33	1.0725	17.5229	1.3761	0.1743	0.0119	0.4199	5.74	0.39	0.77	0.056	0.4029	x	High Ba CPS

Grain	U-Pb fractionation correction factor	207/235 ratio	Prop 2SE	206/238 ratio	Prop 2SE	Rho 6/38 vs 7/35	238/206 ratio	Prop 2SE	207/206 ratio	Prop 2SE	Rho 38/6 vs 7/6	Rejected from discordia = x	Rejection Reason
BSK064_34	1.0725	0.2661	0.3303	0.0121	0.0032	0.0798	82.58	21.90	0.13	0.28	-0.0510		
CLA51_1	1.09	0.8298	0.7086	0.0177	0.0103	0.0803	56.45	52.55	0.29	0.34	0.5087		
CLA51_2	1.09	1.4172	0.7832	0.0218	0.0070	0.2783	45.83	32.18	0.58	0.36	0.4591		
CLA51_3	1.09	0.8578	0.6340	0.0200	0.0075	0.0097	50.12	43.97	0.37	0.29	0.5392		
CLA51_4	1.09	2.4242	1.6783	0.0373	0.0093	0.4405	26.81	17.16	0.75	0.44	0.4293		
CLA51_5	1.09	0.6620	0.4476	0.0177	0.0057	-0.0489	56.45	34.32	0.31	0.38	0.4918		
CLA51_6	1.09	0.8858	0.7273	0.0205	0.0131	0.4476	48.75	61.13	0.27	0.42	0.2374		
CLA51_7	1.09	0.8205	0.9138	0.0164	0.0050	0.0591	60.94	18.23	0.21	0.3	0.0851		
CLA51_8	1.09	0.5221	0.5594	0.0173	0.0074	-0.0786	57.66	42.90	0.24	0.45	0.3845		
CLA51_9	1.09	0.1399	0.5128	0.0144	0.0069	-0.1312	69.64	61.13	-0.07	0.4	0.4378		
CLA51_10	1.09	1.1096	0.7086	0.0216	0.0062	0.0700	46.23	20.38	0.39	0.21	-0.0611		
CLA51_11	1.09	0.7273	0.5781	0.0189	0.0074	-0.1322	52.83	37.54	0.35	0.3	0.1914		
CLA51_12	1.09	0.6713	0.7086	0.0162	0.0085	-0.0679	61.64	47.19	-0.80	0.75	0.2058		
CLA51_13	1.09	0.7459	0.7179	0.0197	0.0080	0.2142	50.83	40.76	-0.13	0.59	0.1748		
CLA51_14	1.09	0.8765	0.5874	0.0167	0.0075	-0.1676	59.92	39.68	0.42	0.45	0.5004		
CLA51_15	1.09	1.3054	1.0256	0.0220	0.0066	-0.1786	45.44	36.47	0.61	0.6	0.4849		
CLA51_16	1.09	1.3054	1.2121	0.0183	0.0070	-0.1191	54.72	41.83	0.90	0.95	0.3247		
CLA51_17	1.09	0.6620	0.5408	0.0174	0.0052	-0.2687	57.35	30.03	0.35	0.44	0.3713		
CLA51_18	1.09	0.6434	0.5315	0.0131	0.0061	0.2971	76.61	35.39	0.07	0.39	0.4508		
CLA51_20	1.09	3.5431	1.4918	0.0420	0.0093	0.2914	23.83	17.16	0.57	0.35	0.5367		
CLA51_21	1.09	11.0956	2.8904	0.0848	0.0205	0.3378	11.79	10.30	1.36	0.61	0.5028	x	High Ba CPS
CLA51_22	1.09	3.3566	1.1189	0.0336	0.0076	0.4014	29.79	13.94	0.84	0.48	0.5722		
CLA51_23	1.09	0.7273	0.5408	0.0149	0.0050	-0.0654	67.03	32.18	0.05	0.51	0.2627		
CLA51_24	1.09	0.4196	0.4196	0.0146	0.0051	-0.0667	68.31	41.83	0.00	0.35	0.3910		
CLA51_25	1.09	0.2424	0.4476	0.0175	0.0048	0.4393	57.05	25.74	0.17	0.18	-0.0899		
CLA51_26	1.09	0.9417	0.5967	0.0185	0.0055	-0.1778	54.17	30.03	0.07	0.39	0.5327		
CLA51_27	1.09	1.9580	1.2121	0.0224	0.0140	0.1765	44.69	27.89	0.36	0.39	0.4536		
CLA51_28	1.09	0.2984	0.9231	0.0200	0.0074	-0.1973	49.88	27.89	0.09	0.4	0.0637		
CLA51_29	1.09	0.9883	0.5781	0.0193	0.0081	0.2840	51.81	31.10	0.08	0.36	0.4052		
CLA51_30	1.09	1.0163	0.6900	0.0206	0.0060	-0.2686	48.53	30.03	0.02	0.76	0.4878		
CLA51_31	1.09	0.2145	0.4476	0.0176	0.0060	-0.1041	56.75	30.03	0.08	0.26	0.2701		
CLA51_33	1.09	4.3823	1.3986	0.0420	0.0121	0.0917	23.83	21.45	0.70	0.71	0.6087		
CLA51_34	1.09	1.1841	0.8019	0.0196	0.0103	0.3357	51.07	35.39	0.01	0.42	0.2956		

Grain	U-Pb fractionation correction factor	207/235 ratio	Prop 2SE	206/238 ratio	Prop 2SE	Rho 6/38 vs 7/35	238/206 ratio	Prop 2SE	207/206 ratio	Prop 2SE	Rho 38/6 vs 7/6	Rejected from discordia = x	Rejection Reason
CLA51_35	1.09	0.5221	0.4848	0.0172	0.0059	-0.2208	58.29	37.54	0.28	0.34	0.2914		
CLA51_36	1.09	3.3566	1.0256	0.0364	0.0149	-0.2966	27.50	42.90	0.88	0.37	0.5246		
CLA51_37	1.09	1.6317	0.6993	0.0272	0.0075	0.0403	36.73	25.74	0.47	0.36	0.6317		
BP002d_1	1.09	1.8462	0.8765	0.0231	0.0059	-0.2057	43.25	23.60	0.75	0.41	0.8411		
BP002d_2	1.09	1.9767	0.7739	0.0330	0.0074	-0.1518	30.30	13.94	0.71	0.32	0.4763		
BP002d_3	1.09	1.9394	0.5594	0.0401	0.0112	0.2372	24.94	7.72	0.42	0.13	0.8585		
BP002d_4	1.09	4.6620	0.9324	0.0578	0.0103	0.2118	17.30	3.22	0.59	0.14	0.8373	x	
BP002d_5	1.09	0.7739	0.4382	0.0207	0.0089	0.0822	48.31	49.34	0.37	0.35	0.4049		
BP002d_6	1.09	1.3706	0.6154	0.0225	0.0061	0.0176	44.50	22.52	0.48	0.43	0.7552		
BP002d_8	1.09	4.1958	1.5851	0.0392	0.0186	0.2181	25.54	38.61	0.74	0.97	0.7703		
BP002d_9	1.09	7.2727	1.9580	0.0718	0.0186	0.0565	13.93	10.73	1.31	0.74	0.7550	x	
BP002d_10	1.09	14.7319	2.4242	0.1361	0.0242	0.0863	7.35	2.15	0.93	0.18	0.0847	x	
BP002d_11	1.09	10.9091	1.3054	0.1166	0.0140	0.2156	8.58	1.39	0.70	0.083	0.3997	x	High Ba CPS
BP002d_12	1.09	12.6807	1.4918	0.1175	0.0121	0.1119	8.51	1.07	0.89	0.14	0.4630		
BP002d_13	1.09	10.0699	1.3986	0.1044	0.0159	0.6006	9.58	1.61	0.81	0.13	0.5088		
BP002d_14	1.09	8.2051	2.7040	0.0811	0.0177	0.2985	12.33	3.11	0.76	0.21	0.2043	x	High Ba CPS
BP002d_15	1.09	8.0186	1.7716	0.0690	0.0103	0.2972	14.49	3.54	0.89	0.21	0.3549		
BP002d_17	1.09	3.4499	1.3054	0.0410	0.0103	0.0072	24.37	7.19	0.69	0.28	0.7440		
BP002d_19	1.09	13.8928	2.8904	0.1389	0.0233	0.4009	7.20	1.93	0.77	0.15	0.5929		
BP002d_20	1.09	15.1981	2.6107	0.1427	0.0252	0.6237	7.01	1.72	0.87	0.17	0.6100		
BP002d_21	1.09	5.2214	1.5851	0.0643	0.0103	-0.1106	15.54	3.54	0.53	0.14	0.7288		
BP002d_22	1.09	6.6200	2.7972	0.0755	0.0280	0.6955	13.24	7.72	0.67	0.22	0.4548	x	High Ba CPS
BP002d_23	1.09	1.7716	0.7925	0.0319	0.0073	0.1287	31.36	11.80	0.45	0.22	0.1401		
BP002d_24	1.09	7.2727	1.2121	0.0774	0.0093	0.2226	12.92	1.82	0.77	0.17	0.2236		
BP002d_25	1.09	7.7389	1.8648	0.0802	0.0103	-0.2847	12.47	2.15	0.76	0.26	0.7036	x	
BP002d_26	1.09	5.5012	1.4918	0.0578	0.0177	0.1682	17.30	12.87	1.29	0.5	0.7946		
BP002d_27	1.09	4.1026	1.2121	0.0466	0.0103	0.2862	21.45	7.19	0.80	0.69	0.6940		
BP002d_29	1.09	10.6294	1.7716	0.0988	0.0149	-0.1158	10.12	2.04	0.92	0.24	0.7916		
BP002d_30	1.09	1.1189	0.9324	0.0184	0.0079	0.3590	54.44	51.48	0.52	0.5	0.0215		
BP002d_31	1.09	1.2401	0.9044	0.0213	0.0081	0.3691	47.04	46.12	0.56	0.5	-0.0773	x	
BP002d_32	1.09	4.1119	0.7739	0.0450	0.0072	0.1516	22.20	4.61	0.76	0.18	0.7929	x	
BP002d_33	1.09	3.1235	0.8951	0.0334	0.0065	0.2879	29.96	5.90	0.77	0.2	0.5781		
BP002d_34	1.09	17.4359	1.9580	0.1566	0.0214	0.3850	6.38	1.07	0.96	0.17	0.6157		

Grain	U-Pb fractionation correction factor	207/235 ratio	Prop 2SE	206/238 ratio	Prop 2SE	Rho 6/38 vs 7/35	238/206 ratio	Prop 2SE	207/206 ratio	Prop 2SE	Rho 38/6 vs 7/6	Rejected from discordia = x	Rejection Reason
BP002d_35	1.09	17.4359	2.7972	0.1613	0.0214	0.3311	6.20	1.03	0.83	0.15	0.1279	x	
BP002d_36	1.09	7.9254	3.7296	0.0737	0.0205	-0.0451	13.58	3.11	0.89	0.44	0.2043	x	
BP002d_37	1.09	0.8578	0.4848	0.0270	0.0121	-0.0602	36.98	69.71	0.40	1	0.4944		
BP002d_38	1.09	1.0070	0.5967	0.0249	0.0064	0.2268	40.17	21.45	0.29	0.26	-0.0881		
BP002d_39	1.09	0.8112	0.6154	0.0191	0.0070	-0.1913	52.32	63.28	0.31	0.38	0.3895		
BP002d_41	1.09	6.5268	1.2121	0.0774	0.0112	0.0887	12.92	3.11	0.69	0.13	0.0263	x	High Ba CPS
BP002d_42	1.09	7.0862	1.6783	0.0662	0.0131	-0.0612	15.11	4.50	0.91	0.28	-0.0639	x	
BP002d_43	1.09	1.3893	0.9044	0.0249	0.0067	0.1182	40.17	21.45	0.52	0.29	0.3616		
BP002d_44	1.09	5.1282	2.4242	0.0559	0.0159	0.2865	17.88	5.15	0.67	0.37	0.8691		
BP002d_45	1.09	17.1562	1.9580	0.1660	0.0214	0.2141	6.03	0.92	0.83	0.12	0.4854	x	High Ba CPS
BP002d_46	1.09	0.9510	0.8205	0.0168	0.0052	0.1449	59.58	26.81	0.65	0.57	0.2890		
BP002d_47	1.09	2.4336	0.7646	0.0252	0.0075	0.1110	39.72	20.38	0.79	0.73	0.8528		
BP002d_48	1.09	7.0862	1.0256	0.0662	0.0121	0.2251	15.11	6.22	0.96	0.32	0.7321		
BP002d_49	1.09	8.7646	1.9580	0.0979	0.0112	-0.1826	10.21	1.05	0.69	0.16	0.4129	x	High Ba CPS
BP002d_50	1.09	3.0769	1.1189	0.0309	0.0077	0.0688	32.40	7.61	0.63	0.32	0.2443		
RV_9	1.08125	1.8497	1.8497	0.0555	0.0194	-0.2015	18.02	6.31	-3.30	1.4	0.2359	x	Reverse Disc.
RV_12	1.08125	0.6474	1.0173	0.0185	0.0091	0.0834	54.06	26.49	-0.60	2.2	0.1584		
RV_13	1.08125	0.4624	1.3873	0.0180	0.0092	-0.1260	55.45	28.15	0.10	3.3	0.2226		
RV_16	1.08125	3.6994	2.0347	0.0953	0.0277	0.2437	10.50	3.06	0.08	0.32	0.5160	x	High Ba CPS
RV_19	1.08125	0.3514	0.3607	0.0194	0.0065	0.2889	51.49	17.16	0.07	0.12	-0.1564		
RV_20	1.08125	0.1572	5.9191	0.0202	0.0157	-0.1236	49.60	38.68	-0.21	0.65	-0.1672		
RV_22	1.08125	0.6474	1.2023	0.0251	0.0213	-0.0103	39.90	33.86	-0.15	0.42	0.0610		
RV_25	1.08125	0.5827	0.3422	0.0381	0.0036	0.0005	26.24	2.48	0.11	0.057	-0.0356		
RV_27	1.08125	0.2035	0.0925	0.0251	0.0021	-0.2298	39.90	3.39	0.07	0.028	0.3249		
RV_31	1.08125	0.4624	1.2948	0.0176	0.0213	0.0175	56.91	68.89	0.60	0.74	0.1920		
RV_33	1.08125	0.6474	1.1098	0.0250	0.0157	-0.0557	40.05	25.21	0.04	0.78	0.1632		
RV_37	1.08125	0.2127	0.2867	0.0246	0.0052	-0.0726	40.65	8.56	0.05	0.12	-0.4631		
RV_39	1.08125	0.8509	0.8971	0.0271	0.0092	-0.1540	36.90	12.59	0.66	0.53	0.4118		
RV_10_2	1.08125	0.2062	0.0620	0.0196	0.0011	-0.2659	51.00	2.89	0.08	0.025	0.3851		
RV_10_3	1.08125	0.1304	0.0527	0.0209	0.0011	0.0129	47.84	2.54	0.05	0.019	0.0610		
RV_10_4	1.08125	0.1683	0.0555	0.0207	0.0012	0.0142	48.27	2.80	0.06	0.021	0.2213		
RV_10_5	1.08125	0.1692	0.0666	0.0198	0.0011	0.2867	50.53	2.83	0.07	0.028	-0.1702		
RV_14_2	1.08125	0.3792	0.6474	0.0206	0.0213	-0.0796	48.49	50.01	0.06	0.25	0.7621		

Grain	U-Pb fractionation correction factor	207/235 ratio	Prop 2SE	206/238 ratio	Prop 2SE	Rho 6/38 vs 7/35	238/206 ratio	Prop 2SE	207/206 ratio	Prop 2SE	Rho 38/6 vs 7/6	Rejected from discordia = x	Rejection Reason
RV_14_3	1.08125	0.5549	0.6382	0.0299	0.0045	-0.2159	33.48	5.08	0.26	0.41	0.6863		
RV_19_2	1.08125	0.3514	0.2127	0.0214	0.0023	0.2415	46.81	5.07	0.08	0.071	0.3473		
RV_19_3	1.08125	0.3977	0.2035	0.0208	0.0025	-0.2161	48.06	5.77	0.18	0.1	0.5980		
RV_25_2	1.08125	0.5734	0.2497	0.0352	0.0029	-0.0429	28.38	2.31	0.12	0.049	0.0882		
RV_25_3	1.08125	0.8601	0.2220	0.0431	0.0037	0.3563	23.20	1.99	0.13	0.035	0.3664		
RV_27_2	1.08125	0.2590	0.1295	0.0264	0.0021	0.1962	37.94	3.06	0.07	0.033	-0.0491		
RV_27_3	1.08125	0.3145	0.1202	0.0291	0.0023	-0.1530	34.33	2.72	0.09	0.034	0.2623		
RV_37_2	1.08125	0.2035	0.1942	0.0213	0.0026	0.2368	47.01	5.72	0.07	0.092	0.0027		
RV_37_3	1.08125	0.3145	0.1572	0.0237	0.0028	0.0314	42.24	4.95	0.11	0.061	0.0789		
JAGG_1	1.08125	2.5896	27.7457	0.0342	0.0499	-0.0074	29.22	42.65	0.60	6.1	0.0329	x	Poor
JAGG_2	1.08125	2.4971	1.7572	0.0185	0.0111	0.0614	54.06	32.44	-0.80	1.7	0.2346	x	Poor
JAGG_5	1.08125	2.1272	10.1734	0.0148	0.1757	-0.0502	67.58	802.49	0.35	1.6	0.4284	x	Poor
JAGG_6	1.08125	6.5665	5.0867	0.0740	0.0712	0.0091	13.52	13.01	1.10	1.7	0.0242	x	Poor
JAGG_7	1.08125	4.7168	4.9017	0.0324	0.0499	-0.0475	30.89	47.66	-3.60	4.5	0.2766	x	Poor
JAGG_8	1.08125	0.7399	3.4220	0.0379	0.0388	-0.0653	26.37	27.02	2.60	7.8	0.1618	x	Poor
JAGG_9	1.08125	92.4855	64.7399	3.6069	2.4046	0.1398	0.28	0.18	1.20	9.4	0.9127	x	Poor
JAGG_11	1.08125	0.1850	2.2197	0.0148	0.0129	-0.0388	67.58	59.13	-0.80	42	-0.5109	x	Poor
JAGG_12	1.08125	1.1098	1.2948	0.0296	0.0148	-0.2844	33.79	16.89	14.00	14	0.4755	x	Poor
JAGG_13	1.08125	1.4798	8.3237	-0.0009	0.0287	-0.3296	-1081.25	33518.75	-2.40	10	0.7058	x	Poor
JAGG_14	1.08125	1.5723	1.5723	0.0444	0.0231	-0.0855	22.53	11.73	1.50	1.7	0.6501	x	Poor
JAGG_15	1.08125	4.6243	19.4220	0.0832	0.1387	0.9148	12.01	20.02	-0.50	2.1	0.2779	x	Poor
JAGG_16	1.08125	0.3699	1.0173	0.0120	0.0453	0.1312	83.17	313.50	-0.10	1.4	0.3417	x	Poor
JAGG_17	1.08125	1.7572	3.6994	-0.0055	0.0194	0.0653	-180.21	630.73	-1.80	2.2	-0.0749	x	Poor
JAGG_18	1.08125	-0.0925	2.4046	0.0111	0.0176	-0.0731	90.10	142.66	0.20	1.1	0.0652	x	Poor
JAGG_19	1.08125	-1.0173	4.2543	0.0009	0.0472	-0.0102	1081.25	55143.75	0.20	1.9	0.1745	x	Poor
JAGG_20	1.08125	1.4798	3.0520	0.0194	0.0592	0.6092	51.49	156.92	-0.87	0.91	-0.2954	x	Poor
JAGG_21	1.08125	0.1572	0.4347	0.0118	0.0035	0.3103	84.47	25.08	-0.37	0.95	-0.2407	x	Poor
JAGG_22	1.08125	8.3237	4.1618	0.0703	0.0370	-0.0062	14.23	7.49	0.70	1.4	0.4944	x	Poor
JAGG_23	1.08125	-0.8046	0.5919	0.0106	0.0102	-0.0515	94.02	89.93	0.07	0.51	-0.2661	x	Poor
JAGG_24	1.08125	87.8613	23.1214	0.7214	0.1480	0.1495	1.39	0.28	1.35	0.39	0.3072	x	Poor
JAGG_25	1.08125	82.3121	36.0694	1.8497	1.2023	0.0425	0.54	0.35	0.90	2.5	0.4997	x	Poor
JAGG_26	1.08125	123.9306	52.7168	1.3225	0.5734	-0.0388	0.76	0.33	1.35	0.97	0.0955	x	Poor
JAGG_27	1.08125	-2.4046	4.2543	0.1480	0.1387	-0.0292	6.76	6.34	0.90	1.3	0.0792	x	Poor

Grain	U-Pb fractionation correction factor	207/235 ratio	Prop 2SE	206/238 ratio	Prop 2SE	Rho 6/38 vs 7/35	238/206 ratio	Prop 2SE	207/206 ratio	Prop 2SE	Rho 38/6 vs 7/6	Rejected from discordia = x	Rejection Reason
JAGG_28	1.08125	0.0000	1.5723	0.0037	0.0435	-0.0907	270.31	3176.17	0.29	1.3	0.1097	x	Poor
JAGG_29	1.08125	0.0000	2.4971	-0.0028	0.0139	0.0031	-360.42	1802.08	-0.70	0.77	-0.0143	x	Poor
JAGG_30	1.08125	-0.9249	24.9711	-0.0740	0.1850	0.1838	-13.52	33.79	-0.21	0.63	0.1612	x	Poor
JAGG_31	1.08125	0.3052	0.7861	0.0146	0.0086	0.1149	68.43	40.28	0.48	0.39	0.0945	x	Poor
JAGG_32	1.08125	-3.3295	3.2370	0.0129	0.0305	-0.0032	77.23	182.05	0.23	0.73	0.2013	x	Poor
JAGG_33	1.08125	24.9711	72.1387	0.2220	0.4624	-0.0467	4.51	9.39	-0.50	0.65	0.1666	x	Poor
JAGG_34	1.08125	-0.1387	0.7214	0.0070	0.0071	0.0333	142.27	144.14	0.28	0.54	-0.0608	x	Poor
JAGG_35	1.08125	-0.3699	2.7746	0.0155	0.0268	-0.1108	64.36	111.10	-0.69	0.92	0.1106	x	Poor
JAGG_36	1.08125	46.2428	45.3179	0.5457	0.2405	-0.0145	1.83	0.81	1.90	1.4	0.0179	x	Poor
JAGG_37	1.08125	0.2775	1.4798	0.0139	0.0324	0.0141	72.08	168.19	-0.31	0.64	-0.0519	x	Poor
JAGG_38	1.08125	-2.7746	11.0983	0.0092	0.1110	0.1894	108.13	1297.50	0.28	0.6	-0.0890	x	Poor
JAGG_39	1.08125	-4.6243	9.2486	0.0092	0.1202	-0.2903	108.13	1405.63	-0.19	0.32	0.0561	x	Poor
JAGG_40	1.08125	-0.2775	1.0173	0.0049	0.0080	0.0608	204.01	331.03	-0.02	0.75	0.0078	x	Poor
JAGG_41	1.08125	57.3410	31.4451	0.8601	0.7399	-0.0496	1.16	1.00	1.50	3.1	0.0760	x	Poor
JAGG_42	1.08125	-129.4798	721.3873	-1.3873	4.6243	-0.0333	-0.72	2.40	0.80	3.2	0.0277	x	Poor
JAGG_43	1.08125	0.2775	0.7676	0.0091	0.0222	0.0348	110.33	270.20	0.09	0.67	0.0505	x	Poor
JAGG_44	1.08125	-0.3699	2.3121	-0.0028	0.0194	-0.0098	-360.42	2522.92	0.83	0.61	-0.1354	x	Poor
JAGG_45	1.08125	-0.7399	1.3873	0.0083	0.0111	0.2173	120.14	160.19	-0.27	0.52	-0.0392	x	Poor
JAGG_46	1.08125	-0.7399	2.1272	0.0000	0.0231	0.2314	NA	NA	0.15	0.49	-0.0876	x	Poor
JAGG_47	1.08125	1.4798	2.3121	0.0028	0.0213	0.0509	360.42	2763.19	-0.31	0.55	0.5206	x	Poor
JAGG_48	1.08125	0.0000	2.4971	0.0148	0.0222	0.2225	67.58	101.37	-0.32	0.71	0.3901	x	Poor
JAGG_49	1.08125	-0.0925	1.8497	0.0120	0.0194	0.1062	83.17	134.36	-0.11	0.55	0.0278	x	Poor
JAGG_50	1.08125	-2.0347	4.1618	0.0231	0.0287	-0.1037	43.25	53.63	-0.10	1	-0.0720	x	Poor
JAGG_51	1.08125	0.6289	0.6104	0.0231	0.0111	0.0380	43.25	20.76	0.49	0.94	0.2622	x	Poor
JAGG_52	1.08125	-0.2682	0.8231	0.0176	0.0092	0.3440	56.91	29.65	1.20	0.7	-0.7722	x	Poor
JAGG_53	1.08125	0.2590	1.1098	0.0164	0.0081	-0.1515	61.09	30.37	-1.00	1.9	0.2943	x	Poor
JAGG_54	1.08125	1.2023	1.7572	0.0222	0.1387	0.2828	45.05	281.58	0.31	1.8	0.6658	x	Poor
Reproducibility Sample BSK064, run as unknown in exp 1													
BSK064_PYR_1	1.08125	0.3145	0.1665	0.0154	0.0080	0.0429	65.135538	33.7449	0.157	0.068	-0.0522	NA	
BSK064_PYR_2	1.08125	0.2960	0.2220	0.0154	0.0017	-0.0702	64.7455095	6.97856	0.15	0.13	0.1473	NA	
BSK064_PYR_3	1.08125	3.3480	0.2127	0.0435	0.0028	0.4231	23.0053238	1.46843	0.572	0.038	0.4857	NA	
BSK064_PYR_4	1.08125	2.2659	0.1942	0.0348	0.0023	0.1491	28.7566439	1.91201	0.468	0.043	0.4712	NA	
BSK064_PYR_5	1.08125	1.2671	0.1757	0.0254	0.0022	0.1743	39.3181858	3.43141	0.381	0.063	0.5397	NA	

Grain	U-Pb fractionation correction factor	207/235 ratio	Prop 2SE	206/238 ratio	Prop 2SE	Rho 6/38 vs 7/35	238/206 ratio	Prop 2SE	207/206 ratio	Prop 2SE	Rho 38/6 vs 7/6	Rejected from discordia = x	Rejection Reason
BSK064_PYR_6	1.08125	2.0162	0.1942	0.0331	0.0018	-0.2223	30.202513	1.68729	0.465	0.06	0.6627	NA	
BSK064_PYR_7	1.08125	1.2855	0.1387	0.0264	0.0018	0.2650	37.9385973	2.66236	0.359	0.038	0.1520	NA	
BSK064_PYR_8	1.08125	2.4694	0.2497	0.0338	0.0025	-0.0117	29.6232874	2.19131	0.548	0.067	0.4390	NA	
BSK064_PYR_9	1.08125	3.2277	0.4624	0.0437	0.0058	0.8961	22.8594091	3.0447	0.57	0.068	0.4539	NA	
BSK064_PYR_10	1.08125	1.9792	0.2035	0.0305	0.0019	0.2817	32.7651512	2.08506	0.473	0.052	0.5353	NA	
BSK064_PYR_11	1.08125	1.3318	0.1942	0.0256	0.0020	0.2085	39.0342928	3.1002	0.379	0.059	0.4209	NA	
BSK064_PYR_12	1.08125	9.8035	0.5734	0.1059	0.0054	0.5262	9.44323095	0.47835	0.67	0.033	0.3343	NA	High Ba CPS
BSK064_PYR_13	1.08125	8.0277	0.5549	0.0837	0.0043	0.7298	11.9475098	0.62048	0.687	0.03	0.1220	NA	High Ba CPS
BSK064_PYR_14	1.08125	1.9237	0.2035	0.0315	0.0021	0.3711	31.7082077	2.13868	0.456	0.054	0.2859	NA	
BSK064_PYR_17	1.08125	4.4855	0.3052	0.0592	0.0037	0.2237	16.8945313	1.05591	0.558	0.044	0.5418	NA	
BSK064_PYR_15	1.08125	2.3769	0.2405	0.0369	0.0024	0.2605	27.0990011	1.76585	0.485	0.055	0.4327	NA	
BSK064_PYR_16	1.08125	2.3399	0.1665	0.0369	0.0025	0.2759	27.0990011	1.83377	0.466	0.037	0.4770	NA	
BSK064_PYR_18	1.08125	3.6624	0.2960	0.0462	0.0031	0.4469	21.625	1.4705	0.575	0.042	0.4545	NA	
BSK064PYR_0	1.08125	0.7491	0.3052	0.0333	0.0129	0.0921	30.0347246	11.6802	0.3	0.1	0.2235	NA	
BSK064PYR_1	1.08125	4.4393	1.2023	0.0451	0.0031	0.0709	22.1567588	1.49831	0.73	0.21	-0.1387	NA	
BSK064PYR_2	1.08125	4.8092	0.9249	0.0556	0.0062	0.1389	17.9908539	2.00564	0.612	0.065	0.0166	NA	
BSK064PYR_3	1.08125	2.2566	0.3514	0.0343	0.0032	0.5959	29.1442071	2.74945	0.449	0.047	-0.1106	NA	
BSK064PYR_4	1.08125	0.6751	0.2867	0.0177	0.0019	0.7789	56.6099466	6.22413	0.241	0.067	-0.1679	NA	
BSK064PYR_5	1.08125	1.8867	0.2405	0.0296	0.0026	0.8912	33.7890625	2.95654	0.465	0.049	-0.0391	NA	
BSK064PYR_6	1.08125	0.1942	0.1387	0.0156	0.0020	0.7934	63.9792925	8.32867	0.095	0.066	-0.0026	NA	
BSK064PYR_7	1.08125	5.3179	0.3977	0.0609	0.0038	0.7494	16.4323726	1.0239	0.609	0.041	0.5047	NA	High Ba CPS
BSK064PYR_8	1.08125	6.8439	2.7746	0.0583	0.0194	0.7127	17.1627029	5.7209	0.71	0.19	0.2118	NA	High Ba CPS
BSK064PYR_9	1.08125	3.1908	0.7861	0.0336	0.0032	0.6661	29.7865021	2.87198	0.64	0.14	0.5420	NA	
BSK064PYR_10	1.08125	1.3040	0.3607	0.0253	0.0036	0.3497	39.4616784	5.61681	0.55	0.18	0.1303	NA	
BSK064PYR_11	1.08125	1.4705	0.3422	0.0277	0.0045	0.1688	36.0416631	5.88681	0.399	0.069	-0.0329	NA	
BSK064PYR_12	1.08125	1.8405	0.1757	0.0331	0.0039	0.0911	30.202513	3.54331	0.449	0.05	0.3372	NA	
BSK064PYR_13	1.08125	1.2948	0.2497	0.0263	0.0018	0.6725	38.0721857	2.54708	0.349	0.047	-0.1106	NA	
BSK064PYR_14	1.08125	2.0994	0.1942	0.0341	0.0023	0.8017	29.3021669	1.98524	0.452	0.042	0.3149	NA	
BSK064PYR_15	1.08125	1.1653	0.1665	0.0237	0.0018	0.5874	42.2363281	3.13473	0.365	0.048	-0.0719	NA	
BSK064PYR_16	1.08125	1.3410	0.2312	0.0263	0.0020	0.8797	38.0721857	2.94925	0.363	0.056	0.0270	NA	
BSK064PYR_17	1.08125	2.4231	0.2960	0.0361	0.0031	0.5204	27.7243637	2.41699	0.5	0.052	0.0696	NA	
Garnet References: G1 = Odikhincha; G2 = Afrikanda; G3 = Dashkesan; G4 = Chikskii. Citations in text													
G4_1	1.0725	0.3119	0.0183	0.0402	0.0011	-0.0518	24.8745	0.6812	0.0546	0.0029	0.2311	NA	

Grain	U-Pb fractionation correction factor	207/235 ratio	Prop 2SE	206/238 ratio	Prop 2SE	Rho 6/38 vs 7/35	238/206 ratio	Prop 2SE	207/206 ratio	Prop 2SE	Rho 38/6 vs 7/6	Rejected from discordia = x	Rejection Reason
G4_2	1.0725	0.3202	0.0156	0.0401	0.0011	-0.0723	24.9428	0.6849	0.0565	0.0027	0.4591	NA	
G4_3	1.0725	0.3092	0.0202	0.0397	0.0011	0.2504	25.2198	0.7002	0.0548	0.0031	0.1182	NA	
G4_4	1.0725	0.3505	0.0193	0.0400	0.0011	0.4808	25.0115	0.6887	0.0613	0.0027	-0.0922	NA	
G4_5	1.0725	0.4009	0.0266	0.0404	0.0012	0.2555	24.7502	0.7306	0.0693	0.004	0.0907	NA	
G4_6	1.0725	0.3550	0.0284	0.0396	0.0009	0.0183	25.2373	0.5843	0.0671	0.0052	0.1982	NA	
G4_11	1.0725	0.3009	0.0174	0.0394	0.0010	-0.1662	25.3843	0.6503	0.0536	0.0028	0.2085	NA	
G4_12	1.0725	0.2945	0.0165	0.0397	0.0012	-0.0666	25.2081	0.7579	0.0526	0.0028	0.4473	NA	
G4_1	1.09	0.3002	0.0159	0.0401	0.0006	0.1969	24.9535	0.3539	0.0545	0.0029	0.0766	NA	
G4_2	1.09	0.2956	0.0131	0.0394	0.0008	0.2010	25.3606	0.5255	0.0541	0.0025	0.3273	NA	
G4_3	1.09	0.3068	0.0140	0.0408	0.0008	0.1087	24.4807	0.5255	0.0546	0.0026	0.3040	NA	
G4_5	1.09	0.2928	0.0159	0.0390	0.0008	0.3728	25.6395	0.5363	0.0543	0.0029	-0.0073	NA	
G4_6	1.09	0.2909	0.0159	0.0392	0.0008	0.2749	25.4811	0.5363	0.0537	0.0028	0.1020	NA	
G4_9	1.09	0.2974	0.0159	0.0395	0.0010	0.1634	25.2948	0.6971	0.0545	0.003	0.2234	NA	
G4_10	1.09	0.4224	0.0233	0.0396	0.0017	0.7333	25.2353	1.0618	0.0768	0.0027	0.0417	NA	
G4_11	1.09	0.3030	0.0131	0.0396	0.0008	-0.0622	25.271	0.5363	0.0555	0.0025	0.3530	NA	
G3_1	1.0725	0.7101	0.0330	0.0763	0.0020	0.5829	13.101	0.3464	0.0658	0.0021	-0.0106	NA	
G3_2	1.0725	0.6569	0.0284	0.0769	0.0018	0.3551	13.0072	0.3104	0.0604	0.0019	0.1510	NA	
G3_3	1.0725	0.6826	0.0303	0.0781	0.0019	0.3355	12.8085	0.3161	0.0616	0.0021	0.2354	NA	
G3_4	1.0725	0.7202	0.0312	0.0779	0.0019	-0.1800	12.8386	0.3176	0.0651	0.0026	0.5913	NA	
G3_5	1.0725	0.6624	0.0294	0.0757	0.0017	0.0723	13.2121	0.3043	0.0651	0.0023	0.3248	NA	
G3_6	1.0725	0.5927	0.0266	0.0772	0.0018	0.1813	12.9454	0.3075	0.0572	0.002	0.2863	NA	
G3_7	1.0725	0.7532	0.0367	0.0802	0.0028	0.3841	12.4714	0.4281	0.0658	0.0026	0.3336	NA	
G3_8	1.0725	0.7119	0.0385	0.0816	0.0024	0.4288	12.261	0.3586	0.0609	0.0025	0.0913	NA	
G3_9	1.0725	0.6761	0.0312	0.0783	0.0020	-0.0581	12.7635	0.3288	0.0613	0.0026	0.4867	NA	
G3_10	1.0725	0.6716	0.0321	0.0773	0.0018	0.3405	12.93	0.3068	0.0617	0.0024	0.0638	NA	
G3_1	1.09	0.8373	0.0261	0.0812	0.0011	0.3286	12.3134	0.1716	0.0748	0.0023	0.1038	NA	
G3_2	1.09	0.7273	0.0392	0.0772	0.0009	0.5690	12.9529	0.1609	0.0681	0.0033	-0.3877	NA	
G3_3	1.09	0.6909	0.0317	0.0766	0.0012	0.4530	13.0633	0.2038	0.0646	0.0025	-0.1271	NA	
G3_4	1.09	0.7319	0.0364	0.0784	0.0009	0.3659	12.7481	0.1502	0.0676	0.0031	-0.1742	NA	
G3_5	1.09	0.7235	0.0392	0.0776	0.0011	0.5203	12.8906	0.1823	0.0686	0.0038	-0.3048	NA	
G3_6	1.09	0.6536	0.0140	0.0758	0.0012	0.2836	13.1919	0.2145	0.0625	0.0013	0.2565	NA	
G3_7	1.09	0.8196	0.0727	0.0759	0.0012	0.6298	13.1757	0.236	0.0774	0.0059	-0.4713	NA	
G3_8	1.09	0.6946	0.0205	0.0778	0.0012	0.2820	12.8597	0.2038	0.0647	0.0021	0.2121	NA	

Grain	U-Pb fractionation correction factor	207/235 ratio	Prop 2SE	206/238 ratio	Prop 2SE	Rho 6/38 vs 7/35	238/206 ratio	Prop 2SE	207/206 ratio	Prop 2SE	Rho 38/6 vs 7/6	Rejected from discordia = x	Rejection Reason
G3_9	1.09	0.6890	0.0336	0.0748	0.0012	0.4934	13.3728	0.2145	0.0666	0.0029	-0.2283	NA	
G3_10	1.09	0.6872	0.0224	0.0776	0.0014	0.4710	12.8906	0.2252	0.0641	0.0019	0.0857	NA	
G2_1	1.0725	0.6128	0.0670	0.0642	0.0018	0.7213	15.5714	0.4449	0.067	0.0057	-0.6122	NA	
G2_2	1.0725	0.5055	0.0239	0.0605	0.0015	0.4303	16.5402	0.4016	0.0589	0.002	0.1082	NA	
G2_3	1.0725	0.5101	0.0275	0.0608	0.0015	0.3365	16.4404	0.3968	0.0591	0.0025	0.0159	NA	
G2_4	1.0725	0.6569	0.0495	0.0631	0.0016	0.2953	15.843	0.3915	0.0732	0.0047	-0.1090	NA	
G2_5	1.0725	0.5578	0.0284	0.0617	0.0014	0.3965	16.2106	0.3616	0.0636	0.0024	-0.1081	NA	
G2_6	1.0725	0.4844	0.0239	0.0614	0.0017	0.3842	16.293	0.4384	0.0582	0.0021	0.1288	NA	
G2_7	1.0725	0.4826	0.0220	0.0619	0.0014	0.2554	16.1434	0.3586	0.0576	0.002	0.1647	NA	
G2_8	1.0725	0.5312	0.0266	0.0600	0.0016	0.3062	16.6667	0.4332	0.0621	0.0024	0.1226	NA	
G2_9	1.0725	0.5055	0.0266	0.0600	0.0016	0.3843	16.6667	0.4332	0.0586	0.0023	0.0923	NA	
G2_10	1.0725	0.5257	0.0275	0.0614	0.0016	0.3630	16.293	0.414	0.0609	0.0025	0.0187	NA	
G2_11	1.0725	0.6972	0.0358	0.0624	0.0014	0.3324	16.0365	0.3539	0.0804	0.0036	-0.0804	NA	
G2_12	1.0725	0.5440	0.0303	0.0599	0.0014	0.4341	16.6999	0.3838	0.065	0.003	-0.1307	NA	
G2_1	1.09	0.5305	0.0224	0.0624	0.0010	0.4922	16.0314	0.2681	0.0616	0.0025	-0.0372	NA	
G2_2	1.09	0.5669	0.0205	0.0632	0.0010	0.7415	15.8186	0.2574	0.0652	0.0019	-0.4951	NA	
G2_3	1.09	0.5026	0.0159	0.0629	0.0009	0.5514	15.9054	0.2252	0.0585	0.0019	-0.1561	NA	
G2_4	1.09	0.4858	0.0149	0.0609	0.0011	0.3305	16.4242	0.3003	0.0585	0.0021	0.1874	NA	
G2_5	1.09	0.4951	0.0196	0.0612	0.0011	0.4660	16.3491	0.2896	0.0592	0.0018	-0.0574	NA	
G2_6	1.09	0.4737	0.0177	0.0612	0.0009	0.2098	16.3441	0.236	0.056	0.0021	0.1335	NA	
G2_7	1.09	0.4718	0.0140	0.0610	0.0011	0.5043	16.3991	0.2896	0.0566	0.0017	0.0048	NA	
G2_8	1.09	0.4970	0.0159	0.0609	0.0011	0.3896	16.4242	0.3003	0.0591	0.0019	0.2306	NA	
G2_9	1.09	0.4755	0.0168	0.0604	0.0009	0.2885	16.5509	0.2574	0.057	0.002	0.1636	NA	
G2_10	1.09	0.5138	0.0205	0.0614	0.0010	0.6017	16.2994	0.2574	0.0607	0.002	-0.3386	NA	
G2_11	1.09	0.5343	0.0233	0.0620	0.0009	0.6823	16.1375	0.2467	0.0621	0.0021	-0.4027	NA	
G2_12	1.09	0.4634	0.0159	0.0610	0.0009	0.3030	16.3866	0.2467	0.0549	0.0019	0.0969	NA	
G1_1	1.0725	0.1716	0.0147	0.0228	0.0007	0.3928	43.8103	1.3383	0.0531	0.004	-0.1400	NA	
G1_2	1.0725	0.2165	0.0294	0.0226	0.0007	0.1864	44.2011	1.3443	0.0672	0.0083	-0.0712	NA	
G1_3	1.0725	0.1789	0.0220	0.0232	0.0007	0.3996	43.049	1.2581	0.0542	0.0059	-0.2396	NA	
G1_4	1.0725	0.1569	0.0138	0.0226	0.0007	0.2858	44.327	1.3159	0.0493	0.004	-0.0287	NA	
G1_5	1.0725	0.1899	0.0128	0.0230	0.0007	0.0340	43.5652	1.2711	0.0586	0.0038	0.2347	NA	
G1_6	1.0725	0.1881	0.0174	0.0229	0.0007	0.1451	43.6524	1.3811	0.0603	0.0055	0.0908	NA	
G1_7	1.0725	0.1670	0.0128	0.0226	0.0007	-0.1125	44.345	1.317	0.055	0.0042	0.3946	NA	

Grain	U-Pb fractionation correction factor	207/235 ratio	Prop 2SE	206/238 ratio	Prop 2SE	Rho 6/38 vs 7/35	238/206 ratio	Prop 2SE	207/206 ratio	Prop 2SE	Rho 38/6 vs 7/6	Rejected from discordia = x	Rejection Reason
G1_8	1.0725	0.1853	0.0202	0.0215	0.0007	-0.0589	46.5215	1.4892	0.0599	0.0062	0.1723	NA	
G1_9	1.0725	0.1615	0.0147	0.0225	0.0007	0.0687	44.5261	1.4005	0.0508	0.0045	0.2172	NA	
G1_10	1.0725	0.1881	0.0165	0.0225	0.0006	0.1900	44.4716	1.2338	0.0598	0.0048	0.0384	NA	
G1_12	1.0725	0.1587	0.0128	0.0224	0.0007	0.2905	44.6721	1.3365	0.0509	0.0035	-0.0271	NA	
G1_1	1.09	0.2387	0.0177	0.0238	0.0005	0.1098	42.0423	0.8902	0.0731	0.0056	0.1612	NA	
G1_2	1.09	0.1893	0.0103	0.0230	0.0005	0.1195	43.3859	0.9438	0.0596	0.0032	0.2068	NA	
G1_3	1.09	0.1660	0.0093	0.0232	0.0006	0.0707	43.1937	1.0725	0.0524	0.0034	-0.0693	NA	
G1_4	1.09	0.2210	0.0298	0.0231	0.0006	0.3457	43.2111	1.1798	0.0689	0.0084	-0.1866	NA	
G1_5	1.09	0.5072	0.0793	0.0253	0.0010	0.7861	39.5756	1.6088	0.14	0.016	-0.6690	NA	
G1_6	1.09	0.6434	0.0932	0.0263	0.0011	0.7429	38.0319	1.6088	0.172	0.019	-0.5949	NA	
G1_7	1.09	0.1809	0.0112	0.0225	0.0005	-0.0667	44.4099	0.9974	0.0586	0.004	0.3910	NA	
G1_8	1.09	0.7515	0.0671	0.0280	0.0010	0.6752	35.75	1.3943	0.192	0.014	-0.4165	NA	
G1_9	1.09	0.3655	0.0597	0.0245	0.0007	0.5864	40.8571	1.3943	0.105	0.015	-0.4033	NA	
G1_10	1.09	0.2490	0.0233	0.0234	0.0005	0.4342	42.7291	1.0296	0.0767	0.0065	-0.2555	NA	
G1_11	1.09	0.1958	0.0168	0.0228	0.0005	0.2456	43.9009	0.9867	0.062	0.0051	0.0117	NA	
G1_12	1.09	0.1855	0.0149	0.0231	0.0006	0.4495	43.2983	1.0725	0.058	0.0043	-0.1546	NA	
Mud Tank Zircon													
MudTank_0	1	1.0710	0.0370	0.1207	0.0020	-0.3225	8.285004	0.13728	0.0643	0.0024	0.3893	NA	
MudTank_1	1	1.0940	0.0250	0.1207	0.0018	0.4408	8.285004	0.12355	0.0658	0.0015	0.2449	NA	
MudTank_2	1	1.0740	0.0270	0.1204	0.0018	0.5929	8.305648	0.12417	0.0647	0.0014	0.0131	NA	
MudTank_3	1	1.0680	0.0220	0.1208	0.0020	0.3814	8.278146	0.13706	0.0646	0.0016	0.3551	NA	
MudTank_4	1	1.0800	0.0320	0.1212	0.0026	0.6176	8.250825	0.177	0.0646	0.0016	0.1855	NA	
MudTank_5	1	1.0540	0.0320	0.1204	0.0022	0.1434	8.305648	0.15176	0.0635	0.0022	0.4519	NA	
MudTank_6	1	1.0610	0.0260	0.1195	0.0014	0.1711	8.368201	0.09804	0.0643	0.0017	0.2815	NA	
MudTank_7	1	1.0610	0.0370	0.1178	0.0019	0.3218	8.488964	0.13692	0.0652	0.0022	0.1602	NA	
MudTank_8	1	1.0600	0.0240	0.1186	0.0024	0.3898	8.431703	0.17062	0.0648	0.0016	0.4947	NA	
MudTank_9	1	1.0350	0.0300	0.1178	0.0023	-0.1544	8.488964	0.16574	0.0637	0.002	0.7228	NA	
MudTank_10	1	1.0520	0.0240	0.1180	0.0015	0.2067	8.474576	0.10773	0.0649	0.0019	0.2876	NA	
MudTank_11	1	1.0630	0.0320	0.1200	0.0018	0.4256	8.333333	0.125	0.064	0.0018	0.0675	NA	
MudTank_12	1	1.0610	0.0320	0.1224	0.0022	0.5298	8.169935	0.14685	0.0627	0.0017	0.1759	NA	
MudTank_13	1	1.0610	0.0310	0.1199	0.0021	0.0737	8.340284	0.14608	0.064	0.002	0.4665	NA	
MudTank_0	1	1.0750	0.0470	0.1198	0.0029	0.2117	8.347245	0.20206	0.0644	0.0022	0.3037	NA	
MudTank_1	1	1.0850	0.0500	0.1206	0.0030	0.2919	8.291874	0.20627	0.0644	0.0022	0.0426	NA	

Grain	U-Pb fractionation correction factor	207/235 ratio	Prop 2SE	206/238 ratio	Prop 2SE	Rho 6/38 vs 7/35	238/206 ratio	Prop 2SE	207/206 ratio	Prop 2SE	Rho 38/6 vs 7/6	Rejected from discordia = x	Rejection Reason
MudTank_2	1	1.1140	0.0480	0.1217	0.0029	-0.2074	8.216927	0.1958	0.0654	0.0024	0.5569	NA	
MudTank_3	1	1.0940	0.0460	0.1199	0.0028	0.2356	8.340284	0.19477	0.0653	0.0021	0.2585	NA	
MudTank_4	1	1.0920	0.0480	0.1208	0.0029	0.1748	8.278146	0.19873	0.0645	0.0023	0.3017	NA	
MudTank_5	1	1.0410	0.0430	0.1217	0.0031	0.4119	8.216927	0.20931	0.0626	0.0018	0.3384	NA	
MudTank_6	1	1.0660	0.0450	0.1214	0.0030	0.3844	8.237232	0.20356	0.0644	0.002	0.1766	NA	
MudTank_7	1	1.0620	0.0490	0.1203	0.0028	0.1721	8.312552	0.19348	0.0635	0.0024	0.2640	NA	
MudTank_8	1	1.0730	0.0440	0.1201	0.0028	0.4872	8.326395	0.19412	0.0634	0.002	-0.0086	NA	
MudTank_9	1	1.0780	0.0490	0.1200	0.0028	0.3917	8.333333	0.19444	0.0638	0.0022	0.0283	NA	
MudTank_10	1	1.1000	0.0490	0.1211	0.0029	0.3836	8.257638	0.19775	0.0655	0.0022	0.1804	NA	
MudTank_11	1	1.0960	0.0440	0.1215	0.0029	0.1638	8.230453	0.19645	0.0649	0.002	0.5005	NA	
MudTank_12	1	1.0990	0.0530	0.1205	0.0031	0.3936	8.298755	0.21349	0.0657	0.0024	0.1341	NA	
MudTank_13	1	1.0830	0.0470	0.1200	0.0027	-0.0124	8.333333	0.1875	0.065	0.0022	0.4161	NA	

MMC1: U-Pb isotope ratios for unknowns; internal reproducibility standard; selected orthopyroxene; garnet reference materials; and Mud Tank zircon

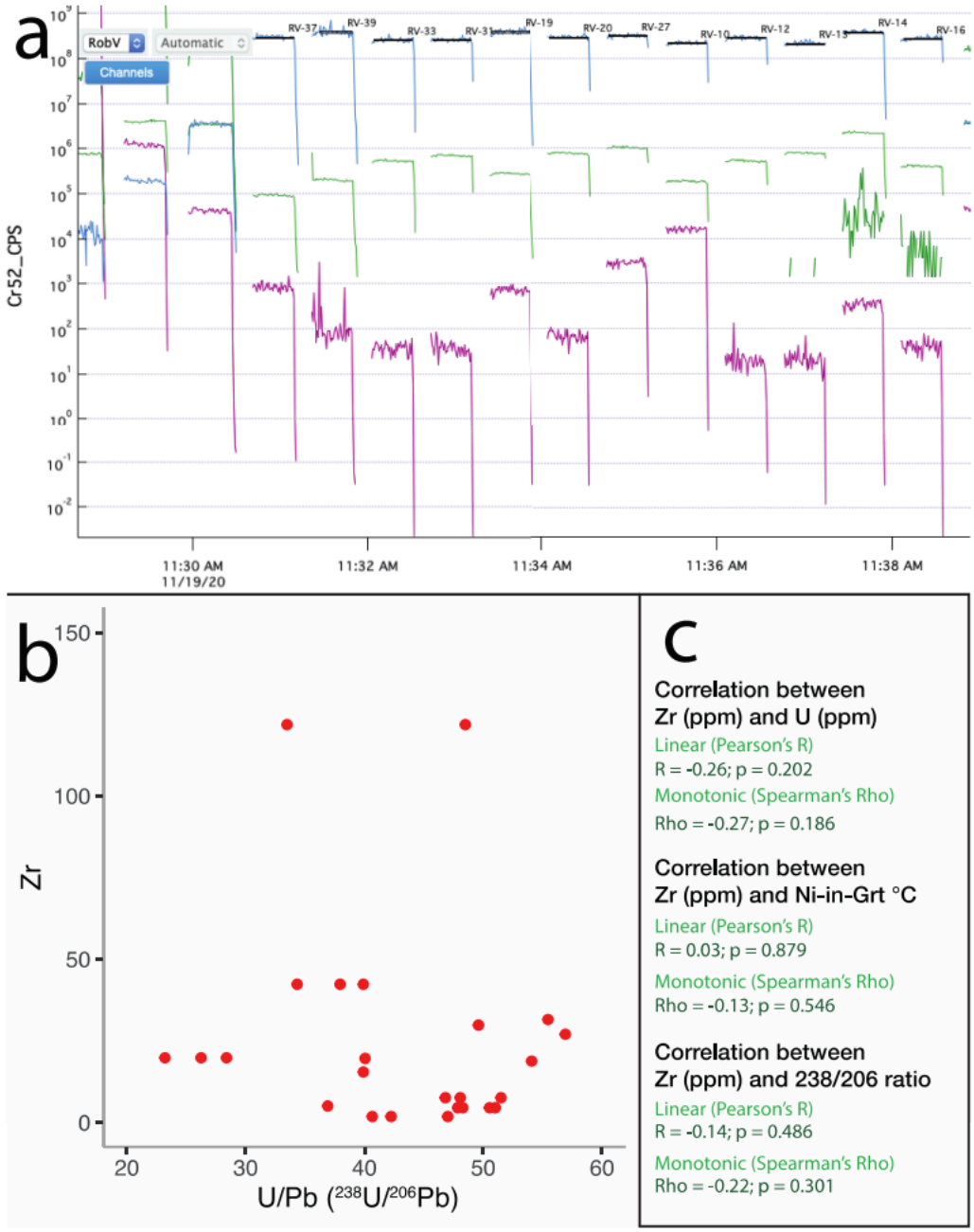

MMC2: data used to exclude the possibility that pyrope U-Pb ages are controlled by inclusions unseen under examination by SEM-BSE or SEM-CL. (a) Example time-series data in the Iolite data reduction environment (Paton et al., 2011). Background-corrected counts for a major element, Cr (blue), and trace elements U (purple), Zr (light green) and Ba (dark green) All data are displayed on logarithmic scale. In this example, RV-14 and RV-16 are excluded from age-calculations as significant counts on Ba-137 are recorded. Note the stability of the signal for U and Zr in each spot, and the lack of correlation between them optically. (b) scatter-plot of Zr (ppm) versus 238U/206Pb ratio in Roberts Victor garnet separate. No correlation is apparent (c) Statistical measures of linear (Pearson's R) and monotonic (Spearman's Rho) correlation between Zr concentration and U, Ni-in-Grt T °C, and 238U/206Pb ratio in Roberts Victor separate garnet. Most correlations between Zr and the above components are in fact negative (negative R and rho's), however, in any case, no statistically significant relationship is found between Zr and any of these components. This is shown by high p-values, none of which can be used to reject the null-hypothesis that there is no significant correlation between these factors at a 2SD level (i.e. where $p < 0.05$).

Chapter 6: Synthesis

Due to the longevity of Earth's cratons several assumptions are made with respect to their formation and thermal evolution. These assumptions (summarized in Chapter 1) are:

1) Geothermal gradients or 'geotherms' within the cratonic lithosphere have remained similar throughout Earth's history,
2) The cratonic lithosphere has remained of similar thickness since formation,
3) That the internal radiogenic heat production in the cratonic mantle either real (i.e., generated by reintroduction of HPE by metasomatism) or 'apparent' (i.e., resulting from the thermal disequilibrium of the crust and lithospheric mantle) is essentially zero,

The aim of this thesis was to investigate these assumptions. It is found that none of the above assumptions bear scrutiny. The main findings of this work are listed below:

Finding #1: The lithospheric mantle underlying Earth's cratons was originally of far thicker than is preserved today indicative of substantial basal erosion

Chapter 2 of this work demonstrates that geothermal gradients or 'geotherms' within the Kaapvaal lithosphere under steady state, of either fixed thickness or basal heat flux since the Archean, is incompatible with the *PT* conditions recorded in either Proterozoic mantle xenoliths or diamond inclusions (DI). Regardless of whether the convecting asthenosphere has cooled since the Archean or not, to reconcile the position of Proterozoic mantle xenolith and DI data (irrespective of age) in *PT* space, the vertical extent of the lithosphere must have been substantially greater during Earth's past. The thicker lithosphere (up to ~350 km) implied from DI and the lack of evidence that the Kaapvaal was substantially above sea-level prior to the Cretaceous strongly suggests that most of the basal erosion must have been gradual, with a probable mechanism being basal drag. If for instance Archean plates were moving slower than today and mantle viscosities were significantly lower, it is possible that basal drag was less significant earlier in Earth's past and that, as plate velocities increased, greater erosion of the lithosphere occurred with time and secular cooling of the convecting mantle (Artemieva and Mooney, 2002).

Recent erosion at the base of the lithosphere of the Kaapvaal Craton may also be consistent with the anomalously 'cool' *PT* estimates obtained on mantle xenoliths from the Finsch group II kimberlite, which was emplaced at 118 ± 3 Ma, earlier than the other mantle xenoliths used in our models which are overwhelmingly from late Cretaceous (~ 85

Ma) kimberlites (e.g., Tappe et al., 2018). The position of the Finsch mantle xenoliths in *PT* space are close to a geotherm at 85 Ma of a lithosphere of 223 km thickness (i.e., the earlier lithospheric thickness inferred from xenoliths from the Premier kimberlite) deeper than the present-day thickness of 197 km, which could imply basal erosion in the Cretaceous as would be supported by the significant uplift of the Kaapvaal at this time. This episode, occurring between 1.15 Ga and 85 Ma, could be consistent with foundering related to mantle plume interaction over the last 200 Ma (e.g., Celli et al., 2020). Indeed, the Kaapvaal Craton has anomalously high elevation, up to ~1.5 km in the central regions, which has been suggested to be at least partly dynamically supported by upwelling of hot asthenospheric mantle (Ravenna et al., 2018). Significant crustal erosion and denudation in the Kaapvaal Craton (which could imply uplift) has occurred since 120 Ma, with erosion of ~500 m of the upper crust in the Kimberley region and a further ~850 m post 85 Ma (Hanson et al., 2009), which lends further support to dynamic uplift and LAB erosion in the Kaapvaal Craton.

Finding #2: The most extreme examples of modally metasomatised lithospheric mantle HPE-rich suites (PKP and MARID) from the Kaapvaal Craton formed during Late Cretaceous magmatic activity in South Africa, despite isotopic evidence for the contrary

Chapter 3 of this thesis reveals the origins of the phlogopite-K-richterite-peridotite (PKP) and mica-amphibole(K-richterite)-rutile-ilmenite-diopside (MARID). These xenolith suites are amongst the most extreme examples of mantle metasomatism thought, at least in part, to be of ancient character (e.g., Kramers et al., 1983; Hawkesworth et al., 1990). Unlike most cratonic xenoliths, which are extremely challenging to date due to a paucity of mineral chronometers, the MARID and PKP suites commonly contain zircon which can be utilized for U-Pb geochronology. It follows that the possibility of absolutely dating (i.e., from geochronological methods) metasomatic events in the lithosphere could offer more firm conclusions into when: 1) the Kaapvaal lithosphere underwent thinning than is offered in Chapter 2 and 2) if ancient metasomatic events could have reintroduced HPE to the cratonic lithosphere, as could be implied from direct measurements of the high HPE in cratonic peridotites.

Unlike previous work, it was undertaken to analyse a far greater number of zircons from each xenolith sample (n = > 40). This approach was taken due to the wide range of ages (outside of analytical error) previously reported for singular xenoliths. Accordingly,

zircon in these rocks could be treated more akin to those in clastic sediments than those in igneous rocks. In provenance studies of clastic sediments, it is known to be necessary to analyse large a significant number of zircons to accurately characterise the variety of rocks of different age which are sampled by sediments.

It is shown that zircon growth is broadly coincident with nearby expressions of Cretaceous kimberlite magmatism and orangeite magmatism, with no earlier activity detected that could be linked to the long-term time integrated isotopic systematics seen in MARID. Whilst the range of zircon U-Pb ages we detect mirrors the range detected by previous workers, the addition of larger sample sizes means we can detect that zircon growth was clearly episodic. By integrating trace element data with zircon ages, it is shown that older zircon, generally has greater geochemical affinity to lamproitic zircon. By contrast, most zircons with ages coincident with peak kimberlite magmatism have trace-element compositions similar to megacrystic zircon - a suite of zircon crystals thought to be connected to early high-pressure proto kimberlitic liquids/fluids. These data strongly indicate that MARID and PKP rocks form during localized and recurrent melting of enriched lithosphere from depth that permeate upward into the shallow lithosphere. The metasomatizing effects of the passage of multiple and varying magmas at shallow depth in the lithosphere is reflected by their complex age and geochemical signatures. Whilst it has become increasingly accepted that the mantle lithosphere undergoes 'preconditioning' some thousands of years prior to kimberlite/orangeite eruption (Jackson and Gibson, 2018), perhaps to produce the requisite melting conditions favourable for their generation (e.g., Yaxley et al., 2017), MARID and PKP rocks seem to demonstrate a degree of 'postconditioning' that occurs after, and in the case of the Kaapvaal in between, major phases of surficial kimberlite or orangeite eruptions. It is also possible MARID and PKP rocks could share some similarities with polymict breccias (i.e., rare mixtures of porphyroclasts and rock clasts, cemented together by variable amounts of ilmenite, rutile, phlogopite, olivine and sulphides; Lawless et al., 1979; Höfer et al., 2009) that have been suggested to represent 'failed' proto kimberlite at mantle depths.

The presence of zircon with U-Pb ages that span the entire range of Cretaceous intra-cratonic magmatism nearby to Kimberley, and trace element compositions that derive from both major phases of intra-cratonic magmatism in a single MARID xenolith, necessitates a more complex origin for the MARID suite than that of a simple magmatic cumulate as has been previously proposed (cf., Dawson and Smith, 1977). This observation

argues for a complex origin for the presumably related PKP suite. The action of recurrent of melting at depth driving metasomatism at shallower levels could be consistent with the heating effects of the impingement of mantle plumes on the base of the Kaapvaal lithosphere from ~ 180 Ma (e.g., Celli et al., 2020). Plume activity is an attractive mechanism for lithospheric erosion during the Late Cretaceous potentially removing ~25 km from the base of the root via thermochemical erosion as suggested in Chapter 2 of this work.

Finding #3: Cratonic lithospheric mantle has an 'apparent' radiogenic heat production due to long-term thermal disequilibrium between the crust and mantle

The absolute dating of metasomatism in the cratonic lithosphere, as demonstrated in Chapter 2, does have drawbacks:

1) It is probable that these rocks fail to accurately reflect metasomatic events in the wider lithospheric mantle,
2) Earlier metasomatic events could be overprinted by later events such that only the last event is recorded by metasomatic phases (e.g., zircon),

Earlier metasomatic events in the Kaapvaal lithosphere are supported by a supposed Archean (Kinny et al., 1989) zircon population recovered from mantle xenoliths in the Permian Jwaneng kimberlite (erupted on the northern margin of the Kaapvaal away from the main Cretaceous magmatic activity) and the multiple diamond forming events detected in the Kaapvaal lithosphere (Howell et al., 2020). Coupled with the dearth of natural mineral chronometers in most cratonic peridotites it follows that an independent method to ascertain the timing of potential metasomatic events in the lithosphere would be valuable. Geothermobarometry of mantle xenoliths offers an alternative approach to identify metasomatic events if such events lead to the introduction of HPE in Earth's cratonic lithospheric mantle. By using a Monte Carlo approach, it was undertaken to randomize input parameters of the heat equation to find the best-fitting values for the internal radiogenic heat production of the lithospheric mantle (H_m) of the Kaapvaal and Slave Cratons at discrete intervals through time. The resulting analysis suggests that both the Slave and Kaapvaal Cratons have a relatively H_m of between 0.04 and 0.05 μW/m^3 near to the present-day (i.e., post Mesozoic time). Similarly, mantle xenoliths from the 1.15 Ga Premier kimberlite suggest similarly high values of H_m (~ 0.04 μW/m^3) earlier in the

Kaapvaal Craton's history. These high values would be difficult to reconcile with the stabilization of the lithosphere in the Archean and the formation an extensive diamond-hosting root prior to 2.5 Ga. Rather, more likely scenarios for such values of H_m are 'apparent' heat production resulting from the thermal disequilibrium of the crust and lithospheric mantle (Michaut and Jaupart, 2004; Michaut et al., 2009) or the later metasomatic refertilization of the cratonic mantle with K, Th and U.

The values of H_m computed from xenolith *PT* data could be consistent with the heat production values calculated from the whole-rock measurement of K, Th and U from typical cratonic peridotites (e.g., Fig. 1.5b). Yet, the similarity of the H_m through time in the Kaapvaal Craton is in stark contrast to metasomatism recorded in MARID/PKP xenoliths (Chapter3), although as previously stated these rocks may not be representative of metasomatism of the whole mantle lithosphere. More tellingly, the similarity of H_m between the Slave and Kaapvaal Cratons would require almost identical metasomatic histories which we argue is unlikely. Indeed, such similar metasomatic histories are unsupported by the direct dating of diamond growth events in the lithospheric root (Howell et al., 2020) or the history of surface expressions of magmas (e.g., kimberlite; orangeite; continental flood basalts), which would be expected to drive metasomatism through their passage through the lithosphere. Rather, the consistently high H_m seen in Slave and Kaapvaal Cratons, the latter also through time, is more consistent with disequilibrium of the crust and mantle resulting in 'apparent' rather than actual heat generation in the root. The 'Apparent' generation in the root derives from the characteristic time for heat diffusion thick root is such that the cratonic lithosphere cannot be in thermal equilibrium with the instantaneous rate of heat production in the coupled crust and mantle (Michaut and Jaupart, 2004), even in circumstances where the lithospheric mantle has had zero internal heat production since its formation. This result can be reconciled with the low internal radiogenic heat production of reconstituted (e.g., Emo and Kamber, 2021) cratonic peridotites (McIntyre et al., 2021) that imply that most of the exogenous K, Th, and U (i.e., that which is unsupported by the major constituent phases in peridotite) simply results from contamination from their host magmas (e.g., Eggins et al., 1998).

In either case, the presence or absence of either real or 'apparent' heat production for modelling geotherms has a large impact on our estimates of the depth to the LAB, with the choice of H_m a key parameter. It follows that the blanket assumption of a lithospheric mantle with zero heat production in steady state (real or otherwise) is not consistent with *PT* data from mantle xenoliths. This may lead to the underestimation of LAB depths in

Earth's cratons and an overestimation of the capacity of cratons to accommodate heat loss from the underlying convecting mantle. Strictly speaking this also means that steady state formulations of geotherms (such as those demonstrated in this thesis) are likely inaccurate representations of the thermal conditions of the cratonic lithosphere. However, any computation that attempts to correct for thermal relaxation of the lithosphere requires either the heat flux or temperature at the LAB as a boundary condition and an assumption that these simply decay through time in line with secular cooling since craton formation (Michaut and Jaupart, 2004). As Chapter 2 of this thesis demonstrates these conditions are unlikely to be met for the cratonic lithosphere due to widescale basal erosion that has occurred since its formation, with such erosion expected to increase both the heat flux at the LAB and basal temperatures through time. Unfortunately, the lack of time-resolved diamond inclusion *PT* data, the relative paucity of *PT* data from mantle xenoliths in kimberlite eruptions prior to the Phanerozoic, and uncertainty in the secular evolution of the T_p hamper efforts to quantify changes to these key parameters.

Finding #4: The U-Pb dating system in garnet is an attractive prospect to complement other, widely utilized but costly and time intensive, methods (e.g., Lu-Hf; Sm-Nd) for dating depletion/metasomatic events in the cratonic lithospheric mantle and kimberlite emplacement

The dating of the formation of mantle peridotites remains troublesome, principally due to a paucity of mineral chronometers and due to the high temperatures observed at depth in the cratonic mantle lithosphere. Perhaps, due to their highly depleted nature it is, or has been, assumed that a wide array of dating methods available for crustal rocks (e.g., U-Pb) would be unsuitable for depleted (i.e., not metasomatised or zircon bearing) mantle peridotites. As a result only time-intensive and costly high precision (i.e., low volume) solution analyses (e.g., Lu-Hf; Sm-Nd; Re-Os) are undertaken precluding the possibility of obtaining comparatively rich datasets that exist for crustal rocks.

Chapter 5 of this thesis provides the basis for a U-Pb methodology for the dating of cratonic mantle garnet in-situ making use of extremely large spot sizes and newly acquired community developed standards (Salnikova et al., 2019, 2018; Stifeeva et al., 2019) by *routine* (single collector) LA-Q-ICPMS. Due to the high ambient temperatures in the mantle prior to entrainment in their host kimberlite, it is inferred that no radiogenic lead is not retained within the garnet until it is entrained, erupted and subsequently cooled in the

kimberlite at the Earth's surface. In this situation garnet U-Pb might be used a useful method for easily obtaining the age of kimberlite emplacement, such as is proven in Chapter 5 for the Bultfontein kimberlite. Perhaps of more interest are the U-Pb data from the Roberts Victor kimberlite which implies the partial retention of ancient radiogenic lead, where garnet plot along a single discordia line with an Archean upper intercept age consistent with either the suturing of the eastern and western blocks of the Kaapvaal craton at ~3.0 Ga along the Colesburg lineament (Schmitz et al., 2004) or depletion events recorded by the Lu-Hf and Re-Os systems in the Kaapvaal cratonic mantle (Pearson et al., 1995a; Lazarov et al., 2009; Shu et al., 2013). Some Roberts Victor garnet (~ 850 °C) correspond to previous estimates (Mezger et al. 1989) of the activation temperature of Pb in the almandine-pyrope system (> 800 °C) suggesting that these garnets could be retaining ancient radiogenic Pb. As the Roberts Victor data derive from mineral separates from the kimberlite rather than from mantle xenoliths it is possible that single disaggregated crystals (i.e., xenocrysts rather than xenoliths) could represent a greater range of temperatures (and hence depths) than is typically found in mantle xenoliths. As a results xenocrysts might provide not only age of emplacement but previous garnet growth event(s) such as those of mantle formation or those relating to later metasomatism, at a far greater fidelity than is possible with costly pre-existing (multi-collector solution) ICPMS methodologies (e.g., Lu-Hf; Re-Os).

Future work

Due to the high ambient temperatures in the cratonic mantle, mantle xenoliths record the prevailing thermal conditions in the lithosphere at the time of the entrainment in their host magmas. In this thesis only mantle xenoliths entrained in < 175 Ma and 1.15 Ga Premier kimberlites were considered, offering two snapshots of the thermal conditions of cratonic lithosphere through time. Whilst, kimberlite emplacement ages are heavily skewed to < 250 Ma (Tappe et al., 2018), the absolute dating of diamond inclusions also offers an attractive method to place firm constraints on the thermal conditions in the cratonic lithosphere through time, as diamond ages are heavily skewed to the Archean (e.g., Howell et al., 2020). As diamond has amongst the lowest diffusivities of any natural material (e.g., Koga et al., 2005), diamond inclusions (which can provide *PT* data) record the thermal conditions at moment at which a diamond inclusion is encapsulated. Unfortunately, diamond inclusions that provide *PT* information have to date provided no absolute ages of when the diamond inclusion was trapped.

Chapter 5 of this thesis provides a methodology for the dating of peridotitic garnet by the U-Pb method, which could be applied to garnet inclusions in diamond. Garnet is by far the most common inclusion paragenesis found in diamond (Stachel and Harris, 2008) and garnet can provide temperatures for the time of its entrapment through Ni-in-grt thermometry (e.g., Ryan et al., 1996) and rarely when present with orthopyroxene depth of formation (e.g., Phillips et al., 2004). Depth of origin might also be estimated for single inclusions of garnet might also be estimated by elastic geobarometry (Mazzucchelli et al., 2021). As such garnet inclusions in diamond offer a unique opportunity to probe the thermal conditions as far back as the Archean due to their ubiquitous formation within the lithospheric mantle since the stabilization of Earth's cratons (e.g., Richardson et al., 1984, 2001, 2004; Pearson et al., 1998, 1999; Stachel et al., 2006; Westerlund et al., 2006; Aulbach et al., 2009b; Smart et al., 2016; Koornneef et al., 2017).

Further constraints on the dynamic evolution of the thermal conditions in the lithosphere could allow for a better understanding of the evolution of the basal heat flux occurred in the Earth's cratonic lithosphere. Such information would allow for the computation of more accurate instantaneous solutions that correctly account for the thermal disequilibrium of the crust and lithosphere mantle over long timescales and a fuller understanding of problems concerning the thermal history of the Earth.

References

Agashev, A.M., Chervyakovskaya, M. V., Serov, I. V., Tolstov, A. V., Agasheva, E. V., and Votyakov, S.L., 2020, Source rejuvenation vs. re-heating: Constraints on Siberian kimberlite origin from U[sbnd]Pb and Lu[sbnd]Hf isotope compositions and geochemistry of mantle zircons: Lithos, v. 364–365, p. 105508, doi:10.1016/j.lithos.2020.105508.

Allsopp, H.L., and Barrett, D.R., 1975, Rb/Sr age determinations on South African kimberlite pipes: Physics and Chemistry of the Earth, v. 9, p. 605–617, doi:10.1016/0079-1946(75)90041-5.

Allwood, A.C., Walter, M.R., Kamber, B.S., Marshall, C.P., and Burch, I.W., 2006, Stromatolite reef from the Early Archaean era of Australia: Nature, v. 441, p. 714–718, doi:10.1038/nature04764.

An, M., Feng, M., and Zhao, Y., 2009, Destruction of lithosphere within the north China craton inferred from surface wave tomography: Geochemistry, Geophysics, Geosystems, v. 10, doi:10.1029/2009GC002562.

Andersen, T., 2005, Detrital zircons as tracers of sedimentary provenance: Limiting conditions from statistics and numerical simulation: Chemical Geology, v. 216, p. 249–270, doi:10.1016/j.chemgeo.2004.11.013.

Anderson, T.W., and Darling, D.A., 1952, Asymptotic theory of some "Goodness of fit" criteria based on stoichastic processes: The Annals of Mathematical Statistics, p. 193–212, doi:10.1214/aoms/1177733256.

Arndt, N.T., Coltice, N., Helmstaedt, H., and Gregoire, M., 2009, Origin of Archean subcontinental lithospheric mantle: Some petrological constraints: Lithos, v. 109, p. 61–71, doi:10.1016/j.lithos.2008.10.019.

Artemieva, I.M., 2011, Lithosphere : an interdisciplinary approach: New York, Cambridge University Press, 773 p.

Artemieva, I.M., and Mooney, W.D., 2002, On the relations between cratonic lithosphere thickness, plate motions, and basal drag: Tectonophysics, v. 358, p. 211–231, doi:10.1016/S0040-1951(02)00425-0.

Aulbach, S., Griffin, W.L., Pearson, N.J., and O'Reilly, S.Y., 2013, Nature and timing of metasomatism in the stratified mantle lithosphere beneath the central Slave craton (Canada): Chemical Geology, v. 352, p. 153–169, doi:10.1016/j.chemgeo.2013.05.037.

Aulbach, S., Griffin, W.L., Pearson, N.J., O'Reilly, S.Y., and Doyle, B.J., 2007, Lithosphere formation in the central Slave Craton (Canada): Plume subcretion or lithosphere accretion? Contributions to Mineralogy and Petrology, v. 154, p. 409–427, doi:10.1007/s00410-007-0200-1.

Aulbach, S., Shirey, S.B., Stachel, T., Creighton, S., Muehlenbachs, K., and Harris, J.W., 2009a, Diamond formation episodes at the southern margin of the Kaapvaal Craton: Re-Os systematics of sulfide inclusions from the Jagersfontein Mine: Contributions to Mineralogy and Petrology, v. 157, p. 525–540, doi:10.1007/s00410-008-0350-9.

Aulbach, S., Stachel, T., Creaser, R.A., Heaman, L.M., Shirey, S.B., Muehlenbachs, K., Eichenberg, D., and Harris, J.W., 2009b, Sulphide survival and diamond genesis during formation and evolution of Archaean subcontinental lithosphere: A comparison between the Slave and Kaapvaal cratons: Lithos, v. 112, p. 747–757, doi:10.1016/j.lithos.2009.03.048.

Ballard, S., and Pollack, H.N., 1988, Modern and ancient geotherms beneath southern Africa: Earth and Planetary Science Letters, v. 88, p. 132–142.

Banerjee, S., Kyser, T.K., and Mitchell, R., 2015, Nitrogen isotopic compositions and concentrations in MARID xenoliths: Chemical Geology, v. 391, p. 83–89, doi:10.1016/j.chemgeo.2014.11.003.

Barry, P.H., Hilton, D.R., Day, J.M.D., Pernet-Fisher, J.F., Howarth, G.H., Magna, T., Agashev, A.M., Pokhilenko, N.P., Pokhilenko, L.N., and Taylor, L.A., 2015, Helium isotopic evidence for modification of the cratonic lithosphere during the Permo-Triassic Siberian flood basalt event: Lithos, v. 216–217, p. 73–80, doi:10.1016/j.lithos.2014.12.001.

Baughman, J.S., and Flowers, R.M., 2020, Mesoproterozoic burial of the Kaapvaal craton, southern Africa during Rodinia supercontinent assembly from (U-Th)/He thermochronology: Earth and Planetary

Science Letters, v. 531, p. 115930, doi:10.1016/j.epsl.2019.115930.

Bea, F., Montero, P., and Palma, J.F.M., 2018, Experimental evidence for the preservation of U-Pb isotope ratios in mantle-recycled crustal zircon grains: Scientific Reports, v. 8, p. 1–10, doi:10.1038/s41598-018-30934-4.

Becker, M., and Le Roex, A.P., 2006, Geochemistry of South African on- and off-craton, group I and group II kimberlites: Petrogenesis and source region evolution: Journal of Petrology, v. 47, p. 673–703, doi:10.1093/petrology/egi089.

Bell, D.R., Grégoire, M., Grove, T.L., Chatterjee, N., Carlson, R.W., and Buseck, P.R., 2005, Silica and volatile-element metasomatism of Archean mantle: A xenolith-scale example from the Kaapvaal Craton: Contributions to Mineralogy and Petrology, v. 150, p. 251–267, doi:10.1007/s00410-005-0673-8.

Belousova, E.A., Griffin, W.L., O'Reilly, S.Y., and Fisher, N.I., 2002, Igneous zircon: Trace element composition as an indicator of source rock type: Contributions to Mineralogy and Petrology, v. 143, p. 602–622, doi:10.1007/s00410-002-0364-7.

Belousova, E.A., Griffin, W.L., and Pearson, N.J., 1998, Trace element composition and cathodoluminescence properties of southern African kimberlitic zircons: Mineralogical Magazine, v. 62, p. 355–366, doi:10.1180/002646198547747.

Belousova, E.A., Jackson, S.E., O'Reilly, S.Y., Griffin, W.L., and Shee, S.R., 2001, Two age populations of zircons from the Timber Creek kimberlites, Northern Territory, as determined by laser ablation ICP MS analysis: Australian Journal of Earth Sciences, v. 48, p. 757–765, doi:10.1046/j.1440-0952.2001.485894.x.

Black, L.P. et al., 2004, Improved 206Pb/238U microprobe geochronology by the monitoring of a trace-element-related matrix effect; SHRIMP, ID-TIMS, ELA-ICP-MS and oxygen isotope documentation for a series of zircon standards: Chemical Geology, v. 205, p. 115–140, doi:10.1016/j.chemgeo.2004.01.003.

Black, L.P., Gale, N.H., Moorbath, S., Pankhurst, R.J., and McGregor, V.R., 1971, Isotopic dating of very early Precambrian amphibolite facies gneisses from the Godthaab district, West Greenland: Earth and Planetary Science Letters, v. 12, p. 245–259, doi:10.1016/0012-821X(71)90208-1.

Blackburn, T.J., Bowring, S.A., Perron, J.T., Mahan, K.H., Dudas, F.O., and Barnhart, K.R., 2012, An exhumation history of continents over billion-year time scales: Science, v. 335, p. 73–76, doi:10.1126/science.1213496.

Bleeker, W., 2003, The late Archean record: A puzzle in ca. 35 pieces: Lithos, v. 71, p. 99–134, doi:10.1016/j.lithos.2003.07.003.

Bowring, S. a., and Williams, I.S., 1999, Priscoan (4.00-4.03 Ga) orthogneisses from northwestern Canada: Contributions to Mineralogy and Petrology, v. 134, p. 3–16, doi:10.1007/s004100050465.

Boyd, F.R., 1989, Compositional distinction between oceanic and cratonic lithosphere: Earth and Planetary Science Letters, v. 96, p. 15–26, doi:10.1016/0012-821X(89)90120-9.

Boyd, F.R., and Mertzman, S.A., 1987, Composition of structure of the Kaapvaal lithosphere, southern Africa: Magmatic Processes-Physiochemical Principles, p. 13–24.

Broadley, M.W., Ballentine, C.J., Chavrit, D., Dallai, L., and Burgess, R., 2016, Sedimentary halogens and noble gases within Western Antarctic xenoliths: Implications of extensive volatile recycling to the sub continental lithospheric mantle: Geochimica et Cosmochimica Acta, v. 176, p. 139–156, doi:10.1016/j.gca.2015.12.013.

Canil, D., 2004, Mildly incompatible elements in peridotites and the origins of mantle lithosphere: Lithos, v. 77, p. 375–393, doi:10.1016/j.lithos.2004.04.014.

Celli, N.L., Lebedev, S., Schaeffer, A.J., and Gaina, C., 2020, African cratonic lithosphere carved by mantle plumes: Nature Communications, v. 11, doi:10.1038/s41467-019-13871-2.

Cherniak, D.J., and Watson, E.B., 2001, Pb diffusion in zircon: Chemical Geology, v. 172, p. 5–24, doi:10.1016/S0009-2541(00)00233-3.

Clifford, T.N., 1966, Tectono-metallogenic units and metallogenic provinces of Africa: Earth and Planetary Science Letters, v. 1, p. 421–434, doi:10.1016/0012-821X(66)90039-2.

Collerson, K.D., Williams, Q., Ewart, A.E., and Murphy, D.T., 2010, Origin of HIMU and EM-1 domains sampled by ocean island basalts, kimberlites and carbonatites: The role of CO2-fluxed lower mantle melting in thermochemical upwellings: Physics of the Earth and Planetary Interiors, v. 181, p. 112–131, doi:10.1016/j.pepi.2010.05.008.

Condie, K.C., 1993, Chemical Composition and Evolution of the Upper Continental Crust : Contrasting Results from Surface and Shales: Chemical Geology, v. 104, p. 1–37, doi:10.1016/0009-2541(93)90140-E.

Corfu, F., Hanchar, J.M., Hoskin, P.W.O., and Kinny, P., 2003, Atlas of zircon textures: Reviews in Mineralogy and Geochemistry, v. 53, p. 469–500.

Creaser, R.A., Gütter, H., Carlson, J., and Crawford, B., 2004, Macrocrystal phlogopite Rb-Sr dates for the Ekati property kimberlites, Slave Province, Canada: Evidence for multiple intrusive episodes in the Paleocene and Eocene: Lithos, v. 76, p. 399–414, doi:10.1016/j.lithos.2004.03.039.

Creighton, S., Stachel, T., Matveev, S., Höfer, H., McCammon, C., and Luth, R.W., 2009, Oxidation of the Kaapvaal lithospheric mantle driven by metasomatism: Contributions to Mineralogy and Petrology, v. 157, p. 491–504, doi:10.1007/s00410-008-0348-3.

Darbyshire, F.A., Eaton, D.W., Frederiksen, A.W., and Ertolahti, L., 2007, New insights into the lithosphere beneath the superior province from Rayleigh wave dispersion and receiver function analysis: Geophysical Journal International, v. 169, p. 1043–1068, doi:10.1111/j.1365-246X.2006.03259.x.

Dave, R., and Li, A., 2016, Destruction of the Wyoming craton: Seismic evidence and geodynamic processes: Geology, v. 44, p. 883–886, doi:10.1130/G38147.1.

Davis, G.L., 1977, The ages and uranium contents of zircons from kimberlites and associated rockstle, *in* Proceedings of the II International Kimberlite Conference, Santa Fe, 2, p. 67–69.

Davis, W.J., Canil, D., MacKenzie, J.M., and Carbno, G.B., 2003, Petrology and U–Pb geochronology of lower crustal xenoliths and the development of a craton, Slave Province, Canada: Lithos, v. 71, p. 541–573, doi:10.1016/S0024-4937(03)00130-0.

Dawson, J.B., 1984, Contrasting types of upper-mantle metasomatism., *in* Developments in petrology, Elsevier, v. 11, p. 289–294, doi:10.1016/b978-0-444-42274-3.50030-5.

Dawson, J.B., and Smith, J. V., 1977, The MARID (mica-amphibole-rutile-ilmenite-diopside) suite of xenoliths in kimberlite: Geochimica et Cosmochimica Acta, v. 41, doi:10.1016/0016-7037(77)90239-3.

Day, H.W., 2012, A revised diamond-graphite transition curve: American Mineralogist, v. 97, p. 52–62, doi:10.2138/am.2011.3763.

DeWolf, C.P., Zeissler, C.J., Halliday, A.N., Mezger, K., and Essene, E.J., 1996, The role of inclusions in U-Pb , and Sm-Nd garnet geochronology: Stepwise dissolution experiments and trace uranium mapping by fission track analysis: Geochimica et Cosmochimica Acta, v. 60, p. 121–136.

Doin, M.-P., Fleitout, L., and Christensen, U., 1997, Mantle convection and stability of depleted and undepleted continental lithosphere: Journal of Geophysical Research: Solid Earth, v. 102, p. 2771–2787, doi:10.1029/96JB03271.

Dornan, T., O'Sullivan, G., O'Riain, N., Stueeken, E., and Goodhue, R., 2020, The application of machine learning methods to aggregate geochemistry predicts quarry source location: An example from Ireland: Computers and Geosciences, v. 140, p. 104495, doi:10.1016/j.cageo.2020.104495.

Eaton, D.W., Darbyshire, F., Evans, R.L., Grütter, H., Jones, A.G., and Yuan, X., 2009, The elusive lithosphere-asthenosphere boundary (LAB) beneath cratons: Lithos, v. 109, p. 1–22, doi:10.1016/j.lithos.2008.05.009.

Eggins, S.M., Rudnick, R.L., and McDonough, W.F., 1998, The composition of peridotites and their minerals: A laser-ablation ICP-MS study: Earth and Planetary Science Letters, v. 154, p. 53–71, doi:10.1016/s0012-821x(97)00195-7.

Emo, R.B., and Kamber, B.S., 2021, Evidence for highly refractory, heat producing element-depleted lower

continental crust: Some implications for the formation and evolution of the continents: Chemical Geology, v. 580, p. 120389, doi:10.1016/j.chemgeo.2021.120389.

Erlank, A.J., Waters, F.G., Hawkesworth, C.J., Haggerty, S.E., Allsopp, H.L., Rickard, R.S., and Menzies, M., 1987, Evidence for mantle metasomatism in peridotite nodules from the Kimberley pipes, South Africa, *in* Mantle metasomatism, p. 221–311.

Field, M., Stiefenhofer, J., Robey, J., and Kurszlaukis, S., 2008, Kimberlite-hosted diamond deposits of southern Africa: A review: Ore Geology Reviews, v. 34, p. 33–75, doi:10.1016/j.oregeorev.2007.11.002.

Finnerty, A.A., 1989, Xenolith-derived mantle geotherms: whither the inflection? Contributions to Mineralogy and Petrology, v. 102, p. 367–375, doi:10.1007/BF00373729.

Finnerty, A.A., and Boyd, F.R., 1987, Thermobarometry for garnet peridotites: basis for the determination of thermal and compositional structure of the upper mantle, *in* Mantle Xenoliths, Wiley & Sons, p. 381–402.

Fiorentini, M.L., O'Neill, C., Giuliani, A., Choi, E., Maas, R., Pirajno, F., and Foley, S., 2020, Bushveld superplume drove Proterozoic magmatism and metallogenesis in Australia: Scientific Reports, v. 10, p. 1–10, doi:10.1038/s41598-020-76800-0.

Fitzpayne, A., Giuliani, A., Hergt, J., Phillips, D., and Janney, P., 2018a, New geochemical constraints on the origins of MARID and PIC rocks: Implications for mantle metasomatism and mantle-derived potassic magmatism: Lithos, v. 318–319, p. 478–493, doi:10.1016/j.lithos.2018.08.036.

Fitzpayne, A., Giuliani, A., Maas, R., Hergt, J., Janney, P., and Phillips, D., 2019, Progressive metasomatism of the mantle by kimberlite melts: Sr–Nd–Hf–Pb isotope compositions of MARID and PIC minerals: Earth and Planetary Science Letters, v. 509, p. 15–26, doi:10.1016/j.epsl.2018.12.013.

Fitzpayne, A., Giuliani, A., Phillips, D., Hergt, J., Woodhead, J.D., Farquhar, J., Fiorentini, M.L., Drysdale, R.N., and Wu, N., 2018b, Kimberlite-related metasomatism recorded in MARID and PIC mantle xenoliths: Mineralogy and Petrology, v. 112, p. 71–84, doi:10.1007/s00710-018-0573-z.

Fitzpayne, A., Prytulak, J., Giuliani, A., and Hergt, J., 2020, Thallium isotopic composition of phlogopite in kimberlite-hosted MARID and PIC mantle xenoliths: Chemical Geology, v. 531, p. 119347, doi:10.1016/j.chemgeo.2019.119347.

Foley, S., 1992, Vein-plus-wall-rock melting mechanisms in the lithosphere and the origin of potassic alkaline magmas: Lithos, v. 28, p. 435–453, doi:10.1016/0024-4937(92)90018-T.

Foley, S.F., Andronikov, A. V., and Melzer, S., 2002, Petrology of ultramafic lamprophyres from the Beaver Lake area of Eastern Antarctica and their relation to the breakup of Gondwanaland: Mineralogy and Petrology, v. 74, p. 361–384, doi:10.1007/s007100200011.

Fraser, K.J., Hawkesworth, C.J., Erlank, A.J., Mitchell, R.H., and Scott-Smith, B.H., 1985, Sr, Nd and Pb isotope and minor element geochemistry of lamproites and kimberlites: Earth and Planetary Science Letters, v. 76, p. 57–70, doi:10.1016/0012-821X(85)90148-7.

Geisler, T., Pidgeon, R.T., van Bronswijk, W., and Pleysier, R., 2001, Kinetics of thermal recovery and recrystallization of partially metamict zircon: a Raman spectroscopic study: European Journal of Mineralogy, v. 13, p. 1163–1176, doi:10.1127/0935-1221/2001/0013-1163.

Gibson, S.., 2021, The lithospheric mantle as a "sink" and "source" in global volatile cycles, *in* Goldschmidt, virtual Lyon,.

Gibson, S.A., McMahon, S.C., Day, J.A., and Dawson, J.B., 2013, Highly refractory lithospheric mantle beneath thetanzanian craton: Evidence from lashaine pre-metasomatic garnet-bearing peridotites: Journal of Petrology, v. 54, p. 1503–1546, doi:10.1093/petrology/egt020.

Giuliani, A., Phillips, D., Maas, R., Woodhead, J.D., Kendrick, M.A., Greig, A., Armstrong, R.A., Chew, D., Kamenetsky, V.S., and Fiorentini, M.L., 2014, LIMA U-Pb ages link lithospheric mantle metasomatism to Karoo magmatism beneath the Kimberley region, South Africa: Earth and Planetary Science Letters, v. 401, p. 132–147, doi:10.1016/j.epsl.2014.05.044.

Giuliani, A., Phillips, D., Woodhead, J.D., Kamenetsky, V.S., Fiorentini, M.L., Maas, R., Soltys, A., and Armstrong, R.A., 2015, Did diamond-bearing orangeites originate from MARID-veined peridotites in

the lithospheric mantle? Nature Communications, v. 6, p. 6837, doi:10.1038/ncomms7837.

Graham, I., Burgess, J.L., Bryan, D., Ravenscroft, P.J., Thomas, E., Doyle, B.J., Hopkins, R., and Armstrong, K.A., 1999, Exploration history and geology of the Diavik kimberlites. Lacde Gras Northwest Territories, Canada, *in* 7th International Kimberlite Conference, p. 262–279.

Grégoire, M., Bell, D., and Le Roex, A.., 2002, Trace element geochemistry of phlogopite-rich mafic mantle xenoliths: their classification and their relationship to phlogopite-bearing peridotites and kimberlites revisited: Contributions to Mineralogy and Petrology, v. 142, p. 603–625, doi:10.1007/s00410-001-0315-8.

Grégoire, M., Moine, B.N., O'Reilly, S.Y., Cottin, J.Y., and Giret, A., 2000, Trace Element Residence and Partitioning in Mantle Xenoliths Metasomatized by Highly Alkaline, Silicate- and Carbonate-rich Melts (Kerguelen Islands, Indian Ocean): Journal of Petrology, v. 41, p. 477–509, doi:10.1093/petrology/41.4.477.

Griffin, W.L., Batumike, J.M., Greau, Y., Pearson, N.J., Shee, S.R., and O'Reilly, S.Y., 2014, Emplacement ages and sources of kimberlites and related rocks in southern Africa: U-Pb ages and Sr-Nd isotopes of groundmass perovskite: Contributions to Mineralogy and Petrology, v. 168, p. 1–13, doi:10.1007/s00410-014-1032-4.

Griffin, W.L., Kobussen, A.F., Babu, E.V.S.S.K., O'Reilly, S.Y., Norris, R., and Sengupta, P., 2009a, A translithospheric suture in the vanished 1-Ga lithospheric root of South India: Evidence from contrasting lithosphere sections in the Dharwar Craton: Lithos, v. 112, p. 1109–1119, doi:10.1016/j.lithos.2009.05.015.

Griffin, W.L., O'Reilly, S.Y., Afonso, J.C., and Begg, G.C., 2009b, The composition and evolution of lithospheric mantle: A re-evaluation and its tectonic implications: Journal of Petrology, v. 50, p. 1185–1204, doi:10.1093/petrology/egn033.

Griffin, W.L., O'Reilly, S.Y., Natapov, L.M., and Ryan, C.G., 2003, The evolution of lithospheric mantle beneath the Kalahari Craton and its margins: Lithos, v. 71, p. 215–241, doi:10.1016/j.lithos.2003.07.006.

Griffin, W.L., O'Reilly, S.Y., Ryan, C.G., Gaul, O., and Ionov, D.A., 1998, Secular variation in the composition of subcontinental lithospheric mantle: geophysical and geodynamic implications, *in* Structure and evolution of the Australian continent, p. 1- 26.

Griffin, W.L., Pearson, N.J., Belousova, E., Jackson, S.E., Van Achterbergh, E., O'Reilly, S.Y., and Shee, S.R., 2000, The Hf isotope composition of cratonic mantle: LAM-MC-ICPMS analysis of zircon megacrysts in kimberlites: Geochimica et Cosmochimica Acta, v. 64, p. 133–147, doi:10.1016/S0016-7037(99)00343-9.

Grigné, C., and Labrosse, S., 2001, Effects of continents on Earth cooling' thermal blanketing and depletion in radioactive elements: Geophysical Research Letters, v. 28, p. 2707–2710.

Grütter, H.S., Gurney, J.J., Menzies, A.H., and Winter, F., 2004, An updated classification scheme for mantle-derived garnet, for use by diamond explorers: Lithos, v. 77, p. 841–857, doi:10.1016/j.lithos.2004.04.012.

Gurney, J.J., Jakob, W.R.O., and Dawson, J.B., 1979, Megacrysts from the Monastery Kimberlite Pipe, South Africa, *in* The Mantle Sample: Inclusion in Kimberlites and Other Volcanics, p. 227–243, doi:10.1029/sp016p0227.

Haggerty, S.E., Grey, I.E., Madsen, I.C., Criddle, A.J., Stanley, C.J., and Erlank, A.J., 1989, Hawthorneite, Ba[Ti3Cr4Fe4Mg]O19: a new metasomatic magnetoplumbite-type mineral from the upper mantle: American Mineralogist, v. 74, p. 668–675.

Haggerty, S.E., and Sautter, V., 1990, Ultradeep (> 300 Kilometers) Ultramafic Xenoliths : Petrological Evidence from the Transition Zone: Science, v. 252, p. 827–830.

Hanson, R.E., Crowley, J.L., Bowring, S.A., Ramezani, J., Gose, W.A., Dalziel, I.W.D., Pancake, J.A., Seidel, E.K., Blenkinsop, T.G., and Mukwakwami, J., 2004, Coeval large-scale magmatism in the Kalahari and Laurentian cratons during Rodinia assembly: Science, v. 304, p. 1126–1129, doi:10.1126/science.1096329.

Hanson, E.K., Moore, J.M., Bordy, E.M., Marsh, J.S., Howarth, G., and Robey, J.V.A., 2009, Cretaceous

erosion in central South Africa: Evidence from upper-crustal xenoliths in kimberlite diatremes: South African Journal of Geology, v. 112, p. 125–140, doi:10.2113/gssajg.112.2.125.

Hasterok, D., and Chapman, D.S., 2011, Heat production and geotherms for the continental lithosphere: Earth and Planetary Science Letters, v. 307, p. 59–70, doi:10.1016/j.epsl.2011.04.034.

Hawkesworth, C.J., Erlank, A.J., Kempton, P.D., and Waters, F.G., 1990, Mantle metasomatism: Isotope and trace-element trends in xenoliths from Kimberley, South Africa: Chemical Geology, v. 85, p. 19–34, doi:10.1016/0009-2541(90)90121-M.

Hawkesworth, C., and Jaupart, C., 2021, Heat flow constraints on the mafic character of Archean continental crust: Earth and Planetary Science Letters, v. 571, p. 117091, doi:10.1016/j.epsl.2021.117091.

Heaman, L.M., Creaser, R.A., Cookenboo, H.O., and Chacko, T., 2006, Multi-stage modification of the northern Slave mantle lithosphere: Evidence from zircon- and diamond-bearing eclogite xenoliths entrained in Jericho Kimberlite, Canada: Journal of Petrology, v. 47, p. 821–858, doi:10.1093/petrology/egi097.

Heaman, L.M., Kjarsgaard, B.A., and Creaser, R.A., 2003, The timing of kimberlite magmatism in North America: Implications for global kimberlite genesis and diamond exploration: Lithos, v. 71, p. 153–184, doi:10.1016/j.lithos.2003.07.005.

Heaman, L.M., Phillips, D., and Pearson, D.G., 2019, Dating kimberlites: Methods and emplacement patterns through time: Elements, v. 15, p. 399–404, doi:10.2138/GSELEMENTS.15.6.399.

Helmstaedt, H., and Schulze, D.J., 1989, Southern African kimberlites and their mantle sample : Implicati ....: pp. 358-368 p.

Herzberg, C., 2004, Geodynamic information in peridotite petrology: Journal of Petrology, v. 45, p. 2507–2530, doi:10.1093/petrology/egh039.

Herzberg, C., Condie, K., and Korenaga, J., 2010, Thermal history of the Earth and its petrological expression: Earth and Planetary Science Letters, v. 292, p. 79–88, doi:10.1016/j.epsl.2010.01.022.

Hirth, G., Evans, R.L., and Chave, A.D., 2000, Comparison of continental and oceanic mantle electrical conductivity: Is the Archean lithosphere dry? Geochemistry, Geophysics, Geosystems, v. 1, doi:10.1029/2000GC000048.

Hoare, B.C., O'Sullivan, G., and Tomlinson, E.L., 2021a, Metasomatism of the Kaapvaal Craton during Cretaceous intraplate magmatism revealed by combined zircon U-Pb isotope and trace element analysis: Chemical Geology, v. 578, p. 120302, doi:10.1016/j.chemgeo.2021.120302.

Hoare, B.C., Tomlinson, E.L., Barnes, J.D., Tappe, S., Marks, M.A.W., Epp, T., Caulfield, J., and Riegler, T., 2021b, Tracking halogen recycling and volatile loss in kimberlite magmatism from Greenland: Evidence from combined F-Cl-Br and δ37Cl systematics: Lithos, v. 385, p. 105976, doi:10.1016/j.lithos.2021.105976.

Höfer, H.E., Lazarov, M., Brey, G.P., and Woodland, A.B., 2009, Oxygen fugacity of the metasomatizing melt in a polymict peridotite from Kimberley: Lithos, v. 112, p. 1150–1154, doi:10.1016/j.lithos.2009.05.037.

Hofmeister, A.M., 1999, Mantle values of thermal conductivity and the geotherm from phonon lifetimes: Science, v. 283, p. 1699–1706, doi:10.1126/science.283.5408.1699.

Hoskin, P.W.O., and Schaltegger, U., 2018, The composition of zircon and igneous and metamorphic petrogenesis: Zircon, p. 27–62, doi:10.1515/9781501509322-005.

Howarth, G.H., Barry, P.H., Pernet-Fisher, J.F., Baziotis, I.P., Pokhilenko, N.P., Pokhilenko, L.N., Bodnar, R.J., Taylor, L.A., and Agashev, A.M., 2014, Superplume metasomatism: Evidence from Siberian mantle xenoliths: Lithos, v. 184–187, p. 209–224, doi:10.1016/j.lithos.2013.09.006.

Howell, D. et al., 2020, Deep carbon through time: Earth's diamond record and its implications for carbon cycling and fluid speciation in the mantle: Geochimica et Cosmochimica Acta, v. 275, p. 99–122, doi:10.1016/j.gca.2020.02.011.

Huang, Y.M., Van Calsteren, P., and Hawkesworth, C.I., 1995, The evolution of the lithosphere in southern

Africa: A perspective on the basic granulite xenoliths from kimberlites in South Africa: Geochimica et Cosmochimica Acta, v. 59, p. 4905–4920, doi:10.1016/0016-7037(95)00335-5.

Jackson, C.G., and Gibson, S.A., 2018, Preservation of systematic Ni and Cr heterogeneity in otherwise homogeneous mantle olivine: Implications for timescales of post-metasomatism re-equilibration: Lithos, v. 318–319, p. 448–463, doi:10.1016/j.lithos.2018.08.026.

Jahn, B.M., and Condie, K.C., 1995, Evolution of the Kaapvaal Craton as viewed from geochemical and SmNd isotopic analyses of intracratonic pelites: Geochimica et Cosmochimica Acta, v. 59, p. 2239–2258, doi:10.1016/0016-7037(95)00103-7.

Janney, P.E., Shirey, S.B., Carlson, R.W., Pearson, D.G., Bell, D.R., le Roex, A.P., Ishikawa, A., Nixon, P.H., and Boyd, F.R., 2010, Age, composition and thermal characteristics of South African off-craton mantle lithosphere: Evidence for a multi-stage history: Journal of Petrology, v. 51, p. 1849–1890, doi:10.1093/petrology/egq041.

Jarosewich, E., 2002, Smithsonian Microbeam Standards: Journal of Research of the National Institute of Standards and Technology, v. 107, p. 681, doi:10.6028/jres.107.054.

Jarosewich, E., Nelen, J. a, and Norberg, J., 1980, Reference samples for electron microprobe analysis: Geostand. Newsl., v. 4, p. 43–47.

Jaupart, C., and Mareschal, J.C., 2007, 6.05 Heat Flow and Thermal Structure of the Lithosphere, *in* Treatise of Geochemistry,.

Jaupart, C., and Mareschal, J.C., 1999, The thermal structure and thickness of continental roots: Developments in Geotectonics, v. 24, p. 93–114, doi:10.1016/S0419-0254(99)80007-X.

Jochum, K.P., Willbold, M., Raczek, I., Stoll, B., and Herwig, K., 2005, Chemical characterisation of the USGS reference glasses GSA-1G, GSC-1G, GSD-1G, GSE-1G, BCR-2G, BHVO-2G and BIR-1G using EPMA, ID-TIMS, ID-ICP-MS and LA-ICP-MS: Geostandards and Geoanalytical Research, v. 29, p. 285–302, doi:10.1111/j.1751-908x.2005.tb00901.x.

Jones, M.Q.W., 2017, Heat flow in the Bushveld Complex, South Africa: implications for upper mantle structure: South African Journal of Geology, v. 120, p. 351–370, doi:10.25131/gssajg.120.3.351.

Jones, A.G., Lezaeta, P., Ferguson, I.J., Chave, A.D., Evans, R.L., Garcia, X., and Spratt, J., 2003, The electrical structure of the Slave craton: Lithos, v. 71, p. 505–527, doi:10.1016/j.lithos.2003.08.001.

Jordan, T.H., 1988, Structure and formation of the continental tectosphere: Journal of Petrology, v. Special_Vo, p. 11–37, doi:10.1093/petrology/Special_Volume.1.11.

Jordan, T.H., 1975, The Continental Tectosphere: Reviews of Geophysics and Space Physics, v. 13, p. 1–12.

Jung, S., and Mezger, K., 2003, U-Pb garnet chronometry in high-grade rocks - Case studies from the central Damara orogen (Namibia) and implications for the interpretation of Sm-Nd garnet ages and the role of high U-Th inclusions: Contributions to Mineralogy and Petrology, v. 146, p. 382–396, doi:10.1007/s00410-003-0506-6.

Kamber, B.S., 2015, The evolving nature of terrestrial crust from the Hadean, through the Archaean, into the Proterozoic: Precambrian Research, v. 258, p. 48–82, doi:10.1016/j.precamres.2014.12.007.

Kamber, B.S., and Tomlinson, E.L., 2019, Petrological, mineralogical and geochemical peculiarities of Archaean cratons: Chemical Geology, v. 511, p. 123–151, doi:10.1016/j.chemgeo.2019.02.011.

Kinny, P.D., Compston, W., Bristow, J.W., and Williams, I.S., 1989, Archean mantle xenocrysts in a Permian kimberlite: two generations of kimerlitic zircon in Jwaneng DK2, southern Botswana, *in* In: Ross, J. (ed.) Proceedings of the Fourth International Kimberlite Conference 2, Kimberlites and Related Rocks: their Mantle/Crus, Geological Society of Australia Special Publication, p. 14, 833–842.

Kjarsgaard, B.A., Heaman, L.M., Sarkar, C., and Pearson, D.G., 2017, The North America mid-Cretaceous kimberlite corridor: Wet, edge-driven decompression melting of an OIB-type deep mantle source: Geochemistry, Geophysics, Geosystems, v. 18, p. 1711–1738, doi:10.1002/2016GC006454.Received.

Koga, K.T., Walter, M.J., Nakamura, E., and Kobayashi, K., 2005, Carbon self-diffusion in a natural diamond: Physical Review B - Condensed Matter and Materials Physics, v. 72, p. 8–11, doi:10.1103/PhysRevB.72.024108.

Konzett, J., Armstrong, R.A., and Günther, D., 2000, Modal metasomatism in the Kaapvaal craton lithosphere: Constraints on timing and genesis from U-Pb zircon dating of metasomatized peridotites and MARID-type xenoliths: Contributions to Mineralogy and Petrology, v. 139, p. 704–719, doi:10.1007/s004100000160.

Konzett, J., Armstrong, R.A., Sweeney, R.J., and Compston, W., 1998, The timing of MARID metasomatism in the Kaapvaal mantle: an ion probe study of zircons from MARID xenoliths: Earth and Planetary Science Letters, v. 160, p. 133–145, doi:10.1016/S0012-821X(98)00073-9.

Konzett, J., Wirth, R., Hauzenberger, C., and Whitehouse, M., 2013, Two episodes of fluid migration in the Kaapvaal Craton lithospheric mantle associated with Cretaceous kimberlite activity: Evidence from a harzburgite containing a unique assemblage of metasomatic zirconium-phases: Lithos, v. 182–183, p. 165–184, doi:10.1016/j.lithos.2013.10.005.

Koornneef, J.M., Gress, M.U., Chinn, I.L., Jelsma, H.A., Harris, J.W., and Davies, G.R., 2017, Archaean and Proterozoic diamond growth from contrasting styles of large-scale magmatism: Nature Communications, v. 8, doi:10.1038/s41467-017-00564-x.

Korenaga, J., 2018, Crustal evolution and mantle dynamics through Earth history: Philosophical Transactions of the Royal Society A: Mathematical, Physical and Engineering Sciences, v. 376, doi:10.1098/rsta.2017.0408.

Korenaga, J., 2008, Urey Ratio and the Structure and Evolution of Earth's Mantle: American Geophysical Union, p. 1–32, doi:10.1029/2007RG000241.1.INTRODUCTION.

Kramers, J.D., Roddick, J.C.M., and Dawson, J.B., 1983, Trace element and isotope studies on veined, metasomatic and "MARID" xenoliths from Bultfontein, South Africa.: Earth and Planetary Science Letters, v. 65, p. 90–106, doi:10.1016/0012-821X(83)90192-9.

Kramers, J.D., and Smith, C.B., 1983, A feasibility study of U–Pb and Pb–Pb dating of kimberlites using groundmass mineral fractions and whole-rock samples: Chemical Geology, v. 41, p. 23–38, doi:10.1016/S0009-2541(83)80003-5.

Kuiper, K.F., Deino, A., Hilgen, F.J., Krijgsman, W., Renne, P.R., and Wijbrans, J.R., 2008, Synchronizing rock clocks of earth history: Science, v. 320, p. 500–504, doi:10.1126/science.1154339.

Larsen, L.M., Heaman, L.M., Creaser, R. a., Duncan, R. a., Frei, R., and Hutchison, M., 2009, Tectonomagmatic events during stretching and basin formation in the Labrador Sea and the Davis Strait: evidence from age and composition of Mesozoic to Palaeogene dyke swarms in West Greenland: Journal of the Geological Society, v. 166, p. 999–1012, doi:10.1144/0016-76492009-038.

Lawless, P.J., Gurney, J.J., and Dawson, J.B., 1979, Polymict Peridotites from the Bultfontein and de Beers Mines, Kimberly, South Africa, *in* F.R. Boyd, H.O.A. Meyer (Eds.), The Mantle Sample. 2nd International Kimberlte Conference, v. 16, p. 145–155.

Lazarov, M., Brey, G.P., and Weyer, S., 2009, Time steps of depletion and enrichment in the Kaapvaal craton as recorded by subcalcic garnets from Finsch (SA): Earth and Planetary Science Letters, v. 279, p. 1–10, doi:10.1016/j.epsl.2008.12.015.

Lee, C.-T.A., 2005, Geochemical / petrologic constraints on the origin of cratonic mantle: AGU Monographs, v. 164, p. 1–23, doi:10.1029/164GM08.

Lenardic, A., Cooper, C.M., and Moresi, L., 2011, A note on continents and the Earth's Urey ratio: Physics of the Earth and Planetary Interiors, v. 188, p. 127–130, doi:10.1016/j.pepi.2011.06.008.

Liati, A., Franz, L., Gebauer, D., and Fanning, C.M., 2004, The timing of mantle and crustal events in South Namibia, as defined by SHRIMP-dating of zircon domains from a garnet peridotite xenolith of the Gibeon Kimberlite Province: Journal of African Earth Sciences, v. 39, p. 147–157, doi:10.1016/j.jafrearsci.2004.07.054.

Liu, J., Pearson, D.G., Wang, L.H., Mather, K.A., Kjarsgaard, B.A., Schaeffer, A.J., Irvine, G.J., Kopylova, M.G., and Armstrong, J.P., 2021, Plume-driven recratonization of deep continental lithospheric mantle: Nature, v. 592, p. 732–736, doi:10.1038/s41586-021-03395-5.

Luvizotto, G.L. et al., 2009, Rutile crystals as potential trace element and isotope mineral standards for microanalysis: Chemical Geology, v. 261, p. 346–369, doi:10.1016/j.chemgeo.2008.04.012.

Mareschal, J.C., Nyblade, A., Perry, H.K.C., Jaupart, C., and Bienfait, G., 2004, Heat flow and deep lithospheric thermal structure at Lac de Gras, Slave Province, Canada: Geophysical Research Letters, v. 31, p. 2–5, doi:10.1029/2004GL020133.

Mather, K.A., Pearson, D.G., McKenzie, D., Kjarsgaard, B.A., and Priestley, K., 2011, Constraints on the depth and thermal history of cratonic lithosphere from peridotite xenoliths, xenocrysts and seismology: Lithos, v. 125, p. 729–742, doi:10.1016/j.lithos.2011.04.003.

Mazzucchelli, M.L., Angel, R.J., and Alvaro, M., 2021, EntraPT: An online platform for elastic geothermobarometry: American Mineralogist, v. 106, p. 830–837, doi:10.2138/am-2021-7693CCBYNCND.

McDonough, W.F., and Sun, S. s., 1995, The composition of the Earth: Chemical Geology, v. 120, p. 223–253, doi:10.1016/0009-2541(94)00140-4.

McIntyre, T., Kublik, K., Currie, C., and Pearson, D.G., 2021, Heat generation in cratonic mantle roots – new trace element constraints from mantle xenoliths and implications for cratonic geotherms: Geochemistry, Geophysics, Geosystems, doi:10.1029/2021gc009691.

McKenzie, D., Jackson, J., and Priestley, K., 2005, Thermal structure of oceanic and continental lithosphere: Earth and Planetary Science Letters, v. 233, p. 337–349, doi:10.1016/j.epsl.2005.02.005.

McKenzie, D., and Priestley, K., 2016, Speculations on the formation of cratons and cratonic basins: Earth and Planetary Science Letters, v. 435, p. 94–104, doi:10.1016/j.epsl.2015.12.010.

McKenzie, D., and Priestley, K., 2008, The influence of lithospheric thickness variations on continental evolution: Lithos, v. 102, p. 1–11, doi:10.1016/j.lithos.2007.05.005.

Mezger, K., Hanson, G.N., and Bohlen, S.R., 1989, U-Pb systematics of garnet: dating the growth of garnet in the late Archean Pikwitonei granulite domain at Cauchon and Natawahunan Lakes, Manitoba, Canada: Contributions to Mineralogy and Petrology, v. 101, p. 136–148, doi:10.1007/BF00375301.

Mezger, K., and Krogstad, E.J., 1997, Interpretation of discordant U-Pb zircon ages: An evaluation: Journal of Metamorphic Geology, v. 15, p. 127–140, doi:10.1111/j.1525-1314.1997.00008.x.

Mezger, K., Rawnsley, C.M., Bohlen, S.R., and Hanson, G.N., 1991, U-Pb Garnet , Sphene , Monazite , and Rutile Ages : Implications for the Duration of High- Grade Metamorphism and Cooling Histories , Adirondack Mts ., New York Author (s): K . Mezger , C . M . Rawnsley , S . R . Bohlen and G . N . Hanson Published by : The Journal of Geology, v. 99, p. 415–428.

Michaut, C., and Jaupart, C., 2004, Nonequilibrium temperatures and cooling rates in thick continental lithosphere: Geophysical Research Letters, v. 31, p. 1–4, doi:10.1029/2004GL021092.

Michaut, C., and Jaupart, C., 2007, Secular cooling and thermal structure of continental lithosphere: Earth and Planetary Science Letters, v. 257, p. 83–96, doi:10.1016/j.epsl.2007.02.019.

Michaut, C., Jaupart, C., and Bell, D.R., 2007, Transient geotherms in Archean continental lithosphere: New constraints on thickness and heat production of the subcontinental lithospheric mantle: Journal of Geophysical Research: Solid Earth, v. 112, p. 1–17, doi:10.1029/2006JB004464.

Michaut, C., Jaupart, C., and Mareschal, J.C., 2009, Thermal evolution of cratonic roots: Lithos, v. 109, p. 47–60, doi:10.1016/j.lithos.2008.05.008.

Mitchell, R.H., 1995, Kimberlites, Orangeites and Related Rocks:

Mitchell, R.H., 1987, Kimberlites: Mineralogy, Geochemistry, and Petrology: New York, Plenum Press, 442 p.

Mitra, A., Dey, S., Zong, K., Liu, Y., and Mitra, A., 2019, Building the core of a Paleoarchean continent: Evidence from granitoids of Singhbhum Craton, eastern India: Precambrian Research, v. 335, p. 105436, doi:10.1016/j.precamres.2019.105436.

Moorbath, S., O'Nions, R.K., and Pankhurst, R.J., 1973, Early Archaean Age for the Isua Iron Formation, West Greenland: Natuer, v. 245, p. 138–139.

Moorbath, S., O'Nions, R.K., Pankhurst, R.J., Gale, N.H., and McGregor, V.R., 1972, Further Rubidium-Strontium Age Determinations on the Very Early Precambrian Rocks of the Godthaab District, West Greenland: Nature, v. 240, p. 226–229, doi:10.1038/239137a0.

Moore, R.O., Griffin, W.L., Gurney, J.J., Ryan, C.G., Cousens, D.R., Sie, S.H., and Suter, G.F., 1992, Trace element geochemistry of ilmenite megacrysts from the Monastery kimberlite, South Africa: Lithos, v. 29, p. 1–18, doi:10.1016/0024-4937(92)90031-S.

Moorkamp, M., Jones, A.G., and Eaton, D.W., 2007, Joint inversion of teleseismic receiver functions and magnetotelluric data using a genetic algorithm: Are seismic velocities and electrical conductivities compatible? Geophysical Research Letters, v. 34, p. 3–7, doi:10.1029/2007GL030519.

Morton, A.C., and Hallsworth, C.R., 1999, Processes controlling the composition of heavy mineral assemblages in sandstones: Sedimentary Geology, v. 124, p. 3–29, doi:10.1016/S0037-0738(98)00118-3.

Muller, M.R. et al., 2009, Lithospheric structure, evolution and diamond prospectivity of the Rehoboth Terrane and western Kaapvaal Craton, southern Africa: Constraints from broadband magnetotellurics: Lithos, v. 112, p. 93–105, doi:10.1016/j.lithos.2009.06.023.

Nickel, K.G., and Green, D.H., 1985, Empirical geothermobarometry for garnet peridotites and implications for the nature of the lithosphere, kimberlites and diamonds: Earth and Planetary Science Letters, v. 73, p. 158–170, doi:10.1016/0012-821X(85)90043-3.

Nicolaysen, L.O., Hart, R.J., and Gale, N.H., 1981, The Vredefort Radioelement Profile Extended to Supracrustal Strata at Carletonville, With Implications for Continental Heat Flow: Journal of Geophysical Research, v. 86, p. 10653–10661, doi:10.20652/kachikunokanri.20.1_58.

Nimis, P., 2002, The pressures and temperatures of formation of diamond based on thermobarometry of chromian diopside inclusions: Canadian Mineralogist, v. 40, p. 871–884, doi:10.2113/gscanmin.40.3.871.

Nimis, P., and Grütter, H., 2010, Internally consistent geothermometers for garnet peridotites and pyroxenites: Contributions to Mineralogy and Petrology, v. 159, p. 411–427, doi:10.1007/s00410-009-0455-9.

Nimis, P., Preston, R., Perritt, S.H., and Chinn, I.L., 2020, Diamond's depth distribution systematics: Lithos, v. 376–377, p. 105729, doi:10.1016/j.lithos.2020.105729.

Nimis, P., and Taylor, W.R., 2000, Single clinopyroxene thermobarometry for garnet peridotites. Part I. Calibration and testing of a Cr-in-Cpx barometer and an enstatite-in-Cpx thermometer: Contributions to Mineralogy and Petrology, v. 139, p. 541–554, doi:10.1007/s004100000156.

Nowell, G.M., Pearson, D.G., Bell, D.R., Carlson, R.W., Smith, C.B., Kempton, P.D., and Noble, S.R., 2004, Hf isotope systematics of kimberlites and their megacrysts: New constraints on their source regions: Journal of Petrology, v. 45, p. 1583–1612, doi:10.1093/petrology/egh024.

Nyblade, A.A., and Pollack, H.N., 1993, A global analysis of heat flow from Precambrian terrains: implications for the thermal structure of Archean and Proterozoic lithosphere: Journal of Geophysical Research, v. 98, doi:10.1029/93jb00521.

O'Sullivan, G., Chew, D., Kenny, G., Henrichs, I., and Mulligan, D., 2020, The trace element composition of apatite and its application to detrital provenance studies: Earth-Science Reviews, v. 201, p. 103044, doi:10.1016/j.earscirev.2019.103044.

Paces, J.B., and Miller, J.D., 1993, Precise U-Pb ages of Duluth Complex and related mafic intrusions, northeastern Minnesota: Geochronological insights to physical, petrogenetic, paleomagnetic, and tectonomagmatic processes associated with the 1.1 Ga Midcontinent Rift System: Journal of Geophysical Research, v. 98.

Paton, C., Hellstrom, J., Paul, B., Woodhead, J., and Hergt, J., 2011, Iolite: Freeware for the visualisation and processing of mass spectrometric data: Journal of Analytical Atomic Spectrometry, v. 26, p. 2508–2518, doi:10.1039/c1ja10172b.

Pearson, D.G., Carlson, R.W., Shirey, S.B., Boyd, F.R., and Nixon, P.H., 1995a, Stabilisation of Archaean lithospheric mantle: A ReOs isotope study of peridotite xenoliths from the Kaapvaal craton: Earth and Planetary Science Letters, v. 134, p. 341–357, doi:10.1016/0012-821X(95)00125-V.

Pearson, D.G., Scott, J.M., Liu, J., Schaeffer, A., Wang, L.H., van Hunen, J., Szilas, K., Chacko, T., and Kelemen, P.B., 2021, Deep continental roots and cratons: Nature, v. 596, p. 199–210, doi:10.1038/s41586-021-03600-5.

Pearson, D.G., Shirey, S.B., Bulanova, G.P., Carlson, R.W., and Mllledge, H.J., 1999, Re-Os isotope measurements of single sulfide inclusions in a Siberian diamond and its nitrogen aggregation systematics: Geochimica et Cosmochimica Acta, v. 63, p. 703–711, doi:10.1016/S0016-7037(99)00042-3.

Pearson, D.G., Shirey, S.B., Carlson, R.W., Boyd, F.R., Pokhilenko, N.P., and Shimizu, N., 1995b, ReOs, SmNd, and RbSr isotope evidence for thick Archaean lithospheric mantle beneath the Siberian craton modified by multistage metasomatism: Geochimica et Cosmochimica Acta, v. 59, p. 959–977, doi:10.1016/0016-7037(95)00014-3.

Pearson, D.G., Shirey, S.B., Harris, J.W., and Carlson, R.W., 1998, Sulphide inclusions in diamonds from the Koffiefontein kimberlite, S Africa: Constraints on diamond ages and mantle Re-Os systematics: Earth and Planetary Science Letters, v. 160, p. 311–326, doi:10.1016/S0012-821X(98)00092-2.

Pearson, D.G., and Wittig, N., 2008, Formation of Archaean continental lithosphere and its diamonds: the root of the problem: Journal of the Geological Society, v. 165, p. 895–914, doi:10.1144/0016-76492008-003.

Pedersen, H.A., Fishwick, S., and Snyder, D.B., 2009, A comparison of cratonic roots through consistent analysis of seismic surface waves: Lithos, v. 109, p. 81–95, doi:10.1016/j.lithos.2008.09.016.

Perry, H.K.C., Jaupart, C., Mareschal, J.C., and Bienfait, G., 2006a, Crustal heat production in the superior province Canadian shield, and in North America inferred from heat flow data: Journal of Geophysical Research: Solid Earth, v. 111, p. 1–20, doi:10.1029/2005JB003893.

Perry, H.K.C., Mareschal, J.C., and Jaupart, C., 2006b, Variations of strength and localized deformation in cratons: The 1.9 Ga Kapuskasing uplift, Superior Province, Canada: Earth and Planetary Science Letters, v. 249, p. 216–228, doi:10.1016/j.epsl.2006.07.013.

Peslier, A.H., Woodland, A.B., Bell, D.R., and Lazarov, M., 2010, Olivine water contents in the continental lithosphere and the longevity of cratons: Nature, v. 467, p. 78–81, doi:10.1038/nature09317.

Petrus, J.A., and Kamber, B.S., 2012, VizualAge: A Novel Approach to Laser Ablation ICP-MS U-Pb Geochronology Data Reduction: Geostandards and Geoanalytical Research, v. 36, p. 247–270, doi:10.1111/j.1751-908X.2012.00158.x.

Phillips, D., Harris, J.W., and Viljoen, K.S., 2004, Mineral chemistry and thermobarometry of inclusions from De Beers Pool diamonds, Kimberley, South Africa: Lithos, v. 77, p. 155–179, doi:10.1016/j.lithos.2004.04.005.

Pointon, M.A., Cliff, R.A., and Chew, D.M., 2012, The provenance of Western Irish Namurian Basin sedimentary strata inferred using detrital zircon U-Pb LA-ICP-MS geochronology: Geological Journal, v. 47, p. 77–98, doi:10.1002/gj.1335.

Poujol, M., Robb, L.J., Anhaeusser, C.R., and Gericke, B., 2003, A review of the geochronological constraints on the evolution of the Kaapvaal Craton, South Africa: Precambrian Research, v. 127, p. 181–213, doi:10.1016/S0301-9268(03)00187-6.

Priestley, K., and McKenzie, D., 2013, The relationship between shear wave velocity, temperature, attenuation and viscosity in the shallow part of the mantle: Earth and Planetary Science Letters, v. 381, p. 78–91, doi:10.1016/j.epsl.2013.08.022.

Rák, Z., Ewing, R.C., and Becker, U., 2011, Role of iron in the incorporation of uranium in ferric garnet matrices: Physical Review B - Condensed Matter and Materials Physics, v. 84, p. 1–10, doi:10.1103/PhysRevB.84.155128.

Ravenna, M., Lebedev, S., Fullea, J., and Adam, J.M.C., 2018, Shear-Wave Velocity Structure of Southern Africa's Lithosphere: Variations in the Thickness and Composition of Cratons and Their Effect on Topography: Geochemistry, Geophysics, Geosystems, v. 19, p. 1499–1518, doi:10.1029/2017GC007399.

Reich, M., Ewing, R.C., Ehlers, T.A., and Becker, U., 2007, Low-temperature anisotropic diffusion of helium in zircon: Implications for zircon (U-Th)/He thermochronometry>: Geochimica et Cosmochimica Acta, v. 71, p. 3119–3130, doi:10.1016/j.gca.2007.03.033.

Richardson, S.H., Gurney, J.J., Erlank, A.J., and Harris, J.W., 1984, Origins of diamond in old enriched mantle: Nature, v. 310, p. 198–202.

Richardson, S.H., Harris, J.W., and Gurney, J.J., 1993, Three generations of diamonds from old continental mantle: Nature, v. 366, p. 256–258, doi:10.1038/366256a0.

Richardson, S.H., and Shirey, S.B., 2008, Continental mantle signature of Bushveld magmas and coeval diamonds: Nature, v. 453, p. 910–913, doi:10.1038/nature07073.

Richardson, S.H., Shirey, S.B., and Harris, J.W., 2004, Episodic diamond genesis at Jwaneng, Botswana, and implications for Kaapvaal craton evolution: Lithos, v. 77, p. 143–154, doi:10.1016/j.lithos.2004.04.027.

Richardson, S.H., Shirey, S.B., Harris, J.W., and Carlson, R.W., 2001, Archean subduction recorded by Re-Os isotopes in eclogitic sulfide inclusions in Kimberley diamonds: Earth and Planetary Science Letters, v. 191, p. 257–266, doi:10.1016/S0012-821X(01)00419-8.

Robinson, D.N., 1979, Surface textures and other features of diamonds: University of Cape Town (South Africa), vol 1: 221 pp, vol 2: 161 pp p.

le Roex, A.P., and Class, C., 2016, Metasomatic enrichment of Proterozoic mantle south of the Kaapvaal Craton, South Africa: origin of sinusoidal REE patterns in clinopyroxene and garnet: Contributions to Mineralogy and Petrology, v. 171, p. 1–24, doi:10.1007/s00410-015-1222-8.

Rolandone, F., Jaupart, C., Mareschal, J.C., Gariépy, C., Bienfait, G., Carbonne, C., and Lapointe, R., 2002, Surface heat flow, crustal temperatures and mantle heat flow in the Proterozoic Trans-Hudson Orogen, Canadian Shield: Journal of Geophysical Research: Solid Earth, v. 107, p. ETG 7-1-ETG 7-19, doi:10.1029/2001jb000698.

Rudnick, R.L., and Fountain, D.M., 1995, Nature and Composition of the Continental-Crust - a Lower Crustal Perspective: Reviews of Geophysics, v. 33, p. 267–309, doi:10.1029/95rg01302.

Rudnick, R.L., McDonough, W.F., and Chappell, B.W., 1993, Carbonatite metasomatism in the northern Tanzanian mantle: petrographic and geochemical characteristics: Earth and Planetary Science Letters, v. 114, p. 463–475, doi:10.1016/0012-821X(93)90076-L.

Rudnick, R.L., McDonough, W.F., and O'Connell, R.J., 1998, Thermal structure, thickness and composition of continental lithosphere: Chemical Geology, v. 145, p. 395–411, doi:10.1016/S0009-2541(97)00151-4.

Ryan, G., Griffin, W.L., and Pearson, N.J., 1996, Garnet geotherms: Pressure-temperature data from Cr-pyrope garnet xenocrysts in volcanic rocks: Journal of Geophysical Research: Solid Earth, v. 101, p. 5611–5625.

Salnikova, E.B., Chakhmouradian, A.R., Stifeeva, M. V., Reguir, E.P., Kotov, A.B., Gritsenko, Y.D., and Nikiforov, A. V., 2019, Calcic garnets as a geochronological and petrogenetic tool applicable to a wide variety of rocks: Lithos, v. 338–339, p. 141–154, doi:10.1016/j.lithos.2019.03.032.

Salnikova, E.B., Stifeeva, M. V., Nikiforov, A. V., Yarmolyuk, V. V., Kotov, A.B., Anisimova, I. V., Sugorakova, A.M., and Vrublevskii, V. V., 2018, Andradite–Morimotoite Garnets as Promising U–Pb Geochronometers for Dating Ultrabasic Alkaline Rocks: Doklady Earth Sciences, v. 480, p. 778–782, doi:10.1134/S1028334X18060168.

Santosh, M., Hari, K.R., He, X.F., Han, Y.S., and Manu Prasanth, M.P., 2018, Oldest lamproites from Peninsular India track the onset of Paleoproterozoic plume-induced rifting and the birth of Large Igneous Province: Gondwana Research, v. 55, p. 1–20, doi:10.1016/j.gr.2017.11.005.

Sarkar, C., Heaman, L.M., and Pearson, D.G., 2015a, Duration and periodicity of kimberlite volcanic activity in the Lac de Gras kimberlite field, Canada and some recommendations for kimberlite geochronology: Lithos, v. 218–219, p. 155–166, doi:10.1016/j.lithos.2015.01.017.

Sarkar, C., Heaman, L.M., and Pearson, D.G., 2015b, Duration and periodicity of kimberlite volcanic activity in the Lac de Gras kimberlite field, Canada and some recommendations for kimberlite geochronology: Lithos, v. 218–219, p. 155–166, doi:10.1016/j.lithos.2015.01.017.

Schmitz, M.D., Bowring, S.A., de Wit, M.J., and Gartz, V., 2004, Subduction and terrane collision stabilize the western Kaapvaal craton tectosphere 2.9 billion years ago: Earth and Planetary Science Letters, v. 222, p. 363–376, doi:10.1016/j.epsl.2004.03.036.

Seman, S., Stockli, D.F., and McLean, N.M., 2017, U-Pb geochronology of grossular-andradite garnet:

Chemical Geology, v. 460, p. 106–116, doi:10.1016/j.chemgeo.2017.04.020.

Semprich, J., and Simon, N.S.C., 2014, Inhibited eclogitization and consequences for geophysical rock properties and delamination models: Constraints from cratonic lower crustal xenoliths: Gondwana Research, v. 25, p. 668–684, doi:10.1016/j.gr.2012.08.018.

Shchukina, E. V., and Shchukin, V.S., 2018, Diamond exploration potential of the northern East European platform: Minerals, v. 8, p. 1–17, doi:10.3390/min8050189.

Shirey, S.B., Cartigny, P., Frost, D.J., Keshav, S., Nestola, F., Nimis, P., Pearson, D.G., Sobolev, N. V., and Walter, M.J., 2013, Diamonds and the Geology of Mantle Carbon: Reviews in Mineralogy and Geochemistry, v. 75, p. 355–421, doi:10.2138/rmg.2013.75.12.

Shu, Q., Brey, G.P., Gerdes, A., and Hoefer, H.E., 2013, Geochronological and geochemical constraints on the formation and evolution of the mantle underneath the Kaapvaal craton: Lu-Hf and Sm-Nd systematics of subcalcic garnets from highly depleted peridotites: Geochimica et Cosmochimica Acta, v. 113, p. 1–20, doi:10.1016/j.gca.2013.03.010.

Simon, N.S.C., Carlson, R.W., Pearson, D.G., and Davies, G.R., 2007, The origin and evolution of the Kaapvaal Cratonic Lithospheric Mantle: Journal of Petrology, v. 48, p. 589–625, doi:10.1093/petrology/egl074.

Sláma, J. et al., 2008, Plešovice zircon - A new natural reference material for U-Pb and Hf isotopic microanalysis: Chemical Geology, v. 249, p. 1–35, doi:10.1016/j.chemgeo.2007.11.005.

Sleep, N.H., 2003, Survival of Archean cratonal lithosphere: Journal of Geophysical Research: Solid Earth, v. 108, p. 1–29, doi:10.1029/2001jb000169.

Smart, K.A., Tappe, S., Ishikawa, A., Pfänder, J.A., and Stracke, A., 2019, K-rich hydrous mantle lithosphere beneath the Ontong Java Plateau: Significance for the genesis of oceanic basalts and Archean continents: Geochimica et Cosmochimica Acta, v. 248, p. 311–342, doi:10.1016/j.gca.2019.01.013.

Smart, K.A., Tappe, S., Stern, R.A., Webb, S.J., and Ashwal, L.D., 2016, Early Archaean tectonics and mantle redox recorded in Witwatersrand diamonds: Nature Geoscience, v. 9, p. 255–259, doi:10.1038/ngeo2628.

Smith, C.B., 1983, Pb, Sr and Nd isotopic evidence for sources of southern African Cretaceous kimberlites: Nature, v. 304, p. 51–54, doi:10.1038/304051a0.

Smith, C.B., Allsopp, H.L., Kramers, J.D., Hutchinson, G., and C., R.J., 1985, Emplacement ages of Jurassic-Cretaceous South African kimberlites by the Rb-Sr method on phlogopite and whole-rock samples: Transactions of the Geological Society of South Africa, v. 88, p. 249–266.

Smith, C.B., Gurney, J.J., Harris, J.W., Otter, M.L., Kirkley, M.B., and Jagoutz, E., 1991, Neodymium and strontium isotope systematics of eclogite and websterite paragenesis inclusions from single diamonds, Finsch and Kimberley Pool, RSA: Geochimica et Cosmochimica Acta, v. 55, p. 2579–2590, doi:10.1016/0016-7037(91)90374-E.

Spencer, C.J., Kirkland, C.L., and Taylor, R.J.M., 2016, Strategies towards statistically robust interpretations of in situ U-Pb zircon geochronology: Geoscience Frontiers, v. 7, p. 581–589, doi:10.1016/j.gsf.2015.11.006.

Stachel, T., Banas, A., Muehlenbachs, K., Kurszlaukis, S., and Walker, E.C., 2006, Archean diamonds from Wawa (Canada): Samples from deep cratonic roots predating cratonization of the Superior Province: Contributions to Mineralogy and Petrology, v. 151, p. 737–750, doi:10.1007/s00410-006-0090-7.

Stachel, T., and Harris, J.W., 2008, The origin of cratonic diamonds - Constraints from mineral inclusions: Ore Geology Reviews, v. 34, p. 5–32, doi:10.1016/j.oregeorev.2007.05.002.

Stanley, J.R., and Flowers, R.M., 2016, Dating kimberlite emplacement with zircon and perovskite (U-Th)/He geochronology: Geochemistry, Geophysics, Geosystems, v. 17, p. 4517–4533, doi:10.1002/2015GC006171.Received.

Stifeeva, M. V., Salnikova, E.B., Samsonov, A. V., Kotov, A.B., and Gritsenko, Y.D., 2019, Garnet U–Pb Age of Skarns from Dashkesan Deposit (Lesser Caucasus): Doklady Earth Sciences, v. 487, p. 953–956, doi:10.1134/S1028334X19080178.

Sudholz, Z.J., Yaxley, G.M., Jaques, A.L., and Brey, G.P., 2021, Experimental recalibration of the Cr - in - clinopyroxene geobarometer : improved precision and reliability above 4 . 5 GPa: Contributions to Mineralogy and Petrology, doi:10.1007/s00410-020-01768-z.

Sweeney, R.J., Thompson, A.B., and Ulmer, P., 1993, Phase relations of a natural MARID composition and implications for MARID genesis, lithospheric melting and mantle metasomatism: Contributions to Mineralogy and Petrology, v. 115, p. 225–241, doi:10.1007/BF00321222.

Tappe, S., Budde, G., Stracke, A., Wilson, A., and Kleine, T., 2020, The tungsten-182 record of kimberlites above the African superplume: Exploring links to the core-mantle boundary: Earth and Planetary Science Letters, v. 547, p. 116473, doi:10.1016/j.epsl.2020.116473.

Tappe, S., Foley, S.F., Jenner, G.A., Heaman, L.M., Kjarsgaard, B.A., Romer, R.L., Stracke, A., Joy, N., and Hoefs, J., 2006, Genesis of Ultramafic Lamprophyres and Carbonatites at Aillik Bay, Labrador: a Consequence of Incipient Lithospheric Thinning beneath the North Atlantic Craton: Journal of Petrology, v. 47, p. 1261–1315, doi:10.1093/petrology/egl008.

Tappe, S., Foley, S.F., Kjarsgaard, B.A., Romer, R.L., Heaman, L.M., Stracke, A., and Jenner, G.A., 2008, Between carbonatite and lamproite—Diamondiferous Torngat ultramafic lamprophyres formed by carbonate-fluxed melting of cratonic MARID-type metasomes: Geochimica et Cosmochimica Acta, v. 72, p. 3258–3286, doi:10.1016/j.gca.2008.03.008.

Tappe, S., Foley, S.F., Stracke, A., Romer, R.L., Kjarsgaard, B.A., Heaman, L.M., and Joyce, N., 2007, Craton reactivation on the Labrador Sea margins: 40Ar/39Ar age and Sr-Nd-Hf-Pb isotope constraints from alkaline and carbonatite intrusives: Earth and Planetary Science Letters, v. 256, p. 433–454, doi:10.1016/j.epsl.2007.01.036.

Tappe, S., Kjarsgaard, B.A., Kurszlaukis, S., Nowell, G.M., and Phillips, D., 2014, Petrology and Nd-Hf isotope geochemistry of the neoproterozoic amon kimberlite sills, Baffin Island (Canada): Evidence for deep mantle magmatic activity linked to supercontinent cycles: v. 55, 2003–2042 p., doi:10.1093/petrology/egu048.

Tappe, S., Pearson, D.G., Nowell, G., Nielsen, T., Milstead, P., and Muehlenbachs, K., 2011, A fresh isotopic look at Greenland kimberlites: Cratonic mantle lithosphere imprint on deep source signal: Earth and Planetary Science Letters, v. 305, p. 235–248, doi:10.1016/j.epsl.2011.03.005.

Tappe, S., and Simonetti, A., 2012, Combined U-Pb geochronology and Sr-Nd isotope analysis of the Ice River perovskite standard, with implications for kimberlite and alkaline rock petrogenesis: Chemical Geology, v. 304–305, p. 10–17, doi:10.1016/j.chemgeo.2012.01.030.

Tappe, S., Smart, K., Torsvik, T., Massuyeau, M., and de Wit, M., 2018, Geodynamics of kimberlites on a cooling Earth: Clues to plate tectonic evolution and deep volatile cycles: Earth and Planetary Science Letters, v. 484, p. 1–14, doi:10.1016/j.epsl.2017.12.013.

Taylor, W.R., 1998, An experimental test of some geothermometer and geobarometer formulations for upper mantle peridotites with application to the thermobarometry of fertile lherzolite and garnet websterite: Neues Jahrbuch für Mineralogie-Abhandlungen, v. 172, p. 381–408, doi:10.1127/njma/172/1998/381.

Tomlinson, E.L., and Kamber, B.S., 2021, Depth-dependent peridotite-melt interaction and the origin of variable silica in the cratonic mantle: Nature Communications, v. 12, p. 1–15, doi:10.1038/s41467-021-21343-9.

Tomlinson, E.L., Kamber, B.S., Hoare, B.C., Stead, C. V, and Ildefonse, B., 2018, An exsolution origin for Archean mantle garnet: Geology, v. 46, p. 1–4.

Ubide, T., Guyett, P.C., Kenny, G.G., O'Sullivan, E.M., Ames, D.E., Petrus, J.A., Riggs, N., and Kamber, B.S., 2017, Protracted volcanism after large impacts: Evidence from the Sudbury impact basin: Journal of Geophysical Research: Planets, v. 122, p. 701–728, doi:10.1002/2016JE005085.

Ulmer, P., and Sweeney, R.J., 2002, Generation and differentiation of group II kimberlites: Constraints from a high-pressure experimental study to 10 GPa: Geochimica et Cosmochimica Acta, v. 66, p. 2139–2153, doi:10.1016/S0016-7037(02)00898-0.

Vermeesch, P., 2018, IsoplotR: A free and open toolbox for geochronology: Geoscience Frontiers, v. 9, p. 1479–1493, doi:10.1016/j.gsf.2018.04.001.

Viljoen, F., Dobbe, R., and Smit, B., 2009, Geochemical processes in peridotite xenoliths from the Premier diamond mine, South Africa: Evidence for the depletion and refertilisation of subcratonic lithosphere: Lithos, v. 112, p. 1133–1142, doi:10.1016/j.lithos.2009.05.004.

Walker, R.J., Carlson, R.W., Shirey, S.B., and F.R, B., 1989, Os, Sr, Nd, and Pb isotope systematics of southern African peridotite xenoliths: Implications for the chemical evolution of subcontinental mantle: Geochimica et Cosmochimica Acta, v. 53, p. 1583–1595, doi:10.1016/0016-7037(89)90240-8.

Wang, C., Liu, Y., Min, N., Zong, K., Hu, Z., and Gao, S., 2016, Paleo-Asian oceanic subduction-related modification of the lithospheric mantle under the North China Craton: Evidence from peridotite xenoliths in the Datong basalts: Lithos, v. 261, p. 109–127, doi:10.1016/j.lithos.2015.12.011.

Wang, D., Romer, R.L., Guo, J. hui, and Glodny, J., 2020, Li and B isotopic fingerprint of Archean subduction: Geochimica et Cosmochimica Acta, v. 268, p. 446–466, doi:10.1016/j.gca.2019.10.021.

Waters, F.G., 1987, A suggested origin of MARID xenoliths in kimberlites by high pressure crystallization of an ultrapotassic rock such as lamproite: Contributions to Mineralogy and Petrology, v. 95, p. 523–533, doi:10.1007/BF00402210.

Waters, F.G., and Erlank, A.J., 1988, Assessment of the vertical extent and distribution of mantle metasomatism below kimberley, south africa: Journal of Petrology, v. Special_Vo, p. 185–204, doi:10.1093/petrology/Special_Volume.1.185.

Weiss, Y., McNeill, J., Pearson, D.G., Nowell, G.M., and Ottley, C.J., 2015, Highly saline fluids from a subducting slab as the source for fluid-rich diamonds: Nature, v. 524, p. 339–342, doi:10.1038/nature14857.

Westerlund, K.J., Shirey, S.B., Richardson, S.H., Carlson, R.W., Gurney, J.J., and Harris, J.W., 2006, A subduction wedge origin for Paleoarchean peridotitic diamonds and harzburgites from the Panda kimberlite, Slave craton: Evidence from Re-Os isotope systematics: Contributions to Mineralogy and Petrology, v. 152, p. 275–294, doi:10.1007/s00410-006-0101-8.

Wiedenbeck, M., Allé, P., Corfu, A., Griffin, W.L., Meier, M., Oberli, F., Von Quadt, A., C;, R.J., and Spiegel, W., 1995, Three Natural Zircon Standards for U-Th-Pb, Lu-Hf, Trace Element and REE Analyses: Geostandards Newsletter, v. 19, p. 1–26, doi:10.1111/j.1751-908X.1995.tb00147.x.

Wiedenbeck, M., Hanchar, J.M., Peck, W.H., Sylvester, P., Valley, J., Whitehouse, M., Kronz, A., Morishita, Y., and Nasdala, L., 2004, Further Characterisation of the 91500 Zircon Crystal: Geostandards and Geoanalytical Research, v. 28, p. 9–39.

Wilde, S.A., Valley, J.W., Peck, W.H., and Graham, C.M., 2001, Evidence from detrital zircons for the existence of continental crust and oceans on the Earth 4.4 Gyr ago: Nature, v. 409, p. 175–178, doi:10.1038/35051550.

Woodhead, J.D., and Hergt, J.M., 2000, Pb-isotope analyses of USGS reference materials: Geostandards Newsletter, v. 24, p. 33–38, doi:10.1111/j.1751-908X.2000.tb00584.x.

Wu, F.Y., Mitchell, R.H., Li, Q.L., Sun, J., Liu, C.Z., and Yang, Y.H., 2013, In situ UPb age determination and SrNd isotopic analysis of perovskite from the Premier (Cullinan) kimberlite, South Africa: Chemical Geology, v. 353, p. 83–95, doi:10.1016/j.chemgeo.2012.06.002.

Wu, T., Polat, A., Frei, R., Fryer, B.J., Yang, K.G., and Kusky, T., 2016, Geochemistry, Nd, Pb and Sr isotope systematics, and U–Pb zircon ages of the Neoarchean Bad Vermilion Lake greenstone belt and spatially associated granitic rocks, western Superior Province, Canada: Precambrian Research, v. 282, p. 21–51, doi:10.1016/j.precamres.2016.06.021.

Wu, F.Y., Yang, J.H., Xu, Y.G., Wilde, S.A., and Walker, R.J., 2019, Destruction of the north China craton in the mesozoic: Annual Review of Earth and Planetary Sciences, v. 47, p. 173–195, doi:10.1146/annurev-earth-053018-060342.

Wu, C.M., and Zhao, G., 2011, The applicability of garnet-orthopyroxene geobarometry in mantle xenoliths: Lithos, v. 125, p. 1–9, doi:10.1016/j.lithos.2011.02.018.

Yaxley, G.M., Berry, A.J., Rosenthal, A., Woodland, A.B., and Paterson, D., 2017, Redox preconditioning deep cratonic lithosphere for kimberlite genesis - Evidence from the central Slave Craton: Scientific Reports, v. 7, p. 1–10, doi:10.1038/s41598-017-00049-3.

Yaxley, G.M., Crawford, A.J., and Green, D.H., 1991, Evidence for carbonatite metasomatism in spinel peridotite xenoliths from western Victoria, Australia: Earth and Planetary Science Letters, v. 107, p. 305–317, doi:10.1016/0012-821X(91)90078-V.

Youssof, M., Thybo, H., Artemieva, I.M., and Levander, A., 2013, Moho depth and crustal composition in Southern Africa: Tectonophysics, v. 609, p. 267–287, doi:10.1016/j.tecto.2013.09.001.

Zack, T., Stockli, D.F., Luvizotto, G.L., Barth, M.G., Belousova, E., Wolfe, M.R., and Hinton, R.W., 2011, In situ U-Pb rutile dating by LA-ICP-MS: 208Pb correction and prospects for geological applications: Contributions to Mineralogy and Petrology, v. 162, p. 515–530, doi:10.1007/s00410-011-0609-4.

Zartman, R.E., and Richardson, S.H., 2005, Evidence from kimberlitic zircon for a decreasing mantle Th/U since the Archean: Chemical Geology, v. 220, p. 263–283, doi:10.1016/j.chemgeo.2005.04.003.

Zeh, A., Ovtcharova, M., Wilson, A.H., and Schaltegger, U., 2015, The Bushveld Complex was emplaced and cooled in less than one million years - results of zirconology, and geotectonic implications: Earth and Planetary Science Letters, v. 418, p. 103–114, doi:10.1016/j.epsl.2015.02.035.

Zhou, G., Wu, Y., Li, L., Zhang, W., Zheng, J., Wang, H., and Yang, S., 2018, Identification of ca. 2.65 Ga TTGs in the Yudongzi complex and its implications for the early evolution of the Yangtze Block: Precambrian Research, v. 314, p. 240–263, doi:10.1016/j.precamres.2018.06.011.

Zindler, A., and Hart, S.R., 1986, Chemical Geodynamics: Annual Reviews of Earth and Planetary sciences, v. 14, p. 493–571.